Analysis and Modeling of Hydrodynamic Components for Ship Roll Motion in Heavy Weather

by

Christopher C. Bassler

A dissertation submitted to the Faculty of
Virginia Polytechnic Institute and State University
in partial fulfillment of the requirements for the degree of

Doctor of Philosophy

in

Aerospace Engineering

Approved:
Alan J. Brown, Chair
Wayne L. Neu
Eric G. Paterson

Disapproved:
Arthur M. Reed

May 02, 2013
Blacksburg, Virginia, USA

Keywords: ship motions, seakeeping, roll motion, roll damping, added mass, added inertia, bilge keel, dead ship condition, beam seas, large amplitude response, viscous forces, potential flow, piecewise systems, nonlinear dynamics, topside geometry, tumblehome, flared, model experiments

Analysis and Modeling of Hydrodynamic Components for Ship Roll Motion in Heavy Weather

Christopher C. Bassler

Abstract

Ship roll motion has been the subject of many studies, because of the complexities associated with this mode of ship motion, and its impact on operability, safety, and survivability. Estimation and prediction of the energy transfer and dissipation of the hydrodynamic components, added inertia and damping, is essential to accurately describe the roll motions of a ship. This is especially true for ship operations in moderate to extreme sea conditions. In these conditions, a complex process of energy transfer occurs, which alters the physical behavior of the hydrodynamic components, and ultimately affects the amplitude of ship roll motion.

Bilge keels have been used on ships for nearly two centuries, to increase damping and reduce the severity of roll motions experienced by a ship in waves. Because ship motions are more severe in extreme sea conditions, large roll angles may occur. With the possibility of crew injury, cargo damage, or even capsize, it is important to understand the behavior of the roll added inertia and damping for these conditions. Dead ship conditions, where ships may experience excitation from beam, or near beam, seas present a worst case scenario in heavy weather. The behavior of a ship in this condition should be considered in both the design and assessment of seakeeping performance.

In this study, hydrodynamic component models of roll added inertia and roll damping were examined and assessed to be unsuitable for accurate prediction of ship motions in heavy weather. A series of model experiments and numerical studies were carried out and analyzed to provide improved understanding of the essential physical phenomena which affect the hydrodynamic components and occur during large amplitude roll motion. These observations served to confirm the hypothesis that the existing models for roll added inertia and damping in large amplitude motions are not sufficient. The change in added inertia and damping behavior for large roll motion is largely due to the effects of hull form geometry, including the bilge keels and topside geometry, and their interactions with the free surface. Therefore, the changes in added inertia and damping must be considered in models to describe and predict roll motions in severe wave environments.

Based on the observations and analysis from both experimental and numerical methods, several time-domain model formulations were proposed and examined to model hydrodynamic components of large amplitude roll motions. These time-domain formulations included an analytical model with memory effects, a piecewise formulation, and several possibilities for a bilge keel force model. Although a piecewise model for roll damping was proposed, which can improve the applicability of traditional formulations for roll damping to heavy weather conditions, a further attempt was undertaken to develop a more detailed model specifically for the bilge keel force. This model was based on the consideration of large amplitude effects on the hydrodynamic components of the bilge keel force. Both the piecewise and bilge keel force models have the possibility to

enable improved accuracy of potential flow-based numerical prediction of ship roll motion in heavy weather. However, additional development remains to address issues for further practical implementation.

Dedication

For my wife, Kayleen

And to future sailors, with the hope that scientific progress will help make their voyages across the seas, especially in perilous conditions, ever safer.

Acknowledgements

The work for this dissertation has been supported by the Office of Naval Research (ONR), under the direction of Dr. Pat Purtell, and by the Independent Applied Research (IAR) program at the Naval Surface Warfare Center, Carderock Division (NSWCCD), under the direction of Dr. John Barkyoumb. I am grateful to both Dr. Purtell and Dr. Barkyoumb for their support and encouragement of this research.

I would like to express my deep appreciation to my committee members for their guidance, support, and encouragement. Since my undergraduate studies, Dr. Brown has been a constant inspiration for further research into ship dynamics and ship design. Since my time at NSWCCD, Dr. Reed has been a mentor and I appreciate his efforts to encourage me to always look a little deeper and be more critical with analysis. Both Dr. Reed and Dr. Brown's patience and support during the long period to undertake this research, coupled with distractions from my day-job, enabled me to complete it. I would also like to thank Dr. Neu and Dr. Paterson for their helpful suggestions with my research.

I would like to thank the management of the NSWCCD Hydromechanics Department (Code 50) and the Seakeeping Division (Code 5500) for continued support and encouragement throughout this work, specifically Jon Etxegoien, Martin Dipper, Dr. Thomas Fu, and Terry Applebee. I would also like to thank Jim Webster (NAVSEA 05) and Nate McKenzie (Fulcrum) for their friendship and encouragement.

I would also like to recognize and express my appreciation to my parents, and many of my friends and colleagues for their support and encouragement. In particular, I would like thank the following people for their specific contributions and support of this work.

In Chapter 2, Justin Freimuth and Larry Leibman (DRS) provided some helpful discussions and additional proof-reading corrections for the equations in the review of the component based frequency-domain model. Dr. Toru Katayama (Osaka Prefecture University) also provided some helpful discussions regarding recent work in Japan to update the frequency-domain component based model for roll damping. Dr. Piotr Bandyk (DRS) also first identified the limitation associated with the wave-making damping component and the consideration of low-frequency effects and memory effects.

Ron Miller (NSWCCD) generated the URANS numerical data using CFDShip-Iowa, presented in Chapters 3 and 5, which has been developed under the support of Dr. Purtell. Dr. Pablo Carrica (University of Iowa) has provided continued guidance and support in using CFDShip-Iowa. The U.S. Department of Defense's High Performance Computing Modernization Program (HPCMP) office provided the computer resources, at NAVO on the IBM P6, for the investigation discussed in Chapters 3 and 5.

Scott Percival, Lisa Minnick, Jesse Geisbert, Dave Grant, and Jason Carneal (NSWCCD) provided invaluable contributions to the set-up and execution of the experiment discussed in Chapter 4. Todd Carrico (formerly NSWCCD) provided helpful discussions related to the experimental design. The design and construction of the 3DoF motion mechanism was also supported by the NSWCCD Independent Applied Research (IAR) program, under the direction of Dr. Barkyoumb. Dave Grant, Scott Percival, and Donnie Walker were collaborators on the design, construction, and testing of the

mechanism. Barry Gleit (G&G Technical, Inc) assembled the control box used with the 3DoF mechanism and Baldwin Britton (BMT Designers & Planners) assisted with the initial construction and control programming of the mechanism. Donnie Walker, Dave Bochinski, Brian Chirozzi, and Kathy Wilson (NSWCCD) also provided additional assistance with the instrumentation for the experiment. Lisa Minnick and Lauren Hanyok (NSWCCD) carried out the initial processing of the PIV data.

Tim Smith (NSWCCD) provided support for performing the WAMIT calculations presented in Chapter 5.

Dr. Vadim Belenky (NSWCCD) also provided helpful discussions regarding the properties of piecewise systems and statistical evaluations of roll motion response, which contributed to the developments presented in Chapter 6.

Table of Contents

ABSTRACT ..... **I**

TABLE OF CONTENTS ..... **VII**

TABLE OF FIGURES ..... **XI**

TABLE OF TABLES ..... **XXI**

NOMENCLATURE ..... **XXIII**

CHAPTER 1 INTRODUCTION AND MOTIVATION **1**

1.1 Introduction and Motivation 1
1.2 The Importance of Hydrodynamic Components in the Ship Equations of Motion 2
1.3 The Significance of Bilge Keels 3
1.4 Large Amplitude Ship Roll Motions 3
1.5 Research Storyline 7
1.6 Dissertation Objectives 8
1.7 Dissertation Outline 9

CHAPTER 2 A REVIEW OF HYDRODYNAMIC COMPONENT MODELS **11**

2.1 Overview 11
2.2 Coordinate System 11
2.3 Roll Added Inertia and Damping in Ship Motions 11
2.4 Roll Damping- Energy Dissipation for Ship Motions 13
2.5 The Importance of Roll Inertia and Damping for Large Amplitude Ship Motions 14
2.6 Roll Motion Models in Potential Flow Simulations 15
2.6.1 Frequency-Domain Models: Component Based Approaches *15*
2.6.1.1 Non-Dimensionalization of Roll Damping Components 18
2.6.1.2 Component Based Models: Assumptions and Limitations 18
2.6.2 Time-Domain Models *20*
2.6.2.1 Time-Domain Models: Assumptions and Limitations 21
2.6.3 Roll Damping in Irregular Waves *21*
2.6.4 Additional Considerations for Roll Motion Models in Potential Flow Simulations *22*
2.7 Bilge Keel Force Models 23
2.7.1 Morison Equation Based Models *24*
2.7.2 Unsteady Lifting Surface Models *24*
2.7.3 Bilge Keel Force Models: Assumptions and Limitations *25*
2.8 Memory Effects and Roll Damping 25
2.9 Further Considerations for this Investigation 26

CHAPTER 3 NUMERICAL (URANS) MODELING, RESULTS, AND ANALYSIS TO ASSESS THE OVERALL PROBLEM OF LARGE AMPLITUDE SHIP ROLL MOTION **27**

3.1 Overview 27
3.2 Hull Form Geometry 28
3.3 URANS Simulations 29
3.3.1 Solver *29*
3.3.2 Obtaining Segmented Forces *29*
3.3.3 Simulation Conditions *30*
3.4 Results 31
3.4.1 3D and Forward Speed Effects *31*
3.4.2 Large Amplitude Roll Motion Effects *37*

3.4.3 Wave Effects *37*
3.4.4 Maneuvering Effects *40*
3.4.5 Observations from the Numerical Results *41*
3.5 Assessment of the Physical Effects for Simulations of Ship Motion in Heavy Weather 41
3.5.1 Relative Importance of the Physical Effects *42*
3.5.2 Implications for Potential Flow Simulations of Ship Motion in Heavy Weather *43*

CHAPTER 4 OBSERVATIONS AND ANALYSIS OF LARGE AMPLITUDE SHIP ROLL MOTION USING EXPERIMENTALMETHODS 45

4.1 Overview 45
4.2 Experimental Objective 45
4.3 Experimental Design 45
4.3.1 Model Design and Construction *46*
4.3.2 Instrumentation and Uncertainty *47*
4.3.3 3DoF Forced Motion Mechanism *47*
4.4 Experimental Set-Up and Test Procedures 49
4.4.1 NSWCCD 140 ft Basin and Model Configuration *49*
4.4.2 PIV Set-Up *51*
4.4.3 Data Collection and Procedures *53*
4.4.4 Test Conditions *55*
4.4.4.1 Topside Configuration 55
4.4.5 Roll Decays *55*
4.4.5.1 Forced Oscillation Conditions 56
4.5 Summary of the Experimental Results 56
4.5.1 Forced Roll Oscillation Measurements *56*
4.5.1.1 Measurement Noise and Repeatability 56
4.5.1.2 Sample Synchronized Measurements 57
4.5.1.3 Bilge Keel Force Measurements 59
4.6 Harmonic Analysis of the Data 62
4.6.1 Decomposition into Added Inertia and Damping *62*
4.6.2 Harmonic Analysis of the Resulting Added Inertia and Damping *63*
4.6.2.1 Hydrodynamic Components as a Function of Roll 63
4.6.2.2 Hydrodynamic Components as a Function of Hydrodynamic Roll Moment 64
4.6.2.3 Hydrodynamic Components as a Function of the Hydrodynamic Roll Moment due to the Bilge Keels 66
4.6.2.4 Frequency Dependence 69
4.6.3 Summary of the Harmonic Analysis Results for Added Inertia and Damping *69*
4.7 Characterization of the Physical Phenomena 70
4.7.1 Bilge Keel Transition at the Free Surface *70*
4.7.2 Vortex Shedding From the Bilge Keel *72*
4.7.3 Deck Edge Interaction with the Free Surface *72*
4.7.4 Near-Field Ship Wave Generation *75*
4.7.5 Frequency Dependence *75*

CHAPTER 5 OBSERVATIONS AND ANALYSIS OF LARGE AMPLITUDE SHIP ROLL MOTION USING NUMERICALMETHODS 77

5.1 Overview 77
5.2 Zero Speed, 2D Numerical Calculations 77
5.2.1 WAMIT Results *78*
5.2.2 Observations from the WAMIT Results *79*
5.3 Examination of 3D Effects on the Bilge Keel Force Using URANS Simulations 83

CHAPTER 6 ON THE DEVELOPMENT OF HYDRODYNAMIC COMPONENT MODELS APPLICABLE TO LARGE AMPLITUDE SHIP ROLL MOTION 89

6.1 Overview 89
6.2 Prioritization of Effects to Include in a Time-Domain Model of Large Amplitude Ship Motion .89
6.2.1 Frequency Dependence of Damping *92*

6.2.2 Development of a Kernel Function Using the Experimental Data *95*
6.2.3 Comparison of Effect of Kernel Function Damping and Constant Damping Formulations on the Roll Motion Response of a 1DoF System in Irregular Waves *98*
6.2.4 The Development of Large Amplitude Ship Roll Motion Models Considering the Relative Importance of Memory and Amplitude Effects *100*
6.2.5 On the Development of Models for Large Amplitude Ship Roll Motion *101*
6.3 Development of a Piecewise Model 101
6.3.1 Physical Phenomena *102*
6.3.2 A Piecewise Method *102*
6.3.2.1 Method Overview 103
6.3.2.2 Properties of a Dynamical System with Piecewise Damping 104
6.3.2.3 Formulation 107
6.3.3 A Case Study for the Piecewise Damping Model *107*
6.3.3.1 Physical Thresholds 108
6.3.3.2 Initialization Values- Small Amplitude Roll Damping 109
6.3.3.3 Solutions for Large Amplitude Roll Damping 109
6.3.3.4 Roll Response 110
6.3.3.5 An Engineering Approximation for Practical Implementation 110
6.3.4 Application of the Piecewise Model *111*
6.3.4.1 Compatibility 111
6.3.4.2 Adaptability for Models with Increased Complexity 112
6.3.4.3 Evaluation of Large Amplitude Ship Roll Damping in Irregular Waves 113
6.3.4.3.1 Method 113
6.3.4.3.2 Practical Implementation 113
6.4 A Bilge Keel Force Model for Large Amplitude Roll Motion 114
6.4.1 Bilge Keel Models and Large Amplitude Ship Roll Motion *115*
6.4.2 Bilge Keel Wave-Making Component *115*
6.4.3 Models for Bilge Keel Transition *117*
6.4.3.1 Sigmoid Function 118
6.4.3.2 Gompertz Function 119
6.4.3.3 Generalized Logistic Function- "Richards' Curve" 120
6.4.3.4 Assumptions and Limitations 120

CHAPTER 7 CONCLUSIONS AND POSSIBLE AREAS FOR FUTURE WORK 121

7.1 Summary 121
7.2 Areas for Future Work 124

REFERENCES 125

APPENDIX A: ADDITIONAL DETAILS ON THE STATE-OF-THE-ART MODELS 137

A.1 Overview 137
A.2 Equations for Roll Damping Components 137
A.2.1 Hull Friction Damping *137*
A.2.2 Hull Eddy Damping *138*
A.2.3 Hull Lift Damping *139*
A.2.4 Hull Wave-Making Damping *140*
A.2.5 Bilge Keel Damping *140*
A.2.5.1 Bilge Keel Normal Force Damping 140
A.2.5.2 Bilge Keel Hull Interaction Damping 141
A.2.5.3 Bilge Keel Wave-Making Damping 142
A.3 Calculation of the Roll Axis 143
A.4 Methods for Obtaining Roll Damping 144
A.4.1 Roll Decay Tests *144*
A.4.2 Forced Oscillation Tests *145*
A.5 A Derivation of a Morison Equation Based Approach for a Bilge Keel Force Model 146
A.6 A Zero Speed Bilge Keel Force Model 147
A.7 Specification of Coefficients and KC Number Dependency 148
A.8 Additional Considerations for Bilge Keel Force Models 149

A.8.1 Multiple Degree-of-Freedom Ship Motions *149*
A.8.2 Wave Effects *150*
A.8.3 Forward Speed Effects *151*

APPENDIX B: DETAILS OF THE URANS COMPUTATIONS 153

B.1 Overview 153
B.2 URANS Solver 153
B.2 Dynamic Overset Grids 154
B.2 Computational Domain 155

APPENDIX C: DETAILS OF THE EXPERIMENTAL SET-UP AND INSTRUMENTATION 159

C.1 Details of the Experimental Design 159
C.1.1 Model Properties and Construction *159*
C.1.2 Model Ballasting *160*
C.1.3 Instrumentation and Uncertainty *162*
C.1.3.1 Force and Moment Measurements on the Hull 162
C.1.3.2 Force and Moment Measurements on the Bilge Keel 163
C.1.3.3 Motion Measurements on the Hull 165
C.1.3.4 Near-Field Wave Measurements 167
C.1.3.5 Velocity-Field Measurements 167
C.1.4 Details of the 3DoF Motion Mechanism- Theory and Design *170*
C.1.4.1 Control Theory 173
C.1.4.2 Construction and Installation 173
C.1.4.3 Mechanism Control and Software 174
C.2 Details of the Experimental Set-Up and Test Procedures 176
C.2.1 Model Configuration for Roll Decay Experiments *176*
C.3 Details of the Experimental Results 176
C.3.1 Roll Decay Results *177*
C.3.2 Measurement Noise *180*
C.3.3 Repeatability of the Experimental Results *181*

APPENDIX D: ADDITIONAL DATA FROM THE EXPERIMENTAL ANALYSIS AND OBSERVATIONS 189

D.1 Hydrostatics 189
D.2 Sample Measurements of the Hydrodynamic Components 189
D.3 Variation in the Bilge Keel Force with Roll Amplitude and Roll Frequency 190
D.4 Proportion of the Hydrodynamic Roll Moment Due to the Bilge Keels 197
D.5 Decomposition of the Hydrodynamic Components of the Bilge Keel Force 198
D.5.1 Decomposition of the Hydrodynamic Roll Moment *198*
D.5.2 Comparison of the Hydrodynamic Components of the Bilge Keel Roll Moment for the Starboard Side Bilge Keel *201*
D.6 Analysis of Added Inertia and Damping from Experimental Measurements 202
D.7 Harmonic Analysis of the Hydrodynamic Components 212
D.8 Hydrodynamic Components as a Function of Amplitude and Topside Configuration 215
D.8.1 Hydrodynamic Components as a Function of Amplitude and Topside for 2.17 rad/s *216*
D.8.2 Hydrodynamic Components as a Function of Amplitude and Topside for 2.85 rad/s *223*
D.9 Vortex Shedding from the Bilge Keels 229
D.10 Variations in the Center of Pressure on the Bilge Keel 233

APPENDIX E: ADDITIONAL DATA FROM THE NUMERICAL ANALYSIS AND OBSERVATIONS OF THE WAMIT RESULTS 237

Table of Figures

Figure 1-1. USS *Essex* in heavy seas (c. 1960) 4
Figure 1-2. A traditional notional naval combatant model (DTMB Model #5514) in hurricane sea conditions, experiencing a large roll angle with bilge keel emergence on the starboard side and deck submergence on the port side 4
Figure 1-3. ONR Tumblehome experiencing large roll after broaching, with bilge keel emergence occurring on the port side 5
Figure 1-4. Cruise ship *Voyager* in a storm in the Mediterranean, as viewed from a helicopter, experiencing large roll motions, resulting in bilge keel emergence 5
Figure 1-5. Large roll angle experienced by the USS *Cowpens*, during Typhoon COBRA (Halsey's Typhoon), 18 December 1944. The ship experienced up to 47 degrees of roll. 6
Figure 1-6. A large roll angle, coupled with waves, results in deck submergence and wetness on the flight deck, aft on a U.S. naval vessel 6
Figure 1-7. Ship in storm conditions, with starboard deck submergence 7
Figure 2-1. Ship-fixed coordinate system reference 11
Figure 2-2. Application of split-time method for the case of changing stability in waves (from Belenky, et al., 2010) 15
Figure 2-3. Relative magnitude of roll damping components, as a function of roll amplitude (from Himeno, 1981) 17
Figure 2-4. Relative magnitude of roll damping components, as a function of roll frequency (from Himeno, 1981) 17
Figure 2-5. Relative magnitude of roll damping components, as a function of forward speed (from Himeno, 1981) 18
Figure 2-6. Bilge keel force, for zero speed, view of the starboard bilge keel, looking forward (from Themelis, 2008) 23
Figure 2-7. Unstead lifting surface (ULS) approach for bilge keel force model (from Greeley and Petersen, 2010) 25
Figure 3-1. Numerical simulation of a naval combatant in heavy seas, experiencing large roll motion, resulting in partial emergence of the starboard bilge keel 27
Figure 3-2. Experimental (Bassler, et al., 2007) and numerical (Miller, et al., 2008) observations of partial bilge keel emergence for DTMB Model #5613-1 at Fn = 0.30, ϕ= 30 deg. 28
Figure 3-3. Post-processing example of longitudinal segments for the hull, with the bow section shown, up to the instantaneous waterline 30
Figure 3-4. DTMB Model #5613-1 with bilge keel divided into 20 segments (shown in red and black) for sectional force analysis 30
Figure 3-5. Simulated axial vorticity contours for DTMB Model 5613-1, at Fn = 0.30, ϕ= 15 deg, ω = 4.83 rad/s, (a) counter-clockwise rotation and (b) clockwise rotation (from Miller, et al., 2008) 32
Figure 3-6. Axial vorticity for DTMB Model 5613-1 at various longitudinal locations, for zero speed (left) and forward speed (right) conditions, ϕ = 25 deg, ω = 2.85 rad/s 33
Figure 3-7. Axial vorticity along the bilge keels, near the midship section of DTMB Model 5613-1, for zero speed (left) and forward speed (right) conditions, ϕ = 25 deg, ω = 2.85 rad/s 33
Figure 3-8. Bilge keel force comparisons between 3D URANS simulations for zero speed (solid black) and forward speed (solid green) for the midship section of DTMB Model 5613-1 at ω = 2.85 rad/s, for ϕ = 15, 25, 30 and 35 deg roll 34
Figure 3-9. Vorticity shown at the locations of bilge keel force sectional analysis: leading edge (LE), forward section (at x/L = 0.4), midship section (at x/L = 0.5), and aft section (x/L = 0.6) 35
Figure 3-10. Unit bilge keel force for DTMB Model 5613-1, at leading edge (black), forward (red), midship (green), and aft (blue) locations, for zero speed (top) and forward speed (bottom) conditions, ϕ = 25 deg, ω = 2.85 rad/s 36
Figure 3-11. Unit bilge keel force for DTMB Model 5613-1, at leading edge (black), forward (red), midship (green), and aft (blue) locations, for zero speed (top) and forward speed (bottom) conditions, ϕ = 35 deg, ω = 2.85 rad/s 37
Figure 3-12. Force on the midship section of the port side bilge keel for 25 (solid) and 35 (dotted) deg roll. Wave phase with crest corresponding to peak of the roll cycle (at t/T = 3/4). 38

Figure 3-13. Force on the midship section of the port side bilge keel for 25 (solid) and 35 (dotted) deg roll. Wave phase with trough corresponding to peak of the roll cycle (at t/T = 3/4). 39
Figure 3-14. Force on the midship section of the port side bilge keel for 25 (solid) and 35 (dotted) deg roll. Wave phase, front slope corresponding to peak of the roll cycle (at t/T = 3/4).....39
Figure 3-15. Force on the midship section of the port side bilge keel for 25 (solid) and 35 (dotted) deg roll. Wave phase, back slope corresponding to peak of the roll cycle (at t/T = 3/4).....39
Figure 3-16. Pressure contours on the submerged portion of the DTMB Model 5613-1, for drift from the windward side (+10 deg), looking aft from the bow. 40
Figure 3-17. Longitudinal distribution of force along the port side bilge keel for drift from the windward and leeward sides (±10 deg).....40
Figure 4-1. ONR Topside Series, flared (left) and tumblehome (right) configurations, with midship sections identified.....46
Figure 4-2. Midship section of the ONR Topside Series, tumblehome configuration (left) and flared configuration (right) with 1.25m bilge keels 47
Figure 4-3. 1DoF roll mechanism, as used for the investigation of Bassler, et al. (2007), with constraints to 30 degrees of roll, due to model side wall deck edge interference with the strut from the motion mechanism.....48
Figure 4-4. Ship model experiencing forced roll motion with a 6DoF motion mechanism (de Jong and Keuning, 2006).....49
Figure 4-5. 3DoF motion mechanism CAD assembly.....49
Figure 4-6. Dimensions of the 140 ft Basin at NSWCCD.....50
Figure 4-7. Illustration of the experimental set-up in the NSWCCD 140 ft basin, with PIV laser on the east side of the basin (in green), facing west 50
Figure 4-8. Model rolled, while attached to the 3DoF mechanism with submerged PIV laser probes (bottom right, facing West) and camera (bottom left, facing North) shown 51
Figure 4-9. PIV set-up in the NSWCCD 140 ft basin, looking East, with camera (right) and calibration target with laser probes (left) shown 52
Figure 4-10. Model shown in roll motion (without bilge keels), with PIV particles on the free surface after seeding.....53
Figure 4-11. Custom designed seeding mechanism shown being used to seed particles in the PIV measurement plane near the hull 53
Figure 4-12. Data collection interfaces, not including PIV, ultrasonic wave probes (top), gyroscopes (top middle), bilge keels (lower middle), and Kistler dynamometer (lower).....54
Figure 4-13. Hook-gages and inclinometer used to check the heel angle of the model.....54
Figure 4-14. Zero position used to center the model in the experimental set-up.....55
Figure 4-15. Unfiltered measurements for ϕ=15 deg, ω= 2.5 rad/s for DTMB Model #5699-1, after peak of the roll cycle. Camera (top left), PIV with bilge keel force vector (top right), roll, roll rate and roll acceleration (middle left), total roll moment and bilge keel portion of the roll moment (middle right), bilge keel force (bottom left), and wave elevation (bottom right) measurements are shown for the instant in time noted by the vertical line.....57
Figure 4-16. Unfiltered measurements for ϕ=35 deg, ω= 2.5 rad/s for DTMB Model #5699-1 after bilge keel re-entry. Camera (top left), PIV with bilge keel force vector (top right), roll, roll rate and roll acceleration (middle left), total roll moment and bilge keel portion of the roll moment (middle right), bilge keel force (bottom left), and wave elevation (bottom right) measurements are shown for the instant in time noted by the vertical line.....58
Figure 4-17. Filtered roll motion measurements and bilge keel force measurements for the DTMB Model #5699, at various roll amplitudes, ϕ=15 (purple), 25 (black), 30 (red), 35 (green) and 40 (blue) deg, ω= 2.5 rad/s, with distinct physical phenomena identified at various stages in the roll cycle.....59
Figure 4-18. Filtered roll motion measurements and starboard bilge keel force measurements for the DTMB Model #5699, at various roll amplitudes, ϕ=15 (purple), 25 (black), 30 (red), 35 (green) and 40 (blue) deg, ω= 2.5 rad/s, with corresponding positions of the starboard bilge keel identified at various stages in the roll cycle 60
Figure 4-19. Filtered roll motion measurements and bilge keel force measurements for the DTMB Model #5699-1, at various roll amplitudes, ϕ=15 (purple), 25 (black), 30 (red), 35 (green), 40 (blue), and 45

(orange) deg, ω= 2.5 rad/s, with distinct physical phenomena identified at various stages in the roll cycle 61
Figure 4-20. Comparison of the magnitude of the sum of the first 10 harmonics of added inertia and damping for roll motion, for DTMB Models #5699 and #5699-1, with and without bilge keels, ω=2.5 rad/s 64
Figure 4-21. Comparison of the magnitude of the sum of the first 10 harmonics of added inertia and damping for the total unit hydrodynamic roll moment, for DTMB Models #5699 and #5699-1, with and without bilge keels, ω=2.5 rad/s 65
Figure 4-22. Comparison of the magnitude of the sum of the first 10 harmonics of damping for the total unit hydrodynamic roll moment, for DTMB Models #5699 and #5699-1, with bilge keels and with the effective influence of the bilge keels, ω=2.5 rad/s 66
Figure 4-23. Comparison of the magnitude of the sum of the first 10 harmonics of added inertia and damping for the unit hydrodynamic roll moment due to the starboard bilge keel, for DTMB Models #5699 and #5699-1, ω=2.5 rad/s 68
Figure 4-24. Comparison of the magnitude of the sum of the first 10 harmonics of added inertia for the unit hydrodynamic roll moment due to the starboard bilge keel, for DTMB Models #5699 and #5699-1, with and without bilge keels, ω=2.5 rad/s 68
Figure 4-25. Comparison of the magnitude of the sum of the first 10 harmonics of damping for the unit hydrodynamic roll moment due to the starboard bilge keel, for DTMB Models #5699 and #5699-1, with and without bilge keels, ω=2.5 rad/s 69
Figure 4-26. Measurements for ϕ=15 deg, ω= 2.5 rad/s for DTMB Model #5699-1, near peak of the roll cycle when the bilge keel is fully submerged. Camera (left), and PIV with bilge keel force vector (right) measurements are shown. 71
Figure 4-27. Measurements for ϕ=35 deg, ω= 2.5 rad/s for DTMB Model #5699-1 after bilge keel re-entry, near peak of the roll cycle when the bilge keel is fully submerged. Camera with air entrainment (left), and PIV with bilge keel force vector (right) measurements are shown 71
Figure 4-28. PIV measurements for ϕ=25 deg, ω= 2.5 rad/s for DTMB Model #5699-1, with bilge keel force measurements shown (red vector). Single roll cycle shown (left to right, top to bottom), beginning after bilge keel re-entry (top left), near peak of the roll cycle when the bilge keel is fully submerged (middle right), and then transitioning to bilge keel emergence (bottom right) 73
Figure 4-29. PIV measurements for ϕ=40 deg, ω= 2.5 rad/s for DTMB Model #5699-1, with bilge keel force measurements shown (red vector). Single roll cycle shown (left to right, top to bottom), beginning after bilge keel re-entry (top left), near peak of the roll cycle when the bilge keel is fully submerged (middle left), and then transitioning to bilge keel emergence (bottom right).....74
Figure 5-1. Comparison of the total unit hydrodynamic roll moment magnitude due to radiation and the added inertia and damping due to radiation for the ONRFL vs heel angle, for ω=2.5 rad/s, with and without bilge keels.....78
Figure 5-2. Comparison of added inertia and damping due to radiation for the ONRTH vs heel angle, for ω=2.5 rad/s, with and without bilge keels 79
Figure 5-5-3. ONRFL added inertia due to radiation vs heel angle vs frequency, with bilge keels 81
Figure 5-5-4. ONRTH added inertia due to radiation vs heel angle vs frequency, with bilge keels.....81
Figure 5-5-5. ONRFL damping due to radiation vs heel angle vs frequency, with bilge keels.....82
Figure 5-5-6. ONRTH damping due to radiation vs heel angle vs frequency, with bilge keels 82
Figure 5-7. Bilge keel force comparisons between 2D (solid blue) and 3D midship section cut (solid black) URANS simulations for DTMB Model 5613-1 and 2D model experiments (solid red) at Fn = 0.0, ω = 2.85 rad/s, for ϕ = 15, 25, 30 and 35 deg roll 85
Figure 5-8. DTMB Model #5613-1 (hull with skeg and bilge keels), computed roll moment due to piezometric pressure for Fr = 0.0, φ = 15 deg, ω = 3.81 rad/s (solid) and ω = 4.83 rad/s (dashed) (from Miller, et al. 2008).....86
Figure 5-9. DTMB Model #5613-1 (hull with skeg and bilge keels), computed roll moment moment due to piezometric pressure for ω = 3.81, φ = 15 deg, Fr = 0.0 (solid) and Fr = 0.30 (dashed) (from Miller, et al. 2008).....86
Figure 5-10. DTMB Model #5613-1 vorticity at the midship section for Fr = 0.30, φ = 30 deg and ω= 4.83 rad/s (from Miller, et al. 2008) 87
Figure 6-1. Example of a roll motion kernel function, computed for a fishing vessel (from Tigkas, 2007) .91

Figure 6-2. Components of the roll damping coefficient vs roll frequency for a ship hull (at zero speed); from Ikeda, et al. (1978). Damping for Series 60, C_B=0.70, without (top left) and with (top right) bilge keels, as well as with bilge keels (bottom right) for increased C_B. Bottom right shows comparisons of damping, with and without bilge keels, for varied roll amplitudes.....94
Figure 6-3. Bilge keel normal force damping vs roll amplitude, with varied roll frequencies shown, calculated using Ikeda's method for Series 60, C_B=0.60, at zero speed; from Bassler & Reed (2009) 95
Figure 6-4. Equivalent linear roll damping coefficient vs roll frequency, with contributions shown from various damping components, B_L, B_E, B_{BKN}, B_{BKH}, B_F, B_W, B_{BKW}; from Himeno (1981) 95
Figure 6-5. Damping coefficient as a function of frequency (rad/s), using the experimental results for φ_A= 15 deg, for the 2D ONRTH, as well as extrapolated values beyond the frequency regime from the experiment. 96
Figure 6-6. Damping coefficient as a function of frequency (rad/s), using the experimental results for φ_A = 35 deg, for the 2D ONRTH, as well as extrapolated values beyond the frequency regime from the experiment. 96
Figure 6-7. Representative kernel function vs time (s), computed using damping, based on experimental measurements for φ_A = 15 deg, for the 2D ONRTH 97
Figure 6-8. Representative kernel function vs time (sec), computed using damping, based on experimental measurements for φ_A = 35 deg, for the 2D ONRTH 97
Figure 6-9. GZ Curve (m) of the 2D ONRTH, φ in rad. 99
Figure 6-10. Sample realization of roll motion response (in rad), using kernel damping based on experimental measurements for φ_A = 35 deg, for the 2D ONRTH 99
Figure 6-11. Comparison of standard deviation of roll motion response, with corresponding variance shown, for an ensemble average of three 1DoF roll motion realizations using constant damping or a kernel formulation for damping of the 2D ONRTH 100
Figure 6-12: Simple illustration of the physical boundaries for large amplitude roll, resulting in bilge keel and deck interaction with the free surface, as defined by angles α and β, respectively 103
Figure 6-13: Simple illustration of hypothesized damping coefficients, δ_i, and transitions for various physical regimes, α and β, as defined by roll angle, ϕ 104
Figure 6-14. A single degree-of-freedom oscillator system with linear (solid black line) and piecewise constant (dotted blue line) damping, as a function of amplitude 105
Figure 6-15. Response for a single degree-of-freedom free oscillator with linear (solid black line) and piecewise constant (dotted blue line) damping.....105
Figure 6-16. Phase plot for a single degree-of-freedom free oscillator with linear (solid black line) and piecewise constant (dotted blue line) damping, with regions of damping transition identified (in gray) 106
Figure 6-17. Response for a single degree-of-freedom forced oscillator with linear (solid black line) and piecewise constant (dotted blue line) damping.....106
Figure 6-18. Phase plot for a single degree-of-freedom forced oscillator with linear (solid black line) and piecewise constant (dotted blue line) damping, with regions of damping transition identified (in gray) 107
Figure 6-19: Illustration of roll transition through large amplitudes for the ONRFL midship section, including bilge keel and deck interaction with the free surface. Ship-specific abrupt physical changes due to variation in heel angle. For the midship section of the ONR Topside Series, flared configuration, bilge keel emergence is observed at 30 deg and deck submergence at 40 deg.....108
Figure 6-20: Illustration of roll transition through large amplitudes for the ONRTH midship section, including bilge keel and deck interaction with the free surface. Ship-specific abrupt physical changes due to variation in heel angle. For the midship section of the ONR Topside Series, tumblehome configuration, bilge keel emergence is observed at 30 deg and deck submergence at 50 deg.....109
Figure 6-21. Comparison of roll response for a linear oscillator system with small amplitude damping only (black), linearized damping over the full range of amplitudes (red), damping for the second region only (green), and piecewise constant damping with a transition at ϕ_t (dotted blue).....110
Figure 6-22: Sectional view of the instantaneous relative position of the ship in irregular waves for determining roll damping at a given time-step 114
Figure 6-23. Decomposition of the physical problem in advanced, but fast, numerical simulations potential flow (from Belknap & Reed, 2010). 115

Figure 6-24. Bilge keel wave-making component vs ϕ for a cargo ship, at zero speed (from Bassler & Reed, 2009) 117
Figure 6-25. Bilge keel wave-making component vs ϕ for Series 60, C_B=0.60, at zero speed (from Bassler & Reed, 2009) 117
Figure 6-26. A model using a sigmoid function for bilge keel transition behavior during large-amplitude roll motion 118
Figure 6-27. A model using a Gompertz function for bilge keel transition behavior during large-amplitude roll motion 119
Figure A-1. Illustration of the half-midship section of a wall-sided hull form 143
Figure A-2. Hull section shape and the distance from the roll axis (from Lloyd, 1998) 143
Figure A-3. Example of a roll decay test 144
Figure A-4. Diagram of the bilge keel force components, for a starboard section of a bilge keel rolling counterclockwise, looking forward (from Grant, et al., 2007) 147
Figure B-1. SUGGAR grid assembly for DTMB Model #5613-1 at two roll positions, with relative grid densities between refinement and background grids 155
Figure B-2. Computational Domain: Moving hull, grid, stationary refinement, and background grids 156
Figure B-3. Hull and bilge keels surface discretizations, shown for DTMB Model #5613-1 156
Figure B-4. CFDShip-Iowa boundary conditions 156
Figure C-1. Endplate for DTMB Model #5699 160
Figure C-2. DTMB Model #5699-1 in the NSWCCD 140 ft basin (left) and the section with instrumented bilge keels, with the strain gages seen protruding through the hull (right) 160
Figure C-3. Illustration of DTMB Model #5699 attached to the small A-frame in Bldg 18, NSWCCD 161
Figure C-4. Illustration top view of internal instrumentation and ballast weight configuration for DTMB Model #5699 161
Figure C-5. Typical gage layout for Kistler dynamometer 163
Figure C-6. Illustration the 2D Model with Kistler gage (gray) and instrumented bilge keel sections (red), with hull penetrations, shown 164
Figure C-7. Illustration of the cross-section of the 2D model with bilge keel strain gages (gray) with strain gages attached to waterproofed end-caps (red) shown 164
Figure C-8. Illustration of the instrumented bilge keel section with strain gages attached to waterproofed end-caps (red) used to transmit data to the data acquisition system 165
Figure C-9. DTMB Model #5699 with topside removed, viewed from forward looking aft, displacement and rate gyroscopes used to obtain motion measurements are shown in foreground (in the near-field compartment) 166
Figure C-10. Displacement gyroscope (clear box) and rate gyroscope (black cylinder) in the model, with topside configuration and plexiglass deckplating installed 166
Figure C-11. Three ultrasonic wave probes with housings (gray), suspended at perpendicular distances of 0.61 m, 0.76 m, and 0.91 m from model centerline 167
Figure C-12. Calibration image (A) and de-warped image (B), with mapping function shown in red 168
Figure C-13. Sample raw image from a PIV vector-field measurement; post-processing masking and window algorithms were applied to generate vorticity-field measurements 170
Figure C-14. Combined sway, heave, and roll actuation with the mechanism, to obtain large amplitude 1DoF roll of the model about a specified roll axis 171
Figure C-15. 3DoF motion mechanism profile view (left) and sway carriage (right) with vertical heave rails (blue and green). 172
Figure C-16. Installation of the 3DoF motion mechanism in the NSWCCD 140 ft basin 174
Figure C-17. DTMB Model #5699-1 attached to the 3DoF motion mechanism (left) and undergoing large amplitude forced roll oscillation (right) 174
Figure C-18. Control box for the 3DoF motion mechanism 175
Figure C-19. Roll decay mechanism, shown attached to the model in the NSWCCD 140 ft basin 176
Figure C-20. Sample roll decay measurement for DTMB Model #5699-1, initial heel angle, θ_0 = 15 deg 177
Figure C-21. Roll extinction curve for DTMB Model #5699-1 with bilge keels 178
Figure C-22. Roll extinction curve for DTMB Model #5699-1 without bilge keels 178
Figure C-23. Decomposition using an FFT of the roll moment signal measurement for the DTMB Model #5699-1, ϕ=15 deg, ω= 2.5 rad/s 180

Figure C-24. Roll moment measurement, unfiltered (red) and reconstructed after digital filtering at 10 rad/s (black), for the DTMB Model #5699-1, ϕ=15 deg, ω= 2.5 rad/s 180
Figure C-25. Unit bilge keel force measurement, unfiltered (red) and reconstructed after digital filtering at 10 rad/s (black), for the DTMB Model #5699-1, ϕ=15 deg, ω= 2.5 rad/s.....181
Figure C-26. Phase plot of roll rate vs. roll measurements, filtered, for DTMB Model #5699-1, ϕ=15 deg, ω= 2.5 rad/s 182
Figure C-27. Phase plot of roll rate vs. roll measurements, filtered, for DTMB Model #5699-1, ϕ=25 deg, ω= 2.5 rad/s 182
Figure C-28. Phase plot of roll rate vs. roll measurements, filtered, for DTMB Model #5699-1, ϕ=35 deg, ω= 2.5 rad/s 182
Figure C-29. Phase plot of roll rate vs. roll measurements, filtered, for DTMB Model #5699-1, ϕ=40 deg, ω= 2.5 rad/s 183
Figure C-30. Phase plot of roll rate vs. roll measurements, filtered, for DTMB Model #5699-1, ϕ=45 deg, ω= 2.5 rad/s 183
Figure C-31. Phase plot of roll moment vs. roll measurements, filtered, for DTMB Model #5699-1, ϕ=15 deg, ω= 2.5 rad/s 184
Figure C-32. Phase plot of roll moment vs. roll measurements, filtered, for DTMB Model #5699-1, ϕ=25 deg, ω= 2.5 rad/s 184
Figure C-33. Phase plot of roll moment vs. roll measurements, filtered, for DTMB Model #5699-1, ϕ=35 deg, ω= 2.5 rad/s 184
Figure C-34. Phase plot of roll moment vs. roll measurements, filtered, for DTMB Model #5699-1, ϕ=40 deg, ω= 2.5 rad/s 185
Figure C-35. Phase plot of roll moment vs. roll measurements, filtered, for DTMB Model #5699-1, ϕ=45 deg, ω= 2.5 rad/s 185
Figure C-36. Phase plot of unit bilge keel force vs. roll measurements, filtered, for DTMB Model #5699-1, ϕ=15 deg, ω= 2.5 rad/s 186
Figure C-37. Phase plot of unit bilge keel force vs. roll measurements, filtered, for DTMB Model #5699-1, ϕ=25 deg, ω= 2.5 rad/s 186
Figure C-38. Phase plot of unit bilge keel force vs. roll measurements, filtered, for DTMB Model #5699-1, ϕ=35 deg, ω= 2.5 rad/s 186
Figure C-39. Phase plot of unit bilge keel force vs. roll measurements, filtered, for DTMB Model #5699-1, ϕ=40 deg, ω= 2.5 rad/s 187
Figure C-40. Phase plot of unit bilge keel force vs. roll measurements, filtered, for DTMB Model #5699-1, ϕ=45 deg, ω= 2.5 rad/s 187
Figure D-1. Measured Hydrostatic Roll Moment, for DTMB Models #5699 and #5699-1 vs heel 189
Figure D-2. Time-synchronized measurements of roll and roll rate, (top), unit hydrodynamic roll moment (middle), and starboard and port unit bilge keel force, for DTMB Model #5699, φ= 15 deg, ω=2.5 rad/s 190
Figure D-3. Filtered roll motion measurements and bilge keel force measurements for the DTMB Model #5699, at various roll amplitudes, ϕ=15 (purple), 25 (black), 30 (red), 35 (green) and 40 (blue) deg, ω= 2.17 rad/s 191
Figure D-4. Filtered roll motion measurements and bilge keel force measurements for the DTMB Model #5699, at various roll amplitudes, ϕ=15 (purple), 25 (black), 30 (red), 35 (green) and 40 (blue) deg, ω= 2.5 rad/s 192
Figure D-5. Filtered roll motion measurements and bilge keel force measurements for the DTMB Model #5699, at various roll amplitudes, ϕ=15 (purple), 25 (black), 30 (red), 35 (green) and 40 (blue) deg, ω= 2.85 rad/s 193
Figure D-6. Filtered roll motion measurements and bilge keel force measurements for the DTMB Model #5699-1, at various roll amplitudes, ϕ=15 (purple), 25 (black), 30 (red), 35 (green), 40 (blue), and 45 (orange) deg, ω= 2.17 rad/s 194
Figure D-7. Filtered roll motion measurements and bilge keel force measurements for the DTMB Model #5699-1, at various roll amplitudes, ϕ=15 (purple), 25 (black), 30 (red), 35 (green), 40 (blue), and 45 (orange) deg, ω= 2.5 rad/s 195

Figure D-8. Filtered roll motion measurements and bilge keel force measurements for the DTMB Model #5699-1, at various roll amplitudes, ϕ=15 (purple), 25 (black), 30 (red), 35 (green), 40 (blue), and 45 (orange) deg, ω= 2.85 rad/s 196
Figure D-9. Comparison of the unit hydrodynamic roll moment and moment contribution of the total unit bilge keel force, for DTMB Model #5699, φ= 15 deg, ω=2.5 rad/s 197
Figure D-10. Comparison of the unit hydrodynamic roll moment and associated hydrodynamic components- added inertia and damping, for DTMB Model #5699, φ= 15 deg, ω=2.5 rad/s 198
Figure D-11. Comparison of the added inertia of the unit hydrodynamic roll moment and the unit hydrodynamic roll moment due to the bilge keels, for DTMB Model #5699, φ= 15 deg, ω=2.5 rad/s 199
Figure D-12. Comparison of the damping of the unit hydrodynamic roll moment and the unit hydrodynamic roll moment due to the bilge keels, for DTMB Model #5699, φ= 15 deg, ω=2.5 rad/s 200
Figure D-13. Comparison of the unit hydrodynamic roll moment due to the starboard bilge keel and associated hydrodynamic components- added inertia and damping, for DTMB Model #5699, φ= 15 deg, ω=2.5 rad/s 201
Figure D-14. 2D ONRTH, Hydrodynamic Coefficients for the Measured Mx with Bilge Keels, Added Inertia Moment and Coefficient (top left and right respectively), and Damping Moment and Coefficient (bottom left and right, respectively), for three roll frequencies 204
Figure D-15. 2D ONRTH, Hydrodynamic Coefficients for the Measured Mx without Bilge Keels, Added Inertia Moment and Coefficient (top left and right respectively), and Damping Moment and Coefficient (bottom left and right, respectively), for three roll frequencies 205
Figure D-16. 2D ONRFL, Hydrodynamic Coefficients for the Measured Mx with Bilge Keels, Added Inertia Moment and Coefficient (top left and right respectively), and Damping Moment and Coefficient (bottom left and right, respectively), for three roll frequencies 206
Figure D-17. 2D ONRFL, Hydrodynamic Coefficients for the Measured Mx without Bilge Keels, Added Inertia Moment and Coefficient (top left and right respectively), and Damping Moment and Coefficient (bottom left and right, respectively), for three roll frequencies 207
Figure D-18. 2D ONRTH, Hydrodynamic Coefficients for the Measured Roll Moment due to the Bilge Keels, Added Inertia Moment and Coefficient (top left and right respectively), and Damping Moment and Coefficient (bottom left and right, respectively), for three roll frequencies 208
Figure D-19. 2D ONRFL, Hydrodynamic Coefficients for the Measured Roll Moment due to the Bilge Keels, Added Inertia Moment and Coefficient (top left and right respectively), and Damping Moment and Coefficient (bottom left and right, respectively), for three roll frequencies 209
Figure D-20. 2D ONRTH, Damping Coefficient for Measured Mx with Bilge Keels, for three roll frequencies 210
Figure D-21. 2D ONRTH, Damping Coefficient for Measured Mx without Bilge Keels, for three roll frequencies 210
Figure D-22. 2D ONRFL, Damping Coefficient for Measured Mx with Bilge Keels, for three roll frequencies 211
Figure D-23. 2D ONRFL, Damping Coefficient for Measured Mx without Bilge Keels, for three roll frequencies 211
Figure D-24. Comparison of the magnitude of the first 10 harmonics of added inertia for roll motion, for DTMB Model #5699, φ= 15 deg, ω=2.5 rad/s 212
Figure D-25. Comparison of the magnitude of the first 10 harmonics of damping for roll motion, for DTMB Model #5699, φ= 15 deg, ω=2.5 rad/s 213
Figure D-26. Comparison of the magnitude of the first 10 harmonics of added inertia for the unit hydrodynamic roll moment, for DTMB Model #5699, φ= 15 deg, ω=2.5 rad/s 213
Figure D-27. Comparison of the magnitude of the first 10 harmonics of damping for the unit hydrodynamic roll moment, for DTMB Model #5699, φ= 15 deg, ω=2.5 rad/s 214
Figure D-28. Comparison of the magnitude of the first 10 harmonics of added inertia for the unit hydrodynamic roll moment due to the starboard bilge keel force, for DTMB Model #5699, φ= 15 deg, ω=2.5 rad/s 214
Figure D-29. Comparison of the magnitude of the first 10 harmonics of damping or the unit hydrodynamic roll moment due to the starboard bilge keel force, for DTMB Model #5699, φ= 15 deg, ω=2.5 rad/s 215

Figure D-30. Comparison of the magnitude of the total of the first 10 harmonics of added inertia and damping for roll motion, for DTMB Models #5699 and #5699-1, with and without bilge keels, ω=2.17 rad/s 216
Figure D-31. Comparison of the magnitude of the total of the first 10 harmonics of added inertia and damping for the unit hydrodynamic roll moment, for DTMB Models #5699 and #5699-1, with and without bilge keels, ω=2.17 rad/s 217
Figure D-32. Comparison of the magnitude of the total of the first 10 harmonics of added inertia and damping for the unit hydrodynamic roll moment due to the starboard bilge keel, for DTMB Models #5699 and #5699-1, ω=2.17 rad/s 218
Figure D-33. Comparison of the magnitude of the total of the first 10 harmonics of added inertia for the unit hydrodynamic roll moment, for DTMB Models #5699 and #5699-1, with bilge keels and with the effective influence of the bilge keels, ω=2.17 rad/s 219
Figure D-34. Comparison of the magnitude of the total of the first 10 harmonics of damping for the unit hydrodynamic roll moment, for DTMB Models #5699 and #5699-1, with bilge keels and with the effective influence of the bilge keels, ω=2.17 rad/s 220
Figure D-35. Comparison of the magnitude of the total of the first 10 harmonics of added inertia for the unit hydrodynamic roll moment due to the starboard bilge keel, for DTMB Models #5699 and #5699-1, with and without bilge keels, ω=2.17 rad/s 221
Figure D-36. Comparison of the magnitude of the total of the first 10 harmonics of damping for the unit hydrodynamic roll moment due to the starboard bilge keel, for DTMB Models #5699 and #5699-1, with and without bilge keels, ω=2.17 rad/s 222
Figure D-37. Comparison of the magnitude of the total of the first 10 harmonics of added inertia and damping for roll motion, for DTMB Models #5699 and #5699-1, with and without bilge keels, ω=2.85 rad/s 223
Figure D-38. Comparison of the magnitude of the total of the first 10 harmonics of added inertia and damping for the unit hydrodynamic roll moment, for DTMB Models #5699 and #5699-1, with and without bilge keels, ω=2.85 rad/s 224
Figure D-39. Comparison of the magnitude of the total of the first 10 harmonics of added inertia and damping for the unit hydrodynamic roll moment due to the starboard bilge keel, for DTMB Models #5699 and #5699-1, ω=2.85 rad/s 225
Figure D-40. Comparison of the magnitude of the total of the first 10 harmonics of added inertia for the unit hydrodynamic roll moment, for DTMB Models #5699 and #5699-1, with bilge keels and with the effective influence of the bilge keels, ω=2.85 rad/s 226
Figure D-41. Comparison of the magnitude of the total of the first 10 harmonics of damping for the unit hydrodynamic roll moment, for DTMB Models #5699 and #5699-1, with bilge keels and with the effective influence of the bilge keels, ω=2.85 rad/s 227
Figure D-42. Comparison of the magnitude of the total of the first 10 harmonics of added inertia for the unit hydrodynamic roll moment due to the starboard bilge keel, for DTMB Models #5699 and #5699-1, with and without bilge keels, ω=2.85 rad/s 228
Figure D-43. Comparison of the magnitude of the total of the first 10 harmonics of damping for the unit hydrodynamic roll moment due to the starboard bilge keel, for DTMB Models #5699 and #5699-1, with and without bilge keels, ω=2.85 rad/s 229
Figure D-44. PIV results of the vorticity field for one roll period, for DTMB Model #5699, φ= 5 deg, ω=2.85 rad/s 230
Figure D-45. PIV results of the vorticity field for one roll period, for DTMB Model #5699, φ= 15 deg, ω=2.85 rad/s 230
Figure D-46. PIV results of the vorticity field for one roll period, for DTMB Model #5699, φ= 25 deg, ω=2.85 rad/s 231
Figure D-47. PIV results of the vorticity field for one roll period, for DTMB Model #5699, φ= 30 deg, ω=2.85 rad/s 231
Figure D-48. PIV results of the vorticity field for one roll period, for DTMB Model #5699, φ= 35 deg, ω=2.85 rad/s 232
Figure D-49. PIV results of the vorticity field for one roll period, for DTMB Model #5699, φ= 5 deg, ω=2.85 rad/s 232
Figure D-50. Variation in the center of pressure on the starboard bilge keel for Fn=0.0, ϕ=15 deg, ω=2.85 rad/s, as measured for DTMB Model #5699-1. 233

Figure D-51. Variation in the center of pressure on the starboard bilge keel for Fn=0.0, ϕ=25 deg, ω=2.85 rad/s, as measured for DTMB Model #5699-1. 234
Figure D-52. Variation in the center of pressure on the starboard bilge keel for Fn=0.0, ϕ=30 deg, ω=2.85 rad/s, as measured for DTMB Model #5699-1. 234
Figure D-53. Variation in the center of pressure on the starboard bilge keel for Fn=0.0, ϕ=35 deg, ω=2.85 rad/s, as measured for DTMB Model #5699-1. 235
Figure D-54. Variation in the center of pressure on the starboard bilge keel for Fn=0.0, ϕ=40 deg, ω=2.85 rad/s, as measured for DTMB Model #5699-1. 235
Figure D-55. Variation in the center of pressure on the starboard bilge keel for Fn=0.0, ϕ=45 deg, ω=2.85 rad/s, as measured for DTMB Model #5699-1. 236
Figure E-1.ONRFL added inertia due to radiation vs. frequency, for 0 deg and 25 deg fixed heel conditions, with and without bilge keels, infinite frequency values shown at 25 rad/s....238
Figure E-2.ONRFL damping due to radiation vs. frequency, for 0 deg and 25 deg fixed heel conditions, with and without bilge keels, infinite frequency values shown at 25 rad/s....238
Figure E-3. ONRFL added inertia due to radiation vs. frequency, for 0-35 deg fixed heel conditions, with and without bilge keels....239
Figure E-4. ONRTH added inertia due to radiation vs. frequency, for 0-35 deg fixed heel conditions, with and without bilge keels....239
Figure E-5. ONRFL damping due to radiation vs. frequency, for 0-35 deg fixed heel conditions, with and without bilge keels....240
Figure E-6. ONRTH damping due to radiation vs. frequency, for 0-35 deg fixed heel conditions, with and without bilge keels....240
Figure E-7. ONRFL added inertia due to radiation vs. frequency, for 0-35 deg fixed heel conditions, without bilge keels....241
Figure E-8. ONRTH added inertia due to radiation vs. frequency, for 0-35 deg fixed heel conditions, without bilge keels....241
Figure E-9. ONRFL added inertia due to radiation vs. frequency, for 0-35 deg fixed heel conditions, with bilge keels....242
Figure E-10. ONRTH added inertia due to radiation vs. frequency, for 0-35 deg fixed heel conditions, with bilge keels....242
Figure E-11. ONRFL damping due to radiation vs. frequency, for 0-35 deg fixed heel conditions, without bilge keels....243
Figure E-12. ONRTH damping due to radiation vs. frequency, for 0-35 deg fixed heel conditions, without bilge keels....243
Figure E-13. ONRFL damping due to radiation vs. frequency, for 0-35 deg fixed heel conditions, with bilge keels....244
Figure E-14. ONRTH damping due to radiation vs. frequency, for 0-35 deg fixed heel conditions, with bilge keels....244
Figure E-15. ONRFL added inertia due to radiation vs heel angle, for three roll frequency conditions (same as the experiment), with and without bilge keels....245
Figure E-16. ONRTH added inertia due to radiation vs heel angle, for three roll frequency conditions (same as the experiment), with and without bilge keels....245
Figure E-17. ONRFL damping due to radiation vs heel angle, for three roll frequency conditions (same as the experiment), with and without bilge keels....246
Figure E-18. ONRTH damping due to radiation vs heel angle, for three roll frequency conditions (same as the experiment), with and without bilge keels....246
Figure E-19. ONRFL added inertia due to radiation vs heel angle vs frequency, without bilge keels....247
Figure E-20. ONRTH added inertia due to radiation vs heel angle vs frequency, without bilge keels 247
Figure E-21. ONRFL damping due to radiation vs heel angle vs frequency, without bilge keels....248
Figure E-22. ONRTH damping due to radiation vs heel angle vs frequency, without bilge keels....248
Figure E-23. Alternate view of ONRFL added inertia due to radiation vs heel angle vs frequency, without bilge keels....249
Figure E-24. Alternate view of ONRTH added inertia due to radiation vs heel angle vs frequency, without bilge keels....249
Figure E-25. Alternate view of ONRFL added inertia due to radiation vs heel angle vs frequency, with bilge keels....250

Figure E-26. Alternate view of ONRTH added inertia due to radiation vs heel angle vs frequency, with bilge keels....250
Figure E-27. Alternate view of ONRFL damping due to radiation vs heel angle vs frequency, without bilge keels....251
Figure E-28. Alternate view of ONRTH damping due to radiation vs heel angle vs frequency, without bilge keels....251
Figure E-29. Alternate view of ONRFL damping due to radiation vs heel angle vs frequency, with bilge keels....252
Figure E-30. Alternate view of ONRTH damping due to radiation vs heel angle vs frequency, with bilge keels....252
Figure E-31. Comparison of the phase of the unit hydrodynamic roll moment due to radiation for the ONRFL vs heel angle, for ω=2.5 rad/s, with and without bilge keels....253
Figure E-32. Comparison of the phase of the unit hydrodynamic roll moment due to radiation for the ONRTH vs heel angle, for ω=2.5 rad/s, with and without bilge keels....253

Table of Tables

Table 3-1. Barehull hydrostatic parameters for DTMB Model 5613-1 (Bassler, et al., 2007) 28
Table 3-2. Simulated conditions for DTMB Model 5613-1 31
Table 4-1. Roll Decay Test Conditions 55
Table 4-2. Forced Oscillation Test Conditions 56
Table B-1. DTMB Model 5613-1 grid sizes and decomposition 157
Table C-1. DTMB Model #5699 and #5699-1 Principal Particulars 159
Table C-2. Inertial Properties for DTMB Model #5699 162
Table C-3. Inertial Properties for DTMB Model #5699-1 162
Table C-4. 3DoF Mechanism Design Capabilities 172
Table C-5. Damping Coefficients determined from roll decay tests- DTMB Model # 5699-1 (with bilge keels) 179
Table C-6. Damping Coefficients determined from roll decay tests - DTMB Model # 5699-1 (without bilge keels) 179
Table C-7. Equivalent linear damping coefficient, B_e, as a function of roll amplitude and frequency for DTMB Model # 5699-1 (with bilge keels) 179
Table C-8. Equivalent linear damping coefficient, B_e, as a function of roll amplitude and frequency for DTMB Model # 5699-1 (without bilge keels) 179

Nomenclature

A_{44}	mass moment of inertia in roll
A_{WP}	waterplane area
$b(x)$	sectional half beam= B/2
b_{BK}	bilge keel span (m)
$b_{BK}(x)$	bilge keel span at location x (m)
B	beam (m)
$B(x)$	sectional beam (m)
B_{44}	linearized total roll damping
B_1	linear roll damping component
B_2	quadratic roll damping component
B_3	cubic roll damping component
B_F	roll friction damping component
B_E	roll eddy damping component
B_L	roll lift damping component
B_W	roll wave-making damping component
B_{BK}	bilge keel roll damping component
B_{BKN}	bilge keel normal damping component
B_{BKH}	bilge keel-hull interaction damping
B_{BKW}	bilge keel wave-making damping
C_{44}	roll restoring component
C_B	block coefficient
C_D	drag coefficient
C_M	midship section coefficient
C_P	pressure coefficient
d	draft (m)
$d(x)$	sectional draft (m)
d_{BK}	distance from the free surface to the bilge keel (m, positive below waterline)
F_{BK}	unit normal force on the bilge keel (N/m), + in the opposite direction of motion. This is the normal force on the bilge keel, non-dimensionalized by a unit length, effectively the normal force on a 2D cross-section of the bilge keel.
Fn	Froude number
g	gravitational acceleration (m/s^2)
GM	metacentric height (m)
$H_0(x)$	half breadth/draft for a given section = $B(x)/(2d(x))$
H/λ	wave steepness
I_{XX}	roll moment of inertia
k_{44}	roll radius of gyration (m)
KC	Keulegan-Carpenter number = $(\pi r\phi)/b_{BK}$
KG	vertical center of gravity (m)
L	ship length (m)
LWL	waterline length (m)
M_{44}	total roll moment

M_{xx}	roll moment, due to pure roll, in the equations of motion
OG	distance from the origin (roll axis) to the center of gravity (m, positive down)
p	ship-fixed roll rate in the equations of motion
$r(x)$	distance from roll axis to bilge keel for a given section (m)
r_{max}	maximum distance from roll axis to hull surface (m)
Re	Reynolds number
$R(x)$	radius of the bilge circle for a given section (m)
t	time
T	draft (m)
T_ϕ	roll period (s)
U	forward speed (m/s)
$\overline{U}$	averaged forward speed for 15 seconds (m/s)
$Uref$	reference velocity
x/L	longitudinal ship section location
Y	sway displacement
y_0	initial sway displacement
Z	heave displacement
Δ	displacement mass (kg, freshwater)
ε	initial phase angle
λ	scale ratio
λ/L	ratio of wavelength to ship length
ν	kinematic viscosity (m^2/s)
ω	angular velocity
ω	roll frequency
ω_e	frequency of encounter (head seas)
ϕ	roll angle (deg), + for clockwise motion
ϕ_a	roll amplitude
ϕ_0	initial roll angle
ρ	fluid density (kg/m^3)
$\sigma(x)$	sectional area coefficient
θ	heel angle (deg)
z_0	initial heave displacement
DTMB	David Taylor Model Basin
FFT	Fast Fourier Transform
NSWCCD	Naval Surface Warfare Center, Carderock Division
ONR	Office of Naval Research
PIV	Particle Image Velocimetry
MDoF	Multiple Degree-of-Freedom
2D	two dimensional

Chapter 1 Introduction and Motivation

1.1 Introduction and Motivation

Even in the 21st century, ships remain a primary mode of transportation in the global economy and an essential component of national defense. Naval architecture has become a discipline of engineering science that combines elements of mechanics, materials, oceanography, and optimization.

In the context of the modern global economy and international security climate the tasks that ships are required to perform, for either economic or defense reasons, continue to increase. During their lifetime, both naval and commercial ships may have an increased probability of experiencing harsh conditions, and the consequences of loss of crew and cargo, as well as vessel loss are severe. In order to improve safety for the vessel and crew, as well as operational capability, these extreme environmental conditions must be considered in the design, assessment, and operation of ships.

Despite the maturation of naval architecture as an engineering science, many of the models and tools developed to design and assess ships continue to be based on mathematical conveniences, achieved through small amplitude approximations or linearization. However, for ships designed to operate in heavy weather, and for some ships with novel hull form geometries– departing from historical experience with more traditional hull forms, the effect of the nonlinearities, both in excitation and response, becomes significant.

Much progress has been made since the seminal paper of St. Denis & Pierson (1953), which initiated the modern era of ship motions theory. However, many elements have not yet been fully developed, and some nonlinearities have not yet been considered or applied in standard ship motion models and methods. This presents inherent limitations for the application of modern ship motions simulation tools to the assessment of ship performance in heavy weather (Beck & Reed, 2001).

In particular, roll motion remains the subject of many ship motions studies. This is due in part to its importance in ship motions, impacting operability, safety, and even survivability, and the complex physical processes associated with this mode of motion. In the mechanical oscillator model for ship motion, nonlinearities are typically only considered in the stiffness term of the roll equation of motion, and not the hydrodynamic components, added inertia and damping.

Estimating the roll hydrodynamic components (added inertia and damping) is essential to accurately describe the motions of a ship, particularly for ships operating in moderate to extreme sea conditions. The formulation for the hydrodynamic components may drastically affect the predicted amplitude of roll motion, under certain conditions.

For many years, bilge keels have been used on ships to increase damping and reduce the severity of roll motions experienced by a ship in waves. Because ship motions are more severe in extreme sea conditions, large roll angles may occur. Therefore, it is important to understand how the hydrodynamic components of the roll equation of motion are altered under these types of conditions.

The development of models for large amplitude ship roll motion necessitates improved understanding of the physical phenomena which occur during large amplitude roll motion, an assessment of the effect of these phenomena on the magnitude of the added inertia and damping,

and understanding the importance of nonlinearities in the hydrodynamic components for large roll. New models should continue to accurately model damping at small roll amplitudes, while extending the range of prediction to large roll amplitudes.

It is hypothesized that the effects of hull form geometry, including the bilge keels and deck edge, and the free surface, significantly alter the hydrodynamic components during large amplitude roll motions. This study seeks to provide improved understanding of the physical processes which occur during large amplitude roll motions and identify what considerations must be made in the development of more accurate models to describe and predict roll motions in more severe wave environments.

1.2 The Importance of Hydrodynamic Components in the Ship Equations of Motion

Ship motions are often modeled as a mechanical oscillator. The forces for each degree of motion are represented as spring-mass-dampers. The spring-mass-damper system model decomposes each of the six degrees-of-freedom of ship motions into three components: added inertia, which is proportional to acceleration, damping, which is proportional to velocity, and stiffness, which is proportional to displacement.

In the spring-mass-damper formulation, the hydrodynamic added mass, or inertia, component is used to model, or quantify, the amount of additional inertia, created when the body displaces a volume of fluid while in motion. The damping component is used to model, or quantify, the amount of energy dissipation in the system. The added inertia and damping components are linked, as the in-phase and out-of-phase components of the hydrodynamic force/moment. For the roll mode of motion, both terms are very important, due to the dependence of ship roll motion performance on the rate of energy dissipation. If the energy dissipation is too low, the ship will experience large roll motions, possibly including "hanging rolls," where a large heel angle occurs due to excitation forces (waves and wind) and the ship remains in this position for some duration, or in the most extreme case, capsize.

For parametric roll in regular wave conditions, the magnitude of the energy dissipation determines the threshold for the onset of parametric roll and large roll motions (e.g. Bassler 2008). In irregular waves, the magnitude of energy dissipation directly influences the amplitude of parametric roll that may occur (e.g. Belenky, et al., 2004; Bulian, et al., 2006).

Additionally, methods used to determine probability of capsizing due to large roll, such as the split-time method (Belenky, et al., 2008; 2009), depend on accurate calculation of the magnitude of roll velocity and roll acceleration at an upcrossing threshold. Therefore, in the split-time approach to probabilistic assessment of ship capsizing, there is a sensitivity of the solution, and the subsequent calculation of capsize risk, to the accuracy of predicting the hydrodynamic components of roll motion.

Finally, despite many advances with high-fidelity numerical simulation tools, potential flow based methods remain the fundamental practical tool used for ship design and assessment. Because of their fast computational time, many simulations can be performed, which enable many design alternatives to be considered and a high resolution of environmental and operational conditions to be modeled for the assessment of ship designs. However, these potential flow numerical codes still require additional models to account for viscous effects. In most modern potential flow tools, linear formulations are used for roll added inertia, and roll damping models

are based on results from experiments (roll decay or forced oscillation tests), or from a traditional component-based analysis method. However, the formulations for both roll added inertia and damping are implemented and used without consideration for the effects of large amplitude roll motions.

1.3 The Significance of Bilge Keels

Since the late-1800s, ships have commonly used bilge keels to mitigate roll motions. The use of bilge keels to minimize ship roll motion was first suggested by Froude (1865). Bilge keels originally featured flat plate designs and later also included discontinuous fins and wedges (Thews, 1938). One of the primary motivations for the original use of bilge keels was to minimize resonant roll motion in beam seas (Davidson, 1945).

For ship roll motion, the bilge keels account for the greatest physical contribution to energy dissipation (Himeno, 1981). However, bilge keels are most effective where they are fully submerged, typically only for small and moderate roll motion, and at lower speeds (Ikeda, 1978; Himeno, 1981). At higher speeds, lift damping becomes more dominant (Baitis, et al., 1981). Although larger size bilge keels are typically more effective, constraints limit the practical span of bilge keels, due to hull geometry, operations, and structures.

Historically, bilge keels were constructed of metal plate and filled with wood. The bilge keels were riveted to the hull, in the proper location (Spear, 1896). More modern bilge keels are constructed entirely of metal plate and filled with foam-based material. Due to considerations about docking at the pier, and operations in shallow water, bilge keels are typically constrained to not protrude beyond the beam or the keel of the ship. Therefore, the size of bilge keels is limited, and their size cannot be increased substantially to provide more effectiveness. As ships, both naval and commercial, have increasingly expanded their operations into more severe environments, bilge keels have become less effective.

1.4 Large Amplitude Ship Roll Motions

As discussed, factors such as increased exposure to severe sea conditions may result in a higher probability for large amplitude roll motions. Additionally, the increasing prevalence of novel hull form geometries results in an unknown level of accuracy for existing methods to assess ship performance in heavy weather. Increased operation in harsh environments, for both naval and commercial ships, necessitates a comprehensive understanding of the safety risk to the vessels. An example of operations in heavy weather for a naval vessel, the USS *Essex*, is shown in Figure 1-1.

The effect of the environment and hull form may result in large amplitude response and corresponding events such as bilge keel emergence, which has been observed both at model-scale (Figure 1-2 and Figure 1-3) and full-scale (Figure 1-4). Additionally, severe weather conditions, resulting in deck submergence for both naval vessels (Figure 1-5 and Figure 1-6) and commercial vessels (Figure 1-7) have also been observed. For deck submergence, the drastic change in ship geometry may also affect roll damping and subsequent roll motions.

As discussed in more detail in the Chapter 2, current ship motion prediction tools and methods are considered inadequate for predicting large amplitude motions. However, by including additional effects due to bilge keel emergence, topside geometry, and free surface effects, which are significant at large roll angles, it is likely possible to obtain more accurate ship

roll motion predictions. Without these considerations, the hydrodynamic components of roll are inaccurate, resulting in poor ship roll motion predictions.

Figure 1-1. USS *Essex* in heavy seas (c. 1960)[1]

Figure 1-2. A traditional notional naval combatant model (DTMB Model #5514) in hurricane sea conditions, experiencing a large roll angle with bilge keel emergence on the starboard side and deck submergence on the port side[2]

[1] Photograph courtesy of the U.S. Navy

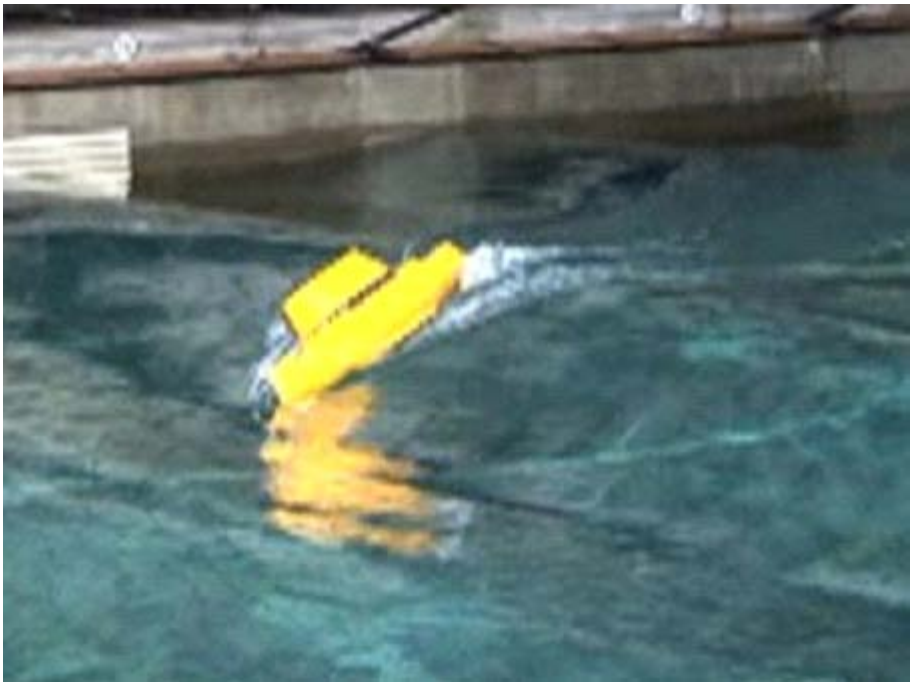

Figure 1-3. ONR Tumblehome experiencing large roll after broaching, with bilge keel emergence occurring on the port side[3]

Figure 1-4. Cruise ship *Voyager* in a storm in the Mediterranean, as viewed from a helicopter, experiencing large roll motions, resulting in bilge keel emergence[4]

[2] Photograph from model experiments conducted by Hayden, *et al.* (2006) at NSWCCD
[3] Photograph provided by Prof. Naoya Umeda and Dr. Hirotada Hashimoto (Osaka University, Japan)
[4] From footage available on YouTube (http://www.youtube.com/watch?v=tChJ2fBKw6w)

Figure 1-5. Large roll angle experienced by the USS *Cowpens*, during Typhoon COBRA (Halsey's Typhoon), 18 December 1944[5]. The ship experienced up to 47 degrees of roll.

Figure 1-6. A large roll angle, coupled with waves, results in deck submergence and wetness on the flight deck, aft on a U.S. naval vessel

[5] Photograph courtesy of Wikipedia (http://en.wikipedia.org/wiki/Typhoon_Cobra_(1944))

Figure 1-7. Ship in storm conditions, with starboard deck submergence

1.5 Research Storyline

The application of interest is to prediction of ship motions in heavy weather, and understanding the physical behavior which results in large amplitude roll motions is essential. In particular, understanding how the hydrodynamic components of the roll equation of motion are altered under these types of conditions can provide a physical basis for the development of improved ship motions models to better predict ship behavior in extreme sea conditions. Because the investigations presented in this work involved a mixed methods approach, a research storyline is presented, in order to assist the reader with understanding how the different methods used helped to illuminate different aspects of interest for this problem.

The modeling of hydrodynamic components, added inertia and damping, for large amplitude ship roll motion had not been previously addressed. This motivated an examination of existing models that revealed limitations for application to modeling ship roll motion in heavy weather. Due to the lack of previous knowledge, multiple methods of investigation and analysis were used to further examine this problem, including both experimental and numerical methods. URANS simulations were first used to identify dominant physical phenomena affecting the behavior of hydrodynamic components for large amplitude roll motion. The influence of topside geometry was also included. This is another aspect which had not previously been systematically addressed, but further influences the behavior of the hydrodynamic components for large amplitude ship motions.

Although viscous effects are important for ship roll motion, because the emphasis was on seakeeping predictions, Froude scaling was determined to be more important and chosen instead of Reynolds scaling, for the numerical and experimental components of the investigation. This was also the same assumption used by Ikeda, et al. (1978) for investigations into ship roll damping.

Based on the findings from the URANS simulations, an experiment was devised and performed, where the dominant physical phenomena were measured and characterized. The experiment consisted of a simplified system, a 2D model of a ship hull form, with two topside geometry configurations. The experiments provided an opportunity to gain fundamental physical understanding, since no systematic observations of these phenomena had been previously made.

The experimental results were then compared to the numerical simulations, and further increase fundamental understanding through the analysis of a wider range of conditions than was permissible for an experimental investigation.

The combined knowledge from the mixed methods approach and subsequent analysis was then used to develop and examine several approaches to modeling the physical phenomena observed during both the experiments and numerical simulations. This investigation revealed additional physical phenomena which occur during large amplitude roll motions, due to the interaction of the bilge keel and the free surface, as well as the topside geometry and the free surface, which are different from the behavior of these components for small amplitude motions, necessitating consideration for additional physical phenomena in modeling of the hydrodynamic components. The findings from this investigation provided some insight into the physical phenomena, as well as suggested some possibilities for modeling approaches for the hydrodynamic components of large amplitude roll motion.

1.6 Dissertation Objectives

The objectives of this dissertation are:

1) To examine the hypothesis that existing motion models are not applicable to model the hydrodynamic components of large amplitude roll motion
2) To observe the physical processes which occur during large amplitude ship roll motion, using both experimental and numerical methods, and analyze their effects on the hydrodynamic components of roll motion
3) To examine and quantify the influence of bilge keel, topside, and free surface effects on the hydrodynamic components of roll motion during large amplitude ship roll motion
4) To assess differences in the behavior of roll motion hydrodynamic components, for small and large amplitude motions
5) To determine the significance of the physical processes which occur during large amplitude events, and give consideration of these processes in models to describe and predict roll motions in severe wave environments
6) To develop and propose some initial models for the roll hydrodynamic components, which include considerations for large amplitude motions and the associated physical phenomena, and resulting nonlinearities in added inertia and damping.

In order to formulate the models presented in Chapter 6, simplifying assumptions were made. This assumption was the separation of the nonlinear response, the ship motions, from the stochastic excitation, the waves. The work described in this study only considers modifications to the motions side of the equation of motion. Additional considerations related to the improvement of the forcing side (the waves) of the equations of motion are not addressed.

The primary tasks of this dissertation are:

- Review existing literature on roll hydrodynamic components, added inertia and damping, and identify roll components which are affected by large amplitude motions. Deficiencies will be identified in existing roll motion models for large amplitude motion effects. Because the bilge keel component constitutes the majority of total energy dissipation in roll, it is assumed that modeling the effects of large amplitude motion on the bilge keel will have the greatest impact on considering these effects for total roll damping (Chapter 2)
- Examine the physical complexities of the total problem of large amplitude ship roll motion, prioritize the observed physical phenomena, and identify further simplifications which are made for the purposes of this study (Chapter 3)
- Perform a series of experimental observations and subsequent analysis to develop an understanding of the physical phenomena which occur during large amplitude motion. Determine how these physical processes for energy dissipation are altered for large amplitude motion, compared to small amplitude motion. Summarize the physical phenomena and identify their relative influence on the hydrodynamic components of roll motion for large amplitude motion (Chapter 4)
- Perform a series of numerical observations and analysis to further develop understanding of the effects in the physical phenomena occurring for large amplitude roll motion, including additional amplitudes and frequencies. Identify their relative influence on the hydrodynamic components of roll motion for large amplitude motion (Chapter 5)
- Develop initial models to consider large amplitude roll motion, which can improve potential flow numerical simulations of ship motions. These initial models should build off of the experimental and numerical observations and analysis (Chapter 6).

1.7 Dissertation Outline

Chapter 1 includes an introduction and motivation for the dissertation.

Chapter 2 summarizes existing roll damping models and bilge keel force models, including some recent work to extend the state-of-the-art.

Chapter 3 discusses numerical simulations which were used to illustrate the complexity of the problem and identify further simplifications which were made for the purposes of this study.

Chapter 4 presents experimental observations and analysis of various physical phenomena, which occur during large amplitude ship roll motion and their affect on the hydrodynamic components, and a summary of the physical processes observed and their effect on the hydrodynamic components

Chapter 5 presents numerical observations and analysis of physical phenomena which affect the hydrodynamic components during large amplitude roll motion.

Chapter 6 discusses the formulation and initial developments of models for hydrodynamic components for large amplitude ship roll motion, including a time-domain component based model, a piecewise model coupled with ship-specific physical thresholds, and a bilge keel force model.

Chapter 7 presents a summary and conclusions from this study and identifies some areas for future work.

Chapter 2 A Review of Hydrodynamic Component Models

2.1 Overview

This chapter discusses the background regarding ship hydrodynamic components, roll added inertia and damping. Two types of models for the hydrodynamic components are discussed, frequency-domain and time-domain models. Details of the general approaches for each type are discussed, along with assumptions, limitations, and subsequent modifications that have been made to increase the applicability of the models. Some additional recent work, which has provided insight into additional deficiencies with the existing models, is also discussed. However, the existing models remain limited in their application to model large amplitude effects on the hydrodynamic components of ship roll motion.

2.2 Coordinate System

For this dissertation, a consistent, right-handed orthogonal coordinate system is used. The coordinate system is ship-fixed, with *X* positive forward, *Y* positive to port, and *Z* positive up. The origin is located at the center of gravity (Figure 2-1). All results are reported using this coordinate system.

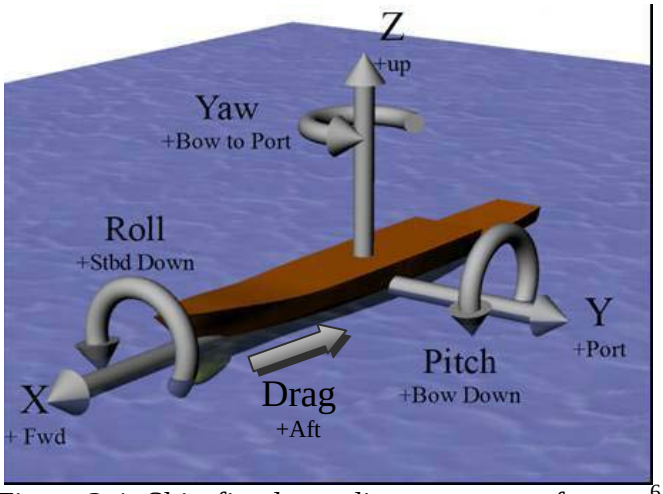

Figure 2-1. Ship-fixed coordinate system reference[6]

2.3 Roll Added Inertia and Damping in Ship Motions

A model for the single degree of freedom ship roll equation is given as a 2nd-order ordinary differential equation (ODE), in the form of the spring-mass-damper type system.

$$a\ddot{\phi} + b\dot{\phi} + c\phi = f(t) \tag{2.1}$$

[6] Standard notation and diagram from the Seakeeping Divison, NSWCCD

where *a* is the roll inertia; *b* is the damping; *c* is the stiffness; ϕ is the roll angle; and *f(t)* is the excitation forcing function. For single-degree-of-freedom ship roll motion, the spring-mass-damper system is given as

$$\left(I_{44} + a_{44}\right)\ddot{\phi} + b_{44}\dot{\phi} + \rho g \nabla \cdot GZ(\phi) = f(t) \tag{2.2}$$

where I_{44} is the roll moment of inertia, a_{44} is the roll added inertia; b_{44} is the roll damping; and $\rho g \nabla$ is the displacement, comprised of the density, gravity constant, and submerged volume, and $GZ(\phi)$ is the righting arm curve as a function of heel angle.

In this formulation, nonlinearities are often only considered in the hydrostatic portion of the roll motion equation, with the Froude-Krylov assumption of separation of the hydrostatics and wave disturbance, as well as the excitation from the surrounding wave-field. Nonlinearities in the wave-field and disturbance pressures caused by the presence of the hull are not explicitly considered in this formulation, but can also be included. Therefore, the single degree of freedom ship roll equation can be expressed as

$$\ddot{\phi} + 2\delta\dot{\phi} + c(\phi) = F(t) \tag{2.3}$$

Equation (2.2) can be rewritten to the standard form for a spring-mass-damper oscillator, as given in (2.3), with the damping, 2δ, stiffness, $c(\varphi)$, and forcing function, $F(t)$, given as, respectively,

$$2\delta = \frac{b_{44}}{\left(I_{xx} + a_{44}\right)} \tag{2.4}$$

$$c(\phi) = \frac{\rho g \nabla \cdot GZ(\phi)}{\left(I_{xx} + a_{44}\right)} \tag{2.5}$$

$$F(t) = A_W \sin(\omega t) \tag{2.6}$$

where A_W is the amplitude of the wave, and ω is the wave frequency. Furthermore, the stiffness, with dependency on roll angle, can also be expressed as

$$c(\phi) = \omega_n{}^2 \frac{GZ(\phi)}{GM} \tag{2.7}$$

where the roll natural frequency, ω_n, is given as

$$\omega_n = \sqrt{\frac{\rho g \nabla \cdot GM}{\left(I_{xx} + a_{44}\right)}} \tag{2.8}$$

and *GM* is the metacentric height. Equation (2.7) expressed the stiffness as a function of the righting arm curve, the roll natural frequency, and the metacentric height. This rearrangement of the terms was performed to provide the relationship between the stiffness, as a function of roll angle, and the roll natural frequency, which is determined using static parameters, as given in Equation (2.8).

In the standard model of single-degree-of-freedom ship roll motion as a spring-mass-damper system, added inertia is proportional to the acceleration and characterizes the additional inertial effect of the fluid that is displaced by the body during motion. Correspondingly, damping is proportional to velocity and characterizes the energy dissipation of the system. The portion of

the roll moment due to roll velocity is typically given as M_{xx}. This is the portion of the total roll moment, M_{44}, due to roll damping.

Considering a single degree-of-freedom model for ship roll motion (as denoted by the index *44*),

$$\left(I_{44} + A_{44}(\omega)\right)\ddot{\phi} + B_{44}\left(\dot{\phi}\right) + C_{44}(\phi) = M_{44}(t) \tag{2.9}$$

the damping term is decomposed into both linear and nonlinear components.

$$B_{44}\left(\dot{\phi}\right) = B_1\dot{\phi} + B_2\dot{\phi}\left|\dot{\phi}\right| + B_3\dot{\phi}^3 + \ldots \tag{2.10}$$

This polynomial representation of damping is explained physically as the sum of the viscous contributions (the linear term), the vortex component (quadratic term), and additional "correction" factors, which are represented by the cubic (or higher-order) term (e.g. see Lewandowski, 2004). The linear and nonlinear damping coefficients, B_1, B_2, and B_3, may be obtained using roll decay regression analysis.

Because of the difficulty in accurately obtaining and analyzing nonlinear roll damping, it is traditionally assumed that the nonlinear terms are approximated using an equivalent linear damping coefficient, B_e (Ikeda, et al., 1978; Himeno, 1981).

$$B_{44}\left(\dot{\phi}\right) = B_e\dot{\phi} \tag{2.11}$$

The equivalent linear damping coefficient combines all of the physical aspects from the polynomial formulation into a single coefficient of damping. However, this assumption is typically only valid for smaller roll motions, where linearization is applicable. The equivalent linear damping coefficient, B_e, may be obtained using either forced roll oscillation results or Ikeda's component analysis method (Ikeda, et al., 1978; Himeno, 1981).

For time-domain prediction of roll damping in most modern potential flow ship motions simulation tools, the equivalent linear damping coefficient is used and typically obtained using the component analysis method (Beck & Reed, 2001). However, this may have limitations for the accuracy of predictions of ship roll behaviour in moderate to heavy seas, where linearization is not appropriate. For both moderate and heavy seas, where large roll events may occur, ship roll damping may be over-predicted, due to assumptions about the effectiveness of the bilge keels, resulting in under-prediction of the roll motions that a ship will actually experience in these wave conditions.

2.4 Roll Damping- Energy Dissipation for Ship Motions

The hydrodynamic components of roll motion may be separated into in-phase, or added inertia, and out-of-phase, or damping contributions. Existing theoretical models for roll motion consider the physical processes of roll motion damping with various means of energy dissipation. These physical processes include friction, lift, wave-making, and vortex generation from the hull, as well as the influence of deeply submerged bilge keels, including vortex generation (Ikeda, et al., 1978; Schmitke, 1978; Himeno, 1981). Although ship roll damping is influenced by the hull shape, the primary mechanism of roll damping is the bilge keels.

Bilge keels provide a mechanism to transfer energy from the body (the ship) to the surrounding fluid, through mechanisms of vortex generation and added inertia effects of fluid displacement during roll motion. They are most effective at zero speed in beam sea conditions. Although larger size bilge keels are more effective, some constraints, due to hull geometry,

operational requirements, and structures, limit the practical span of bilge keels (as discussed in Chapter 1). Additionally, theoretical models to determine ship roll damping assume relatively small bilge keel sizes and small to moderate motions, where the bilge keels are deeply submerged. For large amplitude ship roll motion, the bilge keels become less effective, as they interact with the free surface and also experience possible emergence (Bassler & Reed, 2009). Without considerations for the physical phenomena for large amplitude roll motion, where the bilge keels interact with the free-surface, and emergence may occur, damping may be over-predicted, resulting in a subsequent under-prediction of roll motion (Reed, 2009; Bassler, et al., 2010).

For ship roll motion at low forward speed, bilge keels still account for the largest component of this energy dissipation for small and moderate roll motion, because they remain deeply submerged. At higher forward speeds, the lift damping component becomes a more significant aspect of damping (Baitis, et al., 1981). At these higher speeds, the bilge keels are also no longer optimized for resistance (Lloyd, 1998).

2.5 The Importance of Roll Inertia and Damping for Large Amplitude Ship Motions

Roll damping is essential to accurately describe the motions of a ship, particularly when operating in moderate to extreme sea conditions, and is most important for beam seas/synchronous or parametric roll phenomena (e.g. McCue, et al., 2007; Bassler, 2008a). Two of the primary modes of intact dynamic stability (Brown & Deybach, 1998) are affected by roll damping: dead ship condition and parametric roll. A summary of the approaches previously attempted to characterize these stability failure modes is given in Bassler, et al. (2009). Typical critical damping ratios must be specified for the level 2 vulnerability criteria approaches for parametric roll and results may vary, depending on the damping that is specified for a given ship type (Belenky, et al., 2010).

Specifically for dead ship conditions, the current foundation of the U.S. Navy intact stability criteria (Sarchin & Goldberg, 1962) and the IMO "Severe Wind and Rolling Criterion (Weather Criterion)" (IMO, 2008) remains dependent on the roll-back angle calculation. A historical overview and some suggested improvements are detailed in Brown & Deybach (1998). Because of the nonlinearity of roll motion, sensitivity to initial conditions, along with roll damping, can drastically alter ship motion behavior (e.g. Soliman & Thompson, 1991; Kan, et al., 1992; Bassler, et al., 2007; McCue & Campbell, 2007).

Methods to predict rare dynamic stability failures, particularly for large roll motions, are fundamentally also dependent on accurate prediction of roll inertia and damping to determine roll acceleration and roll velocity. A summary of these methods is available in Belenky, et. al. (2010a; 2012). All three methods of the currently known methods to solve the general "problem of rarity" are dependent on accurate prediction of the hydrodynamic components of roll motion. Particularly, the "split-time" approach (Belenky, et al., 2008; 2012), which used the theory of upcrossing based on roll rate to determine the probability of experiencing a large angle, or capsizing, is the most sensitive to roll damping because of its dependence on accurate determination of the critical roll rate (Figure 2-2).

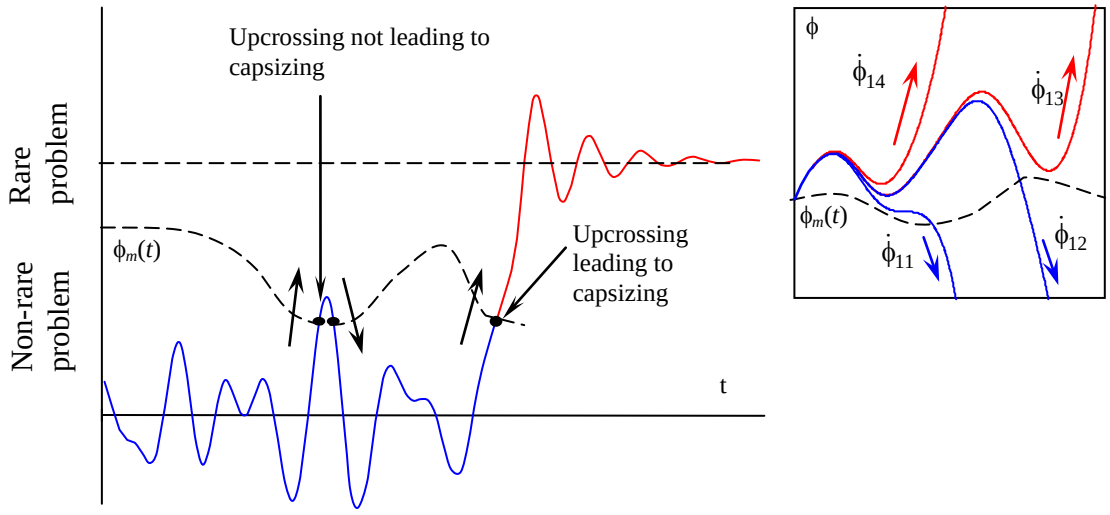

Figure 2-2. Application of split-time method for the case of changing stability in waves (from Belenky, et al., 2010)

2.6 Roll Motion Models in Potential Flow Simulations

Potential flow-based simulation codes remain the standard numerical tool for practical assessment of ship response in waves. Potential flow codes are commonly used because of their fast computational time, but require corrections to account for viscous effects. Explicit roll damping models are added to the potential flow codes to increase their accuracy for ship roll motion prediction. However, the common formulations for considering the viscous effects used were developed without consideration for the effects of large amplitude roll motion.

Roll damping models were developed to be used for ship seakeeping analysis. The original motivation was to predict small to moderate amplitude roll motions, where the submerged geometry of the ship hull does not vary dramatically. Roll damping models have been proposed using both frequency-domain and time-domain formulations. Details of the general approaches for each type are discussed in subsequent sections of Chapter 2, as well as Appendix A, along with deficiencies and subsequent modifications that have been made to attempt to increase the applicability of the models. Some recent work, which has provided insight into additional deficiencies with the existing models, is also discussed in section 2.6.1.2.

2.6.1 Frequency-Domain Models: Component Based Approaches

In the 1950-60s, the first scientific investigations to study the individual physical aspects of ship roll damping were performed (Sasajima, 1954; Tanaka, 1957; 1958; 1959; 1961; Martin, 1958; Kato, 1958; 1965). In the 1970s, a component method was developed to more accurately describe the roll damping of ships and integrate methods to describe distinct physical phenomena to determine total roll damping (Ikeda, et al, 1978a; 1978b; 1978c; 1978d; 1978e; Schmitke, 1978; Himeno, 1981). During this period, ships were often nearly wall-sided, without prominent flare or transom stern features. Additionally, ships often had a large bilge radius near midships. The impact of these typical geometric features for ships during this time period, as it relates to the assumptions used to develop the models, is discussed more in Appendix A.

The component method decomposed roll damping into seven parts and combined them linearly to calculate roll damping for conventional hull forms at small angles, with and without forward

speed. Roll damping coefficients, which are dependent on roll amplitude, frequency, and forward speed, were specified and the relative contribution to total roll moment was determined based on the product of the damping coefficient and the instantaneous roll rate (Ikeda, et al., 1978e). Further restrictions on roll amplitude resulted from linearization, which was necessary for application of the models in the frequency domain. Predictions using this method demonstrated the ability of frequency domain models to provide sufficiently accurate description of roll damping for small to moderate amplitude motions.

The component approach compared well with experimental data and was the first comprehensive model for ship roll damping with consideration of distinct physical phenomena. Schmitke (1978) also developed a component based formulation, dividing roll damping into contributions from the bilge keel, eddy-making, hull friction, and additional appendages (other than bilge keels) at zero speed. Since its development, Ikeda's component-based model, or some derivative, has generally been the state-of-the-art for roll damping computations.

Ship roll damping may be computed using Ikeda's component analysis method. In this method, the equivalent linear damping coefficient in the roll equation, B_e, can be obtained using a linear combination of physical components, each as a function of roll amplitude, roll frequency, and forward speed (Ikeda, *et al.*, 1978e, Himeno, 1981).

$$B_e = B_F + B_E + B_L + B_W + B_{BK} \tag{2.12}$$

Where, the bilge keel component is decomposed into the following sub-components,

$$B_{BK} = B_{BKN} + B_{BKH} + B_{BKW} \tag{2.13}$$

The components include both empirical (friction, B_F; eddy, B_E; and wave-making B_W,) and semi-empirical (hull lift, B_L; bilge keel normal force, B_{BKN}; and bilge keel-hull interaction, B_{BKH}) formulations. The bilge keel wave-making component, B_{BKW}, is typically neglected.

Even at small roll amplitudes, the bilge keel damping components contribute a large portion to the total damping. For small to moderate roll amplitudes, the contributions of the bilge keel components increase with both roll amplitude (Figure 2-3) and roll frequency (Figure 2-4). The damping component dependence on forward speed (Figure 2-5) and roll frequency is also shown. However, the bilge keel-hull interaction component is assumed not to depend on forward speed (Ikeda, et al., 1978b). From the schematic representation given in Figure 2-5, the bilge keel components are shown not have forward speed dependence, and only have slight frequency dependence, primarily for the bilge keel wave-making component.

According to Ikeda, because the friction damping is the only component with Reynolds number dependency, other scale effects are neglected for the components and non-dimensionalized coefficients may be used. The total damping contribution for each of these components is obtained by integrating these results over the ship length. Additional details and the formulae for computing the individual damping components are given in Appendix A.

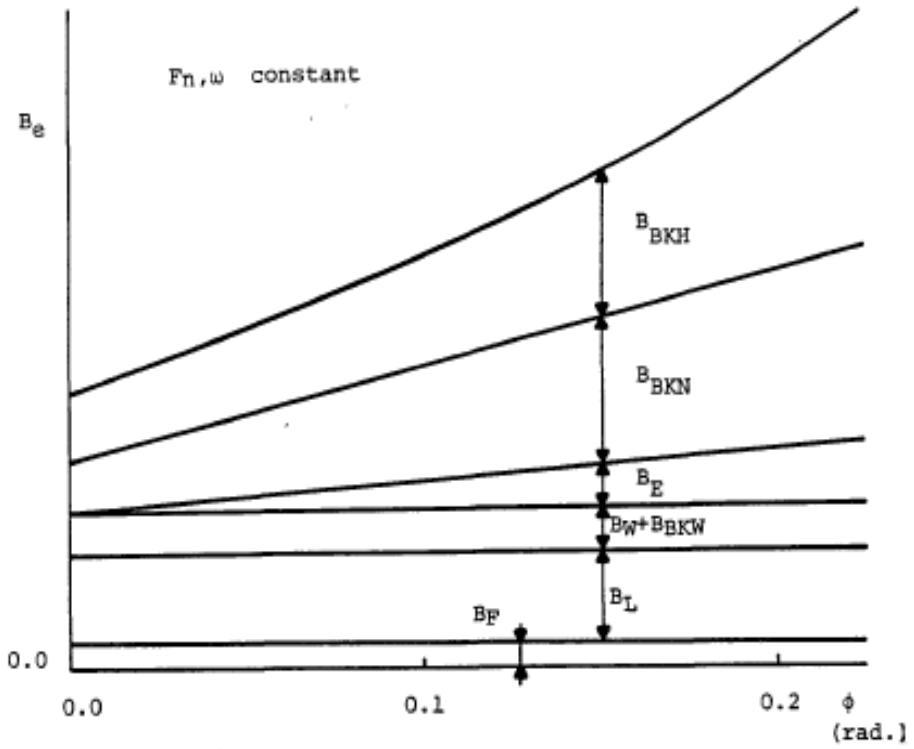

Figure 2-3. Relative magnitude of roll damping components, as a function of roll amplitude (from Himeno, 1981).

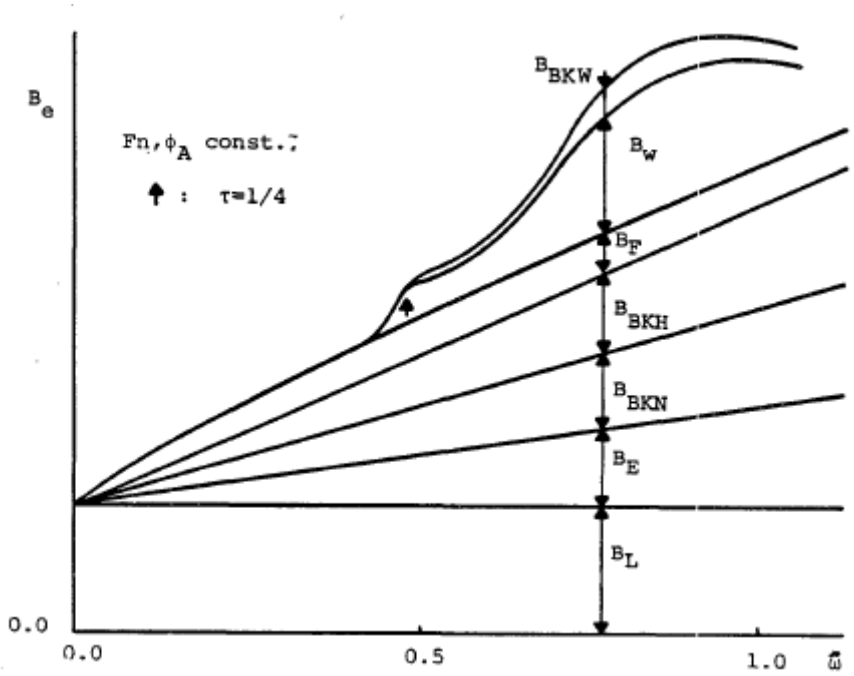

Figure 2-4. Relative magnitude of roll damping components, as a function of roll frequency (from Himeno, 1981).

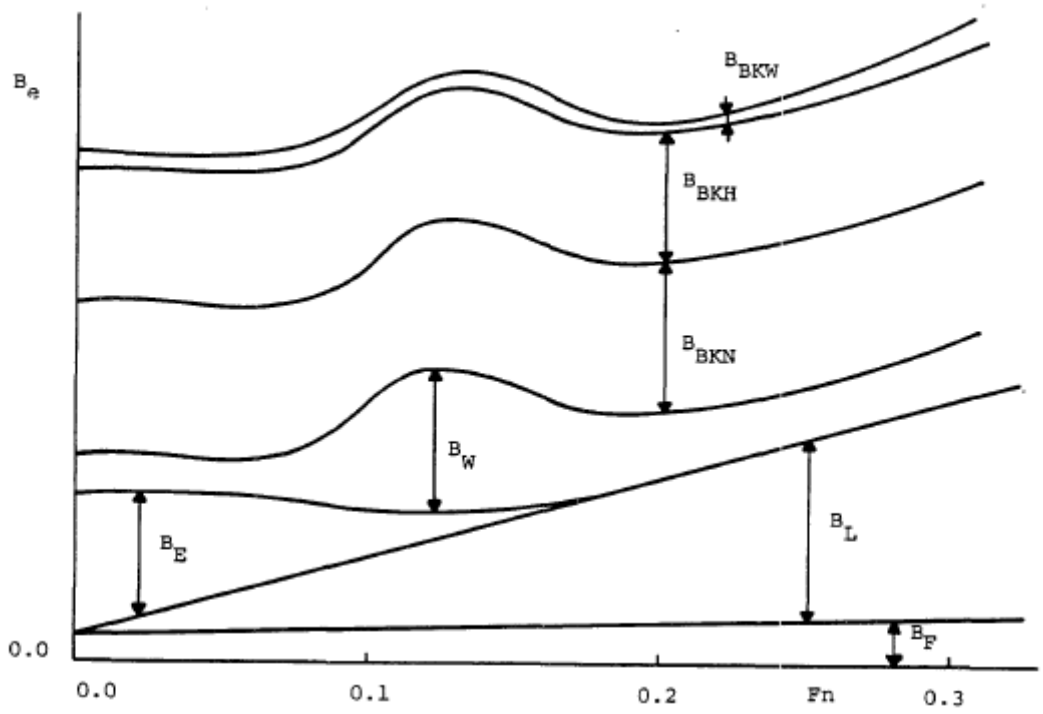

Figure 2-5. Relative magnitude of roll damping components, as a function of forward speed (from Himeno, 1981).

2.6.1.1 Non-Dimensionalization of Roll Damping Components

Ikeda presented non-dimensionalized damping coefficients for many of the experimental results performed for the development of the component method. The following representations were used, where B_i is the damping coefficient, and B is the beam of the ship.

$$\hat{B}_i = \frac{B_i}{\rho \nabla B^2}\left(\sqrt{\frac{B}{2g}}\right)^{2-i} \quad i = 1(or\ e), 2, 3$$
$$\hat{\omega} = \omega\sqrt{\frac{B}{2g}} \tag{2.14}$$

2.6.1.2 Component Based Models: Assumptions and Limitations

Since the 1970s, methods based on the component analysis model have been used to predict roll damping. Some derivative of the method developed by Ikeda, et al. (1978d) is used to predict ship motion performance in most modern potential flow codes. It is important to acknowledge several assumptions inherent to the roll damping prediction methods discussed.

These semi-empirical frequency-domain models are based on data from wall-sided hull forms, experiencing motion at small roll angles. Because ship response was considered for small to moderate conditions, the original calculations were only performed for roll amplitudes up to 10 degrees, and later extended to 15 degrees. Although these limitations were acknowledged in the development of the models, the limits of applicability are not well known for ships at larger roll amplitudes and with hull form geometries that deviate from being nearly wall-sided.

Predictions using common potential flow codes have shown significant variation in roll decay results that include forward speed, when compared to experimental results. This is especially true for hull form geometries different from the wall-sided ones, such as the ONR Topside Series (Bassler, 2007), for which the models where originally developed. For ship types outside of the wall-sided assumption, discrepancies between the predicted roll moment and experimental results are due in part to the difficulty of calculating the eddy and bilge keel components in a potential flow simulation (Bassler, 2008b). This presents inherent limitations for the application of modern ship motion simulation tools (Beck & Reed, 2001).

In the traditional formulation, the applicable hull forms are restricted to monohulls, with the draft greater than the bilge radius (due to using an empirical relationship for the distance to the bilge keel), rounded bilges with the bilge keels placed at the maximum distance from the roll axis, and small bilge keel size (with bilge keel span to beam ratios, $b_{BK}/B < 0.06$). However, the exact position and size of the bilge keels for specific ship geometries can be used to overcome the limitations of the bilge radius.

Based on the formulation for roll axis, *r*, and bilge radius, *R*, given by Ikeda, et al. (1978e), the bilge keel is assumed to be attached to the hull at the midpoint of the quarter circle circumscribed by the bilge circle radius. These parameters are used in both the bilge keel normal force and bilge keel-hull interaction components. Although this assumption appears to be adequate for wall-sided ship types, variation of the deadrise angle on modern ships, such as naval combatants, may invalidate this assumption and necessitate a different formulation. Variations in hull form geometry must also be considered when applying the formulation for the depth of the bilge keel from the free surface to determine the influence of the bilge keel wave-making component.

For larger roll amplitudes and larger bilge keel sizes, the relative increase in bilge keel wave-making damping suggest that accurate computations of the bilge keel wave-making damping component must be made, instead of neglected, so that its significance relative to the bilge keel normal force and bilge keel-hull interaction damping components can be determined (Bassler & Reed, 2009). As part of these computations, the bilge keel added interia contribution to the roll moment of inertia of the entire vessels should also be examined.

The use of hull geometry sectional properties in Ikeda's component model assumes the sectional properties are given relative to calm water. For ship motions in waves, future modifications may be made to instead consider the instantaneous sectional properties of the hull form, to account for time-varying damping. For a particular section, the eddy-making damping component can become negative, which is not physically possible. Therefore, the minimum component value should be established as zero. For components which depend on roll amplitude and/or roll frequency, if either the roll amplitude or frequency becomes zero, such as in head or following seas respectively, the given formulation will result in an undefined coefficient. Therefore, in head or following seas scenarios, those coefficients should be specified as zero.

Based on the roll frequency due to incoming waves, the appropriate roll damping coefficient is determined and then used in the time-domain implementation roll motion. In the time-domain formulation used in some codes (Belknap & Reed, 2010), the roll amplitude and roll frequency used to compute the roll damping coefficient for a given time-step are determined from a running FFT of the roll motion.

Additional work has been performed to extend the application of the component model. De Kat (1988) computed the roll damping coefficients at the natural roll frequency and then used

these for other roll frequencies. Blok & Aalbers (1991) decomposed the roll damping due to the bilge keels into two components, the lift on the bilge keel and the eddy generation from the bilge keels. Other methods have been developed where each component is determined for zero speed and then forward speed corrections are applied. Ikeda (2004) also detailed improvements to his method to determine optimal location for placement of the bilge keels. Changes have also been made to extend Ikeda's method to high-speed planning craft, with modifications to the lift component (Ikeda & Katayama, 2000), and high-speed multi-hull vessels, with modifications to the wave-making, eddy, and lift components (Katayama, *et al.*, 2008). For these high-speed vessels, predictions were performed for forward speeds, up to Fn = 0.6. Kawahara, et al., (2009) also gave consideration to ships with high centers of gravity and a further examination of the limitations of the component analysis method for buttock flow and shallow draft ships.

Improvements have also been made in roll damping predictions using viscous flow codes (Yeung, et al., 1998, 2000; Roddier, et al., 2000; Seah, 2007; Seah & Yeung, 2008) and unsteady RANS codes (Korpus & Falzarano, 1997; Miller, et al., 2002, 2008; Wilson, et al., 2006), but these simulation tools require long computational times. Because of the wide-spread use of faster, potential flow-based codes, particularly early in the ship design process, the limitations for roll damping predictions must be better understood.

However, despite these advances in viscous flow codes, to determine roll motion characteristics for different ship types, experimental results remain a preferred method. Experiments have been performed for naval vessels at the United States Experimental Model Basin (e.g. McEntee, 1920; 1931), a predecessor of the David Taylor Model Basin; for cylindrical sections (e.g. Stefun, 1955; Vugts, 1968; Gersten, 1969; Yeung, et al., 2000; Miller, et al., 2002); for a cargo ship, Series 60 hull forms with varied block coefficient, C_B, and a tanker (Ikeda, et al., 1978a-e; Himeno, 1981); for modern naval hull forms (e.g. Bishop, et al., 2005; Hayden, et al., 2006; Bassler, et al., 2007); and for ships with instrumented appendages (e.g. Irvine, et al., 2006; Atsavapranee, et al., 2007; Grant, et al., 2007; Etebari, et al., 2008; Bassler, et al., 2010a).

Although substantial work has been performed to extend the applicability of the component analysis model, the semi-empirical nature of the formulation may result in difficulties particularly for ships with proportions that differ greatly from those of the 1960s and 1970s, and for physical phenomena in more severe seas, such as the interaction of the bilge keel and free surface and deck submergence, which may significantly alter the roll damping characteristics for a given ship. An improved understanding of these differences and the limitations of the current models will enable further efforts to increase the robustness of applicability of ship roll damping models.

2.6.2 Time-Domain Models

Use of a frequency-domain method, by definition, does not allow for consideration of nonlinearities in roll damping. In order to obtain time-histories of ship motion, and also consider nonlinearities, a time-domain formulation must be used. In time-domain formulations, the damping term is comprised of both linear and nonlinear components (Haddara, 1973; Lewison, 1976; Dalzell, 1978; Himeno, 1981; Cotton & Spyrou, 2000; Spyrou & Thompson, 2000; Spyrou 2004). Typically, roll decay data regression analysis, based on a "best fit" method, is used to determine the components, without considerations of distinct physical phenomena. Frequency-domain models were developed with considerations for physical phenomena, but it is difficult to

equate the associated physical components from those models to properly determine associated nonlinear damping terms in the time-domain.

Two regression analysis methods are used to determine ship specific roll damping: roll decay and forced roll oscillations. Additional details regarding these two methods is provided in Appendix A. Typically, roll damping is obtained from experimental data, using regression curves with either of these two methods to determine the coefficients. However, appropriately validated higher-fidelity numerical tools, such as RANS solvers, may instead be used to provide the required data for regression analysis.

Using the results from one of the regression analysis methods, a look-up table of coefficients for a range of forward speeds (and frequency for forced roll oscillation tests) can be supplied, for use in the ship motions simulation tool. Once the look-up table is established, the speed and instantaneous roll angle at each time-step can then evaluated to determine the proper roll damping coefficient to use from the look-up table.

2.6.2.1 Time-Domain Models: Assumptions and Limitations

Roll decay data regression analysis is typically used to determine the polynomial components of damping, without consideration of distinct physical phenomena. These regression analysis methods for time-domain formulations do not account for frequency dependence, and it is necessary to perform a large series of tests to determine a sufficient number of coefficients to capture frequency dependence.

Because frequency dependence is not included in either of the regression analysis methods, the coefficients are only applicable for linear regular waves. To obtain roll damping coefficients for larger roll amplitudes, the forced roll oscillation method is preferable. The regression analysis methods can be used to create a look-up table of coefficients. Based on the roll frequency due to incoming waves, the appropriate coefficients may then be used in the time-domain implementation of roll motion. In newer potential flow methods (e.g. Belknap & Reed, 2010) with a time-domain formulation, the roll amplitude and roll frequency are based on the instantaneous attitude of the ship and frequency resulting from the incoming wave-field, as computed from the radiation and diffraction forces, for a given time-step. This was based on suggestions from the author in the early stages of development of the code. However, the viscous contributions to roll damping are still considered using constant coefficients for a given time-step.

Aside from the contribution to roll damping from the barehull wave-making, as considered in the computation of radiation and diffraction forces, memory effects for the other terms are not considered in time-domain formulations. Memory effects for the other hydrodynamic components, besides wave-making, may not be significant when considering the changes in hydrodynamic coefficients for roll motions. However, this requires further analysis and assessment.

2.6.3 Roll Damping in Irregular Waves

To determine roll damping in irregular waves, the typical method is an energy-spectrum analysis, based on the principle of linear superposition (Himeno, 1981). This method assumes that roll motion is a Gaussian process. The motion response spectrum is given by

$$S(\omega) = \left|A(\omega)^2\right| \times S_w(\omega) \tag{2.15}$$

where $S(\omega)$ is the response spectrum, $A(\omega)$ the roll motion RAO, and $S_w(\omega)$ is the long-crested wave spectrum. However, the roll motion RAO is dependent on characterization of the roll damping. Using a least-squares method, the equivalent linear damping, B_e, which is dependent on roll velocity, can be determined. This formulation is also equal to a functional relationship dependent on the standard deviation of roll velocity.

$$B_e = \left(B_1\dot{\phi}^2 + B_2\dot{\phi}^3\right)/\dot{\phi}^2 = B_1 + \sqrt{\frac{8}{\pi}}B_2\sigma_{\dot{\phi}} \tag{2.16}$$

In order to obtain the standard deviation of roll velocity, $\sigma_{\dot{\phi}}$, the following equation must be solved iteratively

$$\sigma_{\dot{\phi}}^{\ 2} = 2\int_0^\infty S(\omega)\omega^2 d\omega \tag{2.17}$$

Because of the difficulty of obtaining a solution to (2.17), a simplified method to determine the standard deviation of roll velocity, without iteration, is also presented by Himeno (1981). The standard deviation of roll velocity is assumed to be equal to the product of the roll natural frequency and the standard deviation of roll motion.

$$\sigma_{\dot{\phi}} = \omega_n\sigma_{\phi} \tag{2.18}$$

This is the formulation using linear systems theory to describe roll damping in irregular waves. Here the standard deviation of roll velocity can be solved iteratively and used to provide input to the damping formulation using a least squares method. The simplified method (without iteration) can also be used.

This formulation for irregular waves assumes that roll is a Gaussian process. However, this assumption is not necessarily valid for large amplitude roll motions, particularly when significant changes in geometry are experienced.

In some modern codes (e.g. Belknap & Reed, 2010), roll damping is computed in the time-domain for ship motions in irregular waves, the "instantaneous" roll frequency and amplitude, using the running FFT of the roll angle, and average forward speed are used from the previous time-step to determine the proper roll damping coefficient(s). This coefficient is multiplied by the roll rate from the previous time-step to determine the roll moment, due to pure roll, in the equations of motion for the given time-step.

2.6.4 Additional Considerations for Roll Motion Models in Potential Flow Simulations

It is necessary to discuss some additional considerations for ship roll damping predictions. Roll damping due to additional appendages, such as a skeg or rudders, is not included in Ikeda's component model. However, it can be included implicitly in the time-domain models of coefficients, which are obtained from experimental results. Cross-coupled damping terms, and the influence from other degrees-of-freedom are also not included in the current model formulations. Particularly for the problem of predicting motions of a ship maneuvering in waves, contributions from other motions may become significant. As discussed previously, scale effects are only included in the barehull friction component.

The methods detailed above are intended for application to monohull vessels. Application to other types of hull form geometries, such as multi-hulls, SWATHs, etc., are not intended with the standard formulation, and should be carefully considered.

2.7 Bilge Keel Force Models

Many potential flow ship motions codes use some variation of Ikeda's bilge keel component (Ikeda, et al., 1978), which considers the bilge keel force as a combination of the normal force component and the hull interaction component and neglects wave-making due to the bilge keel, which are significant for large amplitude roll motion (Bassler & Reed, 2009).

However, some potential flow codes instead model the bilge keel force directly, instead of considering it as part of the roll added inertia and damping model. The simplest formulation uses a flat plate. General studies of the forces on flat plates in a fluid were conducted by Morison, et al. (1950; 1953); Keulegan & Carpenter (1958); Martin (1958); Ridjanovic (1962); Sarpkaya & Isaacson (1981); Sarpkaya & O'Keefe (1996); and Klaka, et al. (2007). A number of experiments were also carried out specifically to study the influence of bilge keels on ship roll motion. These include Bryan (1900), Serat (1933), Adams (1938), Gawn (1940), Tanaka (1961), Gersten (1969), Sasajima (1954), Kato (1966), Bolton (1972), Lofft (1973), Miller, et al. (1974), Cox & Lloyd (1977), Ikeda, et al. (1978a-e), Himeno (1981), Irvine, et al. (2006), Atsavapranee, et al. (2007), Grant, et al. (2007), and Bassler, et al. (2010a).

Existing bilge keel force models are typically based on a Morison equation formulation, for zero or slow speed, or more advanced bilge keel models which consider unsteady vortex shedding. Both types of models are discussed in the following sections. However, there is still a need to improve these models, with consideration for large amplitude roll motions.

Early models for the bilge keel force only considered the drag induced force on the bilge keel, F_B, and a normal force on the bilge keel, obtained by the product of the moment arm from the CG and the roll velocity, $r_A\dot{\phi}$, (Figure 2-6) for zero speed (Lloyd, 1998; Themelis, 2008). However, even for zero speed conditions, the bilge keel force should still experiences some effect from added inertia, particularly for thick span bilge keels. This is not accounted for in the existing bilge keel force models.

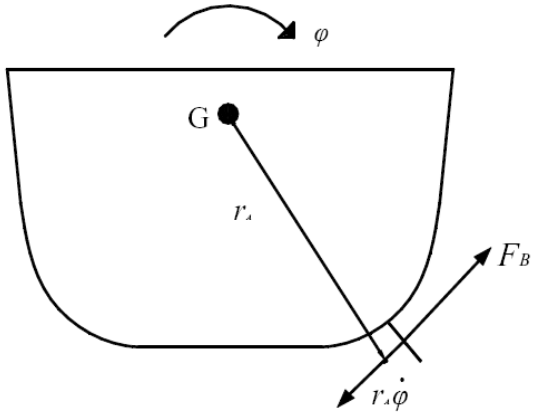

Figure 2-6. Bilge keel force, for zero speed, view of the starboard bilge keel, looking forward (from Themelis, 2008)

2.7.1 Morison Equation Based Models

The Morison equation (Morison, et al., 1950, 1953) is a robust engineering formulation for drag/inertia dominated problems of a body in an oscillatory fluid. However, it has somewhat limited application, due to its semi-empirical form and its basis of using harmonically oscillating planar motion. The semi-empiricism requires precision in selecting values for the inertia and drag coefficients. For applications in non-harmonically oscillating fluids, such as ship motions in irregular waves, application of this method may be limited. A derivation of a Morison-based model is presented in Appendix A.

The non-dimensionalized normal force on the bilge keel, as a function of length, or unit normal force on the bilge keel, can be modeled, using a Morison equation, as the sum of viscous drag and added inertia due to roll motion. Morison's equation appears to be most appropriate for conditions where the Keulegan-Carpenter number is less than 8, or greater than 25 (Sarpkaya & Isaacson, 1981). Keulegan & Carpenter (1958) were the first to attempt to improve on the Morison equation, by specifying a remainder value, while still neglecting diffraction effects. Additional modifications have included consideration of higher-order harmonics (Sarpkaya, 1981).

A Morison equation formulation was used to study oscillating flow around 2D and 3D bilge keels, as represented by flat plates (Sarpkaya & O'Keefe, 1996). However, wall effects that are significant are not accounted for in typical flat plate formulations. Additional studies were carried out to examine the hydrodynamic forces on flat plates in forced oscillation (Klaka, et al., 2007). Additionally, Irvine, et al. (2006) detailed a similar bilge keel force model formulation to describe the force on the bilge keel during roll decays. This model is for a two-dimensional bilge keel section in forced single-degree-of-freedom roll in calm water at zero speed. This formulation was expanded with a suggested possible forward speed correction in Atsavapranee, et al. (2007) and with considerations for multiple degree-of-freedom (roll and heave) motions and the effects of wave orbital velocities in Grant, et al. (2007). These modifications are discussed in more detail in Appendix A. An additional proposal for the inclusion of considerations for large amplitude roll is presented in Chapter 7.

2.7.2 Unsteady Lifting Surface Models

Additional models for the bilge keel force in potential flow codes have been developed using unsteady lifting surface theory, based on a vortex-lattice method. Liut (1999) and Liut & Lin (2006) used a vortex-lattice method to model arbitrary lifting shapes, such as rudders and fins. This is the approach applied in the *Large Amplitude Motions Program* (*LAMP*), and considers the lift force on the bilge keels (Lin & Yue, 1990; Lin, et al., 2006). Additionally, if the lifting surface stalls, then an eddy-making force is computed. This is equivalent to the force on a flat plate, with the flow normal to the surface of the plate. The typical angle of stall considered for the bilge keels is 12 deg.

Greeley & Petersen (2010) presented a bilge keel force model using an unsteady lifting surface (ULS) approach, based on a vortex-lattice method (Figure 2-7). In this model, the vortex shedding from the bilge keel is computed, based on the local flow conditions, and then tracked downstream from the bilge keel. This model is applicable for determining the force on the bilge keel at forward speed. The model showed good comparisons to the experimental and RANS results given in Miller, et al. (2002) for a 3D circular cylinder with instrumented bilge keels. In order to expand the application of this model to low speed conditions, based on the suggestions of the author, the ULS model was coupled with a Morison-equation based approach for very low

speeds and the bilge keel force is obtained by switching between the two models, depending on the speed conditions. In order to couple these two approaches in a robust single model, determination of the Kuelgan-Carpenter number is essential to enable the transition between the two models for the low-speed regime. More detail on the KC number dependency is given in Appendix A. This formulation is currently utilized in the potential flow ship motions code TEMPEST (Belknap & Reed, 2010).

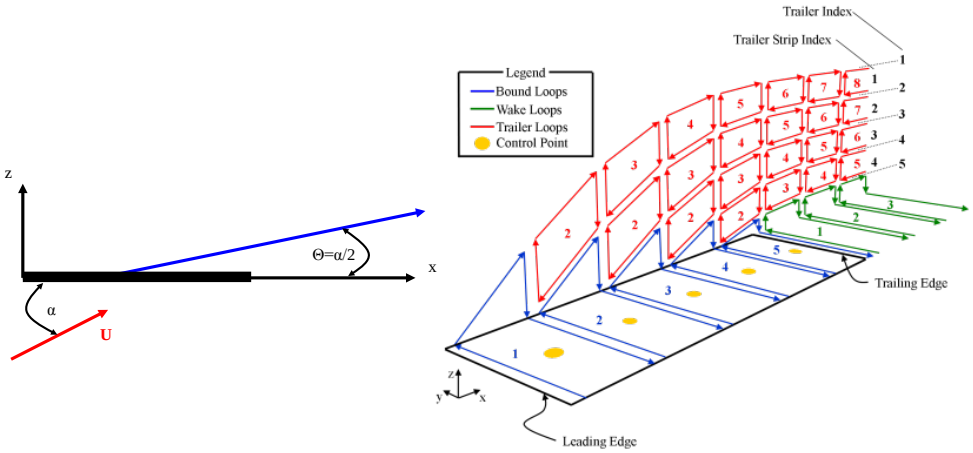

Figure 2-7. Unstead lifting surface (ULS) approach for bilge keel force model (from Greeley and Petersen, 2010).

2.7.3 Bilge Keel Force Models: Assumptions and Limitations

Several inherent assumptions are contained within the zero-speed bilge keel model. First, all of the models assume small amplitude roll motions, that the bilge keel remains deeply submerged and the interaction effects with the free surface can be neglected. Second, the local flow effects from waves, specifically the orbital velocities, are generally not considered. Third, 3D effects, both in the longitudinal direction and span-wise direction are not explicitly considered. In the longitudinal direction, these are particularly important for forward speed conditions. In the span-wise direction, the bilge keel is wall-bounded on one side, by its attachment to the hull.

Linear wing theory is not applicable for a bilge keel force model. Because the bilge keel exists in a viscous fluid and is a low-aspect ratio wing, nonlinear lift occurs even at relatively moderate roll motions and side edge vortex shedding occurs along the length of the bilge keel, throughout the roll motion cycle.

In particular, because the interest of the present work is on the application of models for heavy weather operations, where large amplitude ship roll motions may occur at zero to low speed, then the primary considerations which must be included in further development of a model is for physical phenomena the bilge keels experience during large amplitude roll motions.

2.8 Memory Effects and Roll Damping

Except for the radiation and diffraction forces, hydrodynamic memory effects are typically neglected for roll motions in potential flow based numerical tools. The radiation and diffraction components model the barehull wave-making damping component. However, other components,

such as the bilge keel, hull lift, and hull eddy-making damping do not consider any memory effects.

The unsteady lifting surface (ULS) approaches for bilge keel force models consider memory effects from shed vorticity, where the tracking duration after the vortices are shed from the bilge keel and the hull can be specified. However, the computational cost compared to the required accuracy must be carefully considered when determining the appropriate time duration of vortex tracking.

2.9 Further Considerations for this Investigation

In this chapter, models for ship roll hydrodynamic components were reviewed. Details, assumptions, and limitations for both frequency-domain and time-domain approaches were presented and discussed. Additionally, models for the force on the bilge keel were also reviewed.

For this investigation, the focus remains on single degree-of-freedom models for roll motion. However, considerations for large amplitude effects and the influence on the hydrodynamic components of ship roll motion are of interest for further understanding and development. Even with the single-degree-of-freedom simplification, knowledge can still be gained which is of interest to model one of the primary intact dynamic stability failure modes-dead ship condition, or roll in beam seas at zero speed. As one of the worst case scenarios for a ship in heavy weather, it is important to expand the applicability of hydrodynamic component modes to accurately assess ship performance in this condition.

In the next Chapter, high-fidelity numerical simulations (unsteady RANS) are used to examine the physical phenomena which occur during large amplitude roll motion and then prioritize the relative influence of these phenomena on the roll hydrodynamic components.

Chapter 3 Numerical (URANS) Modeling, Results, and Analysis to Assess the Overall Problem of Large Amplitude Ship Roll Motion[7]

3.1 Overview

Realistic conditions of ship roll motion in heavy weather result in a complex interaction of factors, including the environment and the ship response. The environment model includes the distribution of spectral energy, the relative heading between the waves and the ship, and the steepness of the waves, which are modeled as the forcing function input to the roll motion equation. The ship geometry and loading condition govern the behavior of the response of the ship to the surrounding environmental conditions. An illustration of this for a naval combatant, is seen in Figure 3-1. From this illustration, the complex interaction of the hull form geometry, including bilge keels, rudders, and topside, with the surrounding wave environment, can be observed.

This chapter examines the physical complexities of the total problem of ship roll motions in heavy weather using a high-fidelity numerical tool, and identifies the relative significance of the physical effects, which are then assessed for the purpose of further study of large amplitude roll motion.

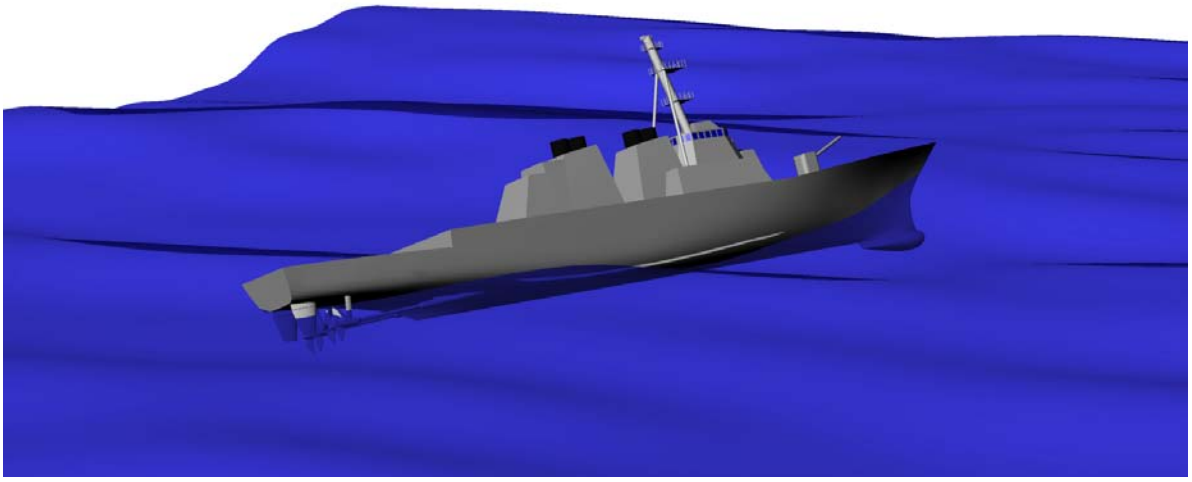

Figure 3-1. Numerical simulation of a naval combatant in heavy seas, experiencing large roll motion, resulting in partial emergence of the starboard bilge keel[8]

[7] Portions of this chapter have been published previously in Bassler and Miller (2011) and Bassler, et al. (2011)
[8] Figure provided by Dr. William Belknap (Seakeeping Division, NSWCCD)

3.2 Hull Form Geometry

The ONR Topside Series hull forms were designed in the Seakeeping Division at NSWCCD[9] (Bishop, et al., 2005). These hull forms represent a notional modern naval combatant ship design, and feature a common below waterline geometry, with varied topside shapes, including flared, tumblehome, and wall-sided configurations. Since the design of the ONR Topside Series at the beginning of the 21st century, these hulls have been tested and analyzed throughout the world. Additionally, being representative of modern naval combatants, these hull forms present an attractive choice for further study for the problem of large amplitude roll motion.

A 32nd-scale model (Table 3-1) of the ONR Topside Series tumblehome topside configuration (DTMB Model #5613-1) was previously used for experiments (Bassler, et al., 2007) and numerical studies (Miller, et al., 2008) of forced roll motions at NSWCCD. During these studies, bilge keel emergence was observed (Figure 3-2). In this figure, the forward section of the starboard bilge keel has emerged, the midsection is shipping water, and the aft section remains submerged.

Table 3-1. Barehull hydrostatic parameters for DTMB Model 5613-1 (Bassler, et al., 2007)

Displacement	260.14 kg
Draft	0.172 m
Lpp	4.8125 m
Beam	0.5875 m
KG	0.172 m
Roll Gyradius/Beam	0.361
Scale Ratio	32

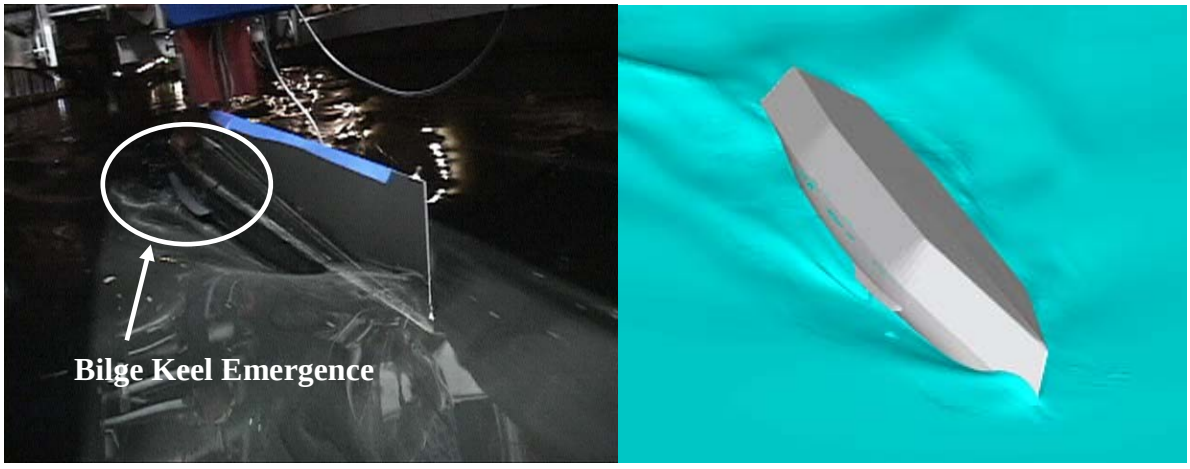

Figure 3-2. Experimental (Bassler, et al., 2007) and numerical (Miller, et al., 2008) observations of partial bilge keel emergence for DTMB Model #5613-1 at Fn = 0.30, ϕ= 30 deg.

[9] The ONR Topside Series hull forms were designed by Martin J. Dipper, Jr., Brad Campbell, and William Belknap

3.3 URANS Simulations

A series of unsteady Reynolds Averaged Navier Stokes (URANS) simulations were performed at NSWCCD by Ron Miller, for the 3D ONR Tumblehome topside configuration, representative of DTMB Model #5613-1. These simulations were for large amplitude roll motion at both zero and forward speed conditions, in calm water and in waves. The purpose of this study was to analyze high-fidelity numerical results on both the hull and the bilge keel, to improve understanding of the physical effects including forward speed and waves, which should be considered for future developments of strip-theory approaches for ship motions prediction in heavy weather. The results were also examined to assess the relative importance of the physical effects, for their consideration in future developments of hydrodynamic component models for the hull and bilge keels of a representative modern naval combatant hull form. In this section, an overview of the solver, the simulation conditions, and a new post-processing method that was developed for obtaining the sectional forces on the hull and bilge keel in a URANS solver are presented and discussed.

3.3.1 Solver

Previously, Miller, et al. (2002) demonstrated that URANS solvers could be used to accurately predict the roll moment and bilge keel forces on a 3D cylinder undergoing forced oscillations. The forces were predicted well with the UNCLE code, developed at Mississippi State University. Subsequent predictions with CFDShip-Iowa, Version 3 (e.g. Wilson et al., 2006), demonstrated a similar level of capability. Version 3 of CFDShip-Iowa utilizes a free surface tracking algorithm, where the computational grid must be updated to conform to the free surface deformations. Due to limitations presented by the free surface tracking algorithms in these codes, and the lack of a robust 6 degree-of-freedom (6DOF) grid motion and prediction capability, roll amplitudes were limited and a wide range of conditions could not be computed for realistic ships.

CFDShip-Iowa, Version 4 utilizes a level-set free surface capturing technique. This technique solves an advection equation for the level-set function, representing the distance to the free surface. The free surface is the surface where the level set function is zero. In this technique, the grid does not need to conform to the free surface topology. However, sufficient grid resolution is required to discretize the level-set function gradients. Version 4 also uses dynamic overset grid technology, which allows for the prediction and/or the prescription of arbitrary 6 DOF motions. Previous comparisons between numerical and experimental results have shown good agreement (Miller, et al., 2008). In this study, both of these enhancements from Version 4 are used. Further details regarding the solver for CFDShip-Iowa, Version 4, overset grids, and the computational domain used for this study are discussed in Appendix B.

3.3.2 Obtaining Segmented Forces

CFDShip-Iowa sums the force/moment contributions from all of the wetted wall surface elements at each time step. For this study, both the total and segmented forces and moments on the hull form and bilge keels were of interest. In order to obtain segmented forces, a post-processing routine was developed to create longitudinal segment distributions, Δx, over the hull and appendages. These segments were obtained from the URANS simulations by integrating the predicted stresses on a set of finite width sections. By decomposing the total force on all the

wetted surface elements at each time step into these longitudinal segments, a force/Δx is obtained at each specified x location segment (Figure 3-3).

The development of this post-processing routine to obtain segmented forces and moments[10] enabled changes to be made to the constraints, which do not necessarily conform to the surface meshes, or the regions of interest on the hull form, after the simulations have been performed, without having to re-run them. This enables local regions of interest, such as pressures on the bow dome, or forces on the appendages (bilge keels, rudders, shafts, struts) to be further interrogated and re-examined, after a series of computations have been performed. For simulations of DTMB Model #5613-1, 20 segments were specified (Figure 3-4) to interrogate the bilge keel force during the prescribed roll motions.

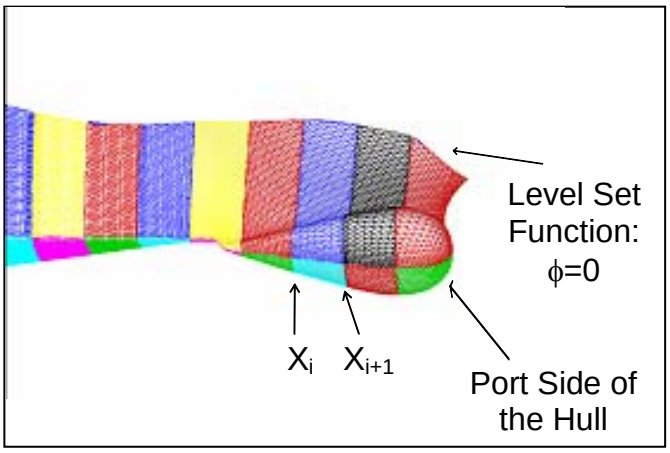

Figure 3-3. Post-processing example of longitudinal segments for the hull, with the bow section shown, up to the instantaneous waterline

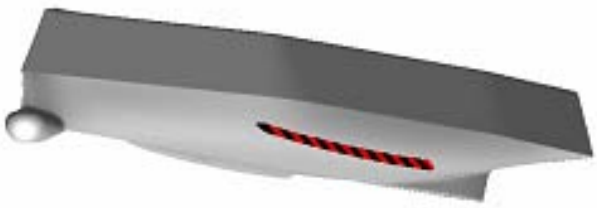

Figure 3-4. DTMB Model #5613-1 with bilge keel divided into 20 segments (shown in red and black) for sectional force analysis

3.3.3 Simulation Conditions

Several physical effects, which are relevant to modeling a ship maneuvering in waves, were examined. These included 3D, forward speed, and waves for ship roll motions, and maneuvering effects. Each of these effects were examined individually, to assess their relative significant to the forces observed on the hull and bilge keel.

[10] This routine was developed by Ron Miller, at NSWCCD, in 2010.

Simulations were performed for forced oscillation 1-DoF roll motions, with moderate to large amplitude, in calm water at zero speed and with forward speed. Additionally, simulations were performed in beam sea regular waves, to simulate 1-DoF dead ship condition, with wavelength equal to ship length and a steepness of 1/100, for zero speed, and for steady drift in calm water at forward speed, to examine cross-flow drag effects (Table 3-2).

For the calculations presented, fixed yaw angles (±10 deg) and single degree-of-freedom (1-DoF) roll motion were prescribed, and a constant forward speed was imposed using uniform inflow into the computational domain. The axis of rotation was along the ship's center plane, through the vertical center of gravity. The body sway, heave, pitch, and yaw modes of motion were fixed for the 1-DoF roll calculations.

Table 3-2. Simulated conditions for DTMB Model 5613-1

Froude Number	**Roll Frequency (rad/s)**	**Motion Amplitude (deg)**	**Sea Conditions**
0.0, 0.30	2.85	1-DoF Roll: 15, 25, 30, 35	Calm Water
0.0	2.85	1-DoF Roll: 25, 35	Beam Waves ($\lambda/L = 1.57$, $H/\lambda = 1/100$)
0.3	0	1-DoF Yaw: ± 10	Calm Water

3.4 Results

Physical effects relevant to modeling a ship maneuvering in waves, are presented, including 3D, forward speed, waves, maneuvering, and large amplitude roll effects. By examining the URANS results for the 3D hull form at several sections along the model length, longitudinal variations of the roll moment, bilge keel force, and flow-field features were analyzed. Simulations for the model undergoing steady forward motion show significant differences in the flow-field quantities as compared to the zero forward speed cases.

3.4.1 3D and Forward Speed Effects

Results are presented for both axial vorticity and bilge keel force at various longitudinal locations along the hull, for both zero and forward (Fn = 0.3) speeds.

With the combination of forward speed and roll motion, the vortex shedding from the bilge keels, bow, and skeg all influence the forces and motions on the hull. For the simple case of 1DoF roll motion at forward speed, the convection of shed vortices downstream is significant (Figure 3-5). Even at moderate roll angles, the vortices shed from the bow dome are convected downstream along the keel beneath the hull and interact with the skeg. The vortices shed from the bilge keels and the skeg, including the influence from the bow dome, are convected

downstream and will interact with the propulsor(s). Multiple-DoF ship motions and wave effects will further influence and complicate vortex shedding along the hull.

During roll motion the vortices shed from the bilge keels and bow dome remain clustered near their shed position for zero speed (Figure 3-6). As expected, at forward speed, the vortices are convected downstream. At forward speed, the magnitude of the vorticity near the midship section is reduced, compared to zero speed, but the additional presence of the bow-dome vortices was observed (Figure 3-7).

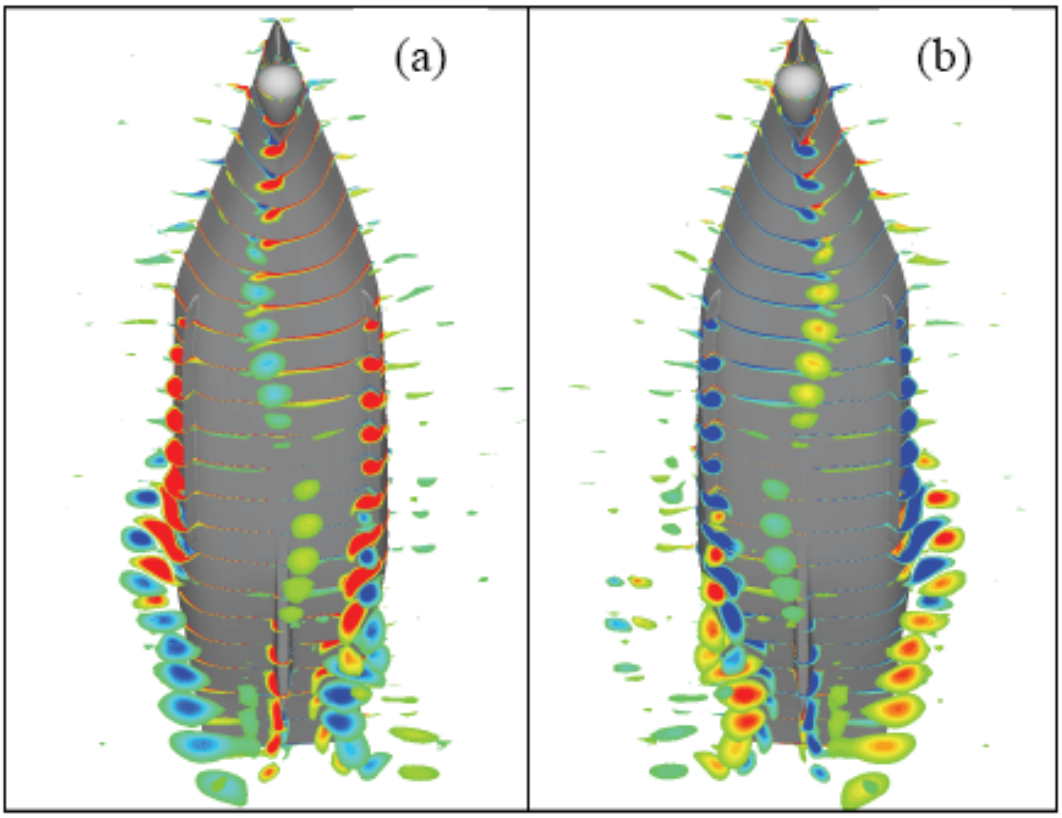

Figure 3-5. Simulated axial vorticity contours for DTMB Model 5613-1, at Fn = 0.30, ϕ= 15 deg, ω = 4.83 rad/s, (a) counter-clockwise rotation and (b) clockwise rotation (from Miller, et al., 2008)

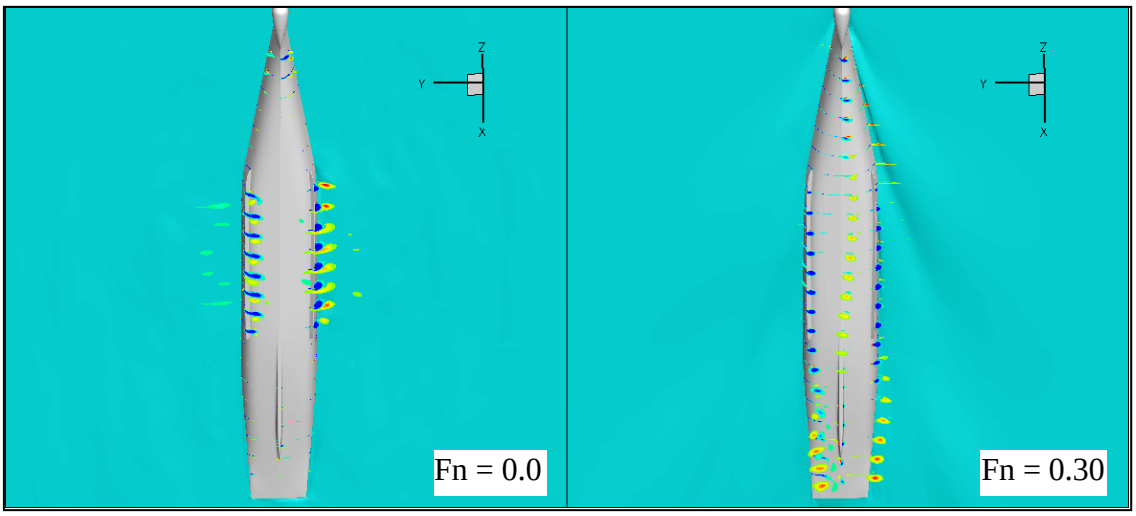

Figure 3-6. Axial vorticity for DTMB Model 5613-1 at various longitudinal locations, for zero speed (left) and forward speed (right) conditions, ϕ = 25 deg, ω = 2.85 rad/s

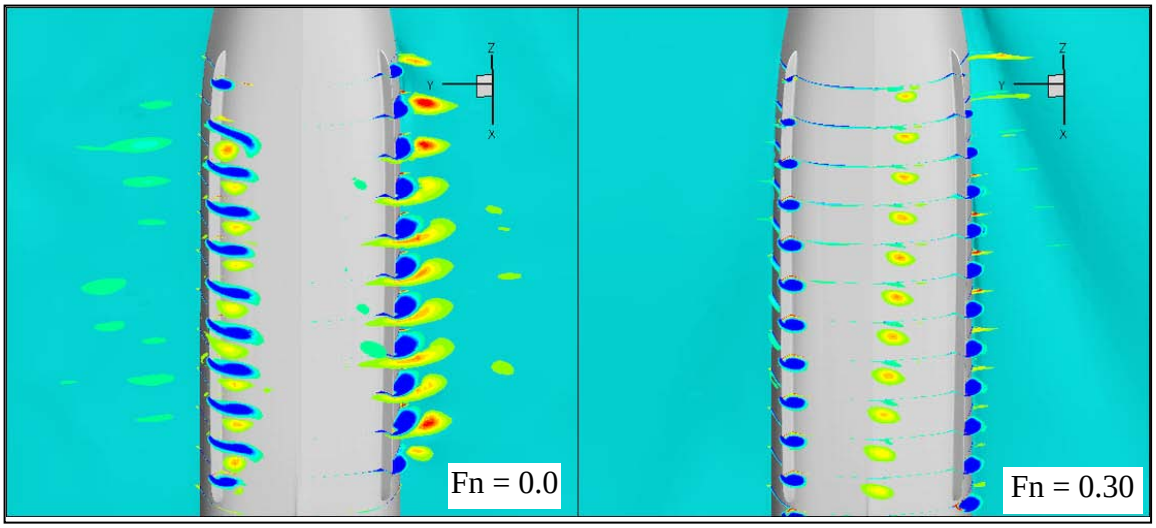

Figure 3-7. Axial vorticity along the bilge keels, near the midship section of DTMB Model 5613-1, for zero speed (left) and forward speed (right) conditions, ϕ = 25 deg, ω = 2.85 rad/s

URANS results are presented to examine the influence of forward speed (Fn = 0.3) compared to zero speed (Fn = 0.0) on the midship section bilge keel force (Figure 3-8). As observed, even for smaller amplitude roll motion, the differences in the unit bilge keel force are greater due to forward speed effects than due to 3D effects. Overall, the greatest difference due to forward speed occurs during the peak of the roll cycle just after the bilge keel is fully submerged.

For the portion of the roll cycle where the bilge keel is near the free surface, the zero and forward speed results agree quite well. This is likely due to the shedding of vorticity from the bilge keel at the fully submerged position in the roll cycle, and the reduction in force on the bilge keel due to the vortex when it is convected downstream in the forward speed condition.

For the 25 and 30 deg roll cases, the difference in the bilge keel force at the peak of the roll cycle for zero and forward speed becomes larger. This is likely due to the interaction of the

bilge keel with the free surface, and again the bilge keel force is less for the forward speed condition than for the zero speed condition, due to the downstream convection of vorticity.

For the 35 deg roll case, the portion of the roll cycle corresponding to the emergence of the bilge keel agrees well between the zero speed and forward speed conditions. For this case, the impulse loading on the bilge keel during re-entry is significant during at both speeds. However, the influence of "water shipping" (or lingering) on the topside of the bilge keel is reduced for the forward speed case, compared to the zero speed case.

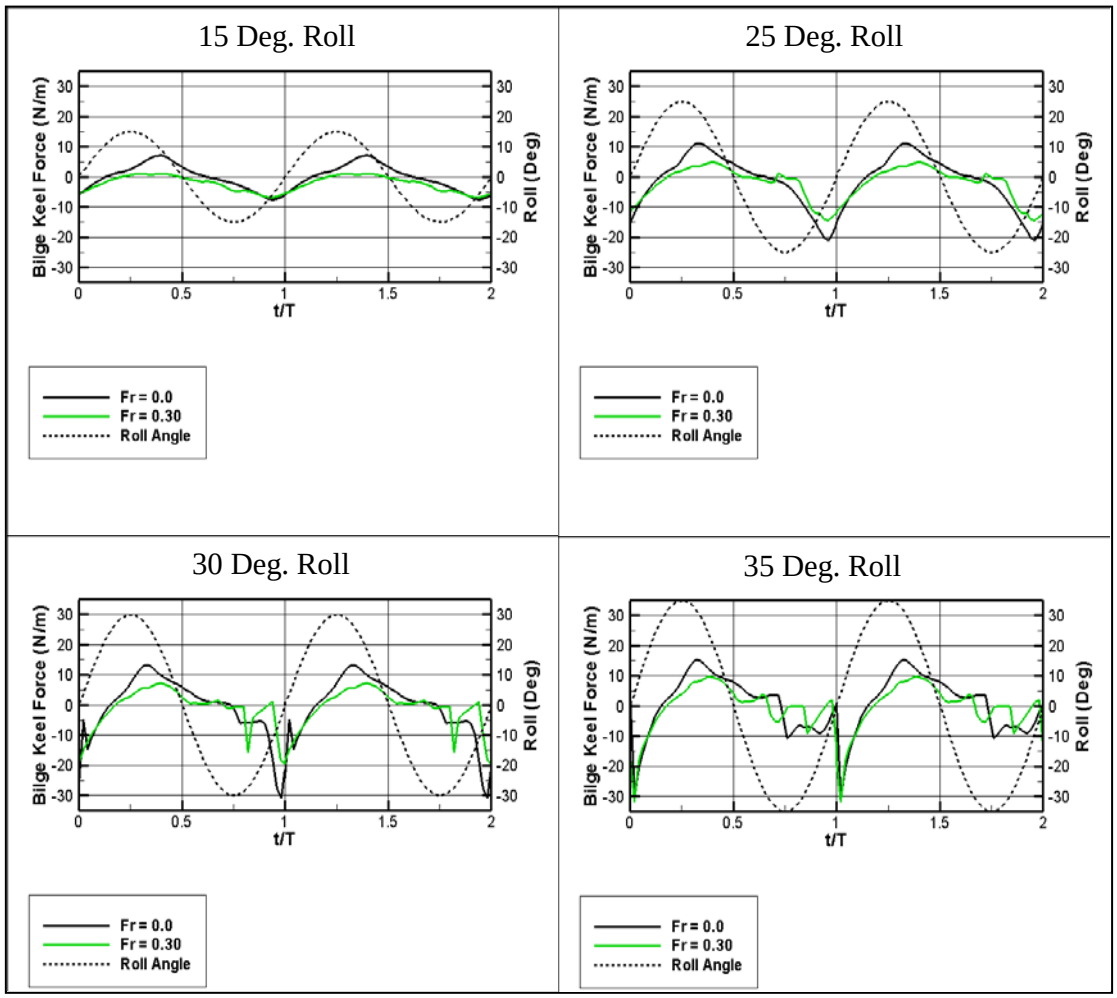

Figure 3-8. Bilge keel force comparisons between 3D URANS simulations for zero speed (solid black) and forward speed (solid green) for the midship section of DTMB Model 5613-1 at ω = 2.85 rad/s, for ϕ = 15, 25, 30 and 35 deg roll

Vorticity and bilge keel forces were examined at four specific locations, to determine the longitudinal variation for each. These locations included the leading edge (LE) of the bilge keel, and forward (x/L = 0.4), midship (x/L = 0.5) and aft (x/L = 0.6) positions on the bilge keel (Figure 3-9).

For 25 deg roll at zero speed (Figure 3-10), all of the positions experience similar forces, and the force variation over a roll cycle is fairly small. However, for forward speed, the leading edge force differs significantly from that at the other three positions, especially for the portion of the roll cycle where the bilge keel is near to the free surface. The maximum force appears just before the maximum upward angular velocity (t/T = 0.5). For the maximum downward angular velocity, for large angles, free-surface re-entry effects occur due to the re-wetting of the leading edge of the bilge keel with the combination of the bow wave generated by the ship at forward speed.

This significant variation for the leading edge bilge keel section is likely because of the pressure differentials which exist at the leading edge at forward speed, corresponding to greater lift generated at the leading edge section. This is even further exacerbated for a low aspect ratio airfoil (such as a bilge keel). The variation between the forward, midship, and aft sections is also more significant than for the zero speed condition. The effect of re-entry after emergence of the bilge keel is more pronounced for the forward speed condition.

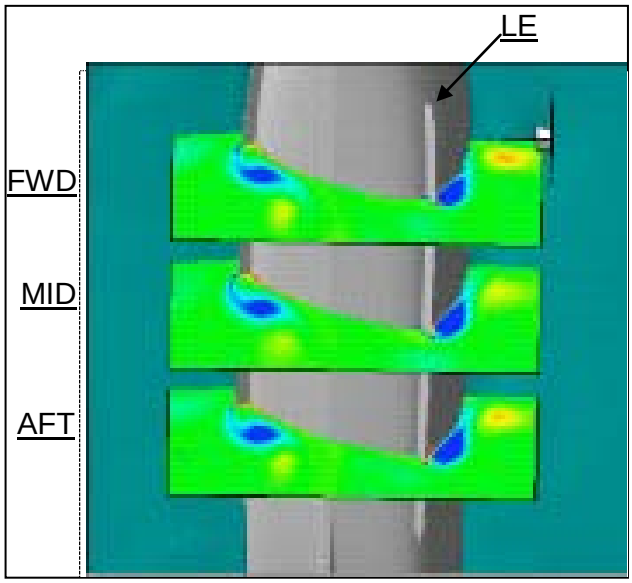

Figure 3-9. Vorticity shown at the locations of bilge keel force sectional analysis: leading edge (LE), forward section (at x/L = 0.4), midship section (at x/L = 0.5), and aft section (x/L = 0.6)

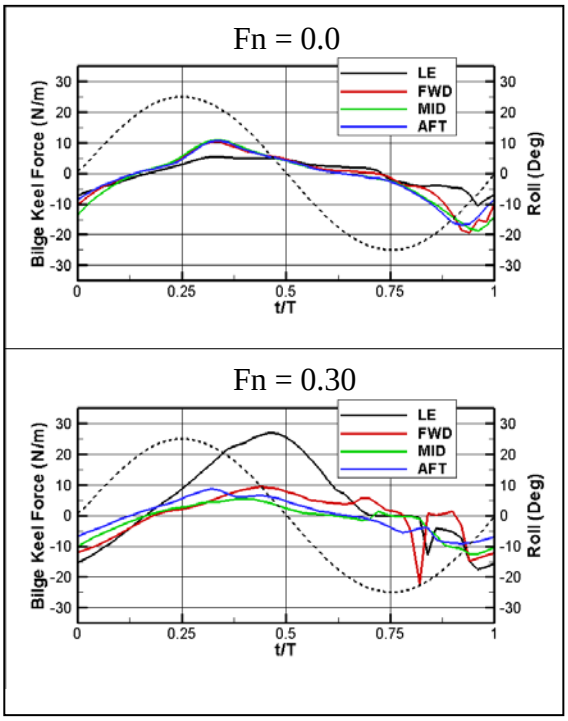

Figure 3-10. Unit bilge keel force for DTMB Model 5613-1, at leading edge (black), forward (red), midship (green), and aft (blue) locations, for zero speed (top) and forward speed (bottom) conditions, $\phi = 25$ deg, $\omega = 2.85$ rad/s

As seen from the bilge keel forces for 35 deg roll (Figure 3-11) at zero speed, the forward, midship, and aft bilge keel sections do not have significant variations. Even for the zero speed condition, the leading edge section of the bilge keel has a more significant impact load on re-entry then for the other sections. This is due to the pressure differential on the bilge keel at an even higher angle of attack of the leading edge, as it follows the streamline along the hull. For the forward speed condition, significant variation is observed for the bilge keel force between the leading edge section and the other three sections. Similar to the 25 deg roll case, the bilge keel force on the leading edge section is larger for the portion of the roll cycle where the bilge keel is near to, and emerging from, the free surface. For the forward speed condition, the forward section, instead of the leading edge, of the bilge keel experienced the most significant impact loading on re-entry. This is due to the bow wave generated along the hull at forward speed, which reduced the disturbance of the bilge keel force on the leading edge section, even for the occurrence of large amplitude roll.

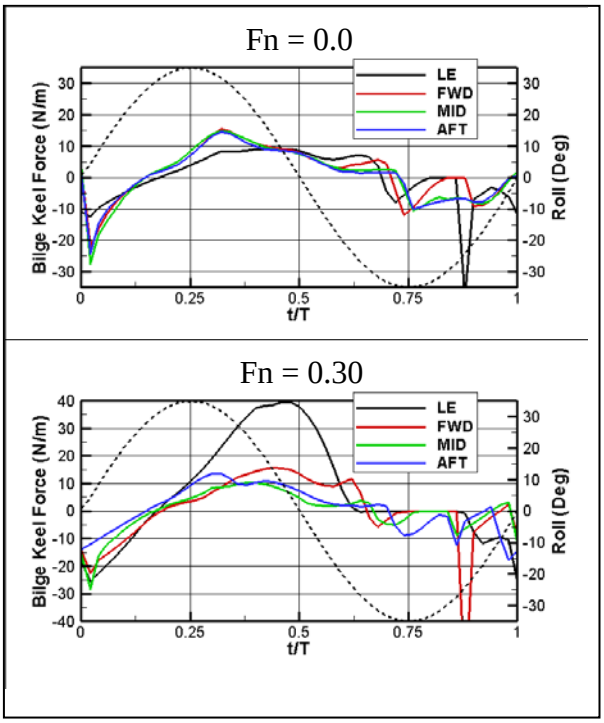

Figure 3-11. Unit bilge keel force for DTMB Model 5613-1, at leading edge (black), forward (red), midship (green), and aft (blue) locations, for zero speed (top) and forward speed (bottom) conditions, ϕ = 35 deg, ω = 2.85 rad/s

3.4.2 Large Amplitude Roll Motion Effects

For large amplitude roll conditions (Figure 3-8, Figure 3-10, Figure 3-11), the bilge keel may emerge from the water, resulting in lingering forces due to water-shipping effects and severe impact loading-type behavior due to re-entry during the roll motion. These abrupt changes may create difficulties for time-domain simulation of large amplitude roll motions in potential flow codes. Additional consideration must be given to how vorticity calculations will be re-started, how the bilge keel will be de/re-wetted upon emergence and re-entry, and to how hysteresis effects due to "water shipping" on the bilge keel, once emerged, will be considered.

3.4.3 Wave Effects

URANS simulations were also performed for the 3D ONR Tumblehome hull undergoing 1-DoF forced roll oscillations, at zero speed, in beam seas regular waves, with H/λ = 1/100 and λ/L = 1.0. The ship was fixed in sinkage and trim to enable more direct comparisons with the calm water forced roll oscillation conditions. The waves impacted the hull from the port side and the variation in the force on the midship section of the bilge keel, was examined, as a function of wave phase.

Four comparisons, based on the wave phase relative to the peak of the roll cycle, are shown for both the 25 and 35 deg forced roll oscillation conditions. These included when the wave crest (max), wave trough (min), front slope of the wave (front) and back slope of the wave (back), coincided with the port side bilge keel at the peak (maximum) of the forced roll cycle, Figure 3-12-Figure 3-15, respectively. As shown in the plots, the synchronization between the

wave and roll frequencies occurred at t/T = 0.75, when the port side bilge keel is closest to the free surface (the maximum of the roll cycle).

For the maximum condition, where the peak of the roll cycle corresponds to the wave crest, the force on the bilge keel varies least, since it remains submerged the longest. In this case, due to re-entry effects, the 35 deg (larger) roll amplitude results in greater force, than the 25 deg (smaller) roll amplitude, where the bilge keel remains submerged.

For the minimum condition, where the peak of the roll cycle corresponds to the trough of the wave, significant force on the bilge keel is observed due to impact loading on re-entry. In this condition, the peak force is largest, due to the higher relative velocity between the bilge keel and the free-surface, and the bilge keel has greater velocity at re-entry. However, the peak force for the 35 deg case is slightly less because of the phase lag (and thus reduced time in the roll cycle) before re-entry.

For the condition with the peak of the roll cycle corresponding to the front slope of the wave (midway between crest and trough), the 25 deg case has a reduced peak force because the bilge keel does not experience emergence. However, the 35 deg case shows impact loading due to emergence of the bilge keel. This is reduced compared to the back slope of the wave, due to the direction of the orbital velocities within the wave relative to the motion of the bilge keel.

For the condition with the peak of the roll cycle corresponding to the back slope of the wave (midway between trough and crest), both the 25 deg and 35 deg cases show large peak forces on the bilge keel, due to the relative velocity on the bilge keel at re-entry.

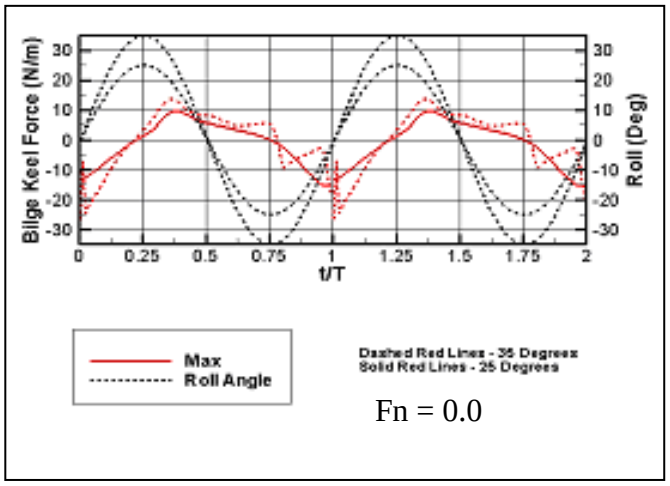

Figure 3-12. Force on the midship section of the port side bilge keel for 25 (solid) and 35 (dotted) deg roll. Wave phase with crest corresponding to peak of the roll cycle (at t/T = 3/4).

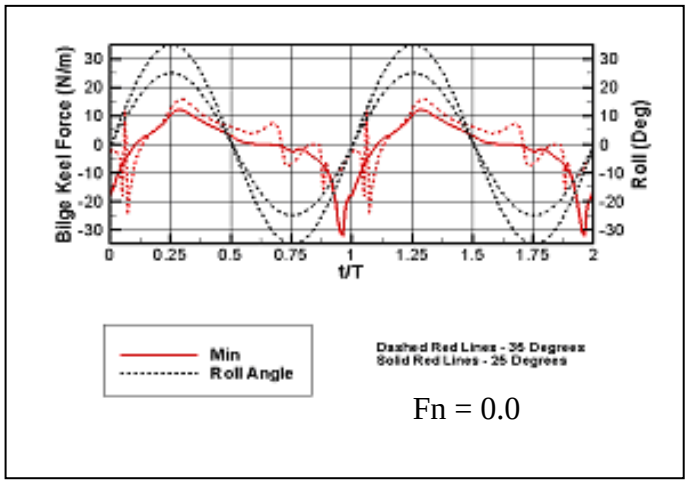

Figure 3-13. Force on the midship section of the port side bilge keel for 25 (solid) and 35 (dotted) deg roll. Wave phase with trough corresponding to peak of the roll cycle (at t/T = 3/4).

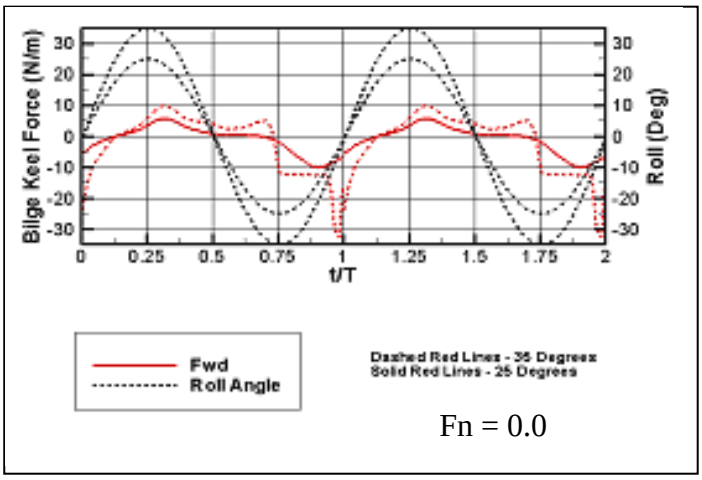

Figure 3-14. Force on the midship section of the port side bilge keel for 25 (solid) and 35 (dotted) deg roll. Wave phase, front slope corresponding to peak of the roll cycle (at t/T = 3/4).

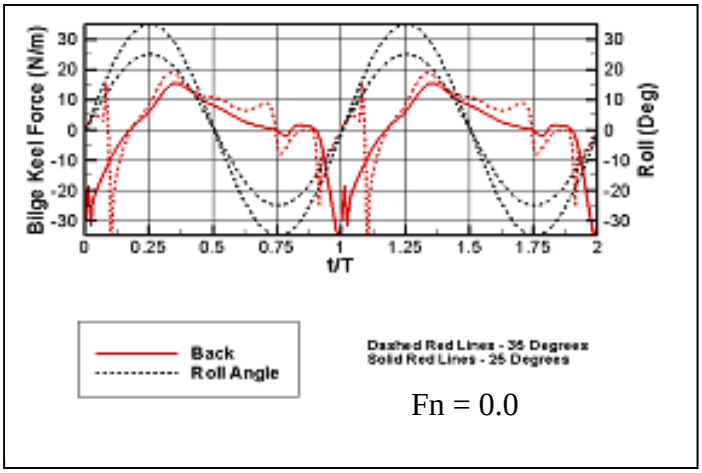

Figure 3-15. Force on the midship section of the port side bilge keel for 25 (solid) and 35 (dotted) deg roll. Wave phase, back slope corresponding to peak of the roll cycle (at t/T = 3/4).

3.4.4 Maneuvering Effects

The effects of coupled motions in waves, including large roll motions, while also maneuvering, are important. Previous work has shown that the vortex shedding and cross-flow drag effects on the bilge keels during steady turning, even at only small heel angles, is already significant (Dai, et al., 2009).

To examine the signifcance of cross-flow drag forces on the bilge keel, a series of URANS simulations were performed for the case of ±10 deg steady drift (fixed yaw) in calm water at forward speed. As seen from the pressure contours observed on the hull for windward (+10 deg) and leeward (-10 deg) drift conditions (Figure 3-16), the bow dome experiences the largest pressure gradient, while the bilge keels also experience large pressure gradients at the leading edge of the windward side bilge keel (going into the flow). Meanwhile, the leeward side bilge keel is effectively sheltered by the hull. This is manifest in the longitudinal force distribution along the port side bilge keel for windward and leeward side conditions (Figure 3-17). When the bilge keel is in the windward condition, a large force results on the leading edge, but is relatively constant along the remainder of the bilge keel, before tapering off at the trailing edge. When the bilge keel is on the leeward side, the sheltering by the hull results in almost no cross-flow drag force on the bilge keel.

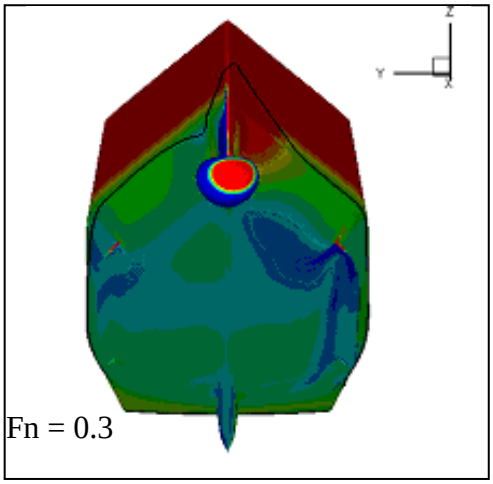

Figure 3-16. Pressure contours on the submerged portion of the DTMB Model 5613-1, for drift from the windward side (+10 deg), looking aft from the bow.

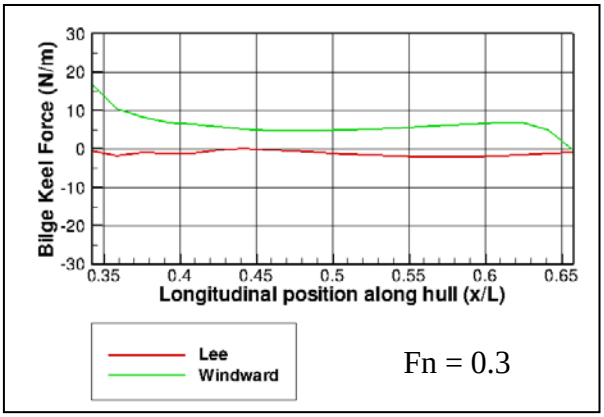

Figure 3-17. Longitudinal distribution of force along the port side bilge keel for drift from the windward and leeward sides (±10 deg).

3.4.5 Observations from the Numerical Results

For the single hull form, bilge keel configuration, wave condition, and drift condition that were examined, for two speeds, the following observations were made. The results were analyzed to give general consideration to the physical effects observed from the numerical results.

- 3D effects were more significant for zero speed conditions, but were also apparent for the forward speed condition, where vorticity is convected downstream
- The effects of vorticity on the bilge keel force were reduced with forward speed; however, at forward speed an additional component of vorticity from the bow dome was observed and may have some influence on the bilge keel force for lower frequency oscillations
- At zero speed, there is not much longitudinal variation in the bilge keel force, except for the re-entry of the leading edge section for large amplitude roll
- At forward speed, lift and free surface effects (near to and emerging from) are greatest for the leading edge section
- At forward speed, the bow wave influences the location and magnitude of the impact loading on the bilge keel
- The presence of waves influences the force on the bilge keel, and depends on the phase of the wave relative to the roll cycle; while the bilge keel is deeply submerged, the influence of the waves is least
- For large amplitude roll conditions in waves, the magnitude of the impact loading on the bilge keel during re-entry is reduced, compared to the same large amplitude roll motion in calm water conditions.
- The effect of different wave phases on the bilge keel force, such as bilge keel re-entry in a wave trough, may lead to an increase in the bilge keel force compared to calm water and compared to other wave phases.
- In calm water, the effect of steady drift on the bilge keel forces was examined. Significant differences in the bilge keel force were observed for the windward and leeward side bilge keels and at the leading and trailing edge.

The roll motion response of a ship in beam waves, at low to zero speed, is the condition for which bilge keels were designed to compensate. As observed from the numerical simulations, the bilge keels have reduced effectiveness at increased forward speed, due to the vortex shedding mechanism. But the effectiveness of the bilge keels is also affected by the influence of large amplitude motions and in waves, due to the interaction of the bilge keels with the free surface and the resulting impact on the physical mechanisms for energy dissipation to reduce ship roll motion.

3.5 Assessment of the Physical Effects for Simulations of Ship Motion in Heavy Weather

High-fidelity (URANS) numerical results were analyzed to assess the relative importance of the physical effects, for their consideration in future developments of hydrodynamic

component models for the hull and bilge keels of a representative modern naval combatant hull form. The comparisons performed for this study enabled examination of the effects of the forces on the hull and bilge keels, due to vortex shedding, forward speed (and resulting flow convection downstream), waves, maneuvering (represented by steady yaw conditions for cross-flow drag), large amplitude roll motions, where bilge keel emergence and immergence occurred.

3.5.1 Relative Importance of the Physical Effects

From the decomposition of the physical effects for consideration in modeling the bilge keel forces during ship maneuvering in waves, several aspects were examined. These included 3D, forward speed, wave, maneuvering (cross-flow drag due to steady drift), and large amplitude roll motion effects. From the URANS simulations, the overall relative importance (greatest to least) of these physical effects for ship motions was assessed and is summarized as follows: forward speed, large amplitude roll, wave effects, maneuvering, 3D effects/longitudal variation along the bilge keel. However, for heavy weather, ship speeds are normally slow speed, or zero speed in the worst condition, when a ship may have lost power and be drifting. Therefore, for ship motion prediction in heavy weather, large amplitude roll motion effects are expected to be the most significant physical phenomena.

Forward speed convects vorticity downstream, but zero (or low) speed allows the vorticity to linger near the bilge keels, which is difficult for potential flow simulations to capture, due to the vortex interaction effects. Other forward speed issues, such as the influence of vortex shedding from the sonar dome on the bilge keels, must also be cnsidered. Bilge keel vorticies will convect downstream, possibly into the shafts, skeg, and finally propulsion and rudder sections fo the hull, depending on the present ship orientation (roll, drift angle, rates, etc). An example of this, for the barehull with bilge keels configuration, at Fn = 0.3, is given in Figure 3-5. Accurate prediction of the vorticies created by the bilge keels and the prediction of their interactions with other sections of the ship geometry are important.

Large amplitude roll motion may result in the largest reduction in bilge keel performance while the ship is maneuvering in waves. Jumps in forces caused by bilge keel interaction with the free surface may also cause computational difficulties due to discontinuities across time-steps in potential flow simulations.

Wave effects were examined and wave phase was shown to have a significant effect on the bilge keel force, particularly when coupled with large amplitude roll motion, where the bilge keel may interact with the free surface during emergence and re-entry. Because of the variation in relative velocity between the bilge keel and the free surface, the peak loading on the bilge keel varies signficantly with the phase of the motion relative to that of the wave.

Maneuvering imparts a significant force on the leading edge of the windward side bilge keel, and is important for consideration due to the impact of the inflow conditions on the bilge keel for computation of the vortex shedding in ULS methods for the bilge keel force.

From the cases examined, the 3D effects along the bilge keel, aside from the leading edge, did not appear to be significant. Sectional formulations can be used for the bilge keel force, but care must be taken to account for forward speed, large amplitude roll, and maneuvering effects, given their impact the forces on the leading edge of the bilge keel.

3.5.2 Implications for Potential Flow Simulations of Ship Motion in Heavy Weather

Because of the significance in the bilge keel force and vortex shedding of forward speed effects, future developments for potential flow ship motion simulations should consider these effects for prediction and assessment of typical operating conditions for ships in waves.

Vortex interactions effects, as they are shed from the bilge keels, are significant, particularly near intact stability failure conditions. For these conditions, steep waves may result in large amplitude roll motions, while the ship is typically moving at slower speeds, or is in a dead ship condition, and the vortices will have a lingering presence. At zero or slow speeds, the influence of the vorticity is more difficult to consider in sectional or strip-theory based approaches for ship motion predictions. Additionally, for non-traditional bilge keel designs to improve roll damping performance, including tip geometry variations[11], consideration must be given to the effects of bilge keel geometry variations on damping. Therefore, bilge keel models in potential flow codes must be more physically robust to enable accurate evaluation.

Morison-equation based approaches do not consider these 3D effects. As discussed in Chapter 2, a blended approach, such as coupling Morison equation to a ULS method for forward speed (e.g. Greeley & Petersen, 2010), may help to address this issue. The possibility also exists to alter the coefficients at each time-step, based on some pre-determined specification as a function of forward speed, the location along the bilge keel, and the angle of attack to the local flow. However, blended approaches will likely still have difficulties with re-wetting the sectional bilge keel geometries for large amplitude roll motions and re-starting the vorticity calculation after bilge keel re-entry has occurred. This is particularly likely at low speed conditions, where the trade-off between the ULS model and the Morison-equation based model occurs, and where vorticity is not convected downstream as quickly. Under these low speed conditions, which are most typical for ship heavy weather operations, the determination of the bilge keel force in a potential flow simulation will be difficult using existing models.

Although the URANS simulations enabled the identification of physical phenomena which occur during large amplitude roll motion, additional insight is required in order to be able to understand the effects of the physical phenomena on hydrodynamic components, but also to verify that the URANS results are adequately modelling these effects. In the next Chapter, an experiment is performed to measure the variations of the hydrodynamic components during large amplitude roll motion.

11 This was the subject of some studies by the author, and is detailed more in a U.S. Patent Application for "Advanced Bilge Keel Designs," USN Case #100,414 (2011)

Chapter 4 Observations and Analysis of Large Amplitude Ship Roll Motion Using Experimental Methods[12]

4.1 Overview

For large amplitude ship roll motion, in addition to the stiffness, hydrodynamic effects are assumed to also have a significant impact on the response behavior of the ship. However, the behavior of the hydrodynamic components is not well understood for these large amplitude conditions. As observed from the numerical results discussed in the previous chapter, the physical mechanisms and the effects of hull form geometry, including the bilge keels and deck edge, are different for these large roll motions, and therefore, must be considered in models to describe and predict roll motions in more severe wave environments.

This chapter describes an experiment which was performed to characterize the various physical phenomena and associated processes for large amplitude ship roll motion. Results from the experiment included measurements, observation, and identification of the discrete processes that result for several physical phenomena relevant to large amplitude roll motion, including bilge keel interaction with the free-surface (emergence and re-entry), vortex shedding, and their effect on the forces and moments of both the hull and bilge keels.

Although viscous effects are important for the hydrodynamic components of roll, Froude scaling was used instead of Reynolds scaling. This determination was made based on the consideration of identifying the dominant physical phenomena which occur during large amplitude motions. Specific phenomena, such as the strength of vortex shedding, are not accurately captured with this assumption, but this was a secondary consideration to the primary objective of identifying and analyzing the physical phenomena.

4.2 Experimental Objective

The experimental measurements and observations were intended to quantify and provide insight regarding the relevant physics for large amplitude ship roll motions. The experimental results enabled characterization of the specific phenomena which occur during large amplitude ship roll motion. From these observations, additional understanding of the processes will help to determine which processes should be modeled to enable more accurate predictions of ship roll motion. It was expected that these phenomena could result in distinctly different behavior compared to the small amplitude roll motion regime. Aspects of the experimental design, test conditions, results, and characterization of the physical phenomena that were observed during the experiments are discussed in this chapter.

4.3 Experimental Design

Forced oscillation experimental techniques provide a practical means to measure and characterize the forces and moments on both the hull and appendages during ship motion.

[12] Portions of this chapter have been published previously in Bassler, et al. (2010)

Additionally, the data from these experiments can be used for the development and validation of numerical codes used for the prediction of ship motions (Beck and Reed, 2001).

However, earlier experiments have not systematically examined in detail, or with instrumented appendages, the distinct physical phenomena which occur for large amplitude roll motions. The objective of this experiment was to make observations and quantitatively characterize changes in the system conditions and modes of energy dissipation that affect the behavior of a ship hull section experiencing large amplitude roll motion. These included forces and moments on the hull and bilge keels, the near-field hull and bilge keel interactions with the free-surface, and energy dissipation in the near-field, primarily through vortex generation and ship generated waves.

The experiment was designed as a single degree-of-freedom (1DoF) experiment, with a sectional (2D) model, in order to enable observation and measurement of the isolated physical processes which occur during large amplitude roll motion. Additionally, the 2D nature of the experiment also was intended to provide consideration for the development and modification of sectionally-based, or strip theory-type, ship motions models.

4.3.1 Model Design and Construction

In this section, the selection and design of the model used for the experiment is discussed. Details of the model properties and construction, instrumentation, and ballasting are also presented.

A two-dimensional model was designed and constructed for the experiment to represent the midship section of the ONR Topside Series hull forms (Figure 4-1). As discussed in the previous chapter, these hull forms represent a notional modern naval combatant ship design, featuring a common below waterline geometry, with varied topside shapes, including flared, tumblehome, and wall-sided configurations. For this investigation, the flared and tumblehome configurations were considered, to examine the difference between a more traditional (flared) naval combatant and a more modern (tumblehome) naval hull form.

The use of a section model enabled isolated characterization of significant events during the large amplitude roll motion, without additional consideration of the effects of forward speed and the 3D effects of the hull. This also provided validation data for sectional-based ship motion prediction methods.

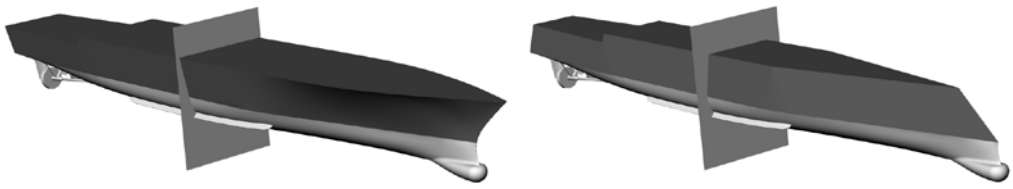

Figure 4-1. ONR Topside Series, flared (left) and tumblehome (right) configurations, with midship sections identified

The 2D model featured both flared (DTMB Model #5699) and tumblehome (DTMB Model #5699-1) configurations (Figure 4-2). The 2D model is an extruded geosym of the midship section of DTMB Model #5613 (and #5613-1), a 32nd-scale model used for previous experiments (Bishop, et al., 2005; Bassler, et al., 2007). Details of the model properties, construction, and ballasting are given in Appendix C (Sections C.1.1 and C.1.2).

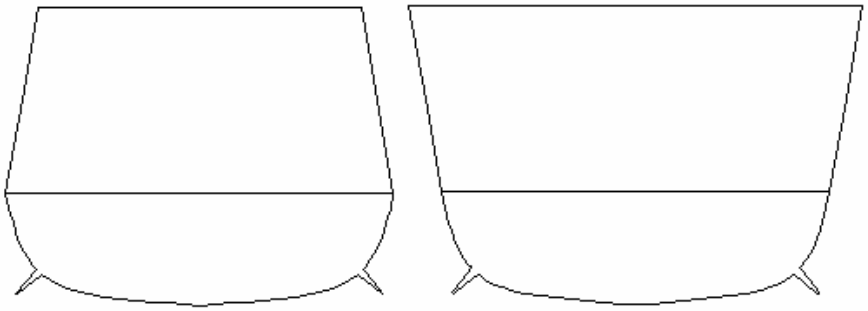

Figure 4-2. Midship section of the ONR Topside Series, tumblehome configuration (left) and flared configuration (right) with 1.25m bilge keels

4.3.2 Instrumentation and Uncertainty

In order to characterize the various physical phenomena at large roll amplitudes, various measurements were required. These included force and moments on the hull and bilge keels, motions of the hull, and near-field wave and vortex generation measurements. Additional details regarding the specific instrumentation used for the experiment, and the associated measurement uncertainties, are given in Appendix. C (Section C.1.3).

4.3.3 3DoF Forced Motion Mechanism[13]

This section describes the design, construction, and utilization of the 3DoF mechanism. The mechanism was built to enable large amplitude roll motions to be achieved, and the experiment to be performed. A three degree-of-freedom (3DoF) motion mechanism was designed and constructed at NSWCCD to enable forced oscillation of the model for large roll angles up to 50 degrees. The mechanism can actuate the model in sway, heave, and roll/pitch, either separately or in combination, to achieve large amplitude motions (Grant, et al., 2010). Aspects of the theory, design, construction, and installation are discussed.

A series of 1DoF force roll oscillation experiments (Fullerton, et al., 2006; 2008; Bassler, et al., 2007) were performed with David Taylor Model Basin (DTMB) Model #5613-1. For these experiments different 1DoF motion mechanisms were used that utilized a roll actuator fixed at the model's roll axis. An example is shown in Figure 4-3. Other experiments have been performed which use similar approaches. These mechanisms are limited in their ability to

[13] An invention disclosure for this design was submitted and a patent application is pending (Navy Case #100,690). Portions of the discussion related to the design, construction, and use of the mechanism have been published previously in Grant, et al. (2010).

produce large amplitude roll motion, due to interference between the supporting strut attached to the model and the model side walls and deck edges. For DTMB Model #5613-1 in particular, achieving roll angles above 30 degrees is difficult, due to the constraints from the topside geometry.

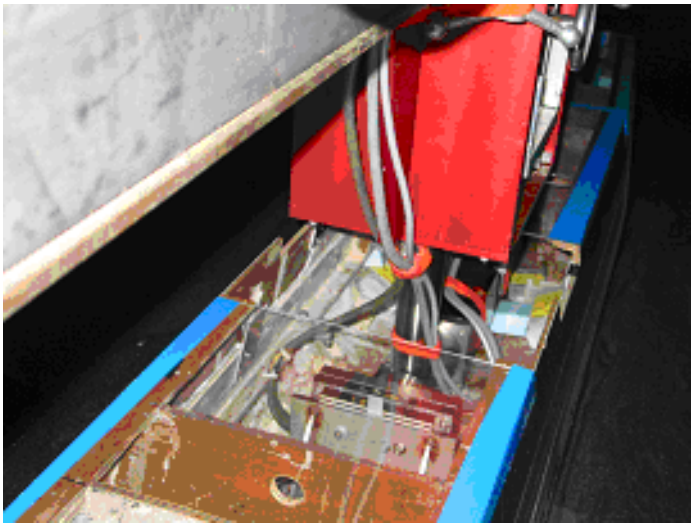

Figure 4-3. 1DoF roll mechanism, as used for the investigation of Bassler, et al. (2007), with constraints to 30 degrees of roll, due to model side wall deck edge interference with the strut from the motion mechanism.

To provide more capability and the ability produce realistic combinations of ship motions, multiple degree-of-freedom (MDoF) forced motion mechanisms, based on the concept of an inverted Stewart platform have been developed (e.g. de Jong and Keuning, 2006). While this type of mechanism can produce forced oscillations in all six degrees-of-freedom, roll motions are still constrained to relatively small amplitudes, due to the maximum stroke of the hydraulic arm components and the mounts on the model (Figure 4-4). The model is rolled about a roll axis using traditional fixed strut mechanisms which are attached internally to the model. This limited testing to angles below where the deck edge contacted the strut. In order to achieve the desired roll amplitudes, and enable observations for large amplitude roll motions, a new mechanism was required. A 3D computer model of the assembly can be seen in Figure 4-5. Further details regarding the theory and design of the 3DoF motion mechanism used for the experiment are provided in Appendix C (Section C.1.4).

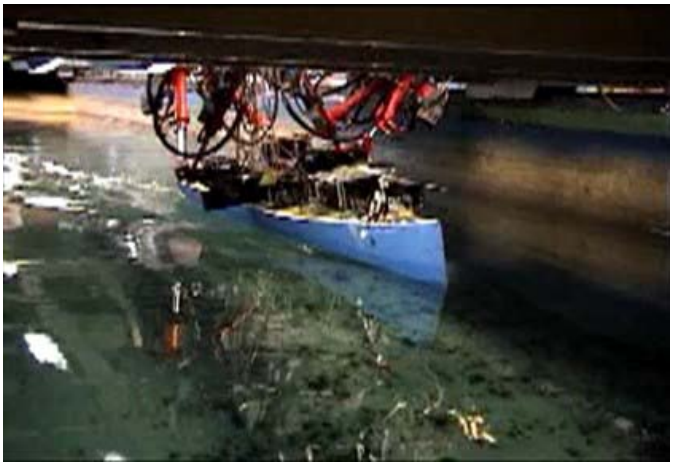

Figure 4-4. Ship model experiencing forced roll motion with a 6DoF motion mechanism (de Jong and Keuning, 2006)

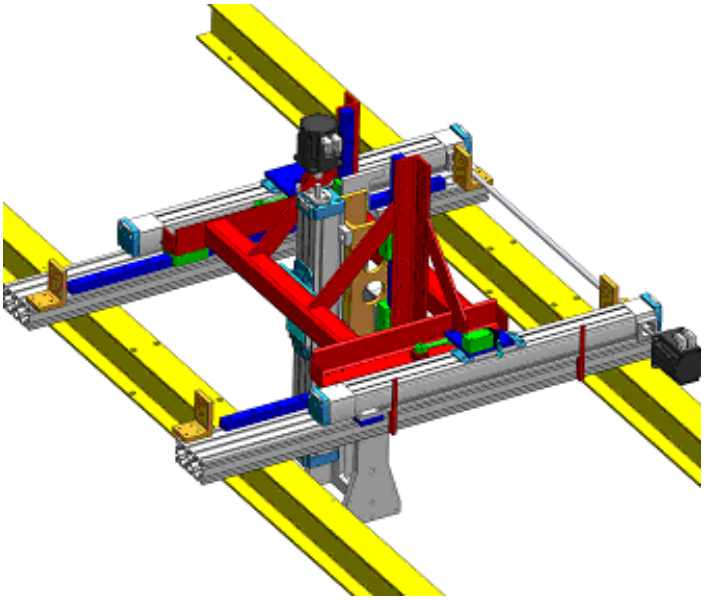

Figure 4-5. 3DoF motion mechanism CAD assembly

4.4 Experimental Set-Up and Test Procedures

This section describes the basin, model, and mechanism configuration, particle image velocimetry (PIV) set-up, and data collection used for the experiment.

4.4.1 NSWCCD 140 ft Basin and Model Configuration

The experiment was conducted in the 140 ft basin at NSWCCD (Figure 4-5). The basin is 42.67 m in length and 3.05 m wide. For the experiments, the water level in the basin was fixed at at a depth of 1.37m. The model was configured in the middle of the basin and oriented transversely across the basin to enable 2D measurements (Figure 4-6).

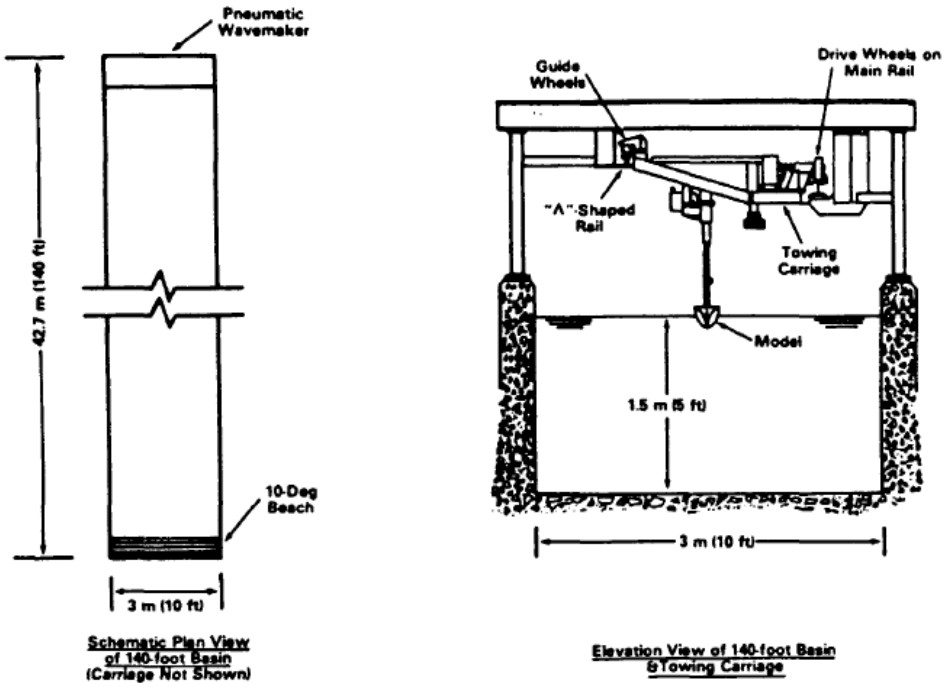

Figure 4-6. Dimensions of the 140 ft Basin at NSWCCD

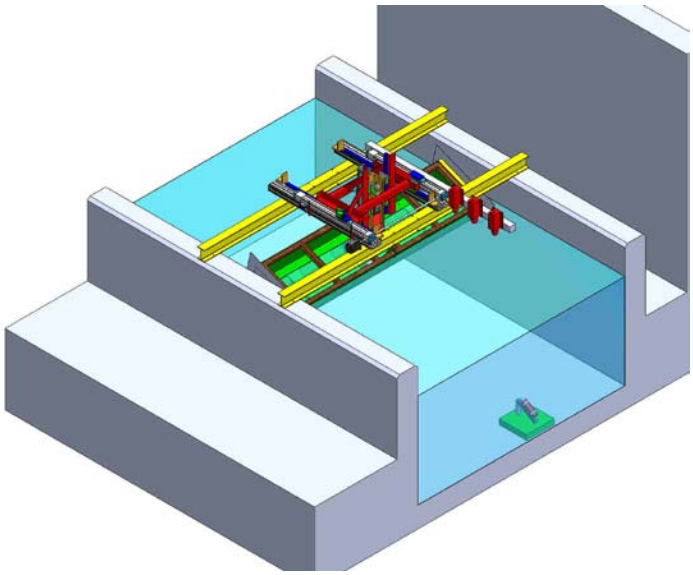

Figure 4-7. Illustration of the experimental set-up in the NSWCCD 140 ft basin, with PIV laser on the east side of the basin (in green), facing west

The model was rolled about the centerline, at the center of gravity, which, for this ballast configuration, matched the calm water draft. Laser probes were submerged and oriented to form a plane near amidships (Figure 4-7).

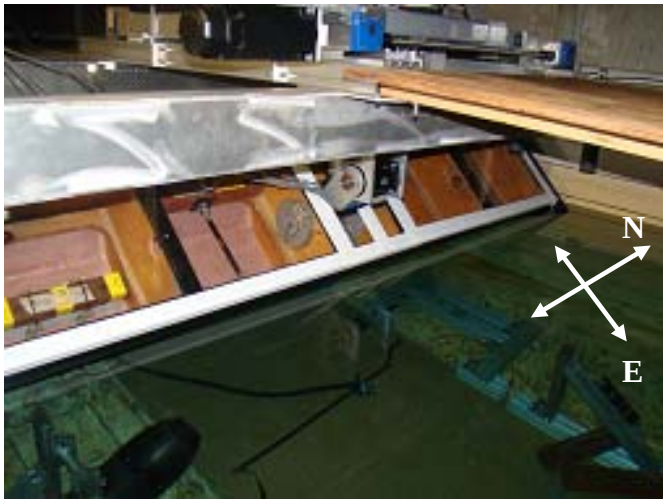

Figure 4-8. Model rolled, while attached to the 3DoF mechanism with submerged PIV laser probes (bottom right, facing West) and camera (bottom left, facing North) shown

4.4.2 PIV Set-Up

A 60.96 x 60.96 cm PIV measurement plane, oriented east-west and vertical, was located 2.17 m north of the south wall of the basin and aligned with the ultrasonic wave sensors, allowing a vertical two dimensional cut of the hull. The bottom of the measurement plane was 0.854 m above the basin floor. The water level during testing was held constant at 1.37 m. This allowed for approximately 7.62 cm of the measurement plane to be above the free surface to capture the effects of the bilge keel as it transited the free surface at the larger roll angles. In addition, the model centerline was offset from the centerline of the measurement plane by 15.24 cm to maximize the region of the flow-field that could be captured in the 60.96 x 60.96 cm field-of-view.

Two waterproofed submerged laser probes were used to illuminate the measurement plane. The lasers were located outside the basin and the laser beams were channeled into fiber optic cables that were connected to the submerged laser probes. Each laser probe is comprised of a 20.32 cm long cylindrical housing which contains a series of optical lens designed to spread the beam into a light sheet. A probe was placed on each side of the model and mounted to a structure made of 80/20 aluminum extrusions that was weighted to the basin floor. Each laser probe was positioned 127 cm from the measurement plane and at a 45 degree look up angle to ensure the entire measurement plane was illuminated (Figure 4-8).

A MegaPlus ES 4.0/E camera was placed in waterproof housing and submerged in the basin. The camera was mounted to an 80/20 aluminum structure that was weighted to the basin floor and positioned so its lens was 152.4 cm south of the center of the measurement plane, and oriented at a look-up angle of 30 degrees (Figure 4-8).

Figure 4-9. PIV set-up in the NSWCCD 140 ft basin, looking East, with camera (right) and calibration target with laser probes (left) shown

The PIV measurement plane was seeded (Figure 4-9) with small silver coated particles, nominally neutrally buoyant and 50 μm in diameter, using a custom designed seeding mechanism. The mechanism consisted of two 1.5 m long, 50.8 mm diameter PVC pipes closed at one end and assembled to create an "L" shape (Figure 4-10), with the other end connected by a hose to a pump in a particle mixing tank. A series of perforations were drilled vertically in the lower (horizontal) pipe. The flow-field was seeded as necessary, typically every 4-5 runs. Each time the measurement plane was seeded the particles were mixed with water in the mixing tank and pumped through the hose to the seeding mechanism. The mix was a compromise between low density and high density and measures were taken to ensure uniform particle dispersion and to minimize the flow rate and subsequently the induced velocities into the measurement region of the flow. The mechanism was placed in the water, in line with the measurement plane, and manually traversed up and down, dispersing particles throughout the entire measurement plane. After the desired particle concentration was achieved, the seeding mechanism was removed from the basin.

Figure 4-10. Model shown in roll motion (without bilge keels), with PIV particles on the free surface after seeding

Figure 4-11. Custom designed seeding mechanism shown being used to seed particles in the PIV measurement plane near the hull

4.4.3 Data Collection and Procedures

In order to collect data, a series of interfaces with the instrumentation and the LabView data acquisition system were used (Figure 4-11). These included interfaces for each of the channels from the Kistler dynamometer, aft and forward strain gages for the port and starboard bilge keels, displacement and rate gyroscopes, and ultrasonic wave probes. In order to overcome potential issues related to transmission and interference losses, amplifiers were used for both the dynamometer measurements and the strain gage measurements.

Figure 4-12. Data collection interfaces, not including PIV, ultrasonic wave probes (top), gyroscopes (top middle), bilge keels (lower middle), and Kistler dynamometer (lower)

Prior to each testing period, the water level and temperature in the basin was checked and recorded and the model was re-set to the "zero" position. This consisted of checking the heel of the model using port and starboard hook-gages and an inclinometer (Figure 4-12). The model was also centered relative to the sway rails of the motion mechanism, and relative to heave, to ensure only buoyancy forces were exerted on the model (Figure 4-13).

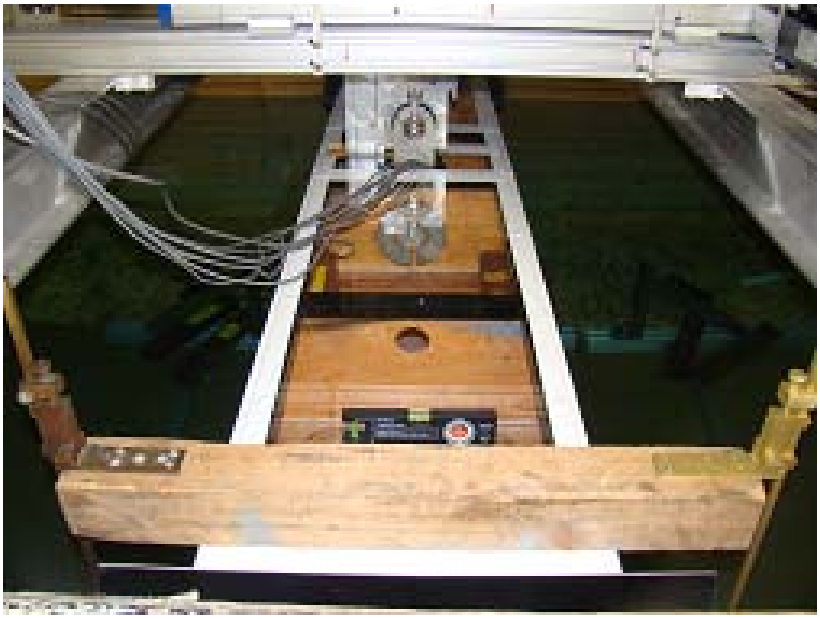

Figure 4-13. Hook-gages and inclinometer used to check the heel angle of the model

Figure 4-14. Zero position used to center the model in the experimental set-up

4.4.4 Test Conditions

The experiment consisted of a series of free roll decay and forced oscillation conditions. The model configuration for the roll decay experiments is discussed in Appendix C (session C.2.1). Specifics of the tested conditions are discussed in this section.

4.4.4.1 Topside Configuration

The experiment was performed with two topside configurations, flared and tumblehome. Data was collected and used to examine the effects of topside geometry on the physical phenomena which occurred during large amplitude roll motion.

4.4.5 Roll Decays

A series of calm water 1DoF roll decays were conducted, with the tumblehome topside geometry configuration, with and without bilge keels. The model was released at several initial heel angles, given in Table 4-1.

Table 4-1. Roll Decay Test Conditions

Heel Angle, θ (deg)	5, 10, 15, 20, 25
Topside Configuration	Tumblehome
Bilge keel configuration	with and without

4.4.5.1 Forced Oscillation Conditions

A series of sinusoidal 1DoF forced roll oscillation experiments were conducted with combinations of roll amplitudes and frequencies (Table 4-2). The frequency conditions are given at model scale. The 2.17 and 3.81 rad/s correspond to the same experimental conditions tested with the 32nd-scale ONR Tumblehome (DTMB Model #5613-1), with the same bilge keel size (Bassler, et al., 2007). The tested frequencies ranged from 9.33 to 16.4 seconds full-scale (for a 32nd-scale midship section), corresponding to the common range of roll periods for many modern vessels, particularly naval surface combatant type hull forms.

For this particular hull geometry, bilge keel emergence occurred just before 30 degree roll, and deck submergence occurred just before 40 degrees for the flared topside configuration. Deck submergence for the tumblehome topside configuration occurred near 50 degrees, which was outside of the test conditions for this experiment, due to the limitations of the experimental set-up and 3DoF motion mechanism. However, for the tumblehome topside, measurements for the 45 degree roll amplitude condition were obtained.

Table 4-2. Forced Oscillation Test Conditions

Fn	0.0
Roll amplitude, ϕ (deg)	5, 15, 25, 30, 35, 40, 45 (TH only)
Roll frequency, ω (rad/s)	2.17, 2.5, 2.85, 3.81
Bilge keel configuration	with and without

4.5 Summary of the Experimental Results

Experimental results are presented here for forced roll oscillation conditions. Results for the roll decay conditions are given in Appendix C (Section C.3.1). Measurements for the roll motion, roll moment on the hull, normal force of the bilge keel, and the near ship flow-field are presented. Issues related to some of the high-frequency noise observed in the measurements during the experiment, as well as the repeatability of the state-state conditions, are discussed in Appendix C (Section C.3.2). Sample plots from the measurements are presented. Additional measurement data, including Hydrostatics and results for additional frequencies are given in Appendix D.

4.5.1 Forced Roll Oscillation Measurements

Data was collected for the flow-field, the roll, roll rate, and roll moment on the hull, the unit normal force on the bilge keel, and the near-field ship generated wave elevation. Sample plots are shown for selected measurements, composite views, and the bilge keel force variation with amplitude, frequency, and topside configuration.

4.5.1.1 Measurement Noise and Repeatability

Measurement noise and filtering are discussed in Appendix C. The repeatability of the experimental results was examined using phase plots of the steady-state forced roll oscillation conditions. As expected, the experiment had a high level of repeatability for the steady-state forced oscillation experiments. Additional details are given in Appendix C.

4.5.1.2 Sample Synchronized Measurements

The measurements were time-synchronized to enable visual observations to be correlated with specific physical phenomena observed in the various data channels. These included images from the camera; post-processed PIV images with bilge keel force vector added; roll and roll rate measurements; total roll moment and bilge keel portion of the roll moment; the unit normal bilge keel force; and wave elevation measurements. Sample composite images are shown for the tumblehome topside configuration, where the bilge keel is near the free-surface (Figure 4-14) and where bilge keel emergence has occurred (Figure 4-15).

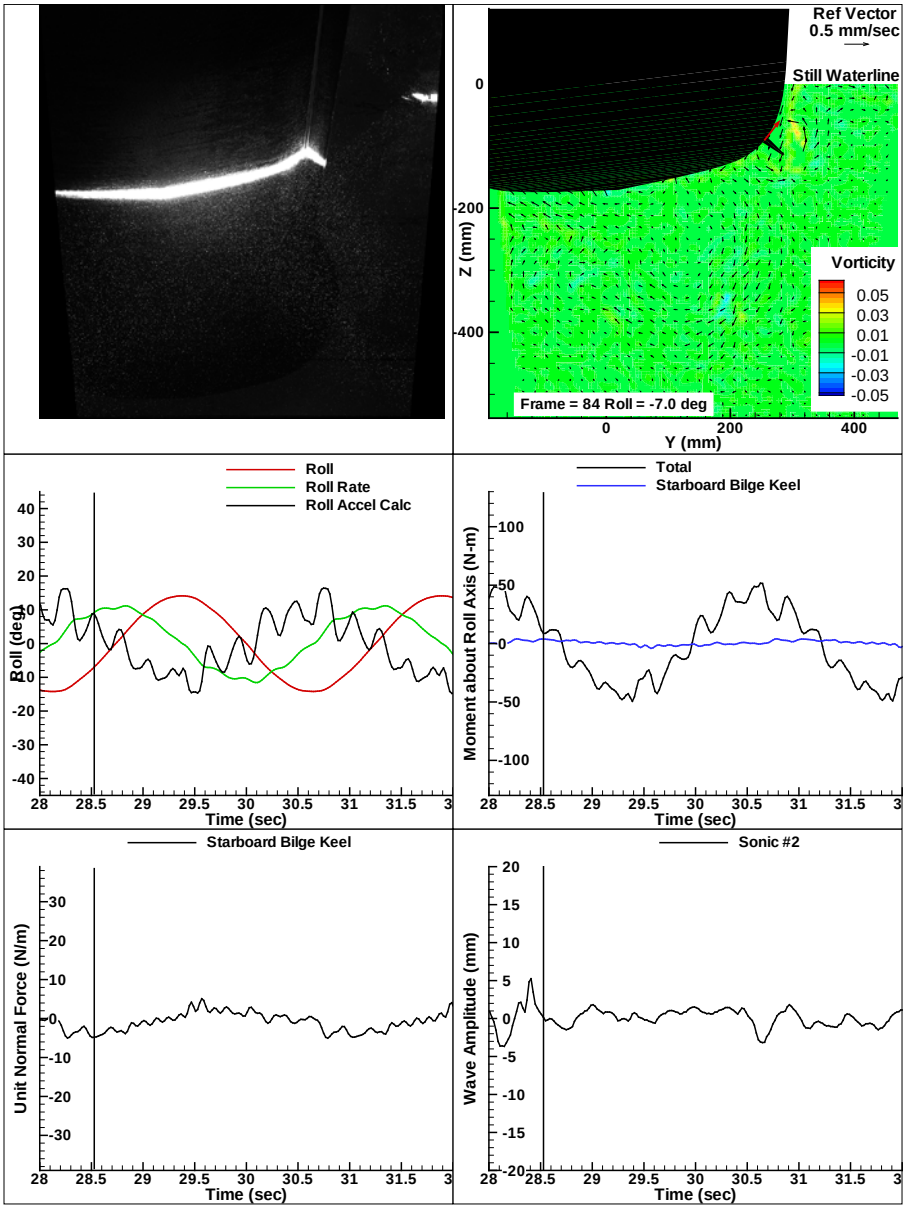

Figure 4-15. Unfiltered measurements for ϕ=15 deg, ω= 2.5 rad/s for DTMB Model #5699-1, after peak of the roll cycle. Camera (top left), PIV with bilge keel force vector (top right), roll, roll rate and roll acceleration (middle left), total roll moment and bilge keel portion of the roll moment (middle right), bilge keel force (bottom left), and wave elevation (bottom right) measurements are shown for the instant in time noted by the vertical line

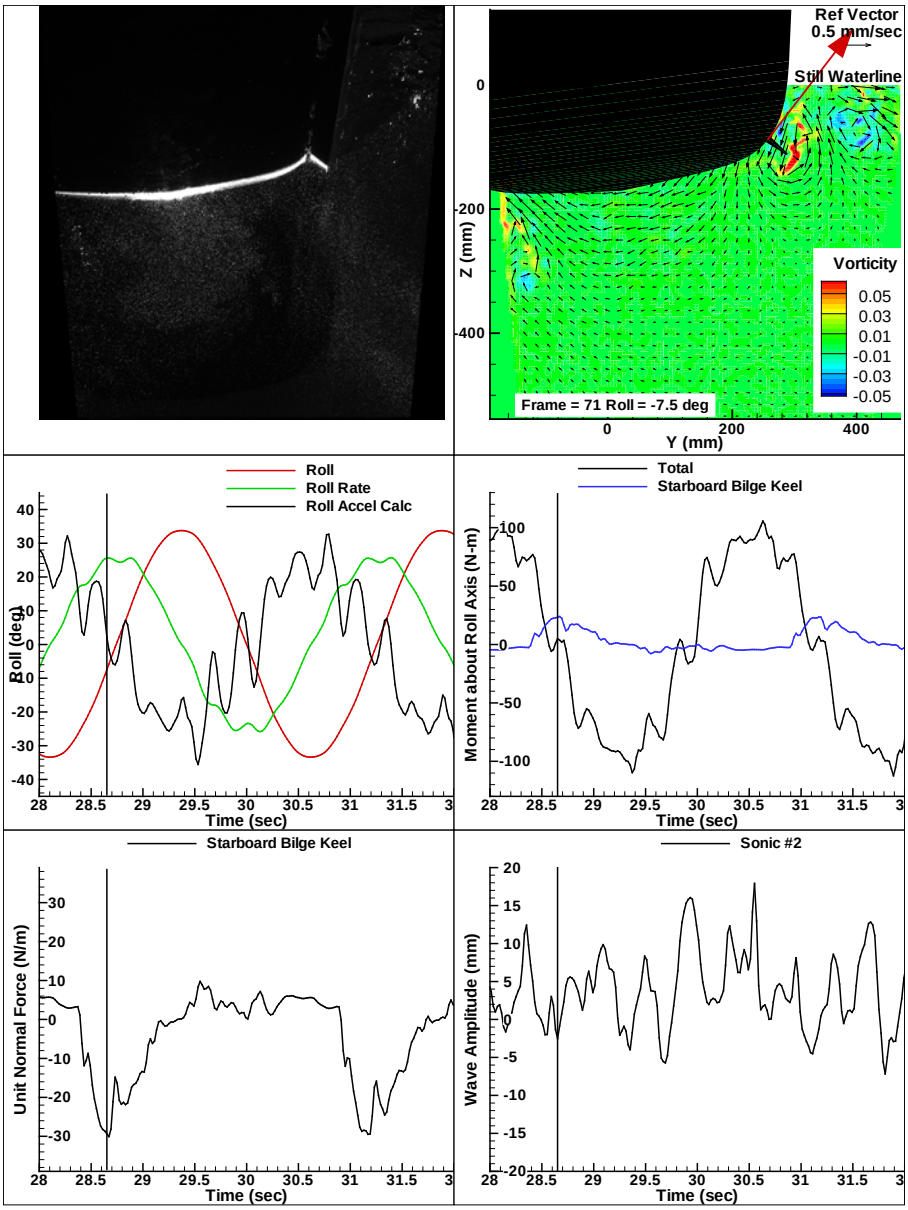

Figure 4-16. Unfiltered measurements for ϕ=35 deg, ω= 2.5 rad/s for DTMB Model #5699-1 after bilge keel re-entry. Camera (top left), PIV with bilge keel force vector (top right), roll, roll rate and roll acceleration (middle left), total roll moment and bilge keel portion of the roll moment (middle right), bilge keel force (bottom left), and wave elevation (bottom right) measurements are shown for the instant in time noted by the vertical line

4.5.1.3 Bilge Keel Force Measurements

With increased roll amplitude, additional physical effects can be observed in the time-history of the unit normal bilge keel force. These correspond to the bilge keel interactions with shed vortices and the free-surface, for emergence and re-entry (Figure 4-16). The influence of the topside and effect of frequency can also be observed, on the hydrodynamic components, and are discussed further in the next section. Results for three roll frequencies are presented in Appendix D (Section D.3).

Results of two period cycles of measurements of roll angle and the unit normal bilge keel force on the starboard side are presented. These include results for the flared (Figure 4-17) and tumblehome (Figure 4-18) topside configurations, for 2.17, 2.5, and 2.85 rad/s for 15-40 degrees, with the addition of 45 degrees for the tumblehome topside configuration. For the midship section of the ONR Topside Series, bilge keel emergence is observed at nearly 30 deg. For the flared topside configuration, deck submergence occurs at nearly 40 deg. For the tumblehome topside configuration deck submergence occurs at nearly 50 deg.

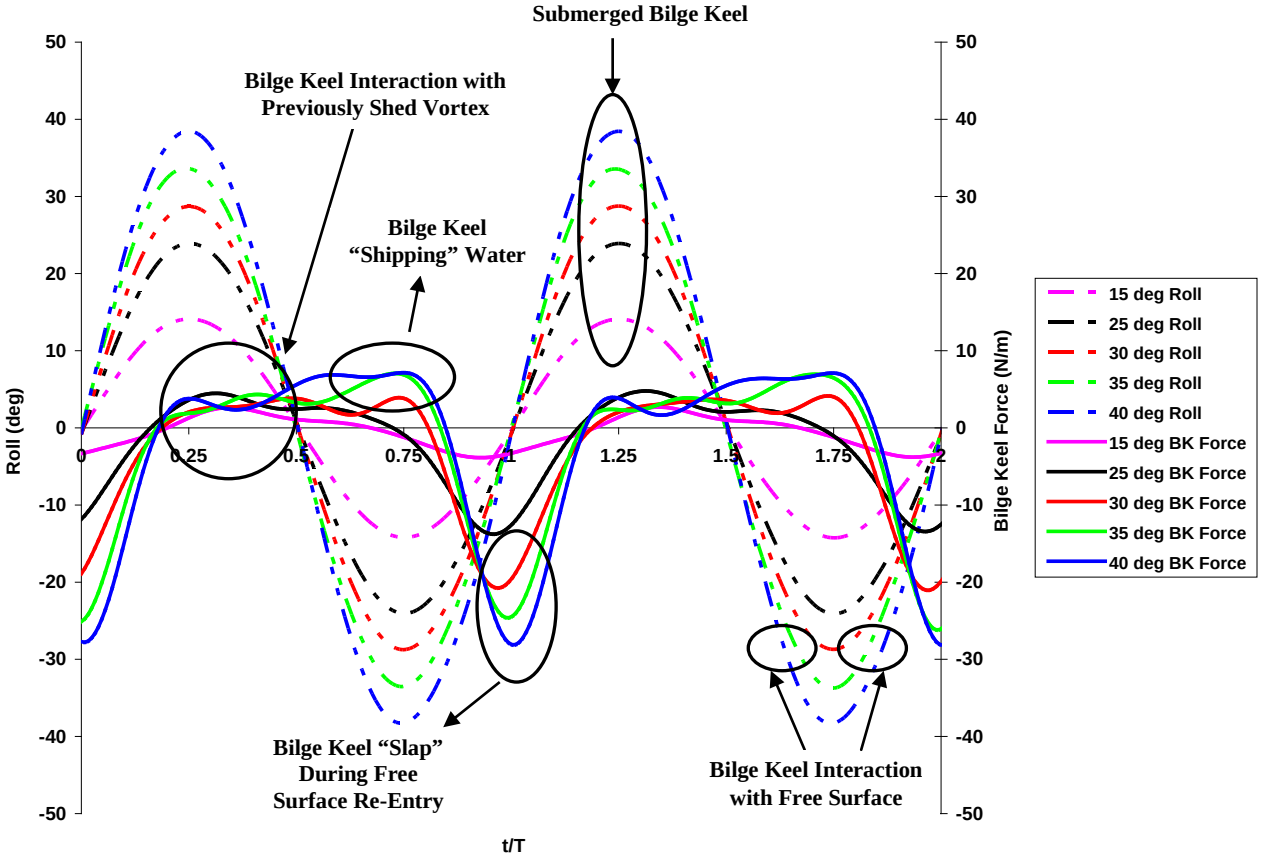

Figure 4-17. Filtered roll motion measurements and bilge keel force measurements for the DTMB Model #5699, at various roll amplitudes, ϕ=15 (purple), 25 (black), 30 (red), 35 (green) and 40 (blue) deg, ω= 2.5 rad/s, with distinct physical phenomena identified at various stages in the roll cycle

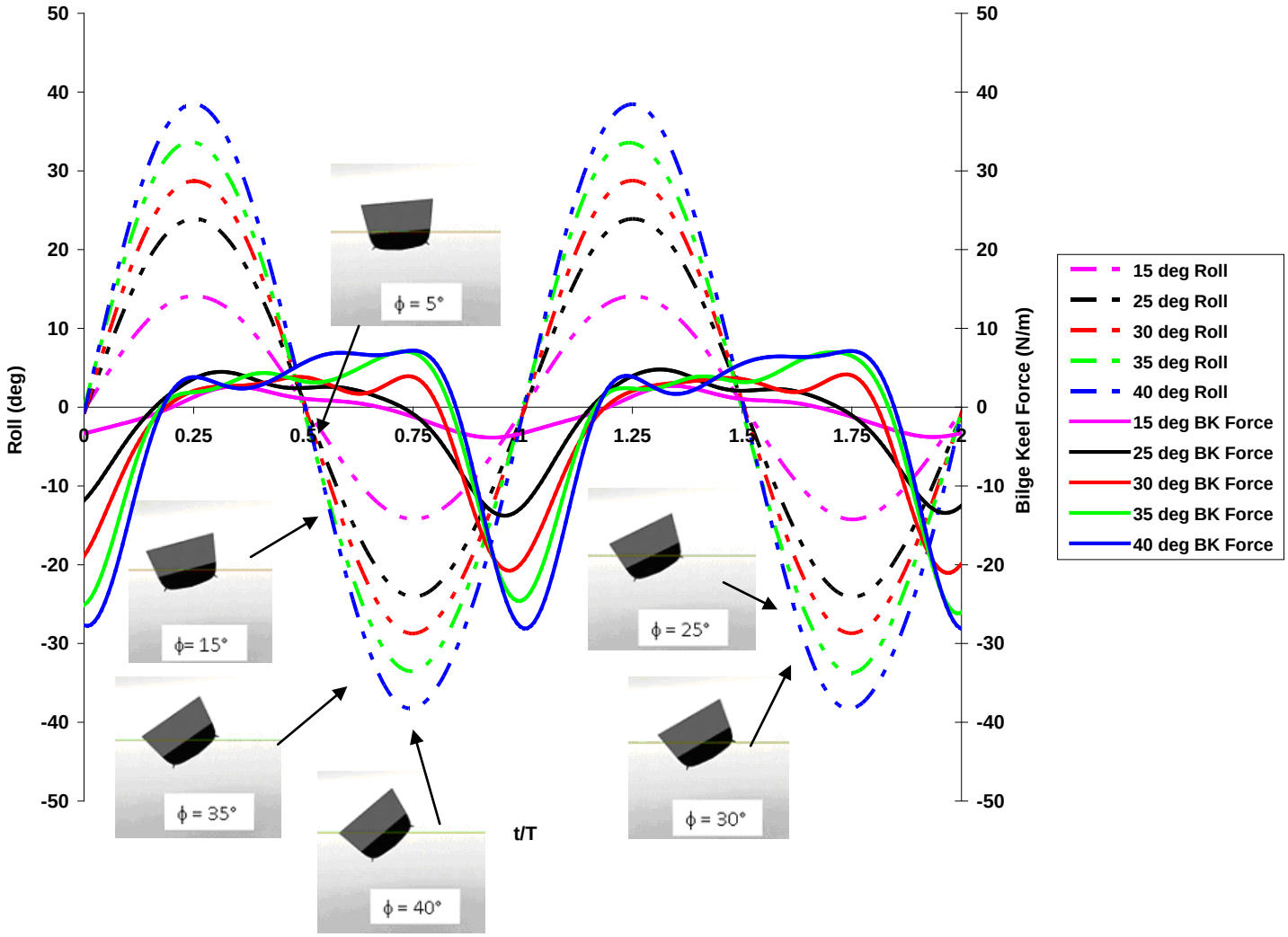

Figure 4-18. Filtered roll motion measurements and starboard bilge keel force measurements for the DTMB Model #5699, at various roll amplitudes, ϕ=15 (purple), 25 (black), 30 (red), 35 (green) and 40 (blue) deg, ω= 2.5 rad/s, with corresponding positions of the starboard bilge keel identified at various stages in the roll cycle

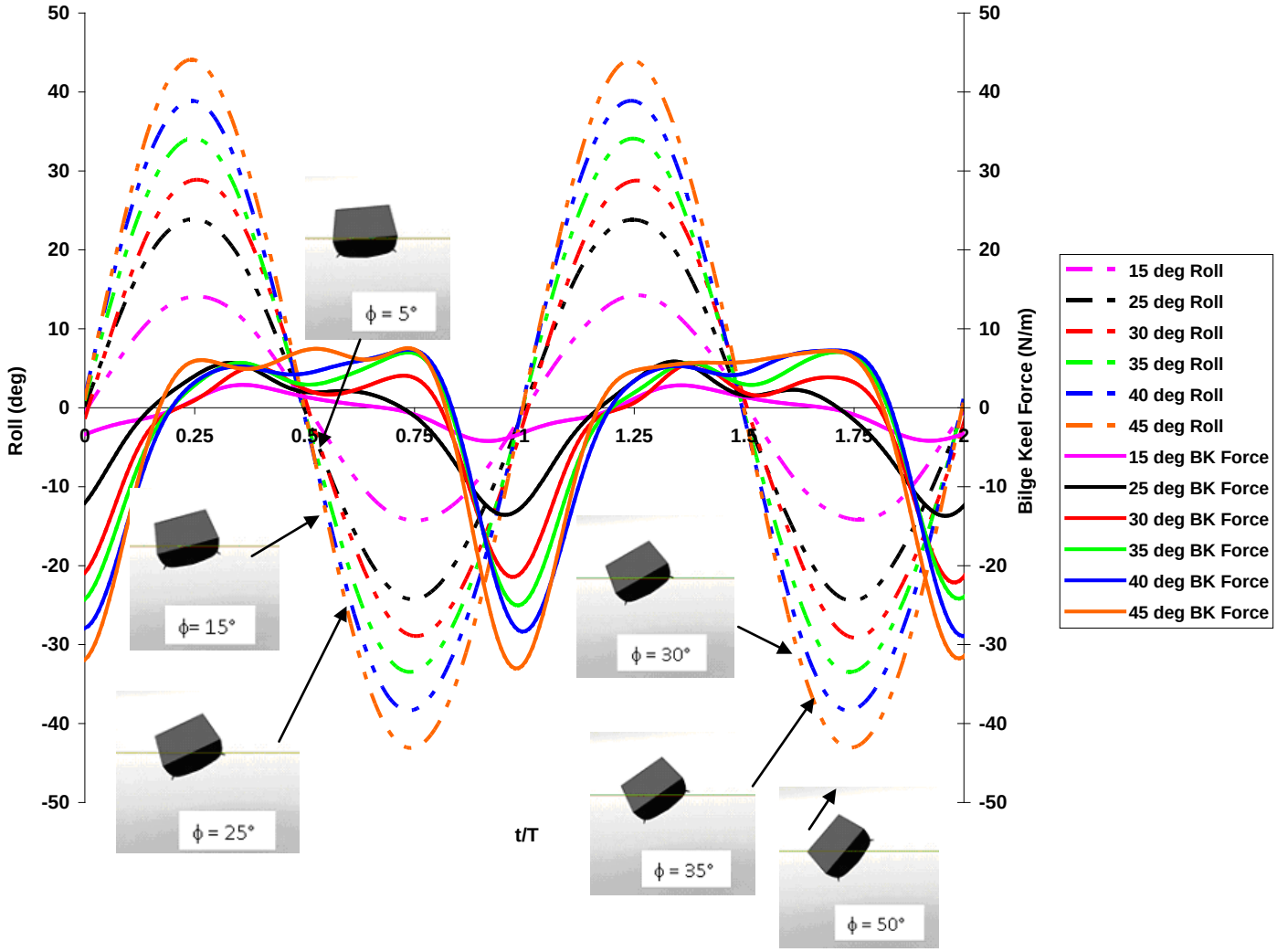

Figure 4-19. Filtered roll motion measurements and bilge keel force measurements for the DTMB Model #5699-1, at various roll amplitudes, ϕ=15 (purple), 25 (black), 30 (red), 35 (green), 40 (blue), and 45 (orange) deg, ω= 2.5 rad/s, with distinct physical phenomena identified at various stages in the roll cycle

4.6 Harmonic Analysis of the Data

Harmonic analysis of the experimental results is presented in this section. The objective of this analysis was to provide additional insight into the nonlinearities associated with the hydrodynamic components. A complete set of results of the harmonic analysis for the 2.5 rad/s roll frequency condition are shown, and additional results from the other roll frequency conditions are presented in Appendix D. However, the results are discussed in the appropriate subsections below. Analysis includes the decomposition of the measurements of roll motion, unit hydrodynamic roll moment, and unit normal bilge keel force into in-phase (added inertia) and out-of-phase (damping) components.

4.6.1 Decomposition into Added Inertia and Damping

In order to carry out harmonic analysis of the measurements, a Fourier series decomposition of a periodic signal was used. Here, the measurement, F(x), was decomposed into added inertia and damping harmonics, as given in the formulation below.

$$F(x) = \frac{a_0}{2} + \sum_{n=1}^{i}\left(a_n \cos(\omega n x) + b_n \sin(\omega n x)\right) = \frac{a_0}{2} + \sum_{n=1}^{i}\left(A_n \cos(\omega n x) + \varepsilon_n\right) \quad (4.1)$$

where a_0, a_n, and b_n, are the Fourier coefficients, given by

$$\begin{aligned} a_0 &= \int_0^{2\pi} F(x)dx \\ a_n &= \int_0^{2\pi} F(x)\cos(\omega n x)dx \\ b_n &= \int_0^{2\pi} F(x)\sin(\omega n x)dx \end{aligned} \quad (4.2)$$

and A_n and ε_n are magnitude and the phase (in rad), respectively.

$$\begin{aligned} A_n &= \sqrt{a_n{}^2 + b_n{}^2} \\ \varepsilon_n &= \tan^{-1}\left(\frac{-b_n}{a_n}\right) \end{aligned} \quad (4.3)$$

For the decomposition of the experimental measurements, only 10 harmonics were used, in order to avoid issues associated with the Nyquist frequency and the instrumentation sampling rates. A sample result for the ONRFL, 15 deg roll amplitude, 2.5 rad/s roll frequency condition is shown in Appendix D (section D.6). From the decomposition of the first 10 harmonics for added inertia and damping for all conditions and configurations, several observations can be made, as described in the following section. For roll motion, only the first harmonic dominates and no difference is observed due to the topside, as expected, because these were forced roll oscillation conditions.

4.6.2 Harmonic Analysis of the Resulting Added Inertia and Damping

Results for the added inertia and damping are presented in this section. These results were decomposed from the measured roll motion, unit hydrodynamic roll moment, and unit hydrodynamic roll moment due to the bilge keels, for the 2.5 rad/s roll frequency condition, for both the flared and tumblehome topside configurations. Additional results for the 2.17 rad/s and 2.85 rad/s roll frequency conditions are given in Appendix D (section D.7). Each subsection discusses the observed dependence of the hydrodynamic components due to roll amplitude and topside configuration, based on the harmonic analysis.

For the total hydrodynamic roll moment, the added inertia of the fundamental harmonic was nearly constant with amplitude for the tumblehome topside, but decreased with amplitude for the flared topside. However, the damping slightly decreased with amplitude for both the flared and tumblehome configurations.

For the unit bilge keel force, the added inertia increases up to 25 deg and then decreases for 30 deg and larger, for both the tumblehome and flared topsides, suggesting that this is due to the emergence of the bilge keel. Similarly, the damping increases up to 30 deg and then remains nearly constant for amplitudes greater than 30 deg, for both the flared and tumblehome configurations. Both the added inertia and damping for the bilge keel are reduced at larger roll amplitudes, due to the emergence of the bilge keel.

4.6.2.1 Hydrodynamic Components as a Function of Roll

The sum of the first 10 harmonics of added inertia, a_n, and damping, b_n, for roll motion of the ONRFL and ONRTH, with and without bilge keels are shown in Figure 4-20. As observed, the magnitude of the harmonic components of the forced oscillation roll motion, the sums of both the added inertia and damping coefficients increase roughly linearly with amplitude. Because the experiment consisted of 1DoF forced oscillation conditions, the trend is linear. Also, the difference between the roll motion for the conditions with and without bilge keel, for both the flared and tumblehome configurations, is insignificant, due to the small variations from the forced oscillation using a mechanical mechanism.

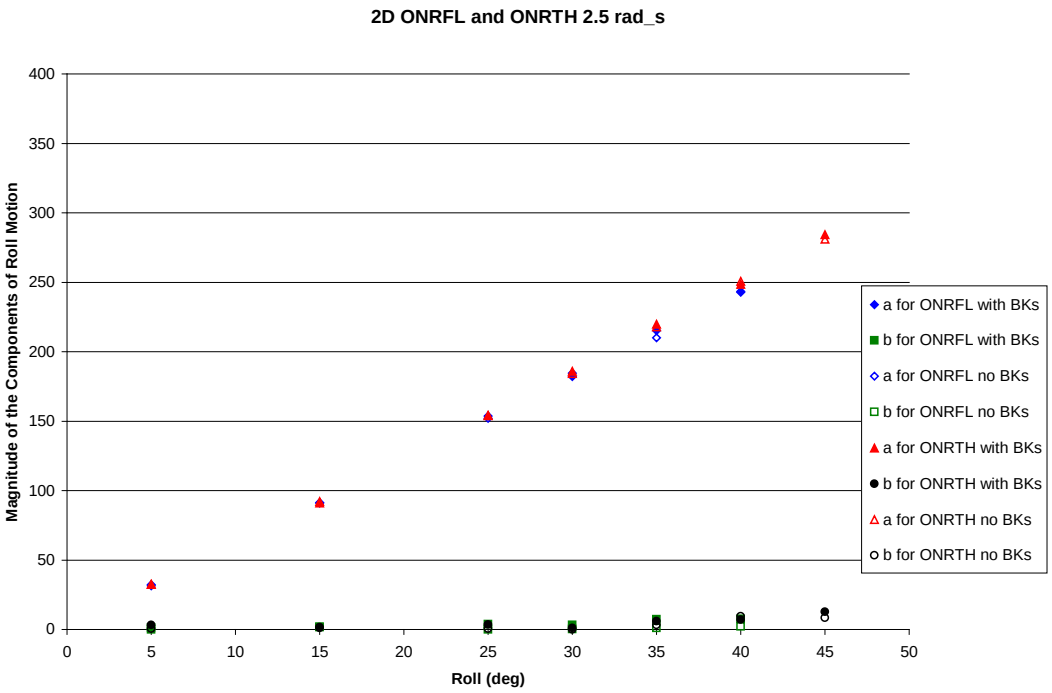

Figure 4-20. Comparison of the magnitude of the sum of the first 10 harmonics of added inertia and damping for roll motion, for DTMB Models #5699 and #5699-1, with and without bilge keels, ω=2.5 rad/s

4.6.2.2 Hydrodynamic Components as a Function of Hydrodynamic Roll Moment

The sum of the first 10 harmonics of added inertia and damping, for the unit hydrodynamic roll moment of the ONRFL and ONRTH, with and without bilge keels are shown in Figure 4-21. The magnitude of the harmonic components of the unit hydrodynamic roll moment, both the added inertia and damping, vary with roll amplitude. The added inertia is a much greater portion of the total hydrodynamic roll moment than the damping, with the added inertia contributing approximately 75% for the smallest roll amplitudes and nearly 90% for the large roll amplitudes (Figure 4-21).

The magnitude of the added inertia for small amplitudes (5 deg) is very similar for both the flared and tumblehome topside configurations. However, at 15 and 25 degrees, where the differences in the above waterline topside configuration have interacted with the free surface, differences were observed. The added inertia for the tumblehome is observed to be reduced compared to the flared topside. As the roll amplitude increased, the added inertia for the flared topside increased, while the added inertia for the tumblehome configuration begins to plateau around 35 degrees. Additionally, the difference between added inertia, for with and without bilge keel configurations, was more significant at larger amplitudes for the flared topside configuration than for the tumblehome topside configuration.

The magnitude of the damping increased for small amplitudes (from 5 to 15 deg) for both the flared and tumblehome topside configurations. However, at 25 degrees and larger roll amplitudes, the damping exhibited nonlinear behavior, plateauing and then even decreasing. At very large amplitudes (35, 40, and 45 deg), the majority of the topside is immerged (although the deck edge does not enter the water until nearly 50 deg for the tumblehome topside configuration). For these large amplitude conditions, the damping with bilge keels is observed to

be greater than the without bilge keel conditions. The same difference in damping with and without bilge keels is not observed for the flared topside configuration. This suggests that the presence of the bilge keels is more important to the overall damping of the tumblehome topside than the flared topside configuration, which is a result of the wave generation of the topside and relative phasing with the energy dissipation of the bilge keels. These differences are further examined in the next section.

The influence and effectiveness of the bilge keels relative to the added inertia and damping for the total unit hydrodynamic roll moment were also examined. The results for damping are shown in Figure 4-22. The results presented in these two figures show the added inertia and damping as measured and decomposed for hull with bilge keels, as well as for the hull without bilge keels and then with the measured hydrodynamic roll moment due to the bilge keels added. For the flared topside, the bilge keels contributed slightly more to the added inertia, because the added inertia of the submerged bilge keel is not reduced while the other bilge keel is out of the water at the larger roll amplitudes. For the tumblehome configuration, the added inertia with bilge keels is less than expected at the largest roll amplitudes.

The damping exhibits nonlinear behavior across the range of amplitudes, for both topside configurations. At larger roll amplitudes, for the flared configuration, the damping from roll moment with bilge keels was less than with the "effective" addition of the bilge keels to the without bilge keel damping. However, for the tumblehome configuration, the damping from roll moment with bilge keels was greater than with the "effective" addition of the bilge keels to the without bilge keel damping. Therefore, some interaction effects between the bilge keel and topside are occurring at large roll amplitudes.

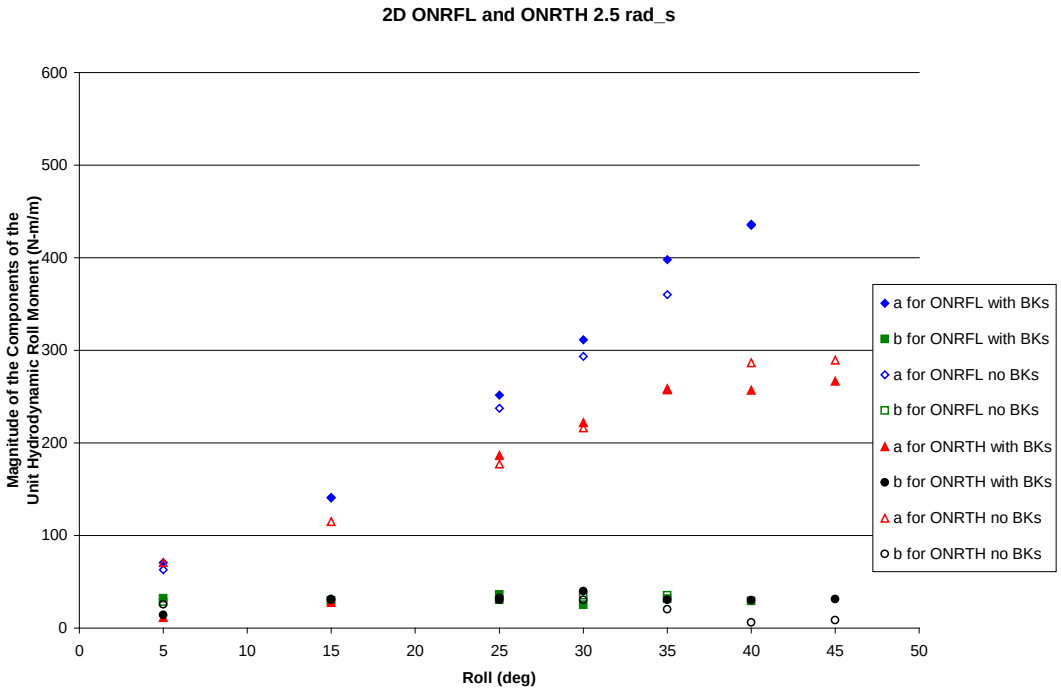

Figure 4-21. Comparison of the magnitude of the sum of the first 10 harmonics of added inertia and damping for the total unit hydrodynamic roll moment, for DTMB Models #5699 and #5699-1, with and without bilge keels, ω=2.5 rad/s

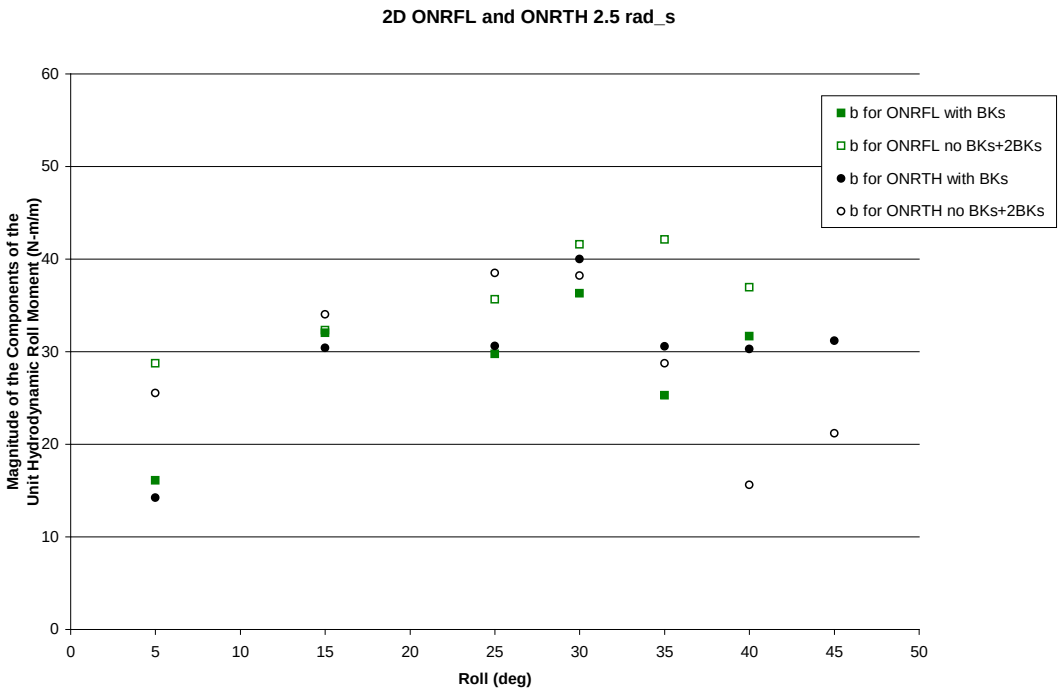

Figure 4-22. Comparison of the magnitude of the sum of the first 10 harmonics of damping for the total unit hydrodynamic roll moment, for DTMB Models #5699 and #5699-1, with bilge keels and with the effective influence of the bilge keels, ω=2.5 rad/s

4.6.2.3 Hydrodynamic Components as a Function of the Hydrodynamic Roll Moment due to the Bilge Keels

The sum of the first 10 harmonics for added inertia and damping, for the total unit hydrodynamic roll moment due to bilge keels of the ONRFL and ONRTH, are shown in Figure 4-23. As discussed in Chapter 4, the measured hydrodynamic roll moment due to the bilge keels was determined by multiplying the moment arm from the roll pivot axis times the unit normal force measured on the bilge keel. The magnitude of the harmonic components of the unit hydrodynamic roll moment due to the bilge keels, both the added inertia and damping, vary with amplitude. However, unlike for the unit hydrodynamic total roll moment, the trends with amplitude are not as clear, and the added inertia and damping as a result of the addition of the bilge keel are further examined (in Figure 4-24 and Figure 4-25 respectively).

As seen in Figure 4-24, the magnitude of the added inertia for small amplitudes (5 deg) is very similar for the flared and tumblehome topside configurations. However, at 15 and 25 degrees, where the differences in the above waterline topside configuration have interacted with the free surface, differences were observed. The added inertia for the tumblehome is observed to be reduced compared to the flared topside. As the roll amplitude increased, the added inertia for the flared topside increased, while the added inertia for the tumblehome configuration begins to plateau around 35 degrees. Additionally, the difference between the added inertia for with and without bilge keel configurations was more significant at larger amplitudes for the flared topside configuration than for the tumblehome topside configuration.

The magnitude of the added inertia was nonlinear across the range of amplitude (Figure 4-24). The added inertia increased for smaller amplitudes (from 5 to 25 deg) for both the flared

and tumblehome topside configurations. However, at 30 and 35 degrees and larger roll amplitudes, the added inertia was significantly reduced. The decrease in added inertia suggests that this is largely due to the bilge keels, which experience emergence from the free surface at nearly 30 deg for these hull forms. Then beginning at 40 degrees, the added inertia was significantly increased again, more so for the flared topside configuration than for the tumblehome topside configuration. The added inertia for the tumblehome topside exhibits a significant increase at 45 degrees. These increases are likely a result of the interaction of the deck edge with the free surface, in addition to the bilge keels, displacing water and resulting in wave generation from the topside. The roll amplitudes where these significant increases occur, correspond to the nearly deck edge interaction with the free surface for the flared (~40 deg) and tumblehome (~50 deg), respectively.

The magnitude of the damping increased nearly linearly for smaller amplitudes (from 5 to 25 deg), for both the flared and tumblehome topside configurations (Figure 4-25). However, at 25 degrees and larger roll amplitudes, the increase in damping was reduced. This effect was more pronounced for the flared topside than the tumblehome, as the magnitude of the damping of the roll moment due to the bilge keel was less for the flared topside than for the tumblehome topside configuration. For the tumblehome topside, the damping at 45 deg also increases more relative to the amplitude, suggesting that the interaction of the deck edge with the free surface results in some increased damping, in addition to the bilge keels, which is likely due to the generation of vorticity from the deck edge, as well as wave generation from the topside.

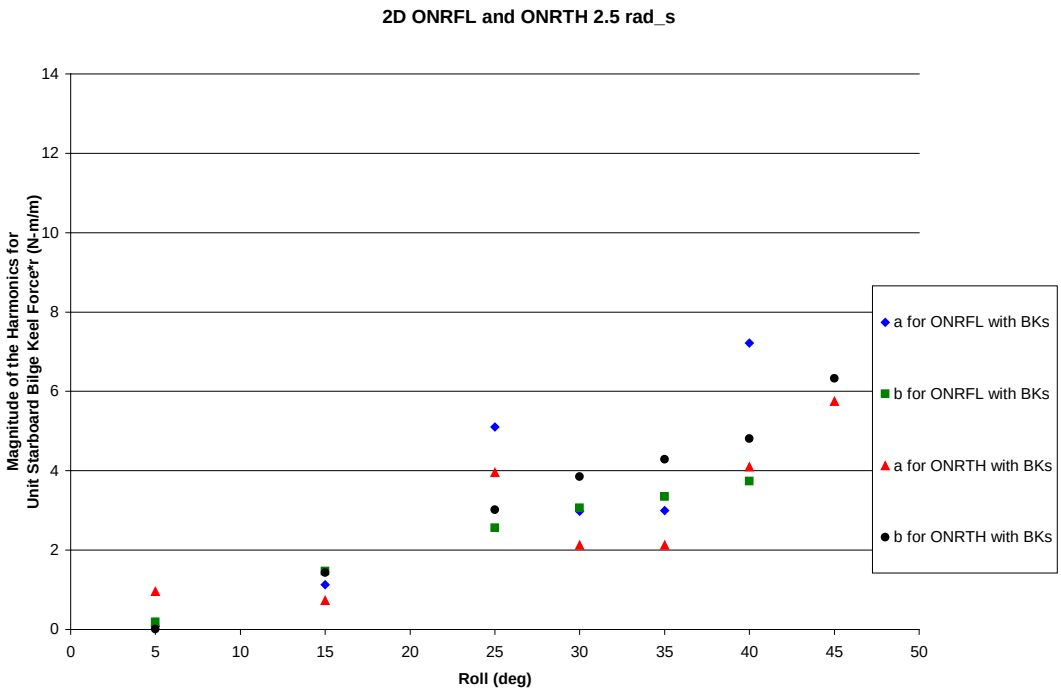

Figure 4-23. Comparison of the magnitude of the sum of the first 10 harmonics of added inertia and damping for the unit hydrodynamic roll moment due to the starboard bilge keel, for DTMB Models #5699 and #5699-1, ω=2.5 rad/s

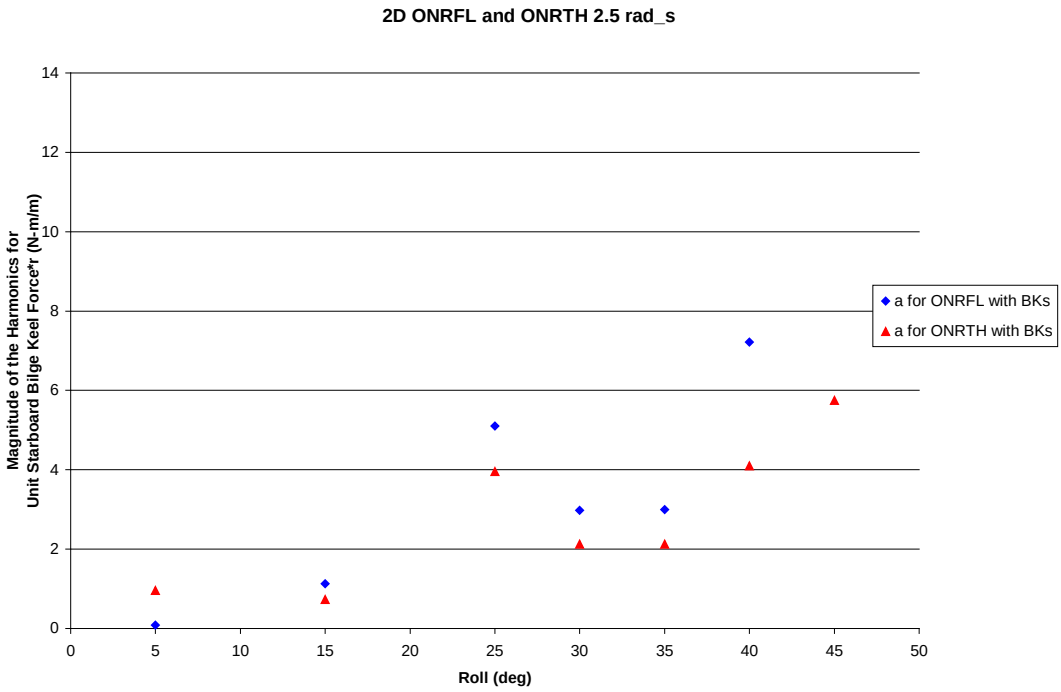

Figure 4-24. Comparison of the magnitude of the sum of the first 10 harmonics of added inertia for the unit hydrodynamic roll moment due to the starboard bilge keel, for DTMB Models #5699 and #5699-1, with and without bilge keels, ω=2.5 rad/s

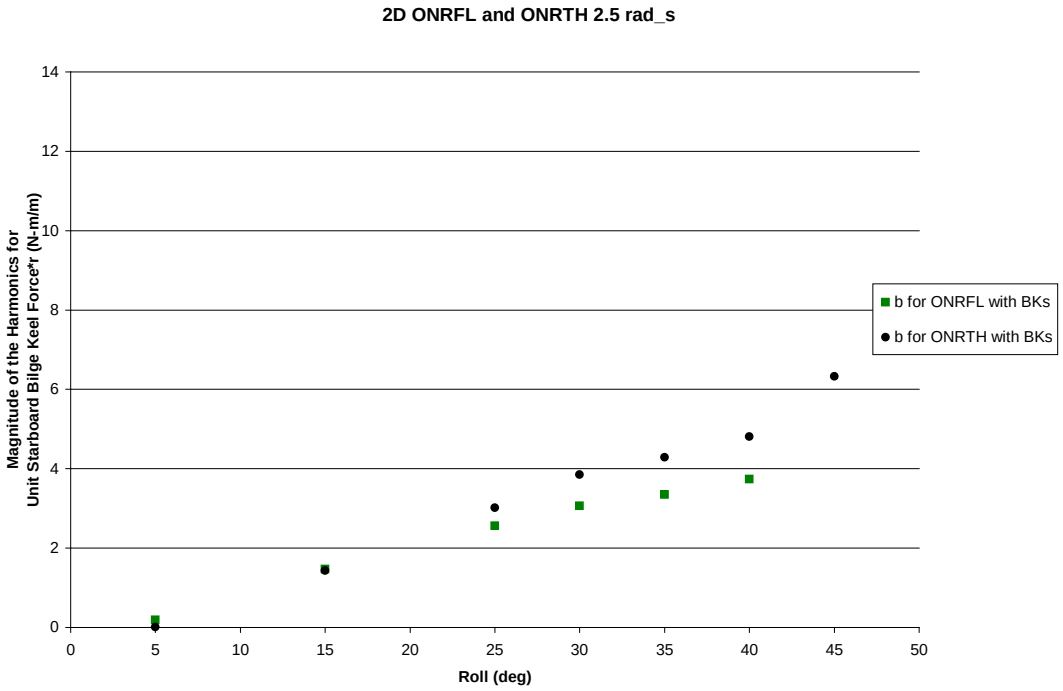

Figure 4-25. Comparison of the magnitude of the sum of the first 10 harmonics of damping for the unit hydrodynamic roll moment due to the starboard bilge keel, for DTMB Models #5699 and #5699-1, with and without bilge keels, ω=2.5 rad/s

4.6.2.4 Frequency Dependence

Additional results for the 2.17 rad/s and 2.85 rad/s roll frequency conditions are given in Appendix D (section D.7). For the magnitude of the harmonic components of roll motion, the added inertia of roll increased with increased frequency and the damping was not as frequency dependent as the added inertia. For the magnitude of the harmonic components of the unit hydrodynamic roll moment, the added inertia increased with increased frequency and the damping was not as frequency dependent as added inertia. For the magnitude of the harmonic components of the unit hydrodynamic roll moment due to the bilge keel force, the added inertia and damping both have nonlinear frequency dependence.

4.6.3 Summary of the Harmonic Analysis Results for Added Inertia and Damping

From the harmonic analysis of the experimental results, several observations can be made. As expected, the hydrostatics comprised the majority of the total measured roll moment. In order to examine the hydrodynamic components of the roll moment, the hydrostatics were subtracted. Also as expected, the added inertia is the largest component of the total hydrodynamic roll moment and the damping is a smaller portion of the total hydrodynamic roll moment, which decreased with increasing amplitude. The added inertia from the hydrodynamic roll moment due to the bilge keel was much smaller than the added inertia of the total hydrodynamic roll moment.

The added inertia for the bilge keels was largest at the peaks of the roll cycle. However, the added inertia was larger when the bilge keel was submerged than when it was near the free surface (or emerged). As expected, the damping due to the bilge keel was largest after peak of

roll cycle, near the peak roll velocity, but was also asymmetric, with the damping of the emerging case being slightly larger than for the submerging case. This suggests that the bilge keel is more effective in the upswing (going from fully submerged toward the free surface) than for the downswing (when the bilge keel is traveling from the free surface toward its fully submerged position). This is attributed to the observed differences in vortex generation from the bilge keels, and are discussed more in the next section of this chapter.

Two additional findings were also made from the analysis of the experimental results, which are significant for the modeling of ship motions. First, the added inertia component of the bilge keel is the same order of magnitude as the damping component of the bilge keels, although the added inertia is still consistently larger, but much smaller than for the hull. Typically in ship motions modeling methods, the added inertia of the bilge keel is neglected. Second, the damping from the roll moment due to the bilge keel was the same order of magnitude as the damping from the total hydrodynamic roll moment and for the smaller amplitudes, the damping due to the bilge keels was typically more than half of the total damping.

4.7 Characterization of the Physical Phenomena

From the experiment, several distinct phenomena occurring at large roll motion were observed. These include distinct physical processes related to the bilge keel interaction with the free surface, vortex shedding, deck submergence, and near-field ship wave generation. Frequency dependence for these processes is also discussed.

4.7.1 Bilge Keel Transition at the Free Surface

The interaction of the bilge keel with the free surface can be separated into three distinct phases: emergence, re-entry, and fully submerged (Figure 4-17). For large roll angles, the bilge keel emerges from the free-surface. During this process corresponding “water shipping” on the topside of the bilge keel occurs. The time duration that the water remains on the topside of the bilge keel depends on both the roll amplitude (i.e. how far the bilge keel comes out of the water) and the roll frequency (i.e. how long the bilge keel is out of the water). Just after the peak of the roll cycle is reached, the water runs off of the bilge keel, reducing the load on the topside. However, this process is very short in duration before the bilge keel interacts with the free-surface again and experiences impulse loading, or “slap,” during bilge keel re-entry. As seen from the camera measurements (Figure 4-26 and Figure 4-27), once the bilge keel re-enters the water, the resulting vorticity is altered by the influence of the free surface, for the large amplitude roll condition, compared to the small amplitude roll condition.

The bilge keel re-entry with the free-surface results in asymmetric loading on the bilge keel. The impulse load caused by re-entry is short in duration and proportional to the roll amplitude and frequency. The re-entry process is also accompanied by air entrainment on the underside of the bilge keel (Figure 4-27). After the bilge keel is re-submerged, air bubbles are trapped. These quickly disperse as the pressure from the water increases, when the bilge keel traverses to the opposite amplitude peak in the roll cycle, where the bilge keel is deeply submerged. This whole process of air entrainment lasts just several tenths of a second, but is observed with the PIV camera and the bilge keel force measurement. However, with the filtered data, this short duration (high-frequency) phenomena is not observed, but is confirmed with the correlation of the camera observations and the unfiltered data. Air entrainment was not observed for the small and

moderate amplitude conditions, even when the bilge keel is near the free-surface, but does not emerge (Figure 4-26).

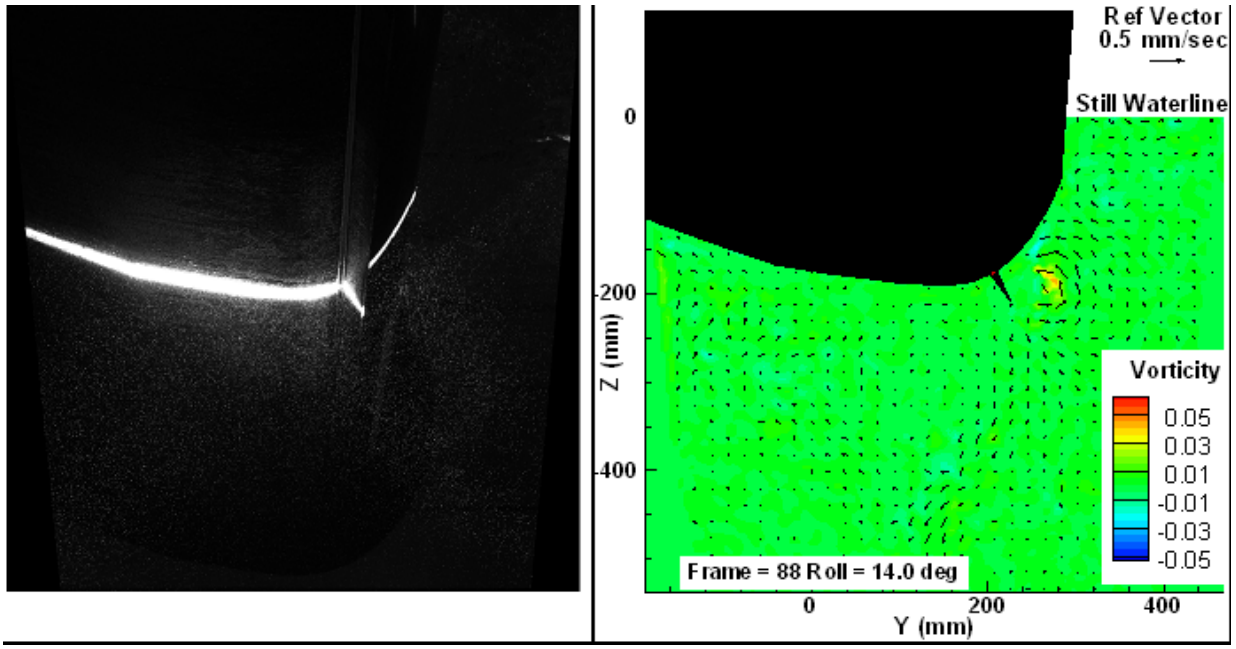

Figure 4-26. Measurements for ϕ=15 deg, ω= 2.5 rad/s for DTMB Model #5699-1, near peak of the roll cycle when the bilge keel is fully submerged. Camera (left), and PIV with bilge keel force vector (right) measurements are shown.

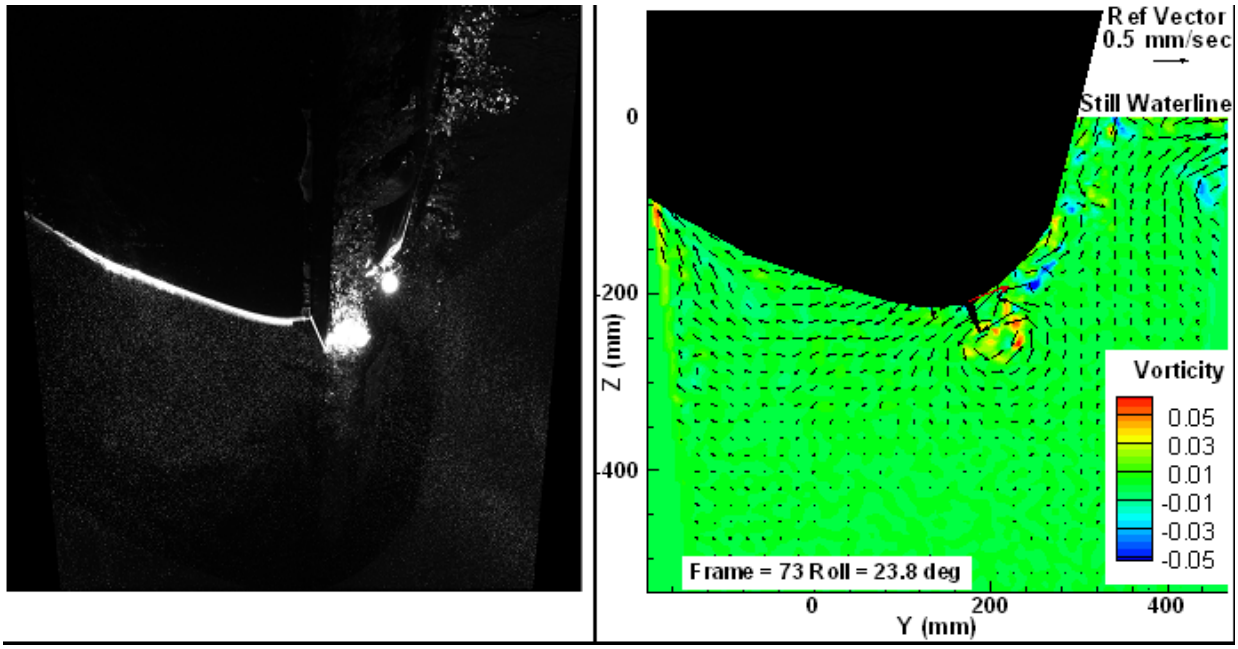

Figure 4-27. Measurements for ϕ=35 deg, ω= 2.5 rad/s for DTMB Model #5699-1 after bilge keel re-entry, near peak of the roll cycle when the bilge keel is fully submerged. Camera with air entrainment (left), and PIV with bilge keel force vector (right) measurements are shown

4.7.2 Vortex Shedding From the Bilge Keel

Vortex generation occurs from the tip of the bilge keel throughout the roll cycle. Once the bilge keel is submerged, vortex shedding from the tip begins to occur. This vortex grows in magnitude until the point of maximum velocity during the roll cycle and then becomes detached from the bilge keel tip. After the bilge keel reaches the maximum roll amplitude during the cycle, while fully submerged, the vortex generation occurs again as the bilge keel transits back towards the free-surface (Figure 4-28). The vorticity generation from the bilge keel also corresponds to changes in the bilge keel force. At its most submerged position, as the bilge keel transitioned direction during the roll cycle increases in the force on the bilge keel were observed. This increase in force corresponds to the interaction of the bilge keel and the attached vortex with the previously shed vortex that was generated as the bilge keel moves away from the free surface. Additional analysis of vorticity and resulting circulation measured in control volume regions near the bilge keels is presented in Minnick, et al. (2012).

However, for large amplitude roll motion, at the peak in the roll cycle when fully-submerged, the bilge keel interacts with the previously shed vortex (Figure 4-29). At the same time, a new vortex is forming before the point of maximum velocity. This results in increased loading on the bilge keel for a short duration, and then disturbed free-surface after re-entry (Figure 4-29). The duration of this interaction depends on both the roll amplitude and roll frequency. For large amplitude roll, after the point of maximum velocity, the vortex shed from the bilge keel travels to the free-surface and is compressed into a jet moving away from the hull. For these large amplitude conditions (25 deg and greater), the free surface acts as a wall-like boundary, trapping the vorticity. During the transitions in the roll cycle, when the bilge keel was near the free surface, the vorticity was shed away from the bilge keels and the hull and compressed as they interacted with the free surface boundary.

4.7.3 Deck Edge Interaction with the Free Surface

The maximum roll amplitude tested, due to the design and operational constraints of the 3DoF mechanism, was 45 degrees, so deck edge submergence for the tumblehome topside configuration, which occurs near 50 degrees, was not observed. However, for the flared topside configuration, deck submergence was observed. Despite the sharp corner formed from the deck edge, no significant vortex shedding was observed. This is due to the duration of deck submergence, since the roll amplitude was not large enough for the deck edge to experience significant submergence. The deck edge, particularly for the flared hull, did contribute to additional wave generation. However, it is difficult to distinguish this particular contribution from the waves generated from the hull throughout forced roll oscillation

The peak force during process of the bilge keel “shipping” water after emergence is more compressed in duration for the flared topside configuration. This is due to the effect of the sidewall. The flared topside, because of its shape, quickly pushes water away that has collected on the topside of the bilge keel away. However, the tumblehome topside, because of its shape, may have some additional “sloshing” type behavior as the water on the topside of the bilge keel rolls up the sidewall, before being pushed away.

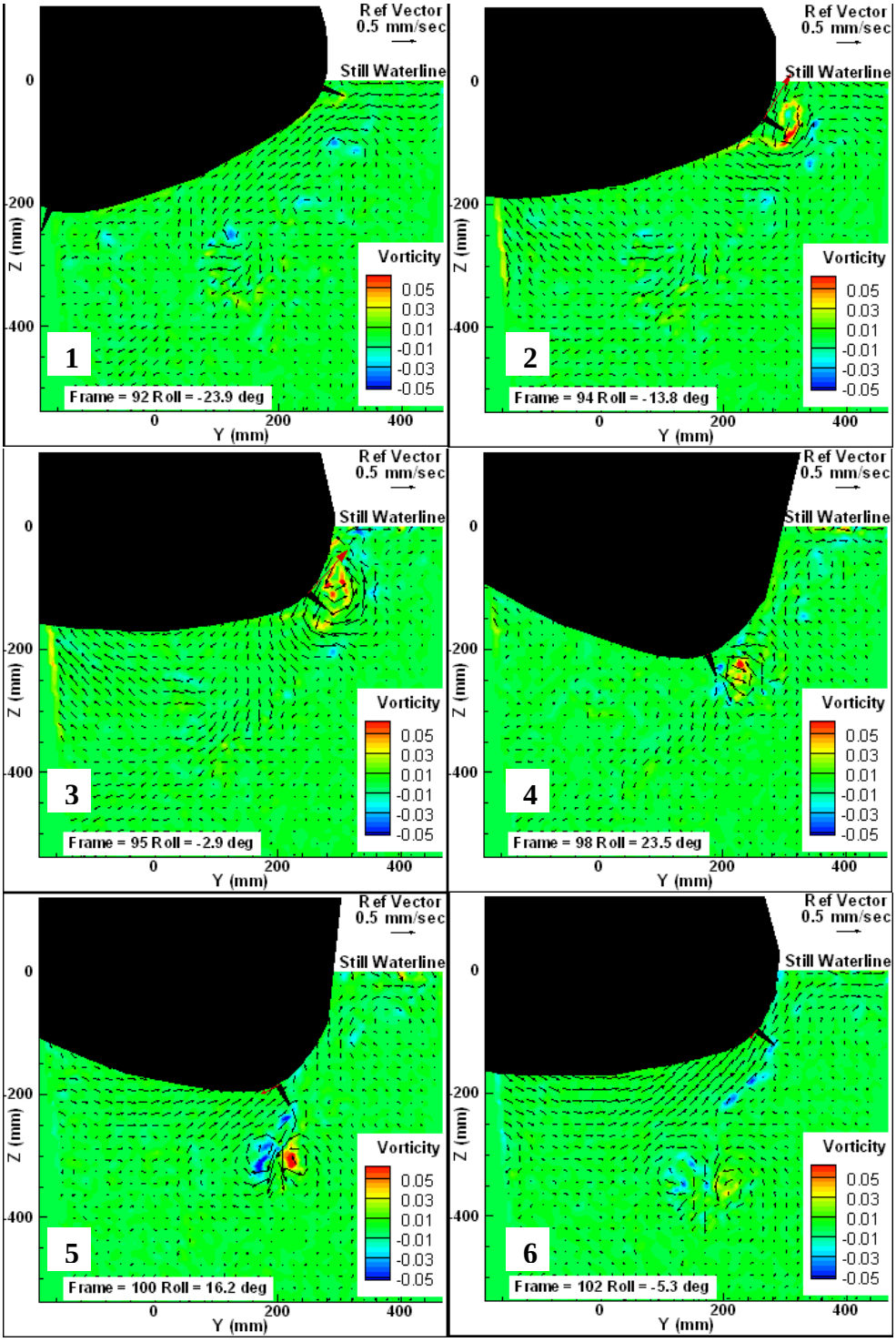

Figure 4-28. PIV measurements for ϕ=25 deg, ω= 2.5 rad/s for DTMB Model #5699-1, with bilge keel force measurements shown (red vector). Single roll cycle shown (left to right, top to bottom), beginning after bilge keel re-entry (top left), near peak of the roll cycle when the bilge keel is fully submerged (middle right), and then transitioning to bilge keel emergence (bottom right)

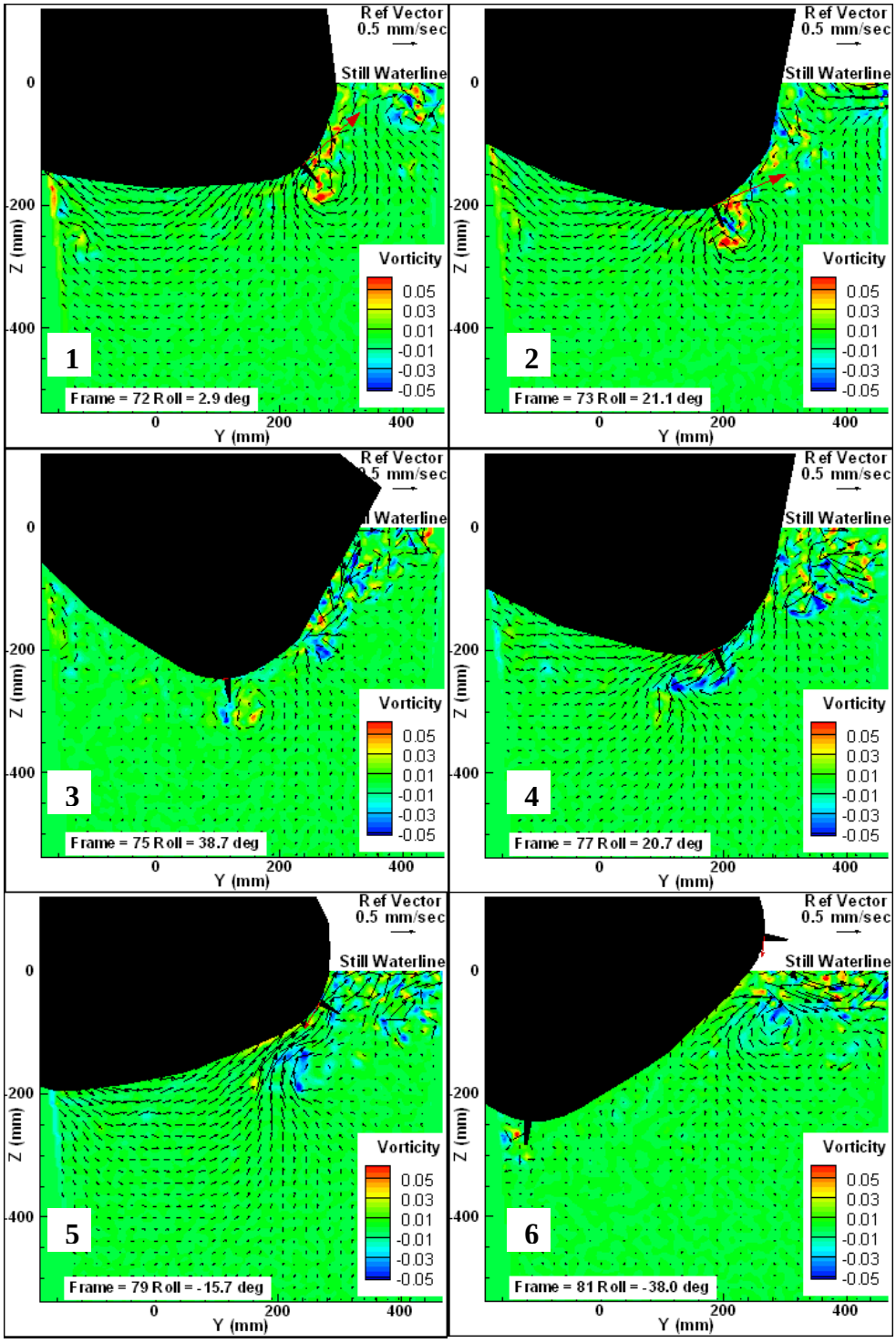

Figure 4-29. PIV measurements for ϕ=40 deg, ω= 2.5 rad/s for DTMB Model #5699-1, with bilge keel force measurements shown (red vector). Single roll cycle shown (left to right, top to bottom), beginning after bilge keel re-entry (top left), near peak of the roll cycle when the bilge keel is fully submerged (middle left), and then transitioning to bilge keel emergence (bottom right)

4.7.4 Near-Field Ship Wave Generation

Wave-making from both the hull and bilge keel was also observed. Although wave probe measurements were collected during the experiments, the wave interaction effects with the basin sidewalls resulted in complex wave patterns at locations away from the hull, where the wave probes were located. Additional numerical analysis is presented in Chapter 5, to quantify the wave-generation effects due to the bilge keels and topside configurations. However, several observations can be made from the experimental results of the near-field ship wave generation.

For the small to moderate amplitude roll conditions (5 and 15 degrees), the bilge keel was submerged enough to not have any appreciable effect on the free-surface. However, for the larger amplitude roll conditions (25, 30, 35, 40, and 45 degrees) waves were produced from the interaction of the bilge keel and the free-surface. As expected, the two topside shapes had very different results in terms of wave-making effects. The flared topside pushed water away from the hull through the roll cycle, generating more regular waves. However, the tumblehome topside "caught" water and also had a pronounced effect of the chine transition at the waterline between the hull and the topside, which was not present for the flared topside configuration. The waves generated by the tumblehome topside were much more irregular in shape, due to this effect from the topside geometry.

4.7.5 Frequency Dependence

Frequency dependence was observed in several of the phenomena measured in the bilge keel force. The results are shown in Appendix D.3 As expected, when the impulsive force occurred during re-entry, after bilge keel emergence, the magnitude of the impulsive force increases with increasing frequency. For increased frequency, the magnitude of the roll moment on the hull decreases.

The bilge keel force component due to interaction with the previously shed vortex also increases with increasing frequency. However, it is also larger for the tumblehome topside configuration than for the flared topside. Despite the topside variation, this phenomenon occurs when the bilge keel is fully submerged.

The peak force during the process of the bilge keel "shipping" water after emergence is approximately the same across the roll frequencies tested. However, the peak force is more compressed in duration for the flared topside configuration, compared to the tumblehome topside configuration. This is due to the effect of the sidewall angle. The flared topside, because of its shape, quickly pushes water away that has collected on the topside of the bilge keel. However, the tumblehome topside, because of its shape, may have some additional "sloshing" type behavior, as the water on the topside of the bilge keel rolls up the sidewall before then being pushed away.

Chapter 5 Observations and Analysis of Large Amplitude Ship Roll Motion Using Numerical Methods[14]

5.1 Overview

Chapter 3 used URANS simulations to provide insight into the relative influence of physical phenomena, which occur during large amplitude ship motions. The results of the numerical study in Chapter 3 where then used to design and perform an experiment, as described in Chapter 4, which was specifically targeted toward obtaining observations and measurements of physical phenomena which influence the hydrodynamic components of large amplitude roll motion. The results from the experiment described in Chapter 4 provided useful insight in the physical phenomena which occur during large amplitude roll motion and helped with the formulation of new models for large amplitude ship roll motion.

To supplement the experimental measurements and observations presented in the previous chapter, additional numerical investigations were carried out to examine results for large amplitude roll motion. The first numerical simulations presented in this chapter utilize a 2D zero-speed potential flow method to further examine the wave-generation effects from the bilge keel and topside, as observed from the experimental results presented in the previous chapter. The second numerical simulations build upon the URANS results presented in Chapter 3 to further examine the effects of large amplitude roll motion on the bilge keel force. Considerations for large amplitude motions on total ship roll damping and for the force on the bilge keel are discussed in Chapter 6.

5.2 Zero Speed, 2D Numerical Calculations

For this investigation, WAMIT was used to determine the roll added inertia and damping components of the radiation portion of the hydrodynamic roll moment for DTMB Models #5699 and 5699-1, the midship section of the ONR Topside Series Flared and Tumblehome configurations, respectively. The conditions examined corresponded to a range of frequencies and amplitude, including those tested during the experiment presented in Chapter 4. Numerical results were calculated to examine the effects of bilge keel and topside geometry on the added inertia and damping for radiation, over a range of roll amplitudes and frequencies. All results are presented in model-scale units.

The results presented below were generated using WAMIT v6.3. WAMIT is a panel method ship motions program that uses linear analysis of the interaction of floating bodies and a free surface to compute the radiation and diffraction velocity potentials on the body wetted surface (Lee, 1995). The potentials are determined from the solution of an integral equation obtained by using Green's theorem with the free-surface source-potential as the Green function. The theoretical formulation in WAMIT assumes ideal flow, infinite depth, and zero-speed conditions and the free-surface is linearized. The lids option was used to suppress irregular frequencies.

[14] Portions of this chapter have been published previously in Bassler and Miller (2011) and Bassler, et al. (2011)

5.2.1 WAMIT Results

Detailed results from the WAMIT simulations are presented in Appendix E. The first WAMIT analysis examined the effect of end plates on the results for added inertia (Figure E-1) and damping (Figure E-2). The end plates were not found to alter the results for the WAMIT calculations. Therefore, all subsequent calculations were carried out using the 2D midship section geometry corresponding to DTMB Models #5699 and #5699-1. The subsequent results for the ONRFL and ONRTH from Appendix E were then combined, using a quasi-steady assumption, to examine the influence of heel angle on radiation added inertia and damping, with and without bilge keels. Results for the 2.5 rad/s roll frequency are shown (Figure 5-1-Figure 5-2). The results are discussed further in the next section.

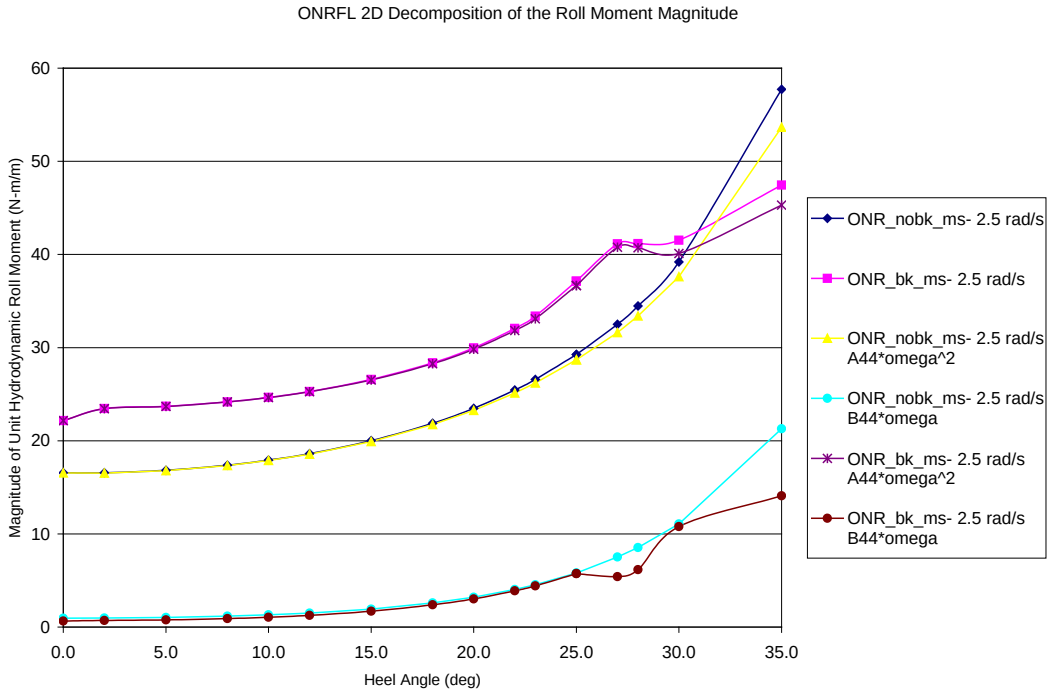

Figure 5-1. Comparison of the total unit hydrodynamic roll moment magnitude due to radiation and the added inertia and damping due to radiation for the ONRFL vs heel angle, for ω=2.5 rad/s, with and without bilge keels

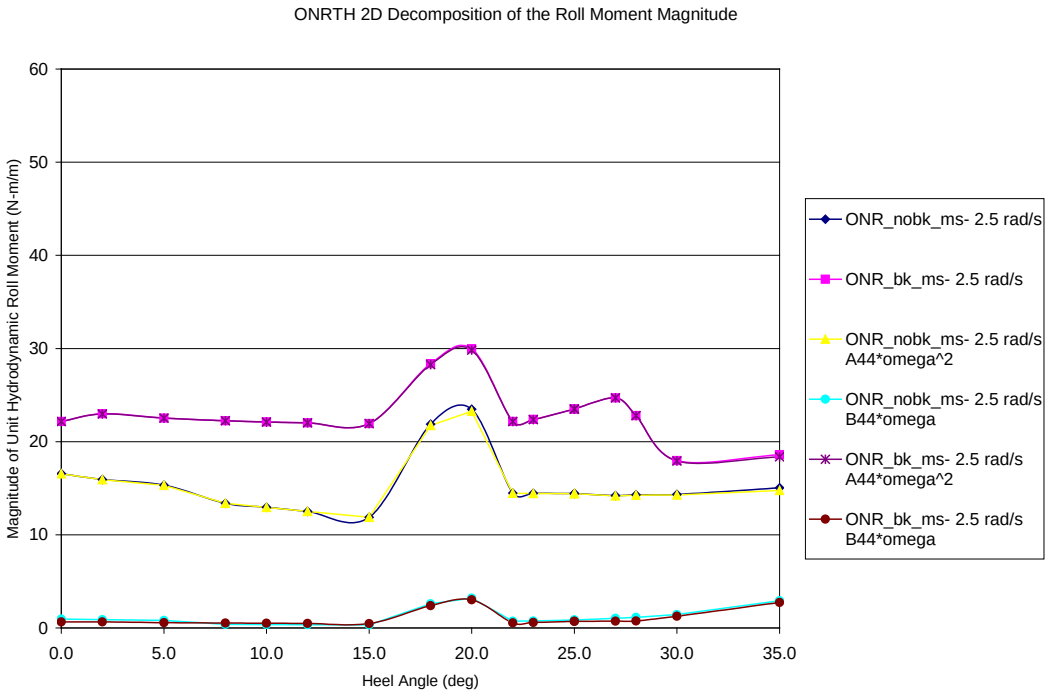

Figure 5-2. Comparison of added inertia and damping due to radiation for the ONRTH vs heel angle, for ω=2.5 rad/s, with and without bilge keels

5.2.2 Observations from the WAMIT Results

The effect of heel angle for constant frequency, using a quasi-steady assumption, was used to examine the influence of amplitude and topside geometry on added inertia and damping due to radiation. As observed from the WAMIT results, increased roll magnitude results in increased added inertia due to radiation, for configurations both with and without bilge keels. The added inertia and damping coefficients, both with and without bilge keels, for the 25 deg heel condition are significantly different from the small heel (0-20 deg) conditions.

The added inertia is larger with the bilge keels, compared to without the bilge keels, effectively the addition of bilge keels increased the roll added inertia. At 25 deg heel, for configurations both with and without bilge keels, a noticeable difference is observed, compared to smaller heel angles. This is a result on the interaction of the bilge keels and topside with the free surface at larger heel angles.

Increased heel also results in increased damping, for both with and without bilge keel configurations. The radiation damping is smaller with bilge keels compared to without. Similar to the added inertia, at 25 deg heel, for configurations both with and without bilge keels, a noticeable change in behavior is observed compared to consistent trends at smaller heel angles. Also, at lower frequencies, the damping even at 25 degrees and above is consistent with the trend of smaller heel angles. However, beginning at roll frequencies of approximately 8 rad/s, the damping begins to deviate. The addition of the bilge keels changes the frequency behavior of the added inertia and damping for both topsides at large heel angles (25 deg and greater).

The topside also affects both the added inertia and damping due to radiation. The topside configuration affects the magnitude of the added inertia, both with and without bilge keels. With the addition of the bilge keels, the 18 and 20 deg heel conditions do not follow the same trend as 15 deg and below, or at 25 deg and above. The topside also affects the magnitude of damping, both with and without bilge keels. For both the flared and tumblehome topside configurations, the added inertia contribution dominates the behavior of the total unit hydrodynamic roll moment (Figure 5-1 and Figure 5-2). For the flared topside, with the bilge keels, the increase in added inertia corresponds to a decrease in damping near 27 deg, where the bilge keel interacts with the free surface (Figure 5-1). For the tumblehome topside, an increase in added inertia occurs at both 18-20 deg and 27 deg, but does not directly correlate to an increase/decrease in damping (Figure 5-2).

For the flared topside, the added inertia increased with increased heel angle, as expected given the geometry (Figure 5-3). However, for the tumblehome topside, the added inertia exhibited more nonlinear behavior, especially at larger heel angles (Figure 5-4). This is likely due to the geometry, where the damping decreases until the side-wall of the hull is nearly vertical (~15 deg heel for this hull form geometry) and then a larger increase in damping is observed afterwards, because the sidewalls of the topside acting more like a wave-maker at these increased heel angles. For the flared configuration, the damping increased with increasing heel angle (Figure 5-5). For the tumblehome configuration, the damping was relatively constant through about 15 deg of heel and then increased rapidly for 18 and 20 deg heel, before decreasing rapidly for 25 deg and greater heel angles (Figure 5-6). The heel angle appeared to be a more dominant effect on both added inertia and damping than frequency. For the added inertia due to radiation, the differences due to both topside configurations with varied heel and bilge keel effects are about the same order of magnitude. For radiation damping, the difference due to topside configurations with varied heel was larger than the difference due to bilge keel effects. Additional results from the WAMIT simulations are presented in Appendix E.

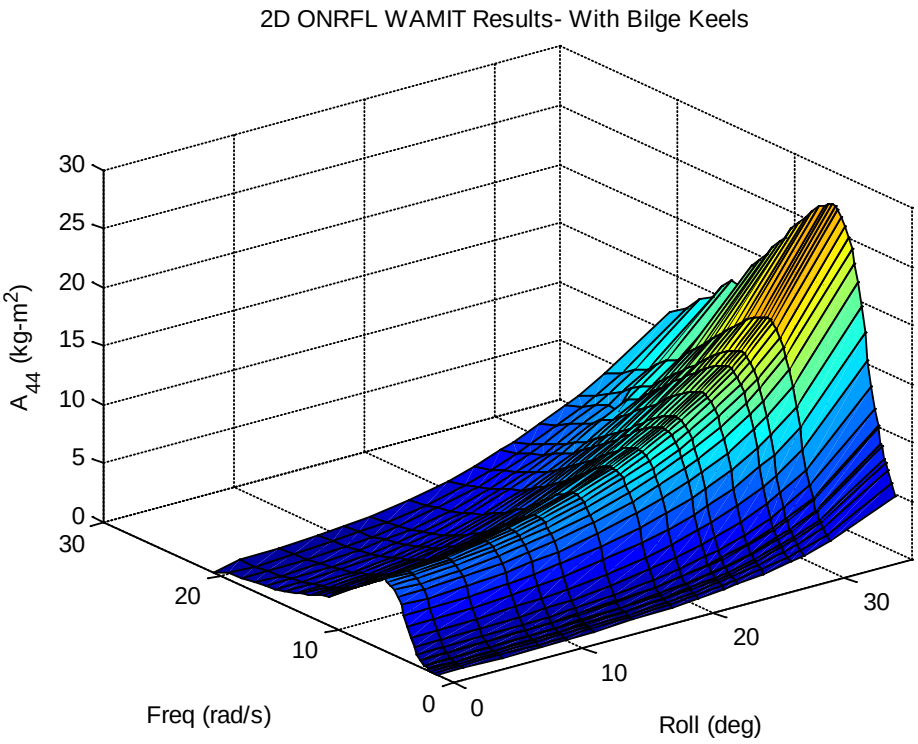

Figure 5-5-3. ONRFL added inertia due to radiation vs heel angle vs frequency, with bilge keels

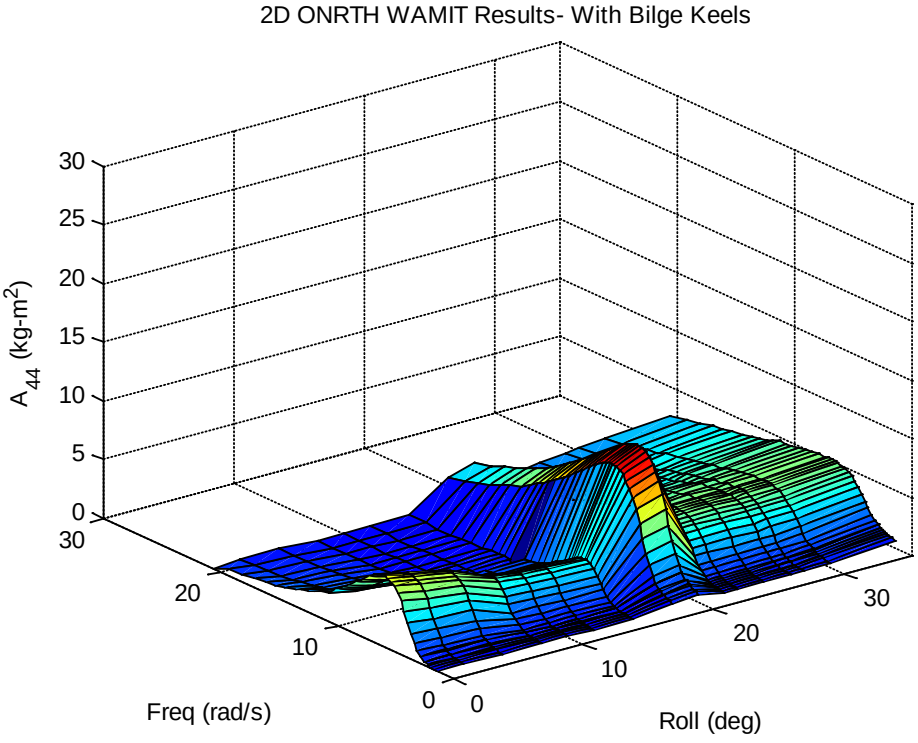

Figure 5-5-4. ONRTH added inertia due to radiation vs heel angle vs frequency, with bilge keels

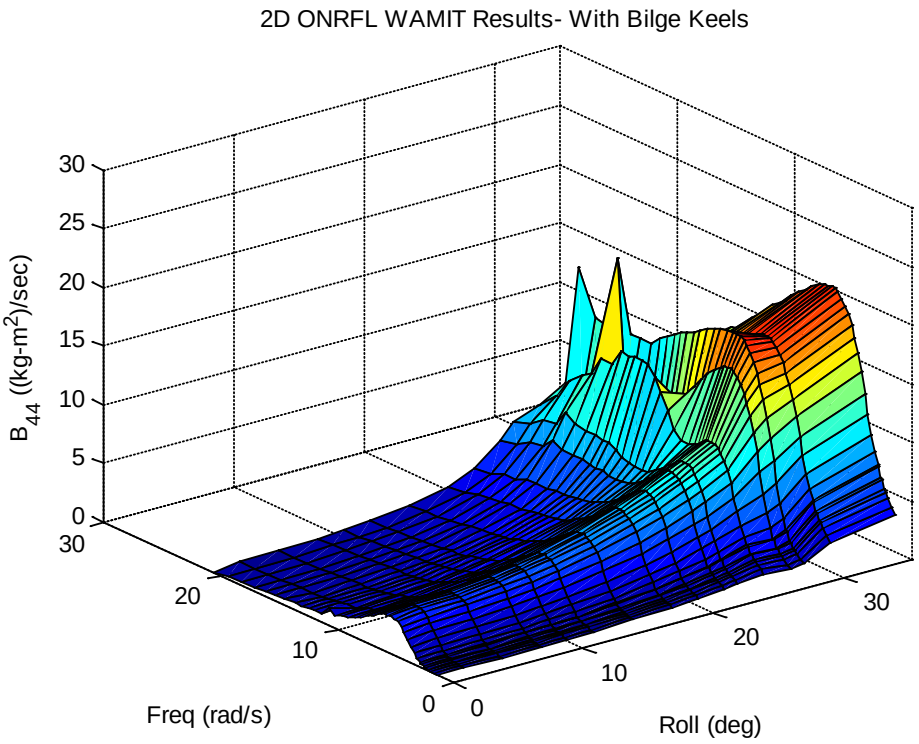

Figure 5-5-5. ONRFL damping due to radiation vs heel angle vs frequency, with bilge keels

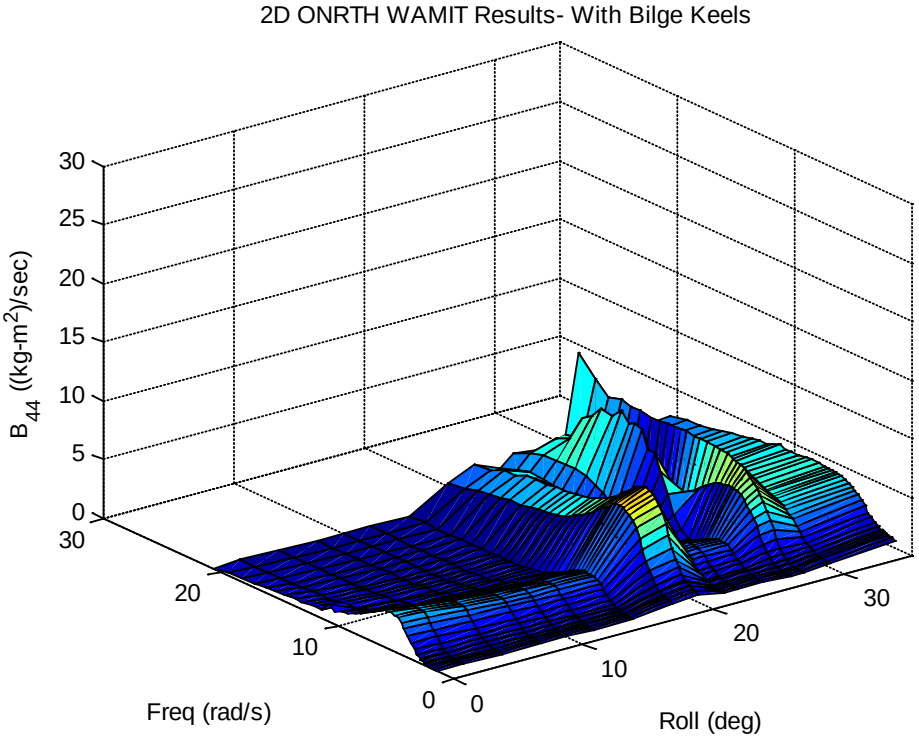

Figure 5-5-6. ONRTH damping due to radiation vs heel angle vs frequency, with bilge keels

5.3 Examination of 3D Effects on the Bilge Keel Force Using URANS Simulations

Because the WAMIT calculations only enabled 2D zero speed investigation of the roll added inertia and damping due to radiation, additional numerical studies were performed, expanding on the URANS work discussed in Chapter 3, but limiting the conditions of investigation only to large amplitude roll motion. Comparisons were made between the zero forward speed 2D RANS simulations and the 2D experiment to determine the differences between simulation and experimental results for the same conditions, for the midship section of DTMB Model #5613-1. Comparisons for the midship section include the sectional roll moment, sectional bilge keel force, and flow-field features (vorticity and free-surface wave amplitude). Then, URANS simulations were performed to examine 3D effects and forward speed effects on the bilge keel force for large amplitude roll motion.

While the measurement uncertainty was assessed for the experimental results, detailed determination of the numerical uncertainty of the URANS calculations was not carried out. The objective of the comparisons between the experimental and numerical results was qualitative, to determine if the same physical phenomena being observed during the experiments was also captured through the numerical modeling. Furthermore, the level-set free surface capturing technique used for the RANS simulations will also affect the resulting accuracy of the solution. For a qualitative comparison, to examine first-order characterization of the physical phenomena, which occur during large amplitude roll motion, this was approach for modeling the free surface was considered to be adequate. In this technique, the grid does not need to conform to the free surface topology, but sufficient grid resolution was required to discretize the level-set function gradients. For further studies, to more accurately quantify some of the physical phenomena, grid sensitivity studies, and alternative free surface modeling approaches should be considered.

URANS simulations were performed for the 2D midship section undergoing 1DoF forced roll oscillations at zero speed conditions, in calm water. Comparisons are shown between the 2D URANS and 2D experiment, as well as the midship section of the bilge keel force URANS results for the 3D hull form at zero speed in calm water (Figure 5-7). 2D results from URANS and experiments generally agreed, even for large amplitude roll motion, although differences were likely due to the limitations of finite difference methods used in the URANS simulations. Comparisons were made to the experimental results presented in Chapter 4. The distinct physical processes occurring during roll motion, as observed from the experimental measurements and identified in Chapter 4, are also observed in the URANS results.

As shown in Figure 5-7, the bilge keel force results from the simulations and the experiments agreed well for roll amplitudes of 15 and 25 deg. However, for larger roll angles (30 and 35 deg), where the bilge keel interacts with and emerges from the free surface, some discrepancies are observed between the simulations and the experiments. The comparisons were made between filtered experimental results and unfiltered numerical results. Due to mechanical noise in the experimental results, filtered results for the measured bilge keel force are presented. For the large roll amplitudes, the general shape and peak values agree well for the 2D midship section. However, the URANS simulations have more noise for the large amplitude cases, likely due to the finite difference method used for the simulations, coupled with a practical time-step, where emergence and re-entry of the bilge keel results in nonlinearities in the instantaneous wetted portion of the bilge keel, including water run-off, entrained air collapse, and impulse loading from their emerging and immerging from the free-surface.

For roll amplitudes up to 30 deg, at zero speed, the differences between the 2D and 3D midship section cuts of the bilge keel force are small. For the 35 deg case, distinct differences occur between the 2D and 3D results for the portion of the roll cycle where the bilge keel is emerging and then re-entering the free surface. This is likely due to 3D effects along the bilge keel due to the flow along chord, while the 2D case does not have any longitudinal variation along the bilge keel during large amplitude roll motions.

Comparisons were also made between the midship section results of the 3D URANS simulations and experiments from Bassler et al. (2007), including the effects of forward speed, which are detailed further in Miller, et al. (2008). The 3D results at zero speed (Figure 5-8) and forward speed (Figure 5-9) exhibit the same behavior observed from the 2D experimental and URANS results. With the addition of forward speed, the total roll moment, as well as components due to the hull and bilge keels, is reduced. The effects of amplitude on the roll moment due to the bilge keel force are more prominent for the zero speed condition (Figure 5-8) than for the forward speed condition, even at smaller roll amplitudes.

For the conditions of water "shipping" on the bilge keels, during large amplitude roll motion, 3D effects can distorte the resulting effect of this phenomenon. As observed during both the 2D, zero-speed, experiment and the numerical studies, this phenomenon can be observed in the measured/predicted bilge keel force. However, under these simplified conditions the manifestation of water "shipping" during emergence of the bilge keel, for large amplitude roll motion, may be exaggerated, since the water is more trapped than for forward speed, or 3D conditions. With forward speed, the water on top of the bilge keel is convected downstream, even on top of the bilge keel. For a 3D geometry, water shipping will still occur, but the additional force on the top of the bilge keel, due to the mass of the water, will be translated along the longitudinal distribution of the bilge keel, and the duration of this effect on the bilge keel force will be small. With additional degrees-of-freedom for ship motions, the duration of the water "shipping" is likely to be reduced even further. So while an interesting physical phenomenon, and that resulted in observable impacts on the bilge keel force, the resulting influence on the hydrodyamic components of ship motion are likely to be minimal.

For the 30 degree roll amplitude conditions, larger differences between the experimental and numerical results are observed during the second half of the roll period. As observed in both the experiments and simulations, the bilge keel exits the water at the peak of the 30 degree roll amplitude cycle. For the 30 degree roll amplitude, nonlinearities in the measured roll moment are due to free-surface effects on the bilge keel, particularly emergence and re-entry at forward speed. This was observed in the URANS results presented and discussed in Chapter 3.

The URANS simulations were also used to examine the vorticity shed from the bilge keels and the results were compared to experimental PIV measurements for the 3D hullform (Figure 5-10). At large amplitudes (25 and 30 degrees), the vorticity shed from the bilge keels, as the bilge keel travels from a deeply submerged position to the free surface, becomes compressed near the free surface. With the addition of forward speed, the shed vortices are not only compressed in the tangential direction to the hull and bilge keel, but also longitudinally, due to the convention of the vorticity downstream.

As also observed from the URANS and experimental results, the bilge keel vortex generation is asymmetric for the roll cycle. As the bilge keel travels from deeply submerged towards the free surface, the vortical structure generated at the tip of the bilge keel is coherent until its detachment near the free surface and compression, due to free surface interaction and forward speed effects. However, as the bilge keel travels from the free surface back to begin

deeply submerged, the interaction between the bilge keel and free surface reduces the coherent structure of the vortex generated and the tip of the bilge keel. This results in asymmetric energy dissipation due to bilge keel vortex shedding. Therefore, the bilge keels have increased damping during their upward rotation to the free surface during the roll cycle, compared to their downward rotation from the free surface. This reduced vortex shedding effect becomes more pronounced for large amplitude roll conditions, where the bilge keel normal force is also reduced, due to interaction with the free surface.

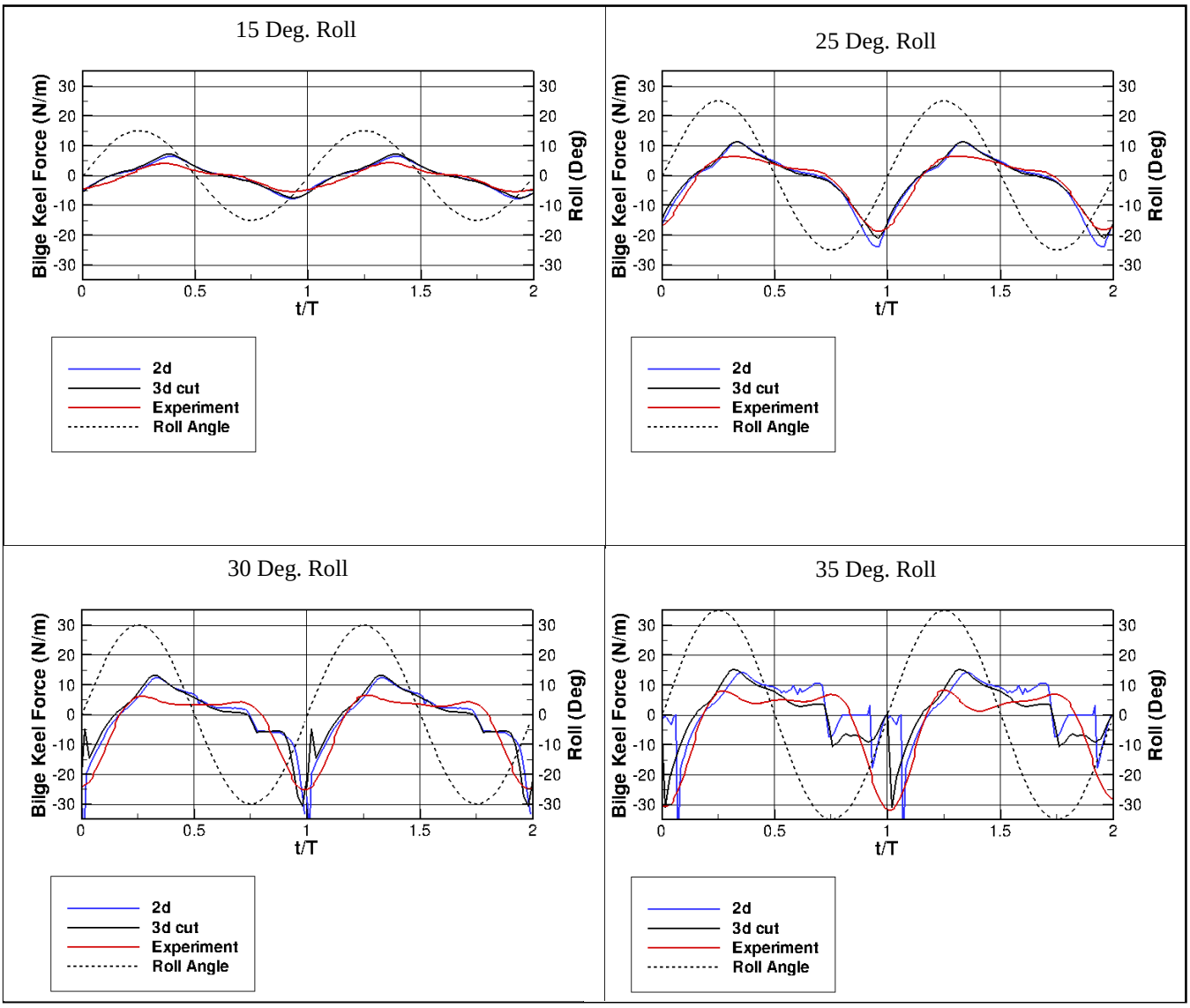

Figure 5-7. Bilge keel force comparisons between 2D (solid blue) and 3D midship section cut (solid black) URANS simulations for DTMB Model 5613-1 and 2D model experiments (solid red) at Fn = 0.0, ω = 2.85 rad/s, for ϕ = 15, 25, 30 and 35 deg roll

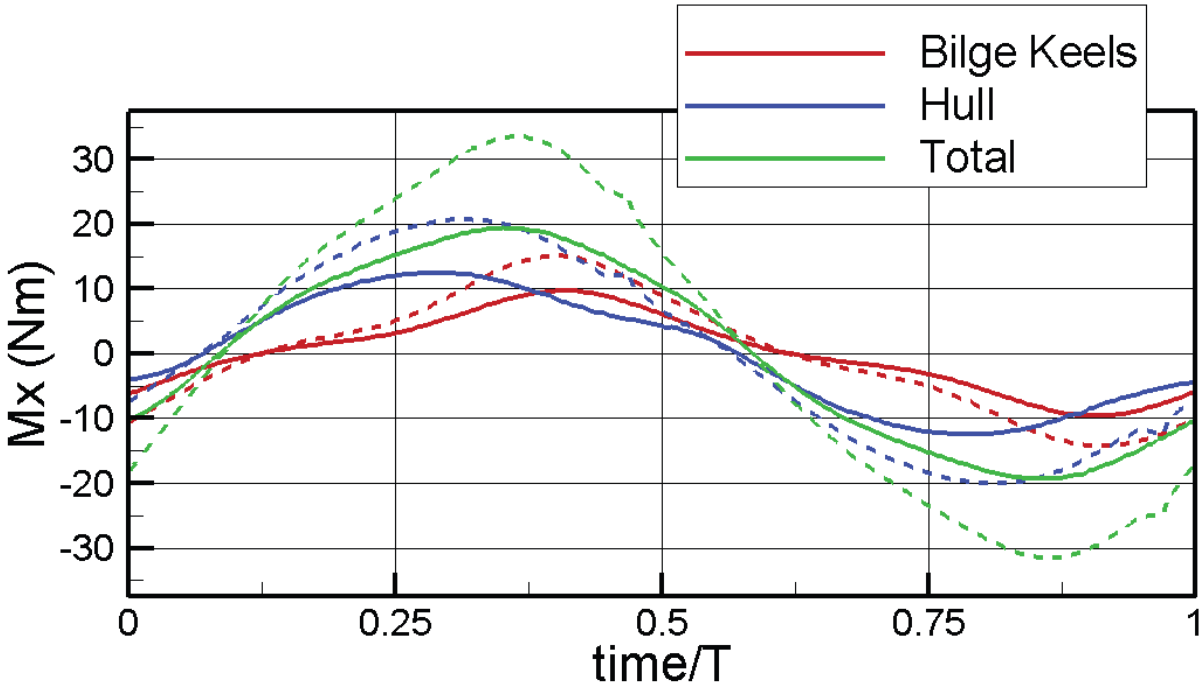

Figure 5-8. DTMB Model #5613-1 (hull with skeg and bilge keels), computed roll moment due to piezometric pressure for Fr = 0.0, φ = 15 deg, ω = 3.81 rad/s (solid) and ω = 4.83 rad/s (dashed) (from Miller, et al. 2008)

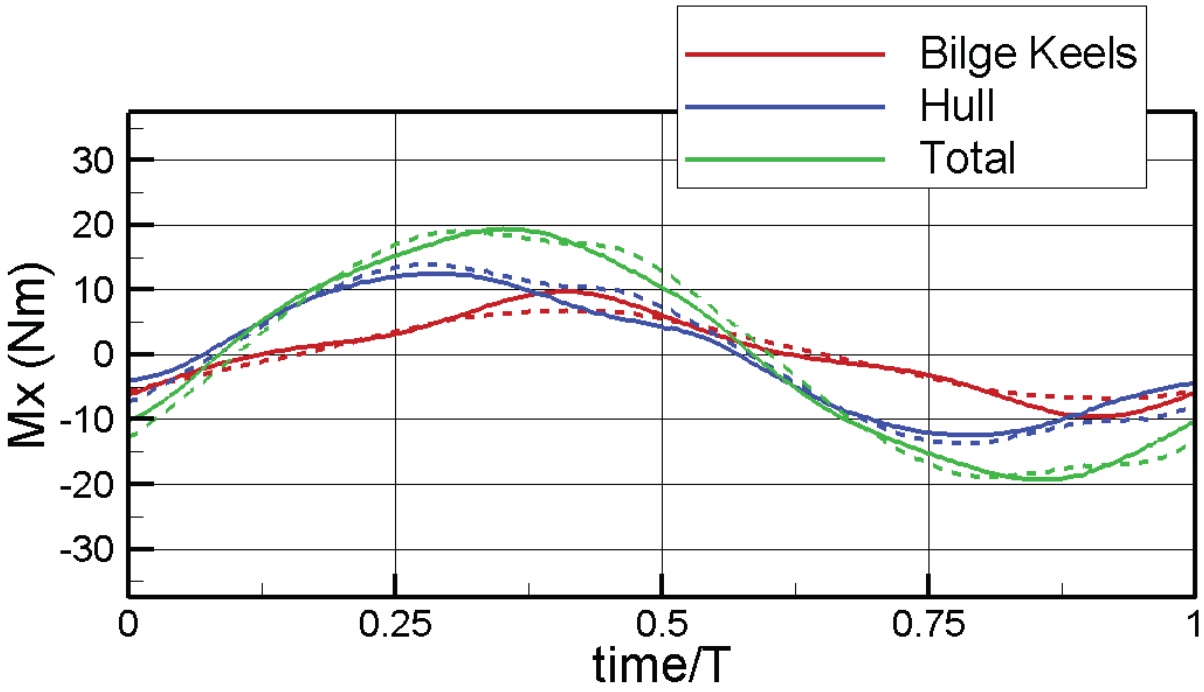

Figure 5-9. DTMB Model #5613-1 (hull with skeg and bilge keels), computed roll moment moment due to piezometric pressure for ω = 3.81, φ = 15 deg, Fr = 0.0 (solid) and Fr = 0.30 (dashed) (from Miller, et al. 2008)

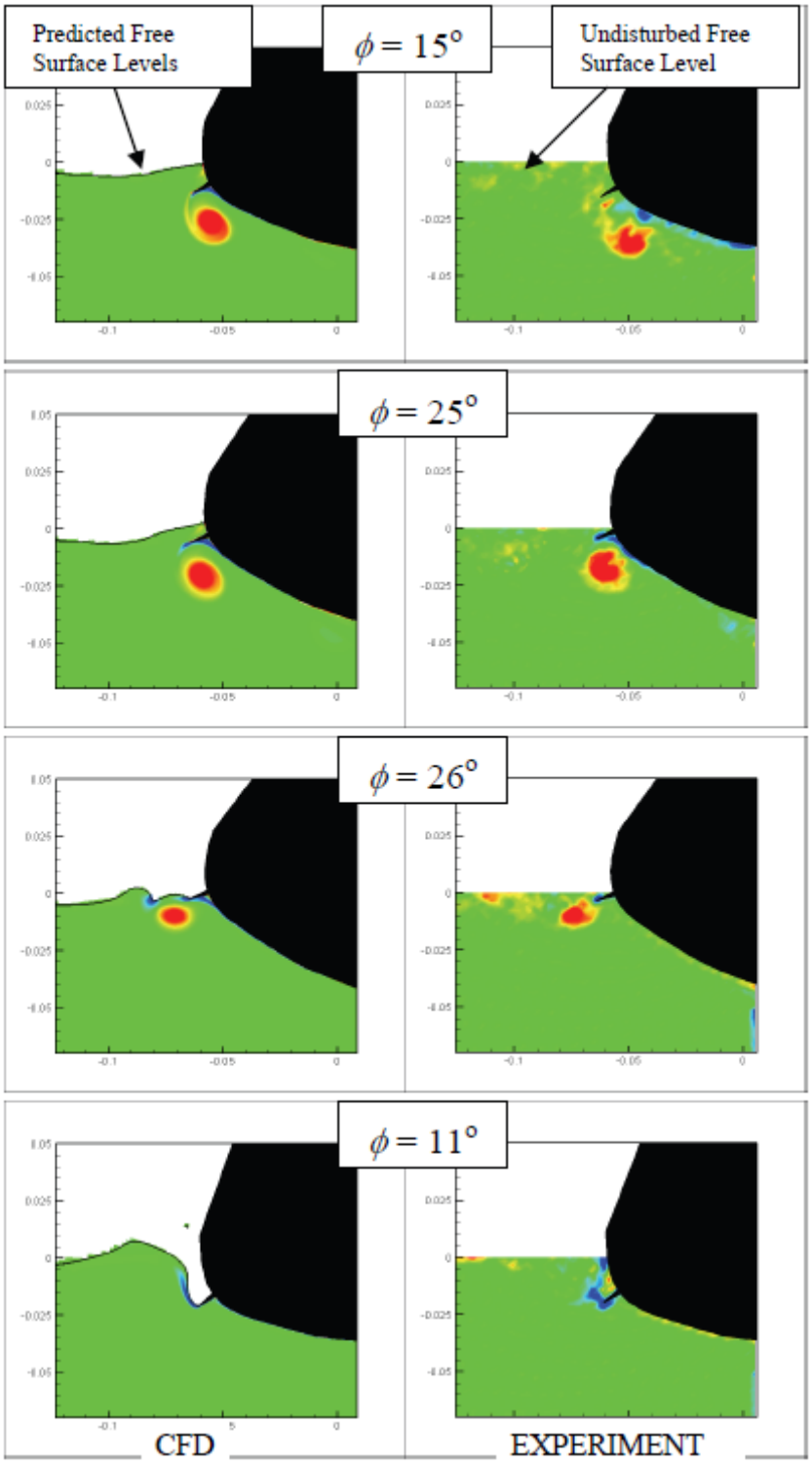

Figure 5-10. DTMB Model #5613-1 vorticity at the midship section for Fr = 0.30, φ = 30 deg and ω= 4.83 rad/s (from Miller, et al. 2008)

Chapter 6 On the Development of Hydrodynamic Component Models Applicable to Large Amplitude Ship Roll Motion[15]

6.1 Overview

The experimental and numerical results presented and discussed in Chapters 3, 4, and 5 provide measurements and observations of physical phenomena which occur during large amplitude roll motion. The resulting effect of these physical processes on the hydrodynamic components, added inertia and damping, of the total hydrodynamic roll moment and bilge keel force, were also examined (Appendix D). Based on this analysis, this chapter explores several possible approaches for theoretical models of the hydrodynamic components in ship motions, which consider large amplitude effects.

6.2 Prioritization of Effects to Include in a Time-Domain Model of Large Amplitude Ship Motion

The first consideration is to determine the relative importance of the physical effects observed for large amplitude roll motion from the experimental and numerical results, so that the effects which have the greatest influence on the hydrodynamic components can be considered. Because the objective of this study is to consider large amplitude ship motions, by definition, frequency-domain approaches cannot be directly applied. Historically, the progression from a frequency-domain to a time-domain model is achieved using kernel functions to model the "memory" effects and determine a time-domain response with considerations of the physical effects typically modeled in the frequency-domain. However, this formulation is still limited to the prediction of small amplitude ship motions, given the limitations of the theoretical foundation.

The historical approach was to use a kernel formulation, which emphasizes the influence of memory effects on the ship motion response. Therefore, the relative influence of memory effects and amplitude effects must be examined, in order to continue with the development of a model for large amplitude ship roll motions. The experimental results presented in Chapter 4 provide a data set to examine this relative importance and prioritize the memory and amplitude effects for the development of a time-domain model.

The impulse response function (6.1) is a fundamental background component of linear systems theory. This formulation enables direct correlation between an output, $y(t)$, and an input, $x(t)$, and is proportional by an impulse response, or kernel function, $h(t)$. The resulting transformation from input to output, using the impulse response, is the convolution integral.

$$y(t) = \int_{-\infty}^{\infty} h(\tau)x(t-\tau)d\tau = \int_{-\infty}^{\infty} h(t-\tau)x(\tau)d\tau \tag{6.1}$$

where $h(t) = 0$, for $t < 0$.

The inclusion of the kernel function enables consideration of "memory" effects, or the effects of the previous response within the linear system, for a duration before a given instant in

[15] Portions of this chapter have been published previously in Bassler, et al. (2010)

time, on the current response at a given instant in time. Several assumptions are inherent with the convolution integral formulation. These include that the system is stable and linear and that the input, output, and kernel functions are real-valued, defined for $-\infty < t < \infty$, and piecewise continuous (Rugh, 1981).

The convolution integral is commonly used in many engineering applications, including linear ship seakeeping theory (Cummins, 1962; Ogilvie, 1964). The impulse response function is used to provide a method for solving the equations of ship motion in the time-domain. This formulation can be used to model the response of a ship to random external excitations without using frequency dependent parameters. This approach assumes a linear system, which typically limits its application to small to moderate amplitude oscillations.

Cummins (1962) proposed the use of the impulse response function for modeling the ship equations of motion as a method for overcoming the limitations of the mathematical model of using a system of second order ordinary differential equations (ODEs) with frequency dependent coefficients.

While roll is also coupled with other degrees-of-freedom, roll is the mode of motion most dominated by viscous effects. Because of the influence of viscosity, roll damping in particular is significant and must accurately capture these effects to model the roll motion behavior of the ship in waves. Coupling of damping terms exists between roll and other modes of motion. However, to determine roll damping, a single degree-of-freedom model is considered initially and then appropriate modifications made to account for other modes of motions.

Following the formulation of Ogilvie (1964) and Takagi, et al. (1984), the following equation is used to describe single degree-of-freedom ship roll motion in the time-domain.

$$\left(I_{44} + A_{44}(\infty)\right)\ddot{\phi} + B_{44}(\infty)\dot{\phi} + \int_{\infty}^{t} K(t-\tau)\dot{\phi}(\tau)d\tau + B_{44q}(\omega)\dot{\phi}\left|\dot{\phi}\right| + \Delta\left(C_0 + C_1\phi + C_3\phi^3 + ...\right) = F(\tau) \tag{6.2}$$

where a polynomial formulation for stiffness, C, is given and the kernel function, $K(\tau)$, is given by

$$\begin{aligned} K(\tau) &= -\frac{2}{\pi}\int_0^{\infty} \omega\left(A_{44}(\omega) - A_{44}(\infty)\right)\sin(\omega\tau)d\omega \\ &= \frac{2}{\pi}\int_0^{\infty} \left(B_{44}(\omega) - B_{44}(\infty)\right)\cos(\omega\tau)d\omega \end{aligned} \tag{6.3}$$

For ship roll motion applications, as shown in (6.3), the kernel function, $K(\tau)$, is a result of the convolution integration of the roll frequency, ω, and the added inertia, A_{44}, or damping, B_{44}, as the damping is 90 degrees out of phase of the added inertia. Physically, the kernel function for roll motion represents the "memory" associated with the hydrodynamic components and the ship motion response. Thus, the kernel function provides a means to consider the influence of physical effects which occurred as a previous time, such as energy dissipation through ship radiated waves, on the current ship motion response. An example roll motion kernel function computed for a fishing vessel (Tigkas, 2007) is given in Figure 6-1.

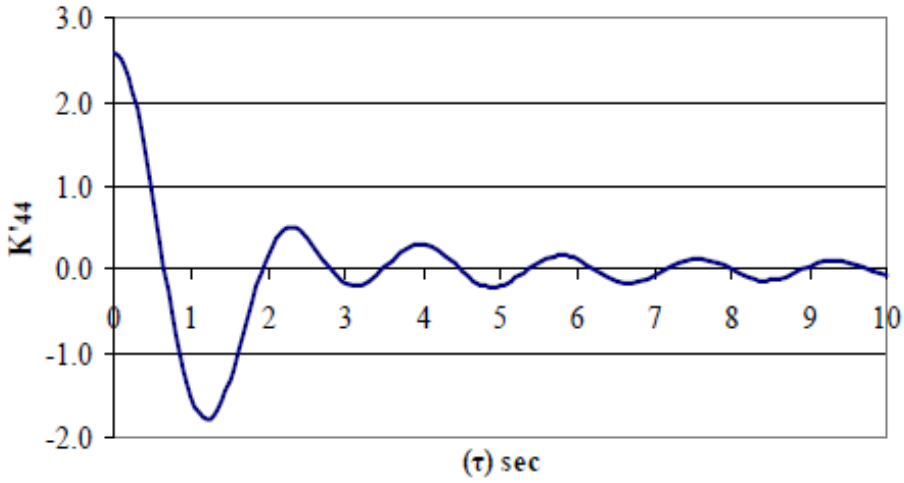

Figure 6-1. Example of a roll motion kernel function, computed for a fishing vessel (from Tigkas, 2007)

The kernel function is also known as the memory function, because it models the dependency of the hydrodynamic roll moment on the cumulative history of the roll velocity (Jiang, et al., 2000). However, using this formulation even for only computing roll damping due to the wave-making, or radiation, is difficult (Themelis 2008). And computing the kernel function is particularly difficult for large amplitude motions (Belknap, et al., 2010).

The memory effects, as represented by the kernel function, are also only considered for the linear damping term. This is due to the practical difficulties associated with specifying nonlinear kernel functions (Rugh, 1981; Dalzell, 1984; Falzarano, et al., 2000; O'Dea, 2001). A polynomial approximation for the nonlinear ship stiffness, the actual instantaneous GZ curve is used to provide accurate predictions of ship roll motions.

As shown in (2.12), the total ship roll damping, B_e, is decomposed into a linear combination of physical components, each as a function of roll amplitude, roll frequency, and forward speed (Ikeda, et al., 1978e; Himeno, 1981). The components include empirically-based formulations for friction, B_F; eddy, B_E; and wave-making B_W, hull lift, B_L; bilge keel normal force, B_{BKN}; and bilge keel-hull interaction B_{BKH}). The bilge keel wave-making component, B_{BKW}, is typically neglected.

The initial formulation presented in this section is an attempt to convert the physical components of roll damping, as expressed in the frequency-domain, into a time-domain formulation for roll damping to enable improved understanding of large amplitude roll motions. However, the mathematical basis for doing so is based on linear theory assumptions, which are not applicable for modeling large amplitude ship roll motions.

Nonlinear components of roll damping are considered in the time-domain formulation. However, this was not directly considered in this investigation, because of the emphasis on trying to incorporate the physical basis for roll damping into a practical time-domain model. The nonlinear model for roll damping in the time-domain (discussed in Chapter 2), is based on a combination of linear and quadratic plus cubic terms. However, the cubic term has no physical basis, and is used as a "corrector" to the linear and quadratic damping terms. Practical

determination of the kernel functions for the nonlinear terms is problematic. This involves convolution of 2nd and 3rd order terms, and although it is analytically possible to construct a formulation using these higher-order kernel functions, it is difficult to appropriately determine them with any physical basis for ship motions modeling (Rugh, 1981; Dalzell, 1984; Falzarano, et al., 2000; O'Dea, 2001).

The specification of the kernel functions for each individual damping component is also problematic. While some components, such as wave-making and eddy-making have a clear physical interpretation, other components are more difficult to associate with physical processes. For example, the "memory" effect due to frictional or bilge keel hull interaction damping does not have a clear physical interpretation, or the ability to determine these kernel functions.

The physical "memory" of each term must be truncated at some practical duration, at some time before ∞, to enable time-domain numerical calculations. This truncation specifies how fast the kernel decays, or the effective "length/duration" of the memory effects that are considered in the roll motion behavior. For typical implementations of the kernel function for wave-making, or radiation damping component, full-scale memory durations on the order of ~60-100 seconds are used. However, this may vary due to considerations for hull-geometry, wave conditions, required accuracy of the solution, and the associated computational cost.

All of the frequency components can be considered when converting to a time-domain solution. However, because the excitation of the ship in roll is effectively a narrow-banded process, only a small subset of frequencies, relative to ∞, will actually generate ship roll motion response. Therefore, the computational costs associated with the Fourier transform are significant. Given the variability of the ship's encounter frequency, due to varying instantaneous ship speed in waves and varied wave frequencies in an irregular wave-field, then the appropriate range of frequencies to be considered are difficult to determine *a priori*, and may vary significantly. As discussed in Themelis (2008), alternative approaches have been proposed to address the difficulties associated with computing the radiation memory kernel function (e.g. Jeffreys, 1984; McCreight, 1986; Holappa & Falzarano, 1999). Essentially, these kernel functions filter the added inertia and damping based on the frequencies of the computed forces and moments. While this reduces the computational time associated with the kernel function, this may still be computationally difficult. And this technique has not been previously applied with any consideration for the viscous damping terms, only for the radiation problem.

6.2.1 Frequency Dependence of Damping

Because the experimental data of the measured total hydrodynamic roll moment, for large amplitude roll motion, was limited to several roll frequencies, the behavior of damping across a wider range of roll frequencies must be considered, in order to develop a kernel function. To supplement the experimental measurements, which were decomposed to determine damping, experimental and predicted results presented in Ikeda, et al. (1978e), Himeno (1981), and Bassler & Reed (2009) regarding the frequency dependence of roll damping components are considered. For the experimental and predicted results shown in Figure 6-2 and Figure 6-4, the non-dimensional roll frequency is given by $\hat{\omega} = \omega\sqrt{B/2g}$.

Figure 6-2 shows experimentally obtained damping results (dots), compared to predicted damping (lines) using Ikeda's method (Ikeda, et al., 1978e). Figure 6-2 shows the total damping,

as estimated by Ikeda (Ikeda, et al, 1978), to nonlinearly increase with increasing frequency. The friction and eddy-making components of damping are predicted to increase linearly with increasing frequency; the wave-making damping component increases nonlinearly, with a peak observed near $\hat{\omega} = 1.0$. Each of the three components which have frequency dependence, friction, eddy-making, and wave-making, are estimated to contribute approximately equally in magnitude to the total damping.

The dimensional range of frequencies shown in Figure 6-2 is ω=0 to 8.67 rad/s, given the principal particulars of DTMB Model #5699. For these frequency conditions, with the Series 60 hull form, C_B=0.70, the damping is not observed to decrease at higher-frequencies, although a near peak condition is observed for the highest frequency condition. This is because the wall-sided configuration of the ONR Topside Series hull form has a greater natural roll period than the flared or tumblehome topside configurations, which means that the peak of damping for frequency was not observed within the range of frequencies considered by Ikeda in his formulation. As observed from the WAMIT simulation results in Chapter 5 (Figure 5-3-Figure 5-6, and in Appendix E), the peak of the damping occurs near 5.5 rad/s, which is equal to $\hat{\omega} = 0.95$ on Ikeda's plots shown in Figure 6-2.

Himeno (1981) builds upon the findings of Ikeda, et al., to indicate that generally, the damping components due to lift, bilge keel hull interaction, and bilge keel normal force do not vary substantially with frequency. This is also shown in the predicted results presented in Bassler & Reed (2009), Figure 6-3. However, the eddy-making and friction components vary linearly with frequency, while the wave-making and bilge keel wave-making components vary nonlinearly with frequency, including a peak in damping before $\hat{\omega} = 1.0$. Additionally, Ikeda, et al. show that the amplitude effects with the bilge keels are more significant than for the same amplitude conditions without the bilge keels (Figure 6-4). Additional details regarding the influence of frequency effects on damping are discussed in Chapter 4 and Appendix D, using the results from the experimental measurements.

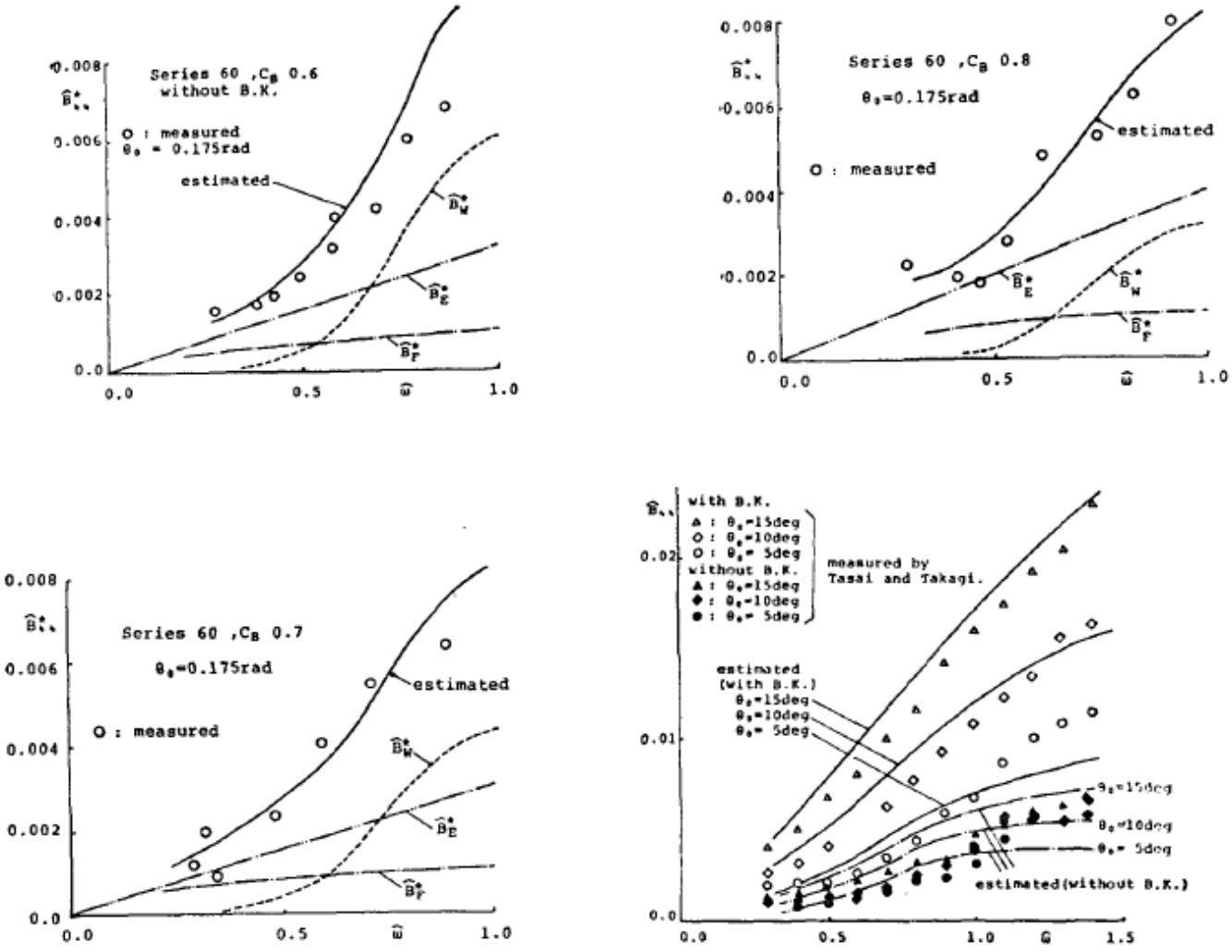

Figure 6-2. Components of the roll damping coefficient vs roll frequency for a ship hull (at zero speed); from Ikeda, et al. (1978). Damping for Series 60, C_B=0.70, without (top left) and with (top right) bilge keels, as well as with bilge keels (bottom right) for increased C_B. Bottom right shows comparisons of damping, with and without bilge keels, for varied roll amplitudes.

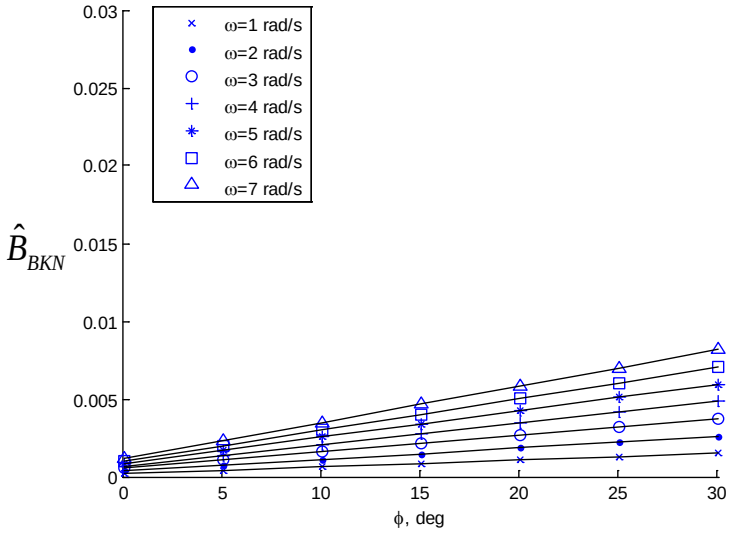

Figure 6-3. Bilge keel normal force damping vs roll amplitude, with varied roll frequencies shown, calculated using Ikeda's method for Series 60, C_B=0.60, at zero speed; from Bassler & Reed (2009)

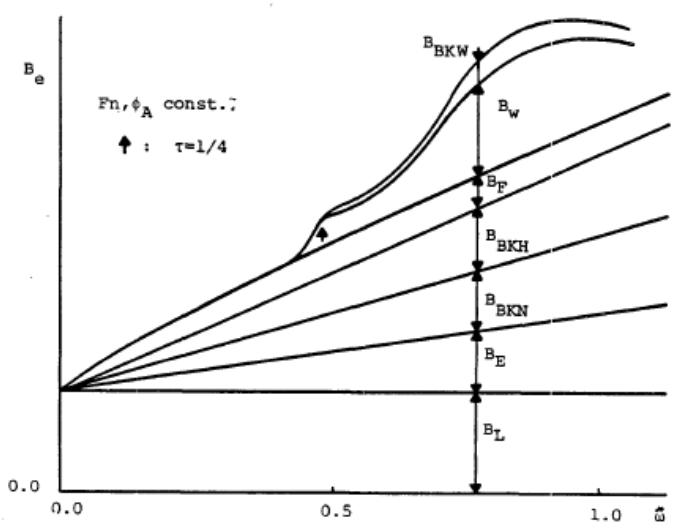

Figure 6-4. Equivalent linear roll damping coefficient vs roll frequency, with contributions shown from various damping components, B_L, B_E, B_{BKN}, B_{BKH}, B_F, B_W, B_{BKW}; from Himeno (1981)

6.2.2 Development of a Kernel Function Using the Experimental Data

The experimental data of the measured total hydrodynamic roll moment, presented in Chapter 4, was used to develop kernel functions. The measured hydrodynamic roll moment for both the total hull and for the bilge keel is decomposed into added inertia and damping (Appendix D). The experiment, presented in Chapter 4, only measured a limited range of frequencies for forced roll oscillation. In order to develop a kernel function, the damping was modeled using the measured experimental results at those frequencies, with interpolation

between zero and the intermediate frequencies and between the intermediate frequencies and infinite frequencies. The intermediate frequencies are specified, based on the results of WAMIT calculations, presented in Chapter 5, and previous predictions of damping by Ikeda (Figure 6-4). Understanding that damping at zero frequency and infinite frequency will be zero and using the experimentally obtained damping, a linear fit was applied to the available data to obtain damping coefficients, as a function of frequency, for use to then obtain corresponding kernel functions.

Damping, obtained from the experimental measurements, are shown for 15 deg (Figure 6-5) and 35 deg roll amplitudes (Figure 6-6). Because the damping uses the experimentally measured values, it can be observed that the damping for the 35 deg forced oscillation amplitude condition is less than for the 15 deg forced oscillation amplitude condition.

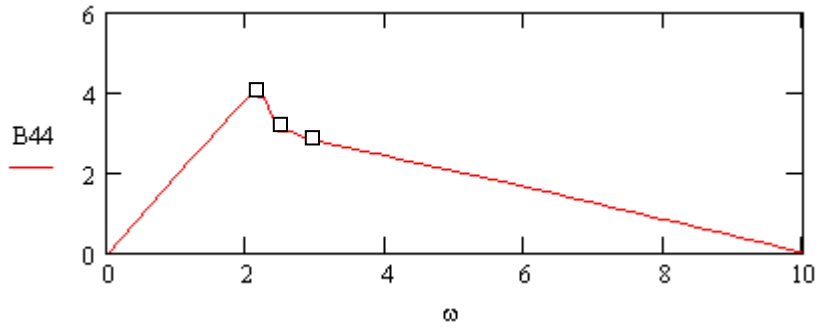

Figure 6-5. Damping coefficient as a function of frequency (rad/s), using the experimental results for φ_A= 15 deg, for the 2D ONRTH, as well as extrapolated values beyond the frequency regime from the experiment.

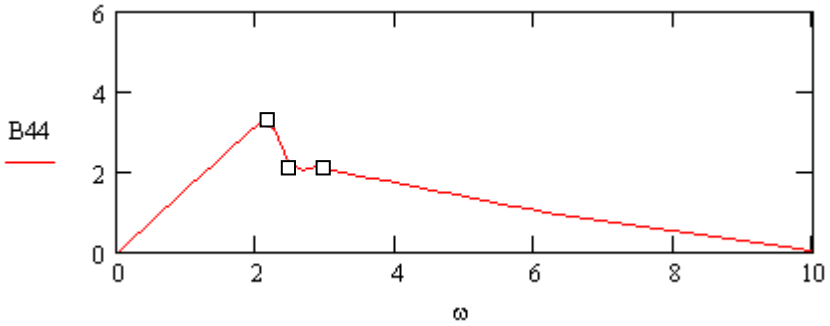

Figure 6-6. Damping coefficient as a function of frequency (rad/s), using the experimental results for φ_A = 35 deg, for the 2D ONRTH, as well as extrapolated values beyond the frequency regime from the experiment.

The frequency dependent damping distribution, which used the experimentally measured damping as a basis and where the infinite frequency damping is zero, was used to determine a kernel function. An example of a computed kernel function is shown in Figure 6-7 and Figure 6-8. Although not a perfect kernel function (as would be determined numerically using computed added inertia or damping), the resulting function obtained from the experimental results can be used to examine the relative influence of the memory effect of the resulting ship motions, and compared to constant damping. This enables a comparison between the relative significance of the memory and amplitude effects, using the 2D experiment as a basis. Representative predicted kernel functions, derived using the experimentally obtained damping results, are shown for 15 deg (Figure 6-7) and 35 deg forced oscillation amplitudes (Figure 6-8). As shown from the two

figures, the effect of amplitude on the kernel functions can be observed. At short time durations (less than two seconds), fluctuations in the kernel can be observed. These are more significant for the small amplitude condition (φ_A=15 deg) than for the large amplitude condition (φ_A=35 deg). The magnitude of the kernel near t=0 is also much larger for the small roll amplitude condition than for the large roll amplitude condition. Both of these kernel functions, for the smaller and larger roll amplitude conditions, show that the memory effect of damping, as determined from the experimental results, remains relatively short in duration. The results are shown at model scale, and beyond 5 seconds (near 30 seconds full-scale), the kernel function has decayed and the memory effect is no longer significant.

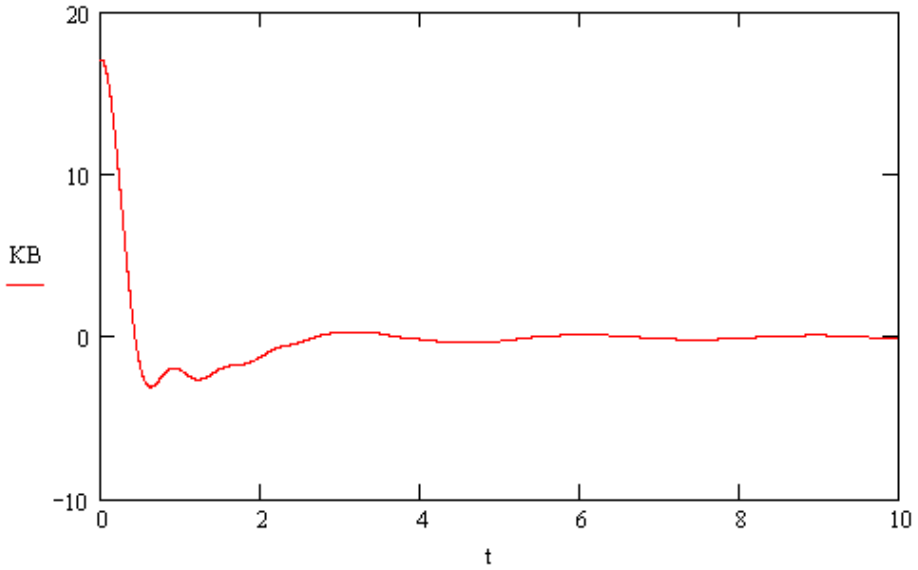

Figure 6-7. Representative kernel function vs time (s), computed using damping, based on experimental measurements for φ_A = 15 deg, for the 2D ONRTH

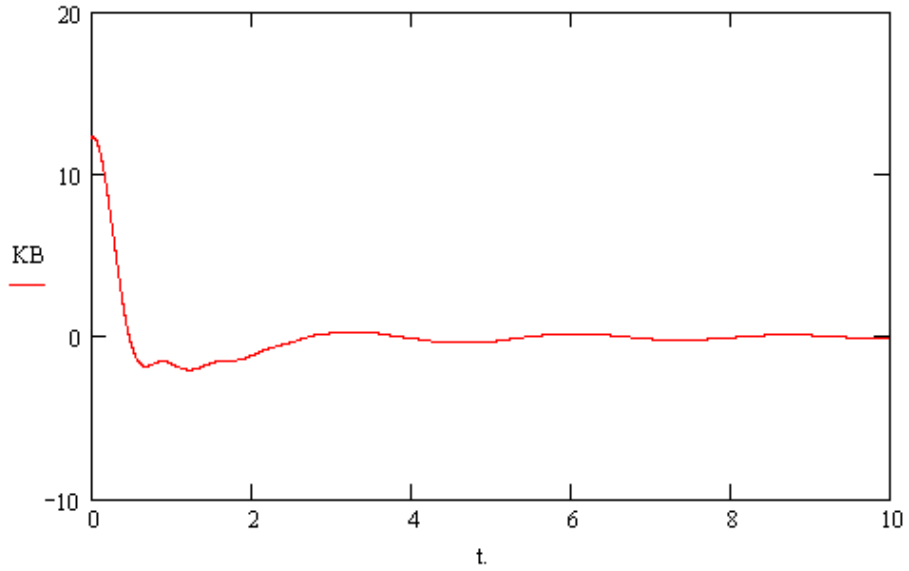

Figure 6-8. Representative kernel function vs time (sec), computed using damping, based on experimental measurements for φ_A = 35 deg, for the 2D ONRTH

6.2.3 Comparison of Effect of Kernel Function Damping and Constant Damping Formulations on the Roll Motion Response of a 1DoF System in Irregular Waves

This section describes an examination of the influence of the "memory effect", as represented by the kernel function damping, on the resulting roll motion response and compared to roll motion response using a constant damping formulation.

Three 300 second realizations were computed, using either constant damping (based on the mean of experimentally measured values, for a given amplitude) or kernel function damping. The roll response was calculated using a Runge-Kutta formulation. Nonlinear stiffness based on the GZ curve for the 2D ONRTH model was included in the computation of the roll response (Figure 6-9). Initial conditions of 0 deg amplitude and 0 deg/s roll velocity were used for all realizations. The wave conditions specified for these realizations were representative of heavy weather conditions (full-scale equivalent of Hs=8.0m and Tm= 16.97 seconds). A sample realization of the roll motion response in these wave conditions is shown in Figure 6-10.

The estimate of the standard deviation of roll motion response and the associated 95% confidence interval were computed for the ensemble average estimate of the realizations. A comparison of the resulting predicted roll motion response for the 2D ONRTH using the constant damping formulation and the kernel damping formulation is shown in Figure 6-11.

For small roll amplitudes, a difference is observed between the two damping formulations. However, beginning at 25 degree forced oscillation amplitude, the variance in the predicted roll motion response results, due to the roll motion in irregular waves, is larger than the difference between the predicted results with the constant damping or kernel damping formulations. For the 45 deg forced oscillation amplitude, a substantial difference exists between the two formulations. However, for this amplitude condition for the 2D ONRTH, the deck edge interacts with the free surface, as well as the bilge keels, which is reflected in the experimental results which are used for the kernel damping formulation, but is not reflected in the constant damping formulation, which was based on the mean of the experimentally measured values.

The difference between the two estimates of the standard deviation can be judged approximately by the overlap of the confidence intervals. For conditions where the confidence intervals overlap substantially, there is a finite probability that the differences between the estimates of the standard deviation is random, therefore, the predicted results for ship roll motion response are statistically the same.

Using the roll motion response data from 1DoF system with irregular wave excitation, estimates of the standard deviation and the variance were obtained. The estimate of the standard deviation, δ^*, variance, $V^* \pm \Delta V^*$, and average roll angle, m_x^*, were determined using the standard formulas, where N is the number of data points available for a particular realization. The estimates of the standard deviation were applied to the roll motion response data, as shown in Figure 6-11, to quantify the statistical uncertainty associated with the simulated roll motion results.

$$\delta^* = \sqrt{V^*}$$
$$V^* = \frac{1}{N-1}\sum_{i=1}^{N}(\phi_i - m_x^*)^2$$
$$\Delta V^* = 1.95\sqrt{V(V^*)} \qquad (6.4)$$
$$m_x^* = \frac{1}{N}\sum_{i=1}^{N}\phi_i$$

As shown in Figure 6-11, above 30 degree roll amplitude, the predicted roll motion response results, using either a kernel damping formulation or a constant damping formulation, are effectively the same. Even for the conditions where the statistics show a substantial difference, where there is no overlap between the confidence intervals, the influence of amplitude is clearly much stronger. This can be observed from the predicted roll motion response results of the 5-30 degree roll amplitudes. For the 5 and 15 degree roll amplitudes, the largest amplitudes considered in typical formulation of roll motions, based on the simplifying assumptions (as discussed in Chapter 2), the effect of frequency is clearly important and should be considered along with amplitude. However, across a larger range of amplitudes, amplitude clearly has a more substantial influence on the damping than frequency.

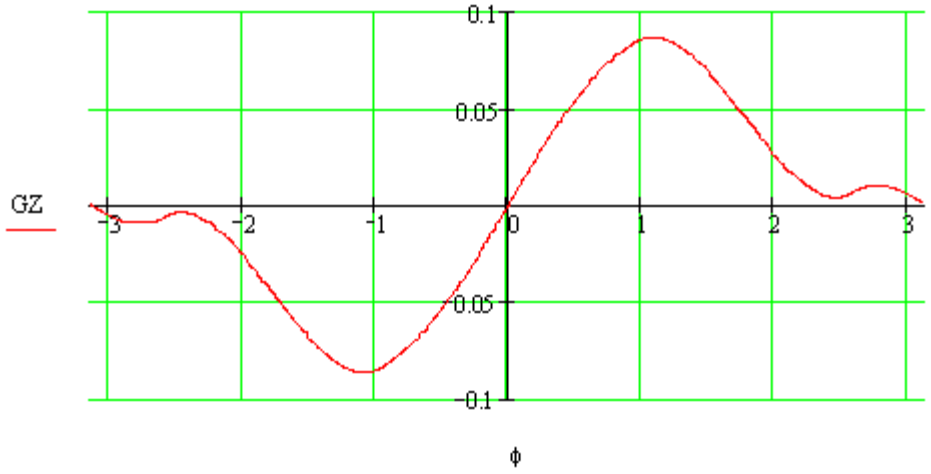

Figure 6-9. GZ Curve (m) of the 2D ONRTH, φ in rad.

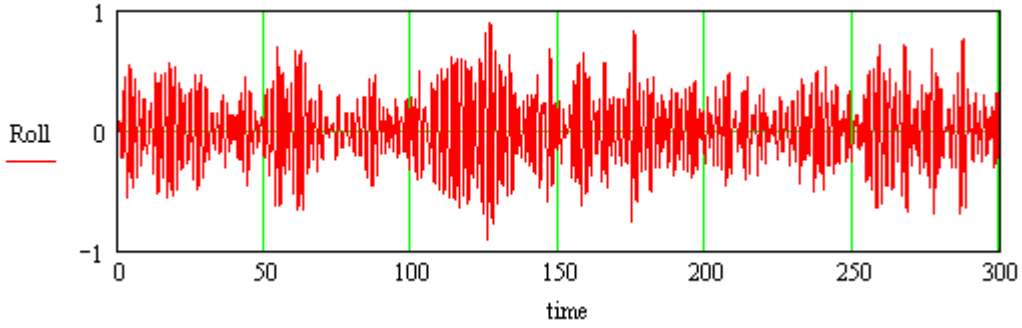

Figure 6-10. Sample realization of roll motion response (in rad), using kernel damping based on experimental measurements for φ_A = 35 deg, for the 2D ONRTH

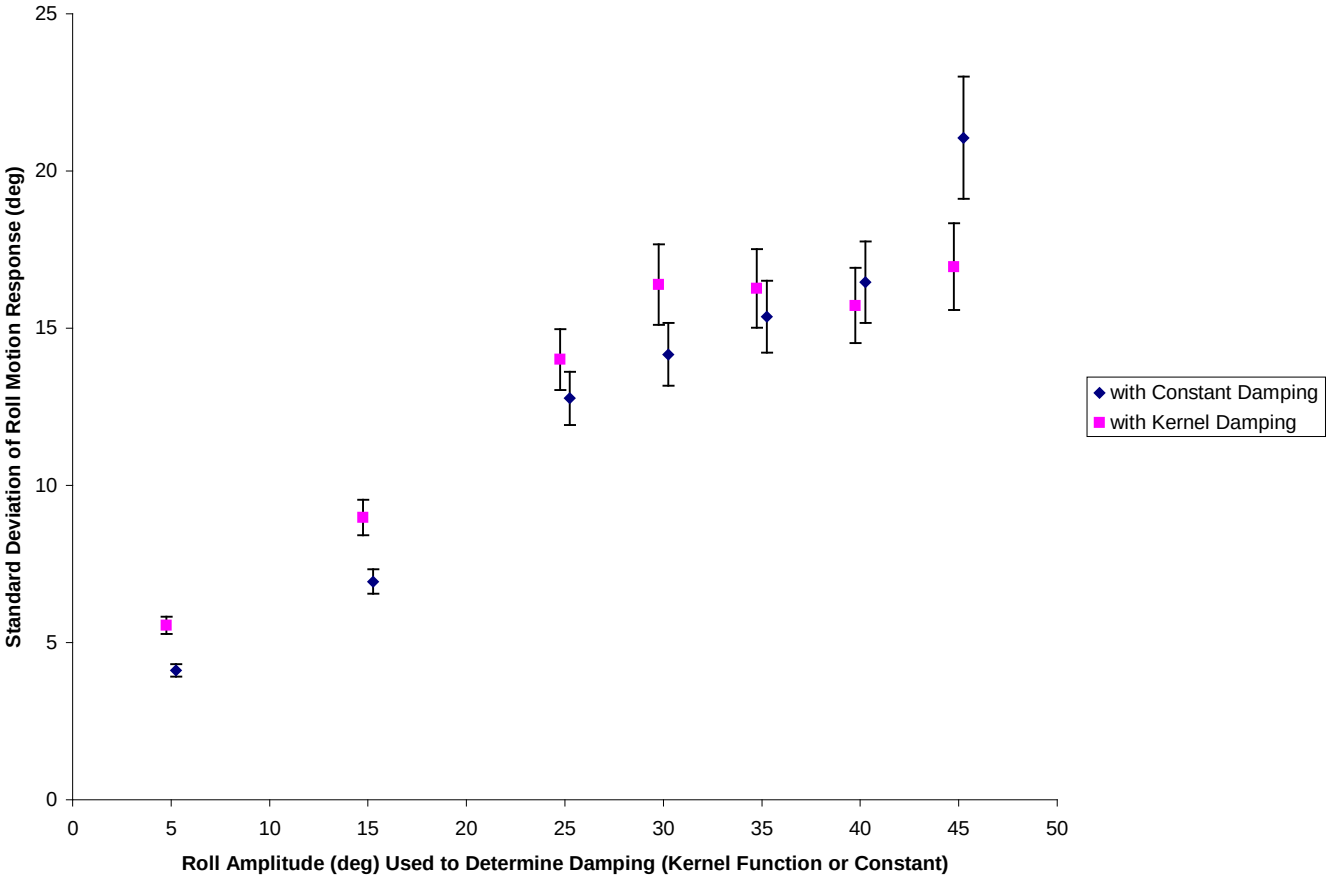

Figure 6-11. Comparison of standard deviation of roll motion response, with corresponding variance shown, for an ensemble average of three 1DoF roll motion realizations using constant damping or a kernel formulation for damping of the 2D ONRTH

6.2.4 The Development of Large Amplitude Ship Roll Motion Models Considering the Relative Importance of Memory and Amplitude Effects

Data from the large amplitude roll motion experiment, presented in Chapter 4, were used to examine the relative importance of memory and amplitude effects for large amplitude roll motion. As observed, at large amplitudes, the effects of amplitude are dominant and the effects of memory are small. At small amplitudes, the amplitude regime where previous models for ship roll motion has been developed, the effects of memory are significant. However, at increased amplitudes, where physical effects occur due to the significant changes of the interaction between the body geometry and the free surface, the amplitude effects are much more dominant than the memory effects. Therefore, the amplitude effects must be considered as 1st-order effects in the development of time-domain models which are applicable to large amplitude roll motion, while memory effects are considered as 2nd-order effects and be added to the models, to further increase their applicability. With these considerations, several formulations for modeling hydrodynamic components for large amplitude ship roll motion are presented in subsequent sections of this chapter.

6.2.5 On the Development of Models for Large Amplitude Ship Roll Motion

The effects of memory were examined in the previous section. However, the effect of amplitude was observed to be more significant on the resulting ship motions behavior for large amplitude roll motion. To consider the dependence on roll amplitude, two general model formulation possibilities are examined: a piecewise model and a bilge keel force model. Both approaches are focused on time-domain model applications for large amplitude ship roll motion. Because the emphasis of this work is on the extension and improvement of ship roll motion prediction for large amplitude motions, specifically the hydrodynamic components, the nonlinearities associated with roll motion must be considered.

As discussed in Chapter 2, current time-domain formulations are based on coefficients specified from regression-based approaches. This chapter examines the possibility of converting a frequency-domain model, where physical components of damping are individually specified, into a time-domain model. This is a logical first step to examine the feasibility of developing a model for roll damping that is applicable to large amplitude roll motions, but that retains physical interpretation of the processes which occur. Based on the assessment of the feasibility of the time-domain model, two additional approaches are also discussed, including a piecewise model and a bilge keel force model.

The a piecewise model considers the dominant physical effects of abrupt physical changes, such as bilge keel or deck edge interaction with the free surface, which influence the ship motion response. A piecewise model is a simple formulation, which characterizes these abrupt changes for large amplitude ship motions.

The second formulation, considers the specific behavior of the bilge keel and its interaction with the free surface during large amplitude roll motion. Given that the bilge keels typically have the most significant influence on damping, and as shown in Chapter 4, a non-trivial influence on the added inertia, then the interaction effects between the bilge keel and the free surface will significantly improve the applicability of a ship motions model to large amplitude motions. For moderate amplitude ship motions, the first model provided under this formulation considers the interaction of the bilge keels with the free surface while still submerged. In this amplitude regime, the bilge keel contributes to wave-making, which is not considered in small amplitude models of ship motions. The next series of four models provided under this formulation consider bilge keel transitions with the free surface, in progressively more complex and more realistic formulations. These include the differences in behavior for bilge keel emergence vs immergence, such as hysteresis effects, due to asymmetric interactions between the bilge keel and the free surface.

6.3 Development of a Piecewise Model

To address the limitations of, and expand the range of applicability of, existing models for roll damping to larger amplitude roll motions, the coefficients for damping should be developed considering the physical phenomena occurring during large amplitude roll motion. For large amplitude roll motions, dramatic changes in damping occur and can be observed based on physical events, for example bilge keel emersion and deck edge immersion. Thus initially, a clear dependence can be assumed between roll damping and roll angle, which has not traditionally been considered.

A method is proposed to model large amplitude ship roll damping that considers the specific physical phenomena which occur during large amplitude roll motion, identified in Chapters 4 and 5. The method is based on distinct ship-specific physical phenomena, such as bilge keel interaction with the free-surface, emergence and deck immergence. Abrupt physical changes to the wetted geometry of the hull form occur with large amplitude roll motion, resulting in significant changes in hydrodynamic components. To model these changes, a piecewise method is proposed to consider the nonlinearities of the dynamical system. Practical implementation of the proposed method is also discussed.

Inclusion of large amplitude in an expanded coefficient-based model for total ship roll damping can enable commonly used potential flow numerical tools (see Beck & Reed, 2001) to be used for the assessment of ship roll motion behavior, while expanding their applicability to problems of larger amplitude roll motion. Depending on the intended application, the accuracy using the modified coefficient-based approach presented in this chapter may not be sufficient, and a more robust, physics-based bilge keel component force model may be necessary.

6.3.1 Physical Phenomena

As identified from the experimental and numerical results in Chapters 4 and 5, when a ship experiences large amplitude roll motion, additional physical phenomena occur which are not considered in traditional roll damping models. These include bilge keel interaction with the free surface, where water shipping occurs during bilge keel emergence, impact loading occurs upon bilge keel re-entry, and air bubble entrainment occurs under the bilge keel after re-entry. The exact conditions for these physical phenomena are ship-specific.

The individual physical phenomena that occur for large amplitude roll motion are highly nonlinear. However, the primary consideration of these events for ship roll motion prediction is their effect on the significant changes in the dynamical properties of the system. For example, it may not be necessary to explicitly model the localized nonlinear occurrence of bubble dynamics generated by the bilge keel upon re-entry after a large roll event. The effects of air bubble entrainment may also not be significant for full-scale behavior of a ship experiencing large roll motion. However, to enable modeling in fast numerical simulation codes of the events which do result in significant dynamical changes, simplifying assumptions must be made. The primary assumption for an initial model is that the effects of these nonlinearities can be attributed to the non-smooth transition at the boundary of the fluid domains, as a function of the changing wetted geometry.

6.3.2 A Piecewise Method

Any method to model large amplitude ship roll motions should be compatible and consistent of with existing ship roll damping models, such that the model can accurately predict ship motions both at small and large amplitude. This will enable accurate predictions of roll damping for small to moderate amplitude roll motion, while also enabling application to large amplitude roll motion behavior. This balance of expanded prediction capability for large amplitude roll motion, while maintaining accurate prediction capability for small to moderate amplitude roll motion, is the objective of the theory presented in this chapter. An overview of the method, the mathematical foundation used to develop the method, details of the formulation and verification of the method, and some examination of the properties exhibited by a dynamical system with piecewise damping are discussed in this section.

6.3.2.1 Method Overview

The procedure for predicting large amplitude roll damping is based on the modeling the abrupt physical changes in the dynamical system, which correspond to events such as bilge keel emergence or deck submergence. For large amplitude roll motion, an explicit dependence exists between roll damping and roll angle. Distinct ship-specific physical regions are identified, which are dependent on the ship-specific geometry, which correspond to where a significant change in damping of the system occurs.

The roll angle can be used as a boundary to create a division of physical regions corresponding to abrupt physical changes associated with transition between the fluid domain boundaries (water and air interface). An example, modeling the effect of bilge keel emergence and immergence on damping, is presented.

In Figure 6-12, α is the roll angle between the bilge keel and free surface and β is the roll angle between the deck edge and the free surface. Based on the experimental observations, it is assumed damping will decrease with the emergence of the bilge keel and increase with the immersion of the deck edge. A reduction in damping occurs from the loss of one bilge keel acting in the viscous fluid, while the other remains fully submerged. The subsequent increase in damping with the immergence of the deck edge is due to the presence of a sharp corner in the viscous fluid, enabling the formation and shedding of vortices, resulting in additional energy dissipation, although not as significant as the shedding from the bilge keel.

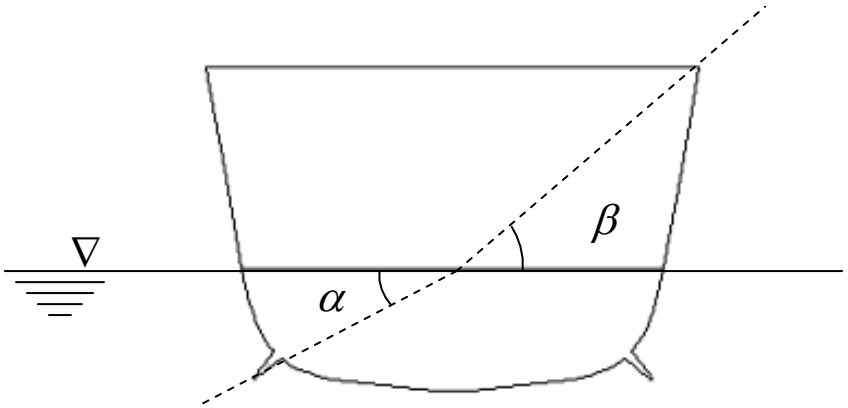

Figure 6-12: Simple illustration of the physical boundaries for large amplitude roll, resulting in bilge keel and deck interaction with the free surface, as defined by angles α and β, respectively

For the simplified case, the physical boundary for each regime is considered to change in a single discrete instant in time. The physical behavior of the large amplitude ship roll damping is considered constant in each physical regime. From the experiments presented in Chapter 4, a series of complex physical phenomena were observed for large amplitude roll motion, including bilge keel emergence, water shipping on the bilge keel, impact loading on the bilge keel during re-entry, and vortex interactions with the bilge keel and with the free surface. However, a first step is to consider a model which can account for the physical process of bilge keel interaction with the free surface, exit and re-entry, around which all of the other physical phenomena at large amplitude conditions is based.

Figure 6-13 illustrates the hypothesized change in roll damping, δ, based on roll angle, ϕ, for the simple case of two transition points with one bilge keel interacting with the free surface, at α, and one deck edge interacting with the free surface, at β. Physically, this hypothesized

behavior suggests a reduction in damping with the emergence of the bilge keel, and subsequent relative increase in damping with the emergence of the deck edge. This hypothesized behavior is consistent with the physical observations that were presented and discussed in Chapter 4.

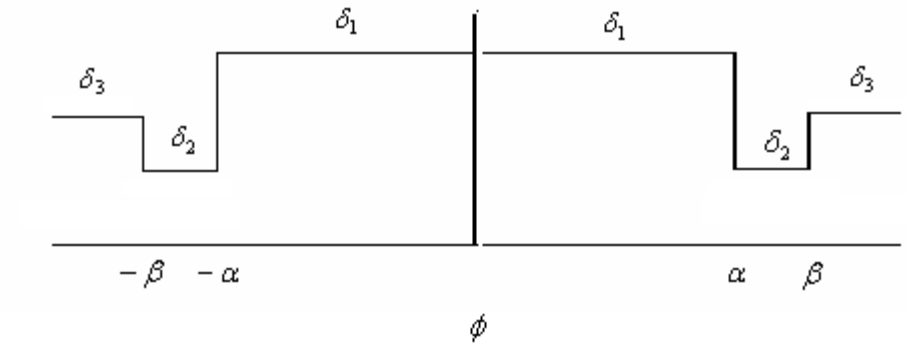

Figure 6-13: Simple illustration of hypothesized damping coefficients, δ_i, and transitions for various physical regimes, α and β, as defined by roll angle, ϕ

Considering roll damping as dependent on roll angle, *in addition* to roll rate, provides a connection to physical phenomena, as modeled in Ikeda's component-based roll damping method (Ikeda, et al. 1978e; Himeno, 1981), but expands the traditional ship roll damping model's application to large amplitude roll motion. Using a modern ship sectional geometry, predictions from the method are compared to predictions by traditional models used in potential flow numerical simulations for small and large amplitude roll motion response.

6.3.2.2 Properties of a Dynamical System with Piecewise Damping

To examine the properties of a dynamical system with piecewise constant damping, a single degree-of-freedom oscillator example is presented. As previously given in (2.3), $\ddot{\phi} + \delta(\phi)\dot{\phi} + c(\phi) = F(t)$, where *F(t)* is the forcing function, given by either of the solutions in (2.3) for the free and forced oscillation conditions, respectively.

$$F(t) = \begin{Bmatrix} 0 \\ \alpha \sin(\omega_e t) \end{Bmatrix} \tag{6.5}$$

Comparisons are made between the oscillator with constant damping and with piecewise constant damping, for both free and forced oscillation conditions. To illustrate the effect of piecewise damping on the dynamical properties of the oscillator system, above a specified threshold, the damping is considered to be five times less than the constant damping for the linear system (Figure 6-14). This was to exaggerate the result of effect of a change in damping above a threshold.

$$\delta(\phi) = \begin{Bmatrix} \delta_1 & \text{if } \phi < |\phi_t| \\ \frac{1}{5}\delta_1 & \text{otherwise} \end{Bmatrix} \tag{6.6}$$

The time-history response and phase plots for the free oscillator system (Figure 6-15 and Figure 6-16) and forced oscillator system (Figure 6-17 and Figure 6-18) were numerically computed are presented. For both free and forced oscillator conditions, the differences between the time-history response (Figure 6-15 and Figure 6-17) of the dynamical systems with constant damping and with piecewise constant damping are hard to discern. However, by examining phase plots of the oscillator behavior (Figure 6-16 and Figure 6-18), additional insight into the difference in behavior is evident as the physical threshold is crossed during oscillations.

Although the transition in damping properties for large amplitude ship roll motion (Figure 6-13) are typically not as severe as the example presented here for illustration, ship roll motion behaves as an under-damped oscillator. For analysis of roll motion in regular waves, a single degree-of-freedom forced oscillator model is often used (see Chapter 2). Understanding that at the physical transitions, inclusion of a reduction in damping affects the response of a dynamical system and that a piecewise model can capture this transition behavior, the application of this principle is used in the next section to develop and present a model for large amplitude ship roll damping.

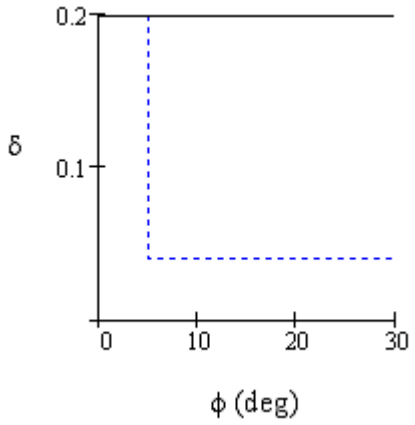

Figure 6-14. A single degree-of-freedom oscillator system with linear (solid black line) and piecewise constant (dotted blue line) damping, as a function of amplitude

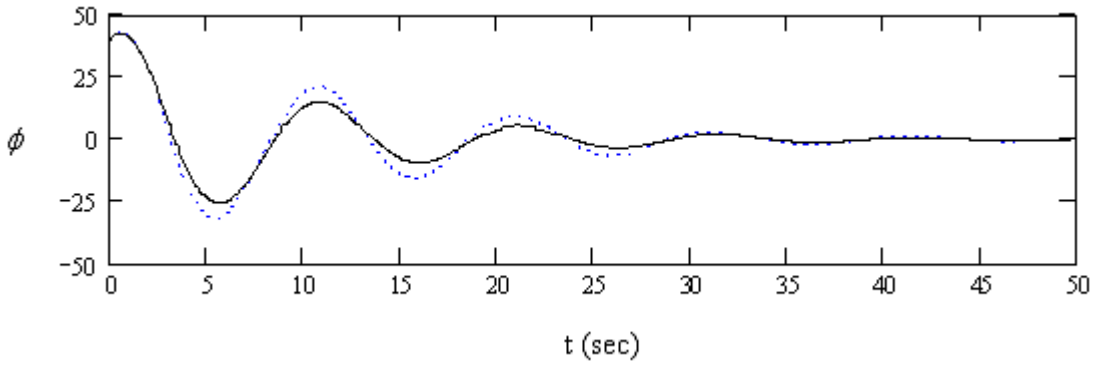

Figure 6-15. Response for a single degree-of-freedom free oscillator with linear (solid black line) and piecewise constant (dotted blue line) damping

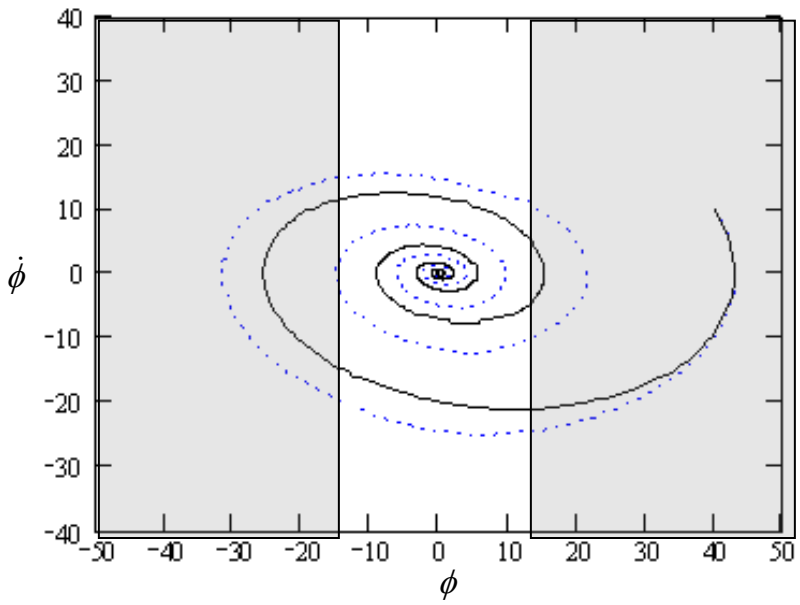

Figure 6-16. Phase plot for a single degree-of-freedom free oscillator with linear (solid black line) and piecewise constant (dotted blue line) damping, with regions of damping transition identified (in gray)

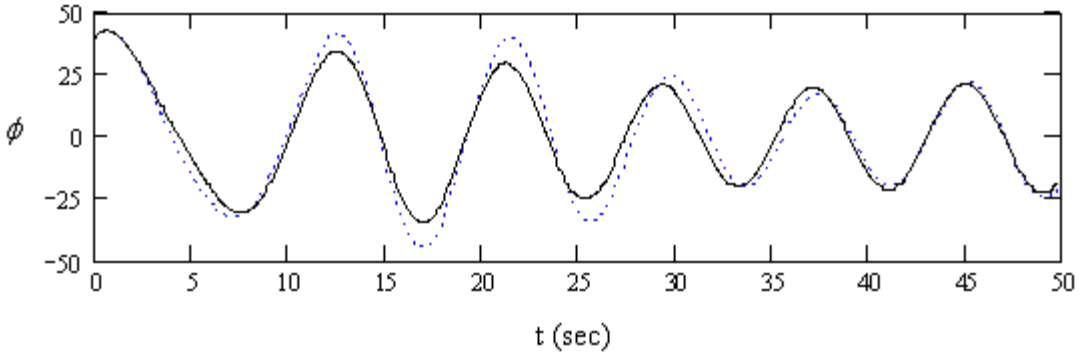

Figure 6-17. Response for a single degree-of-freedom forced oscillator with linear (solid black line) and piecewise constant (dotted blue line) damping

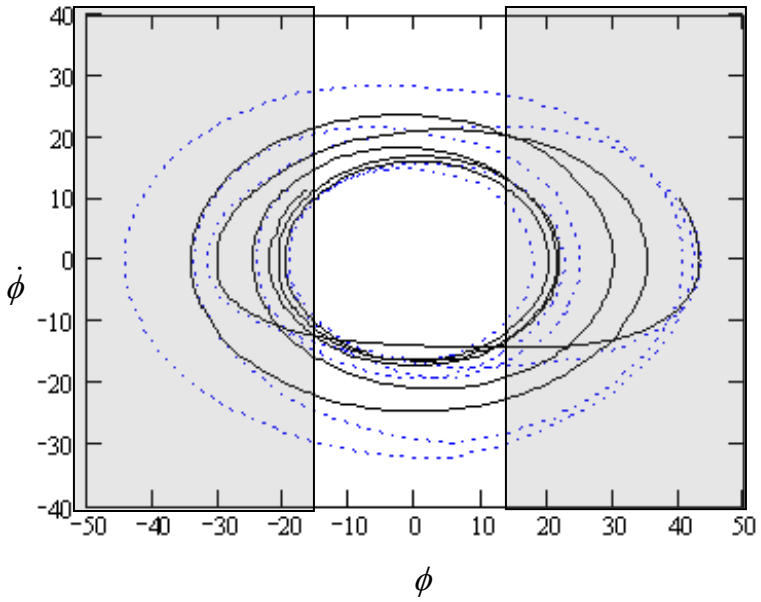

Figure 6-18. Phase plot for a single degree-of-freedom forced oscillator with linear (solid black line) and piecewise constant (dotted blue line) damping, with regions of damping transition identified (in gray)

6.3.2.3 Formulation

A piecewise constant method is proposed to model mechanical oscillator systems with distinct physical regions, such as the case of large-amplitude ship roll motion with the interaction of the bilge keels, or deck edge, with the free surface. A single degree-of-freedom ship roll with a sinusoidal forcing function representing regular waves is assumed.

For this system, the roll angle, ϕ_t, can be specified which represents a physical threshold identified and given by the ship-specific geometry. The transition across the physical boundary for each region, from small to large amplitude damping, can be considered to occur at a discrete instant in time. Therefore, the change in damping during this process is modeled as a "jump" for the non-smooth transition of a component of the body, such as the bilge keel or deck edge, out of the water (or into the water). The time-scale of this transition is small compared to the time-scale of the motion of the body, such as the roll period.

6.3.3 A Case Study for the Piecewise Damping Model

The effect of piecewise damping, obtained using the method detailed in the previous section, was examined using a case study of a notional hull form, the midship section of the ONR Topside Series hull form. The response for a second order linear oscillator system, with the dynamical properties of the ONR Topside Series midship section was examined for several conditions. These conditions included: with damping determined from the small amplitude approximation only, a linearized damping over the entire region, and a piecewise model, with the damping changing after a specified response amplitude threshold was exceeded. Additionally, a comparison was made to an engineering approximation for the piecewise damping, which is discussed later in this section.

6.3.3.1 Physical Thresholds

Figure 6-19 and Figure 6-20 show the ONR Topsides Series hull form, with flared (ONRFL) and tumblehome (ONRTH) topsides, experiencing small to large roll in calm water. Each of the roll angles illustrates a transition through different regions of physical phenomena—related to vortex shedding, and the bilge keels and deck edge emergence and immersion. Because the below waterline geometry is the same for both hull forms, the bilge keel is observed to exit the free surface at 30 degrees of roll. However, because of the different topside geometries, the deck edge is observed to enter the free surface at 37 degrees of roll for the ONRFL and 47 degrees of roll for the ONRTH.

For the purpose of this case study, the damping is modeled to change after exceedance of the first physical threshold, defined as when a bilge keel emerges from the water during large amplitude roll motion. The amplitude of response for this example was selected to be 35 degrees, which for the ONRTH configuration corresponds to a condition where one bilge keel has emerged, but the deck edge is not yet submerged. Therefore, a reduction in total roll damping should occur for the roll motion above the physical threshold where the bilge keel becomes emerged. This example is intended to illustrate the effects of damping during large amplitude roll, and the suitability of a piecewise model for damping in these conditions.

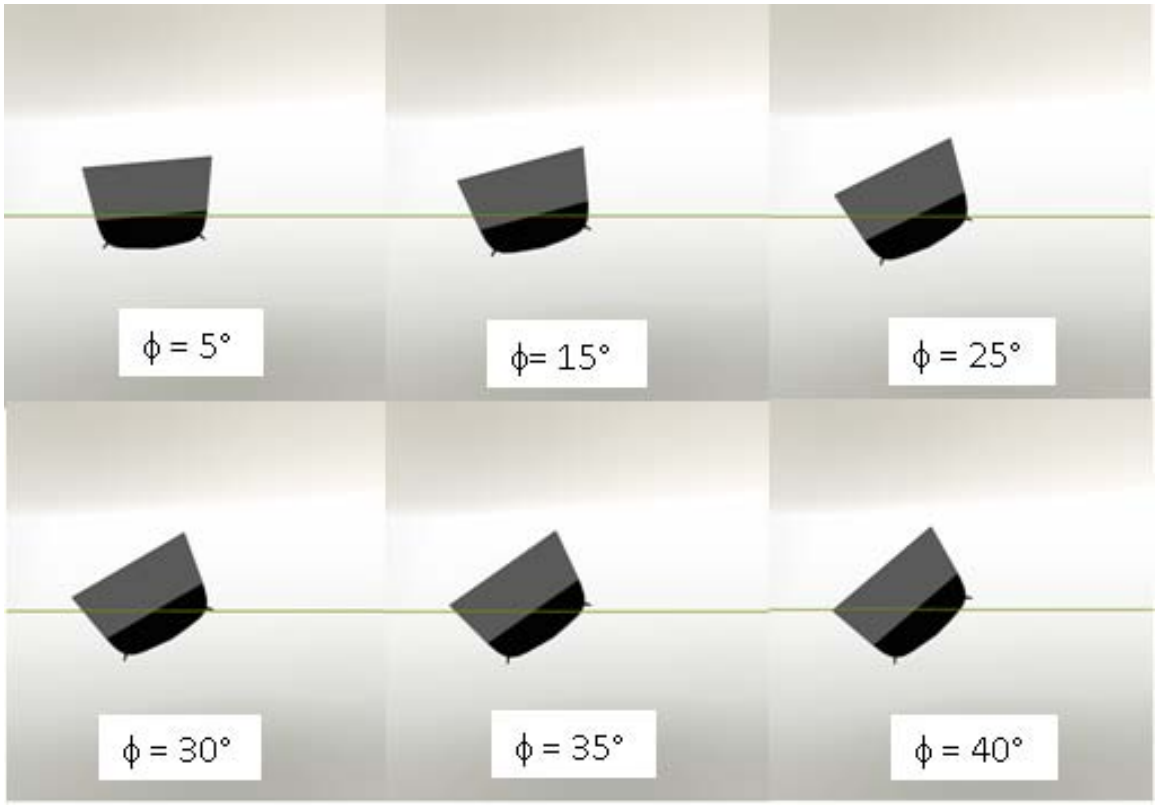

Figure 6-19: Illustration of roll transition through large amplitudes for the ONRFL midship section, including bilge keel and deck interaction with the free surface. Ship-specific abrupt physical changes due to variation in heel angle. For the midship section of the ONR Topside Series, flared configuration, bilge keel emergence is observed at 30 deg and deck submergence at 40 deg

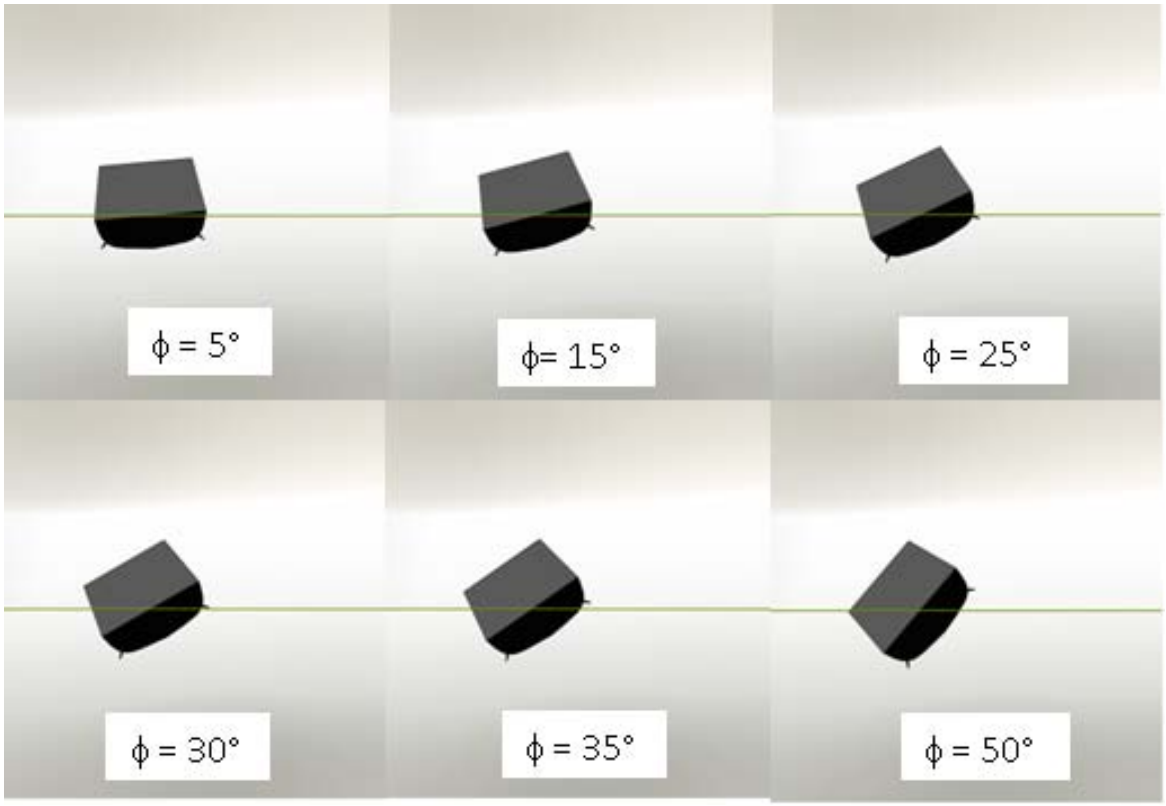

Figure 6-20: Illustration of roll transition through large amplitudes for the ONRTH midship section, including bilge keel and deck interaction with the free surface. Ship-specific abrupt physical changes due to variation in heel angle. For the midship section of the ONR Topside Series, tumblehome configuration, bilge keel emergence is observed at 30 deg and deck submergence at 50 deg

6.3.3.2 Initialization Values- Small Amplitude Roll Damping

Using the experimental results, presented in Chapter 4 and Appendix C, and the traditional method for obtaining roll damping for small amplitude roll motion, discussed in Chapter 2, values for small amplitude damping were obtained. Given that frequency dependence of roll damping is small, relative to the dependence of damping on roll amplitude, the specified small damping for this example was assumed to be constant. For the ONR Topside Series, this corresponded to a threshold damping ratio of 0.174, which is within the normal range for a naval hull form. However, as the damping does not remain constant over the amplitude, due to the physical phenomena, a linearized damping over the entire response range was also considered. Because of the reduction in damping corresponding to the emergence of a bilge keel, the linearized damping must be less than the small amplitude damping. For this example, the linearized damping corresponds to a threshold damping ratio of 0.146. This is presented in the next section (Figure 6-21).

6.3.3.3 Solutions for Large Amplitude Roll Damping

Using the piecewise model presented previously, an iterative solution was obtained for the second region damping by specifying the small amplitude damping coefficient and then solving for the roll response. For the 35 degree roll response condition, the second region damping (when a bilge keel has emerged) was obtained which corresponds to a threshold damping ratio of

0.049. This reduction in damping is significant and results in a markedly different roll response than if only the small amplitude, or even linearized, damping is used.

6.3.3.4 Roll Response

Using the values obtained from the piecewise model, the roll response for a second order linear system was determined (Figure 6-21). Comparisons are shown for the response of the linear system with small amplitude damping only, linearized damping over the full range of amplitudes, damping for the second (or large amplitude) region only, and for piecewise constant damping, with a transition occurring at the physical threshold defined by ϕ_t.

As can be observed from the comparisons shown in Figure 6-21, the response of the piecewise system is quite large (above the threshold- the same as for the second region damping). For the physical system, which is nonlinear, this response will not be as exaggerated. However, the examination of the linear system shown enables insight into the effect of the piecewise damping model on the roll motion response.

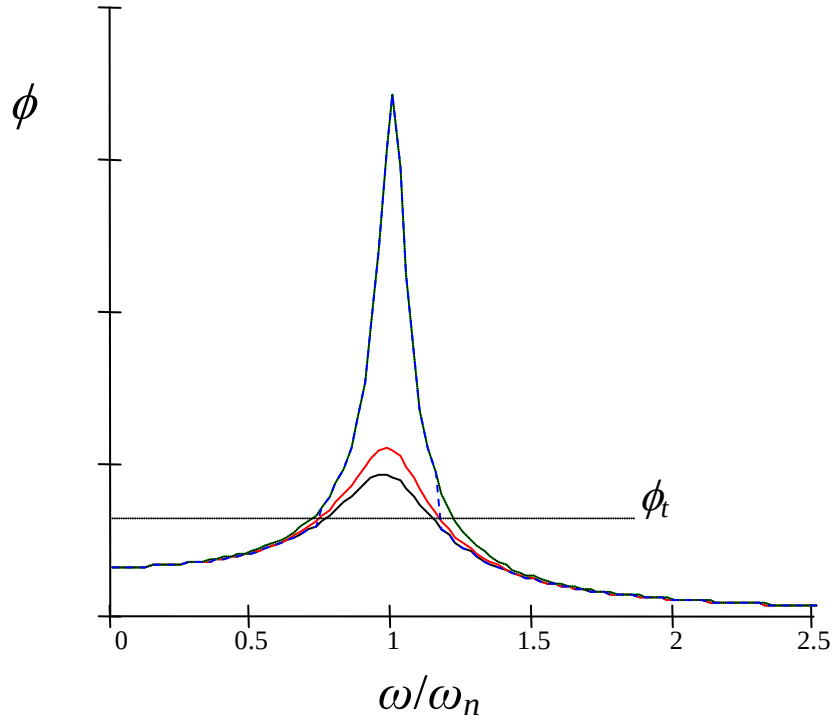

Figure 6-21. Comparison of roll response for a linear oscillator system with small amplitude damping only (black), linearized damping over the full range of amplitudes (red), damping for the second region only (green), and piecewise constant damping with a transition at ϕ_t (dotted blue)

6.3.3.5 An Engineering Approximation for Practical Implementation

Because of the physical phenomena observed during large amplitude roll motion, and the hypothesized behavoir for roll damping at large amplitudes, a simplified model for engineering application is considered. This simplified, or engineering approximation, model is likely suitable in cases where it is not desirable to utilize the piecewise method to determine large amplitude roll damping.

For most ship types the damping due to bilge keels is the most significant and for small roll motion can be between 30–60% of the total roll damping, depending on ship type and bilge keel size. Typically for naval vessels, which have larger bilge keels, the roll damping due to bilge keels is between 50–60% of the total damping. For commercial vessels, typically the roll damping due to bilge keels is between 30–40% of the total damping. Above the ship-specific physical threshold, because one bilge keel has emerged, the contribution of the bilge keel damping to the total ship roll damping is reduced by half. Therefore, for large amplitude roll motion, defined as when one bilge keel is emerged, a 25–30% reduction in equivalent linear damping for naval type vessels with typical bilge keels, or a 15–20% reduction in equivalent linear damping for commercial ships with bilge keels can be expected. Particularly for early-stage design evaluations, when additional information or data may not be available, these standard values can be used to provide the damping behavior during large amplitude roll motion response.

6.3.4 Application of the Piecewise Model

In this section, some issues related to compatibility of the piecewise model with existing roll damping model formulations, adaptability for increased complexity, and practical implementation are discussed. Based on examination of the piecewise model formulation, a simplified engineering approximation is also discussed, which is useful for assessments, particularly early in the ship design process.

6.3.4.1 Compatibility

An important consideration for the development of a model for large amplitude total ship roll damping is compatibility with existing roll damping models. The model proposed in this chapter is intended to provide an enhancement to the prediction and application of models for ship roll damping, and extend them to the assessment of large amplitude ship roll motion occurring in heavy seas.

In the classical model of ship motion as a spring-mass-damper system, damping is proportional to velocity and characterizes the energy dissipation of the system. Existing theoretical models for roll motion consider various physical processes related to roll damping, using various mechanisms of energy dissipation. These include friction, lift, wave-making, and vortex generation from the hull, as well as the vortex generation and influence of deeply submerged bilge keels (Ikeda, 1978; Schmitke, 1978; Himeno; 1981). For roll motion, the effects of the bilge keels typically account for the largest component of energy dissipation and are most effective for small and moderate roll motion at low speeds (Ikeda, 1978; Himeno, 1981). At higher speeds, lift damping becomes dominant (Baitis, et al., 1981). Although larger size bilge keels are typically more effective, constraints, due to hull geometry and structural considerations, limit the practical span of bilge keels.

In most modern potential flow codes, used to predict ship motion performance, roll damping is determined using Ikeda's method (Ikeda, et al., 1978), or results from roll decay experiments to obtain ship-specific damping. These methods assume small amplitude roll motion, where the bilge keels are considered to be deeply submerged and smooth changes occur between the geometry of the body and the fluid domains.

In this system model, the first region, or small amplitude, damping, δ_1, can be determined using Ikeda's method or from experimental measurements, such as roll decay tests. For the

piecewise constant formulation, the use of the equivalent linear damping coefficient formulation enables continuity with existing methods, which have traditionally been very appropriate for their intended use—modeling small to moderate amplitude roll motions.

Large amplitude forced oscillation tests may be carried out using either experiments (e.g. Bassler, et al., 2007; 2010) or high-fidelity simulations tools (e.g. Korpus & Falazarano, 1997; Wilson, et al., 2006; Seah & Yeung, 2008; Miller, et al., 2008), including RANS. For these, the maximum amplitude of the forced oscillation, ϕ_a, and frequency of oscillation, ω_e, are specified and the physical threshold, ϕ_t, is known from the ship-specific geometry. Because forced oscillation is used, the amplitude of wave excitation and phase become virtual quantities. Therefore, the excitation, α, the time of the maximum amplitude, t_1, and the large amplitude, or second region damping, δ_2, are unknowns and are determined from the solution of the indirect problem formulation.

From this piecewise analysis, a series of damping coefficients for roll motion above the specified physical threshold can be obtained. These can be utilized in the ship motions simulation tool to provide a more accurate value for the roll damping during large amplitude motions. Additionally, an engineering approximation model, based on analysis of the typical contribution of the bilge keel to ship roll damping and the effect of large amplitude roll motion, such as bilge keel emergence, was presented. This may also provide a simple, yet more accurate, modification to the existing models commonly used for numerical assessment of ship motions performance.

6.3.4.2 Adaptability for Models with Increased Complexity

The piecewise damping model is given as a simplified formulation using piecewise constant damping coefficients for each motion amplitude region. The use of piecewise constant damping coefficients enabled development and investigation of the suitability of the model to provide improved predictions for the physical effects on total ship roll damping for large amplitude roll motion. However, the damping formulation for each region is not limited to a piecewise constant formulation, and may include the use of more realistic, or complex, models, such as a nonlinear formulation,

$$\delta(\phi)\dot{\phi} = \delta_a(\phi)\dot{\phi} + \delta_b(\phi)\left|\dot{\phi}\right|\dot{\phi} + \delta_c(\phi)\dot{\phi}^3 + \ldots \tag{6.7}$$

$$\delta(\phi) = \begin{Bmatrix} \delta_{a1}, \delta_{b1}, \delta_{c1}, \ldots \ \ if\ \phi < \left|\phi_t\right| \\ \delta_{a2}, \delta_{b2}, \delta_{c2}, \ldots \ otherwise \end{Bmatrix} \tag{6.8}$$

where δ_a, δ_b, and δ_c are linear, quadratic, and cubic damping coefficients for each particular physical region. As discussed in Chapter 2, these nonlinear models have also been used to describe ship roll motion (Dalzell, 1978; Cotton & Spyrou, 2000; Spyrou & Thompson, 2000), although the equivalent linear damping coefficient model remains the most widely used in ship motions numerical tools, due to the difficulty of accurately obtaining the nonlinear coefficients, even for small roll amplitude motion. The multiple sets of δ_a, δ_b, and δ_c for each motion amplitude regime can be combined with the piecewise method to characterize nonlinear damping, including large amplitude roll.

In principle, by using a numerical solver, the nonlinear formulation for each motion amplitude region can be different, such as linear and quadratic in some regions and linear and cubic in others. This formulation may also be further extended to model additional motion amplitude thresholds, such as deck edge immergence, which will alter the damping characteristics of the ship in roll.

6.3.4.3 Evaluation of Large Amplitude Ship Roll Damping in Irregular Waves

Using the piecewise formulation, a procedure can be developed to determine ship roll damping in irregular waves. The instantaneous attitude of the ship, in particular the bilge keel, relative to the local wave field, can be evaluated using a sectional approach with upcrossing theory of a moving boundary (the instantaneous free surface). Based on the assessment of the relative position of the bilge keel, the appropriate damping coefficient(s) from the pre-computed look-up table can be utilized, considering the relative roll angles and subsequent wetted geometry of the ship.

6.3.4.3.1 Method

In order to utilize this procedure for time-domain evaluation of large amplitude roll damping in irregular waves, several assumptions must be satisfied. The numerical code must have the dynamic instantaneous waterline at each section defined, as well as the wave surface and the ship geometry, including appendages. And the time-step must be sufficiently small, to capture the transition behavior, depending on the level of accuracy required from the simulation code.

The ship-specific geometry is used to define the motion amplitude thresholds where changes of damping properties (e.g. chine, bilge keels, deck edge). Forced oscillation or roll decay tests are used to obtain damping coefficients for the 1st region (small amplitude), as a function of roll frequency and forward speed. Then large amplitude forced oscillations are performed (either high-fidelity numerical, such as RANS, or experimental) and the piecewise method, along with small amplitude damping coefficients, is used to obtain large amplitude damping coefficients, as a function of roll frequency and forward speed.

Using these results, a look-up table of coefficients can be obtained from the RANS/experiments of the 1st, 2nd, 3rd, . . .nth region coefficients, as functions of roll frequency and forward speed. Using the formulation for irregular waves (upcrossing theory with a moving threshold) and evaluating the relative position of the instantaneous dynamic waterline and the motion amplitude threshold of interest at a given time-step, the damping coefficient for a specific physical region can be used for a particular hull.

With this implementation, the piecewise method can be expanded using upcrossing of a moving threshold to include irregular waves, multiple degree-of-freedom (MDoF) motions, and forward speed. Then the total model is implemented to obtain “equivalent linear damping” coefficients for large amplitude roll, populating a ship-specific look-up table for use in sectional time-domain evaluation.

6.3.4.3.2 Practical Implementation

The procedure to model the change in roll damping for bilge keel interaction with the free-surface in large amplitude roll motion is extended to include additional motion amplitude regions

which may significantly affect damping based on the ship-specific hull geometry, such as deck-in-water effects (Grochowalski, 1990; Grochowalski, et al., 1998).

Several additional issues also need to be considered in order to implement the method in numerical simulations and to use the procedure for practical prediction of large amplitude total ship roll damping. These include multiple degree-of-freedom ship motions (such as heave and pitch), forward speed, irregular waves, and roll frequency dependence. However, given that many traditional ship roll damping models consist of single degree-of-freedom coefficient-based approaches, the modification proposed may already serve to provide significantly expanded application of these models to large amplitude ship roll damping.

Potential flow-based numerical tools, which use a sectional approach in the time-domain and include the instantaneous relative position of the ship section and the free-surface from irregular waves near the ship (Figure 6-22), may provide more accurate determination of when the motion amplitude threshold for a given ship section is reached and which corresponding component of the piecewise damping should be used at a given time-step. The damping coefficients would be referenced from a pre-computed look-up table. By integrating the sectional damping along the hull at each time-step, the ship-specific total roll damping for large amplitude ship motions can then be determined.

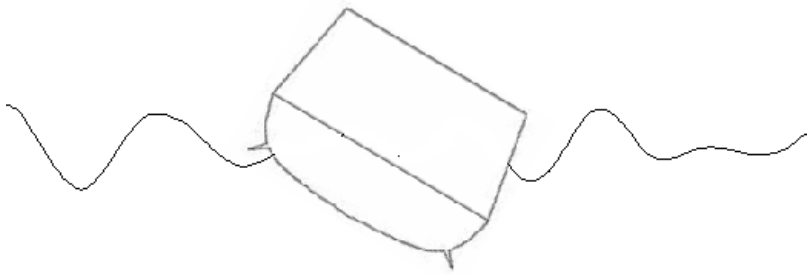

Figure 6-22: Sectional view of the instantaneous relative position of the ship in irregular waves for determining roll damping at a given time-step

To more accurately predict and examine ship motions behavior for extreme seakeeping and dynamic stability problems, a time-domain model to describe ship roll damping explicitly must ultimately be used. For more explicit modeling of ship roll damping behavior, a component-based force model is used to determine the bilge keel force, which still includes of physical phenomena occurring during large amplitude roll motion. This is described in the next section.

6.4 A Bilge Keel Force Model for Large Amplitude Roll Motion

The roll motion of a ship is influenced by both its shape and appendages. Viscous related phenomena, such as flow separation from the bilge, keel and bilge keels with the subsequent vortex formation, account for a large portion of roll damping. Bilge keels also generate a lift force with forward motion, which further tends to dampen the roll motion. For new ship designs, the effectiveness of the bilge keels for damping roll motion needs to be determined for a large range of roll angles and ship speeds. The seakeeping performance of ships which are appended with bilge keels is typically evaluated using experiments or semi-empirical models in potential flow codes.

Fast, potential flow based numerical methods for ship motions assessment depend on accurate modeling of roll damping to determine roll motion. However, the traditional roll damping models (Ikeda, et al., 1978; Himeno, 1981) do not explicitly account for the physical phenomena which occur during large amplitude ship motion, including the reduced effectiveness of the bilge keels (Bassler & Reed, 2009; Reed, 2009; Bassler, et al., 2010, 2010a, 2011).

Even with the implementation of the piecewise method, the accuracy may not be sufficient. In order to obtain more accurate predictions of ship roll motion, high-fidelity codes, such as URANS, may also be used. However, the computational requirements associated with these codes prevent their expansive use for early-stage design assessments, or assessments for a large number of ship headings, speeds, and loading conditions across the range of wave environments, which are necessary for the development ship-specific operator guidance. Therefore, potential flow simulations tools with explicit bilge keel force models may provide a fast, yet sufficiently accurate method to assess ship performance. However, bilge keel force models do not currently have the ability to consider large amplitude roll motion effects.

6.4.1 Bilge Keel Models and Large Amplitude Ship Roll Motion

For large amplitude ship roll motion, the hydrodynamic components of the bilge keel force are reduced, due to the interaction between the bilge keel with the free surface and, for more severe motions, possible emergence. For more accurate modeling, especially for more advanced potential flow numerical tools with discrete force models (e.g. Belknap & Reed, 2010), an explicit model for the bilge keel force, that considerations large amplitude roll motion effects should be used (Figure 6-23).

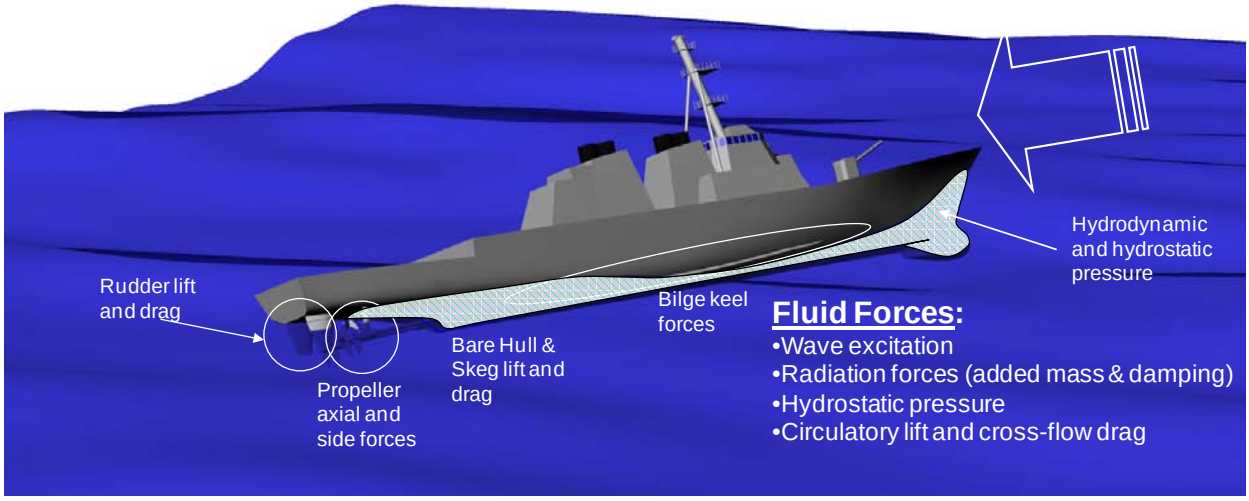

Figure 6-23. Decomposition of the physical problem in advanced, but fast, numerical simulations potential flow (from Belknap & Reed, 2010).

6.4.2 Bilge Keel Wave-Making Component

The wave-making component of the bilge keel damping is typically neglected. This assumption is appropriate for small amplitude roll motions and for small bilge keels. However, for larger amplitude roll motions, where the bilge keel moves close to the free-surface, the significance of the energy dissipation from wave-making by the bilge keel, becomes important.

The bilge keel wave-making term could be accounted for in the wave-making term, B_W, where this would be the total (for a ship that includes bilge keels). The inclusion of this component would require careful calculation of the radiation force to include the influence of the bilge keels when they are near the free-surface and determine the resulting disturbance on the wave-field generated by the hull. Before including the transition of the bilge keel through the free surface, a model for the behavior of the bilge keel near the free surface, but not necessarily emerged, should be examined.

To examine the bilge keel wave-making damping component a simple model is proposed based on a source formulation (Bassler & Reed, 2009). Here the bilge keel wave-making component, B_{BKW0}, is considered to be proportional to the strength of the energy dissipated by waves from the bilge keel, $C_{BK}(b_{BK})$, which is related to the relative size of the span of the bilge keel, b_{BK}, the frequency of oscillation, ω, and the depth of the bilge keel relative to the free-surface, $d_{BK}(\varphi)$. For simplicity, the "source strength" coefficient is approximated by the relative size of the bilge keel span to the wave number of the radiated waves. This simplified model of the bilge keel wave-making includes specification of the bilge keel depth from the free-surface as a function of roll angle.

$$\hat{B}_{BKW0} \sim C_{BK}\left(b_{BK}\right) \cdot \exp\left(-\frac{\omega^2}{g} d_{BK}\left(\phi\right)\right) \tag{6.9}$$

In order to examine this conceptual model for bilge keel wave-making, several conditions were investigated. These included roll amplitudes from ϕ = 0 to 30 degrees, roll frequencies from ω = 1 to 7 rad/s. This conceptual model was constrained to 2D to enable isolated examination of this component. The effects of forward speed were not examined. Additionally assumptions for the results presented include: the roll axis, *OG*, was assumed at the VGC, and the component evaluations were performed for the given normalized model dimensions. As can be seen from the results of the simplified conceptual model for two conventional ships, the cargo ship (Figure 6-24) and the Series 60, C_B=0.60 (Figure 6-25), the bilge keel wave-making component increased for increasing roll amplitude, as the bilge keel nears the free-surface. However, it decreased for increasing roll frequency, as smaller waves are generated in these conditions, compared to the lower frequency conditions.

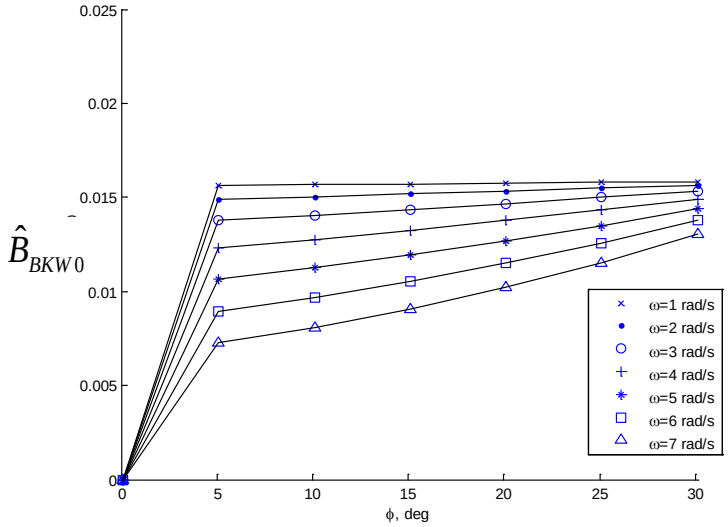

Figure 6-24. Bilge keel wave-making component vs ϕ for a cargo ship, at zero speed (from Bassler & Reed, 2009)

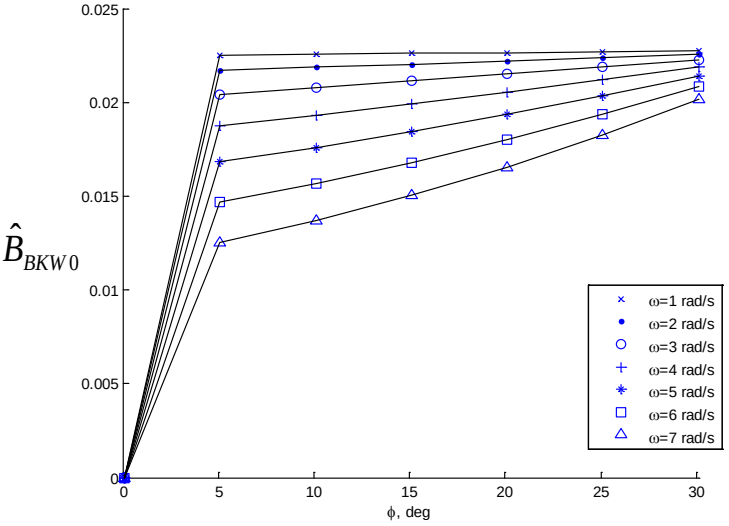

Figure 6-25. Bilge keel wave-making component vs ϕ for Series 60, C_B=0.60, at zero speed (from Bassler & Reed, 2009)

6.4.3 Models for Bilge Keel Transition

A standard model for the bilge keel force is observed to merely increase with increasing roll amplitude, and does not include any consideration for hysteresis effects caused by the bilge keel interaction with the free surface. This is because of the assumptions used for the models, limiting their application to small roll amplitude.

As observed from the 2D experiments and 3D URANS simulations, presented in Chapters 4 and 5, for large amplitude roll conditions, the bilge keel may emerge from the water, resulting in lingering forces due to water-shipping effects and severe impact loading-type behavior due to re-

entry during the roll motion. However, none of the current bilge keel force models consider any of the complex behavior observed from the experiments and the URANS numerical simulations.

Based on the physical observations of the problem, several possible models for the transition behavior of the bilge keel during emergence and re-entry are proposed using analytical functions and are considered to model this behavior. These models include a step-function, Gompertz function, or generalized logistic function (Richard's curve). Each of these models provide increasing complexity, in an attempt to provide a more realistic model of the physical phenomea affecting the bilge keel force during emergence and immersion, and are discussed in more detail below.

The simplest model that is considered for the large amplitude behavior of the bilge keel force is the use of a step function formulation, where the bilge keel is either in the water or out, and this transition occurs instantaneously. This model is the basis of the piecewise model presented earlier in this Chapter. The abrupt changes observed during the bilge keel transition through the free-surface may create difficulties for time-domain simulation of these types of forces (and resulting ship motions) in potential flow simulation codes. Additionally, how the vorticity calculations will be stopped and re-started, to how the bilge keel will be de/re-wetted upon emergence and re-entry, and how hysteresis effects due to "water shipping" phenomena must be considered. A more complex model for the bilge keel force during this transition than the step-function model is necessary, to enable capturing of the physical effects observed during the experiment and numerical investigation. In this section, three more realistic models are presented and discussed. These include a sigmoid function, a Gompertz function, and a generalized logistic function (or Richards' Curve).

6.4.3.1 Sigmoid Function

A model to represent the physical phenomena observed for the bilge keel force is a sigmoid function. The model for bilge keel force transition using a sigmoid function has a similar simplicity to the step-function model, but allows for the physical nature of the transition, which is not instantaneous, to be captured (Figure 6-26).

$$F_{BK}(t) = \frac{C_1}{1+e^{-t}} \tag{6.10}$$

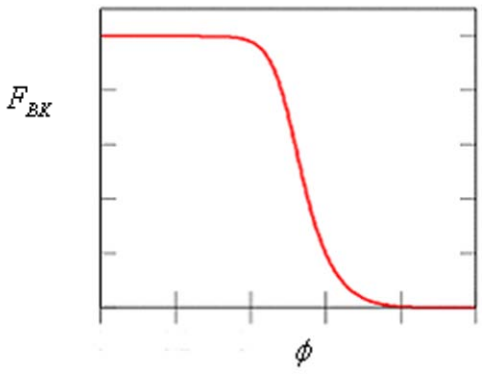

Figure 6-26. A model using a sigmoid function for bilge keel transition behavior during large-amplitude roll motion

Here the asymptotic boundaries of the transition can still be used. These two boundaries are the typical computation of the bilge keel force when submerged and the zero force when completely out of the free surface. Unlike the step-function model, the sigmoid function model provides a formulation to adjust the rate of loss of bilge keel force, when exiting the water, or rate of increase in bilge keel force, when re-entering the water. However, the asymmetries of the rate of change in the bilge keel force between the asymptotes, as observed from the experiments and numerical results (Chapters 4 and 5), still cannot be captured using this type of model.

6.4.3.2 Gompertz Function

Another model for the bilge keel force transition relative to the free-surface is the Gompertz function. This function allows for the steepness of the transition from the upper and lower asymptote to be specified and varied (Figure 6-27).

$$F_{BK}(t) = ae^{be^{ct}} \tag{6.11}$$

where a is an upper asymptote, c is a growth rate and b and c are negative.

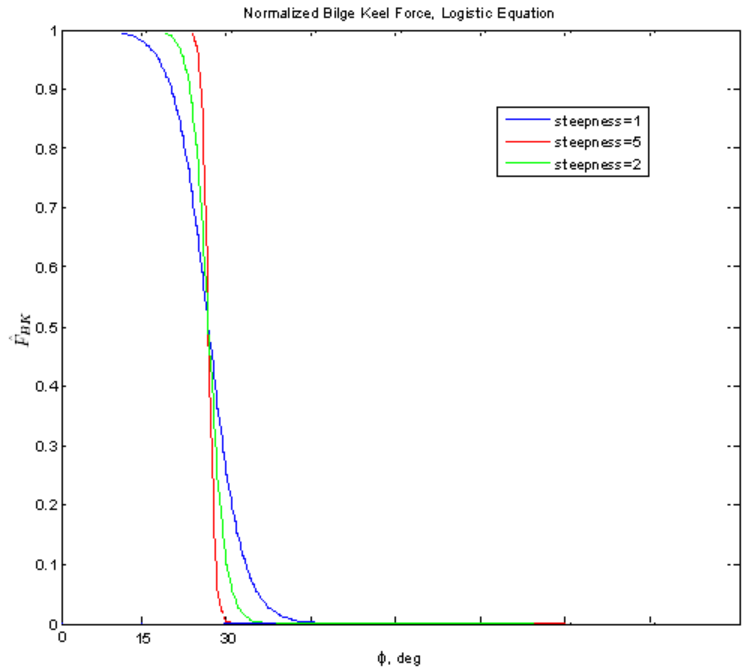

Figure 6-27. A model using a Gompertz function for bilge keel transition behavior during large-amplitude roll motion

Unlike the step-function and sigmoid function models, the Gompertz function model provides a factor to adjust the rate of loss of bilge keel force, when exiting the free surface, or rate of increase in bilge keel force, when re-entering the free surface. Gompertz functions are used to approximate the difference in the behavior of the bilge keel force when exiting or re-entering the free surface. However, the asymmetries of the bilge keel force behavior at the asymptotes, as observed from the experiments and numerical study, still cannot be captured using this type of model.

6.4.3.3 Generalized Logistic Function- "Richards' Curve"

The need still exists to be able to consider the change in both the asymptotic behavior near the transition boundaries, as well as the rate of change in between these transition boundaries. Considering this, a more robust conceptual model for the bilge keel force transition can be developed.

An analytical framework allowing for this rate of change is the generalized logistic function (or Richards' Curve). This function allows for both the steepness of the transition from the upper and lower asymptote to be specified and varied separately, as well as for an asymmetric approach to the upper and lower asymptotes. This allows consideration of the asymmetries of the bilge keel force behavior. The formulation for a bilge keel force model, using the generalized logistic function form is

$$F_{BK}(t) = A + \frac{K - A}{\left(1 + Qe^{-B(t-\mu)}\right)^{\frac{1}{v}}} \tag{6.12}$$

where A specifies the lower asymptote, K the upper asymptote, B the growth rate, $v>0$, which affects which asymptote is near max growth occurs, Q is a constant which depends on $Y(0)$, and μ denotes the time of max growth (if $Q=v$).

6.4.3.4 Assumptions and Limitations

The short-comings of the models presented to consider the transition behavior of the bilge keel at the free surface during large amplitude roll motion are acknowledged. However, given these relatively simple models for the transition, implementations in time-domain formulations for potential flow methods will be possible because of the ability for Fourier series convergence when considering the memory from previous time-steps and these discontinuities in the bilge keel force behavior at large roll motions.

The additional analytical complexity and its relation to the physical processes observed for the bilge keel force in large amplitude roll motion are discussed for each model. However, the the semi-empirical nature of specifiying coefficients for these models results in difficulties for practical implementation of these models in a robust potential flow simulation tool. Experiments and/or URANS simulations can be used to determine the cofficients which must be specified, but the range and sensitivity of these coefficients is unkown, given the range of ships and ship motion conditions that are of interest for the simulations.

Because large amplitude roll motion may result in the biggest reduction in bilge keel performance, while the ship is maneuvering in waves, nonlinearities in forces caused by bilge keel interaction with the free surface may also cause computational difficulties, due to discontinuities of the wetted surface area of the bilge keel across time-steps in numerical simulations.

Vortex interaction with the free surface before bilge keel emergence, or the initialization of vortex shedding from the bilge keels after re-entry with the free surface is also not yet considered in the proposed bilge keel force models. Perhaps, similar to the simplied model proposed and discussed for the bilge keel wave-making contribution, a vortex interaction model could be developed, using an exponential decay term as the bilge keel gets close to the free surface.

Chapter 7 Conclusions and Possible Areas for Future Work

This dissertation details the characterization and modeling of hydrodynamic components, added inertia and damping, for large amplitude roll motion. Although models for hydrodynamic components of ship roll motion have existed for many years, the consideration of large amplitude roll motions is novel. This work consisted of performing both experimental and numerical observations, to provide fundamental understanding and characterization of the physical phenomena which occur during large amplitude roll motion and affect the hydrodynamic components. No systematic observations of these phenomena had been made before. As with any path-breaking work, hopefully this will encourage additional research in this area; to build upon the observations made, and to further develop and apply some of the model formulations proposed and discussed.

7.1 Summary

This work consisted of the analysis of the hydrodynamic components, added inertia and damping, for large amplitude ship roll motion. Experimental and numerical analysis of the hydrodynamic components showed significant difference in their behavior for large amplitude roll motion, compared to smaller amplitudes. The complex physical processes associated with changes in the behavior of the components were identified and analyzed using both experimental and numerical methods. The analysis showed large amplitude roll motion effects on the added inertia and damping of the hydrodynamic roll moment and the hydrodynamic roll moment due to the bilge keel force. The interaction of the bilge keels, as well as the topside geometry, with the free surface at large amplitude roll resulted in changes observed for the added inertia, damping, and vortex shedding behavior. Observations from the measurements also indicated that the added inertia due to the bilge keels was not insignificant. In models of ship roll motion, this effect is never considered. However, the experimental measurements indicate that the added inertia due to the bilge keels is typically about 10-15% of the total added inertia of the hull. Based on these observations, future work should be conducted to incorporate consideration of the added inertia due to the bilge keels into models of the hydrodynamics components for ship roll motion.

As presented in Chapter 4, an experiment was performed to characterize the various physical phenomena for large amplitude ship roll motion. Results included the observation and identification of the discrete processes that result for several physical phenomena, including bilge keel interaction with the free-surface (emergence and immersion), vortex shedding, and wave-making, and their effect on the hydrodynamic roll moments due to the hull and bilge keels. The observations and data from this experiment were used to develop improved understanding of the physical differences between small or moderate motions and large amplitude motions. The results showed that the processes for large amplitude roll motion were nonlinear, such that one emergence was observed, changes were observed in the behavior of the hydrodynamic components, particularly for the damping of the hydrodynamic roll moment due to the bilge keels.

Several important observations were obtained from the experimental results and analysis. The total hydrodynamic roll moment and roll moment due to the bilge keels are amplitude dependent. For smaller roll amplitudes, the relative contribution of the bilge keel to the total roll moment increased with increased roll amplitude. However, near and above the free surface threshold, the bilge keel contribution to the total unit roll moment does not change drastically

and significant nonlinearities are observed, specifically the reduction in the bilge keel force, once emerged. The bilge keel force was also observed to increase with increasing amplitude and became more asymmetric with larger roll amplitude, due to the bilge keel interaction with the free surface. For roll amplitudes were bilge keel emergence occurred, higher peak loads, due to impact loading from re-entry for large amplitude roll, were observed.

Both the added inertia and damping also exhibited amplitude dependence. The added inertia from the total hydrodynamic roll moment (hull and bilge keels) increased with increasing amplitude. Even at smaller amplitudes, the bilge keel component of added inertia was not negligible and increased with increased roll amplitude. However, once bilge keel emerged from the free surface (the 30, 35 and 40 deg roll conditions) the greatest variation in added inertia throughout the roll cycle was observed. This is due to the bilge keel interaction with the free surface, as observed by the water shipping phenomena on the bilge keel. At large amplitudes, the added inertia component was small, relative to the added inertia component of the total unit hydrodynamic roll moment.

At smaller amplitudes (5 and 15 deg), the bilge keel damping was a significant portion of total damping. The damping from the total hydrodynamic roll moment and the hydrodynamic roll moment due to the bilge keels increased with increased amplitude, up to 30 deg roll. However, at 30 deg roll, additional nonlinearities were observed in the bilge keel damping, due to the interaction of the bilge keel with the free surface. This nonlinear behavior is no longer observed for the 35 and 40 cases, once the bilge keel has transitioned through the free surface. Reductions in the total damping were observed above 30 deg, including differences between the total damping and the damping from the hydrodynamic roll moment due to the bilge keel. This suggests that the additional physical mechanisms for damping behavior from the bilge keel, such as vortex shedding, are not captured by only consideration of roll moment due to the measured bilge keel normal force. Additional nonlinearities were also observed in the total hydrodynamic damping once the bilge keel has transitioned the free surface (35 and 40 deg). Above the free-surface threshold, the total damping becomes more non-sinusoidal throughout the roll cycle, due to the manifestation of the nonlinearities in the damping at larger roll amplitudes.

Differences were also observed for the added inertia and damping due to the topside configuration. This was particularly noticeable in the WAMIT results. The topside strongly affects the added inertia of the hydrodynamic roll moment. The added inertia of the flared topside behaves nearly linearly, increasing with increasing roll amplitude. However, the tumblehome topside deviates from this behavior at larger roll amplitudes. This is because the flared topside interaction with the free surface, when heeled, acts as a wave-maker. While the tumblehome topside instead has reduced wave-making properties when heeled, due to the relative angle between the sidewall and the free surface. Additionally, the topside and bilge keels have an interaction effect, which is observed in the measured damping.

The numerical simulations results, presented in Chapter 5, were used to examine the effect of roll amplitude on the radiation added inertia and damping and bilge keel force. For large amplitude roll, the topside configuration was observed to have a significant impact on the radiation added inertia and damping. To enable additional insights into the radiation components of the roll added inertia and damping, the WAMIT results were used to supplement the experimental results presented in Chapter 4. The URANS results also produced the same physical effects for the bilge keel force at large roll amplitudes observed from the experiments. From both the experimental and numerical results, the physical processes associated with large amplitude roll motion, due to interaction with the free surface and the influence of the topside,

are manifested in the resulting added inertia and damping for both the total hydrodynamic roll moment and the bilge keel force. The experimental results from Chapter 4 and the numerical results from Chapter 5 are used in Chapter 6, as a basis to propose models which consider large amplitude effects on the hydrodynamic components during large amplitude roll motion.

The numerical and experimental observations confirmed the hypothesis that existing models for roll added inertia and damping in large amplitude motions do not adequately capture the physical processes and associated changes in the hydrodynamic component behavior. Based on the observations and analysis, several formulations were developed to model the change in roll hydrodynamic components for large amplitude motions. However, additional development remains to address issues for further practical implementation.

A piecewise method for modeling large amplitude roll damping was presented, based on consideration of the abrupt physical changes that occur with events, such as bilge keel emergence. When these events occur, a significant change in damping of the system occurs, which can be modeled explicitly using a piecewise approach. The piecewise model provides the ability to separate out distinct physical phenomena (similar to the frequency-domain component-based model) within each physical region, established by ship-specific geometry. The method presented was developed with the intention to further expand the application and utility of traditional total ship roll damping models, which model roll damping behavior using a coefficient-based method. This will provide additional capability for existing numerical tools used to predict ship motions, while other, more advanced methods are developed and used for practical studies.

By considering the discrete physical events, which alter the damping properties of ship motion behaviour during large amplitude roll motion, a series of damping coefficients for these different regions can be obtained. These can be included in a look-up table and used for ship motions evaluation. An example was shown using the method, with considerations for bilge keel emergence. Despite the formulation of the method to only consider periodic roll, similar to excitation from regular waves, the damping coefficient information can be used to predict ship motion from a stochastic excitation, in a numerical time-domain solver that uses a sectional formulation. The ability to account for additional degrees-of-freedom, forward speed effects, and the local wave-field, is possible using a sectional time-domain approach. However, some additional considerations should still be addressed for practical implementation.

Limitations associated with applications of existing bilge keel force models in potential flow simulations to large amplitude roll motions were discussed. The dependency of existing models on the Keulegan-Carpenter number in the calculation of the hydrodynamic unit normal force on the bilge keel were discussed. The bilge keel force model for large amplitude roll motion also builds on existing formulations, but provides consideration of the effects of bilge keel emergence and immersion, which was previously neglected. This event significantly impacts the roll damping and resulting ship motions behavior during large amplitude motions.

Several additional conceptual models were proposed to consider physical phenomena associated with large amplitude roll motions in the model for bilge keel force. These included a model for the wave-making due to bilge keels, as they get closer to the free surface and wave-generation becomes a more significant source of energy dissipation than in the smaller roll amplitude regime. Additionally, several bilge keel force model formulations beyond the piecewise model were proposed for consideration of the transition of the bilge keel at the free-surface during large amplitude roll motions. Three more realistic formulations to address force behavior associated with the asymptotic behavior near the transition and the rate of change of the

bilge keel force during the transition across the free surface boundary, either bilge keel emergence or re-entry.

Although 2D-based, both the piecewise method and the bilge keel force model can be applied to a 3D ship with forward speed. Although the physics are more complex for a 3D body with forward speed, a sectional formulation can be used to consider the primary effects of large amplitude motions on the roll damping properties in heavy weather conditions.

The development of a mature method using conversion of the frequency-domain component-based model to the time-domain has yet to be realized, and may encounter difficulties due to the linear assumptions necessary to enable this conversion. At this time, continued development of this conversion approach is necessary. Likewise, the nature of the bilge keel force model and its reliance on empirical coefficients result in this model being less than ideal for robust application to ship roll motion prediction in heavy weather. Therefore, from the initial development undertaken in the present study, the piecewise approach appears to be the most likely model to enable consideration of the physical phenomena affecting damping during large amplitude roll motions, to enable robust application in time-domain ship motions prediction numerical tools.

7.2 Areas for Future Work

Some areas for future work still remain. Multiple degree-of-freedom (such as sway, heave, and pitch) are not typically explicitly considered in roll damping models. Given the sectional formulation for both models, the additional effects of heave and pitch can be implicitly considered in the instantaneous relative position of the bilge keel and the free surface. However, the effect of vortex shedding during these MDoF conditions remains the subject of future study.

Also the consideration and significance of memory effects in specific roll damping components, particularly bilge keel vortex shedding, should be investigated. Based on the observations from the 3D numerical simulations presented in this work, the complexity of the vortex shedding, at slow forward speed conditions, is important to consider, particularly for dead ship condition type dynamic stability failure events. At moderate and high forward speed, the vortex convection downstream provides a mechanism to quickly transfer this energy away from the hull, and additional interactions, resulting in complex vortex shedding behavior, is not observed. To accurately quantify and characterize vortex shedding, scaling effects are important and full-scale URANS simulations should be used.

Lastly, the development of a computationally fast bilge keel force model, which has the ability to predict the effects of subtle geometry variations is important. Modern considerations for ship design may result in changes not only to the hull, but also to the appendages, such as along the span and the tip geometry of the bilge keels (this is the subject of ongoing work by the author and two colleagues[16]). Without a bilge keel force model that can consider these effects, large numbers of design variations may not be accurately assessed using computationally fast, potential flow-based, ship motion prediction methods.

[16] U.S. Patent Application #100,414, C. Bassler, S. Percival, and M. Dipper

References

Adams, H. C. (1938), “Some Notes on the Use of Models in the Study of the Rolling of Ships,” *Trans. SNAME*, 46.

Andronov, A., S. E. Khaikin, and A. A. Vitt (1966), *Theory of Oscillators*, New York: Dover Publications Reprint (1987).

Archimedes (c. 260 BCE), in Heath, T. L. (trans.), *The Works of Archimedes*, Dover, 2002, pp. 91–93.

Atsavapranee, P., J. B. Carneal, D. Grant, and A. S. Percival (2007), “Experimental Investigation of Viscous Roll Damping on the DTMB Model 5617 Hull Form,” *Proc. 26th Intl. Conf. on Offshore Mechanics and Arctic Engineering*, San Diego, CA.

Bassler, C. (2007), “Roll Damping Models: Applications to Wave-Piercing Tumblehome Hull Forms,” *Proc. 28th American Towing Tank Conf.*, Ann Arbor, MI. (presentation only)

Bassler, C. (2008a), “Application of Parametric Roll Criteria to Naval Vessels,” *Proc. 10th Intl. Ship Stability Workshop*, Daejeon, Korea, 23-25 March.

Bassler, C. (2008b), “Roll Damping Mechanisms for a Wave-Piercing Tumblehome Hull Form,” *Proc. 6th Osaka Colloquium on Seakeeping and Stability of Ships*, Osaka, Japan.

Bassler, C. C. and A. M. Reed (2009), “An Analysis of the Bilge Keel Roll Damping Component Model,” *Proc. 10th Intl. Conf. on Stability of Ships and Ocean Vehicles*, St. Petersburg, Russia, 22-26 June.

Bassler, C., J. Carneal, and P. Atsavapranee (2007), “Experimental Investigation of Hydrodynamic Coefficients of a Wave-Piercing Tumblehome Hull Form,” *Proc. 26th Intl. Conf. on Offshore Mechanics and Arctic Engineering*, San Diego, CA.

Bassler, C. A. Peters, B. Campbell, W. Belknap, and L. S. McCue (2007a), "Dynamic Stability of Flared and Tumblehome Hull Forms in Waves," *Proc. 9th Intl. Ship Stability Workshop*, Hamburg, Germany, August.

Bassler, C. C., V. Belenky, G.. Bulian, A. Francescutto, K. Spyrou, and N. Umeda (2009), “A Review of Available Methods for Application to Second Level Vulnerability Criteria,” *Proc. 10th Intl. Conf. on Stability of Ships and Ocean Vehicles*, St. Petersburg, Russia, 22-26 June.

Bassler, C. C., A. M. Reed, and A. J. Brown (2010), “A Method to Model Large Amplitude Ship Roll Damping,” *Proc. 11th Intl. Ship Stability Workshop*, June.

Bassler, C. C., A. M. Reed, and A. J. Brown (2010a), “Characterization of Physical Phenomena for Large Amplitude Ship Roll Motion,” *Proc. 29th American Towing Tank Conf.*, Annapolis, MD, August.

Bassler, C. C., A. M. Reed, & A. J. Brown (2011) “A Piecewise Model for Prediction of Large Amplitude Ship Roll Damping,” *Proc. 30th Intl. Conf. Ocean, Offshore and Arctic Engineering*, Rotterdam, The Netherlands, June.

Bassler, C., R. Miller. A. Reed, and A. Brown (2011), “Considerations for Bilge Keel Force Models in Potential Flow Simulations of Ship Maneuvering in Waves,” *Proc. 12th Intl. Ship Stability Workshop*, Alexandria, VA, June.

Bassler, C. and R. Miller (2011), "Three-Dimensional Effects for a Ship Experiencing Large Amplitude Roll Motion," *Proc 30th Intl. Conf. on Ocean, Offshore and Arctic Engineering (OMAE2011),* Rotterdam, The Netherlands, 19-24 June.

Baitis, A. E., W. G. Meyers & T. R. Applebee (1981) "Validation of the Standard Ship Motion Program, SMP: Improved Roll Damping Prediction," Hydromechanics Dept. Technical Report, DTNSRDC Report SPD-0936-02.

Beck, R. F. and A. M. Reed (2001), "Modern Computational Methods for Ships in a Seaway," *Trans. SNAME,* Vol. 109, 1-51.

Belenky, V. L. (1999), "Piecewise Linear Approach to Nonlinear Dynamics of Ships," *Bulletin of National Research Institute of Fisheries Engineering*, Hasaki, Japan, No. 20, August, pp.21-40.

Belenky, V. L. (2000), "Piecewise Linear Approach to Nonlinear Ship Dynamics," in *Contemporary Ideas on Ship Stability*, New York: Elsevier, pp.149-160.

Belenky, V. and N. B. Sevastianov (2007), *Stability and Safety of Ships: Risk of Capsizing*, Jersey City, NJ: Society of Naval Architects and Marine Engineers, pp. 128-130.

Belenky, V. L., K. M. Weems, & W. M. Lin (2008), "Numerical Procedure for Evaluation of Capsizing Probability with Split Time Method," *Proc. 27th Symp. Naval Hydrodynamics.* Seoul, Korea.

Belenky, V., A. M. Reed, & K. M. Weems (2009), "Probability of Capsizing in Beam Seas with Piecewise Linear Stochastic GZ Curve," *Proc. 10th Intl. Conference on Stability of Ships and Ocean Vehicles.* St. Petersburg, Russia.

Belenky, V., C. Bassler, and W. Peters (2010), "Summary of Proposed Methods for Intact Stability Vulnerability Evaluation and a Framework for Direct Assessment," *Proc. 2nd Intl. Workshop on Dynamic Stability Considerations in Ship Design*, Windsor, UK, 2-3 September.

Belenky, V., C. Bassler, M. Dipper, B. Campbell, K. Weems, and K. Spyrou (2010a), "Direct Assessment Methods for Nonlinear Ship Response in Severe Seas," *ITTC Workshop on Seakeeping*, Seoul, Korea, 19-21 Oct.

Belenky, V., K. Weems, C. Bassler, M. Dipper, B. Campbell, and K. Spyrou (2012), "Approaches to Rare Eventsa in Stochastic Dynamics of Ships," *Probabilistic Engineering Mechanics*, 28, pp.30-38, April.

Belknap, W. and A. M. Reed (2010), "TEMPEST: A New Computationally Efficient Dynamic Stability Prediction Tool," *Proc. 11th Intl. Ship Stability Workshop*, June.

Belknap, W., C. Bassler, M. Hughes, P. Bandyk, K. Maki, D. H. Kim, R. Beck, and A. Troesch (2010), "Comparisons of Body-Exact Force Computations in Large Amplitude Motion," *Proc. 28th Symp. on Naval Hydrodynamics*, Pasadena, CA, 12-17 September.

Bishop, R., P. Atsavapranee, S. Percival, J. Shan, & A. Engle (2004) "An Investigation of Viscous Roll Damping Through the Application of Particle-Image Velocimetry" *25th Symp. on Naval Hydrodynamics*, St. John's, Canada.

Bishop, R. C., W. Belknap, C. Turner, B. Simon, and J. H. Kim (2005), "Parametric Investigation on the Influence of GM, Roll Damping, and Above-Water Form on the Roll Response of Model 5613," Hydromechanics Dept. Technical Report, NSWCCD-50-TR-2005/027.

Blok, J. J. and A. B. Aalbers (1991), "Roll Damping Due to Lift Effects on High Speed Monohulls," *Proc. FAST '91*.

Boger D.A & J. J. Dreyer J.J. (2006), "Prediction of Hydrodynamic Forces and Moments for Underwater Vehicles Using Overset Grids," *Proc 44th AIAA Aerospace Sciences Meeting*, Reno, Nevada.

Bolton, W. E. (1972), "The Effect of Bilge Keel Size on Roll Reduction," Admiralty Experiment Works Report.

Brown, A. J. and F. Deybach (1998), "Towards a Rational Intact Stability Criteria for Naval Ships," *Naval Engineers J.*, January

Bryan, G. H. (1900), "The Action of Bilge Keels," *Trans. of the Royal Institution of Naval Architects*, 4.

Bulian, G.., A. Francescutto, & C. Lugni (2006), "On the Nonlinear Modeling of Parametric Rolling in Regular and Irregular Waves," *Intl. Shipbuilding Progress*, 51(2-3), pp. 173-203.

Cao, Q., M. Wiercigroch, E. E. Pavlovskaia, C. Grebogi, and J. M. T. Thompson (2006), "Archetypal Oscillator for Smooth and Discontinuous Dynamics," Physical Review E, 74.

Carrica P. M., R. V. Wilson, R. Noack, T. Xing, M. Kandasamy, J. Shao1, N. Sakamoto, & F. Stern (2006), "A Dynamic Overset, Single-Phase Level Set Approach for Viscous Ship Flows and Large Amplitude Motions and Maneuvering," *Proc 26th Symp. on Naval Hydro.*, Rome, Italy.

Carrica, P.M., R. V. Wilson, R. W. Noack, & F. Stern, (2007a), "Ship Motions Using Single-Phase Level Set with Dynamic Overset Grids," *Computers and Fluids*, 36, pp. 1415-1433.

Carrica, P.M., R. V. Wilson, & F. Stern (2007b), "An Unsteady Single-Phase Level Set Method for Viscous Free Surface Flows," *Intl. J. Numerical Methods in Fluids*, 53, pp. 229-256.

Cartwright, M. L. and J. E. Littlewood (1945), "On Nonlinear Differential Equations of the Second Order, I.," *J. Lond. Math. Soc.*, 20, p. 180-189.

Cotton, B. and K. J. Spyrou (2000), "Experimental and Theoretical Studies of Large Amplitude Ship Rolling and Capsize," *Proc. 7th Intl. Conf. on Stability of Ships and Ocean Vehicles*, February, Launceston, Australia.

Cox, G. C. and A. R. Lloyd (1977), "Hydrodynamic Design Basis for Navy Ship Roll Motion Stabilization," *Trans. SNAME*, 85.

Cummins, W. E. (1962), "The Impulse Response Function and Ship Motions," *Proc. Symp. On Ship Theory, Institut fur Schiffbau der Universitat Hamburg*, 25-27 January (also available as NSRDC Report 1661, October).

Dalzell, J. F. (1984), "Approximations to the Probability Density of Maxima and Minima of the Response of a Nonlinear System," NSRDC Report, EW-22-84, October.

Dai, L. (2008), Nonlinear Dynamics of Piecewise Constant Systems and Implementation of Piecewise Constant Arguments, New Jersey: World Scientific Publishing Co.

Dai, C.M., Miller, R.W, & Percival A.S. (2009), "Hydrodynamic Effects of Bilge Keels on the Hull Flow During Steady Turns," *Proc. 28th Intl. Conf. Ocean, Offshore and Arctic Engineering*, Honolulu, Hawaii.

Dalzell, J. F. (1978), “Note on the Form of Ship Roll Damping,” *J. Ship Research*, 22 (3), pp. 178–185.

Davidson, K. S. M. (1945), “Some Notes on Seaworthiness with Special Reference to Bilge Keels,” *Trans. SNAME*, 53.

de Jong, P. and J. A. Keuning (2006), “6-DOF Forced Oscillation Tests for the Evaluation of Nonlinearities in the Superposition of Ship Motions,” *Intl. Shipbuilding Progress*, 53 (2), pp. 123-143.

de Kat, J. (1988), “Large Amplitude Ship Motions and Capsizing in Severe Sea Conditions,” Ph.D. Thesis, University of California, Berkeley.

Duffing, G. (1918), Erzwungene Schwingungen bei Veranderlicher Eigenfrequenz, Vieweg: Braunschweig.

EMB (1920), “Revised Report of Pitching and Roll Experiments on a Model of Battle Cruisers 1 to 6: With and Without Bilge Keels,” United States Experimental Model Basin, January.

EMB (1931), “Rolling in Waves: Effect of Variations of Form on Roll,” United States Experimental Model Basin, Report No. 303, June.

Etebari, A., P. Atsavapranee, C. Bassler, and J. Carneal (2008), “Experimental Analysis of Rudder Contribution to Roll Damping,” *Proc. 27th Intl. Conf. on Offshore Mechanics and Arctic Engineering*, Estoril, Portugal.

Falzarano, J. M. (1990), “Predicting Complicated Dynamics Leading to Vessel Capsizing,” *Ph.D. Dissertation*, U. Michigan.

Falzarano, J. M., S. W. Shaw, and A. W. Troesch (1992), “Application of Global Method for Analyzing Dynamical Systems to Ship Rolling Motion and Capsizing,” *Intl. J. of Bifurcations and Chaos*, 2(1), pp. 101-115.

Falzarano, J., J. Cheng, S. Das, W. Rodrigues, and R. Vassilev (2000), “MOB Transient Dynamics and Stability,” *Proc. 10th Intl. Offshore and Polar Engineering Conf.*, Seattle, 28 May-2 June.

Felice, J. Longo, and F. Stern (2006), “Comparisons of Free Roll Decay Tests for Model DTMB 5415/2340/5512, and Investigation of Lateral Hydrodynamic Loads on Bilge Keels,” *Proc. 26th Symp. on Naval Hydrodynamics*, Rome, Italy, 17-22 September.

Froude, W. (1865), “On the Practical Limits of the Rolling of a Ship in a Seaway,” *Trans. Institution of Naval Architects*, 6.

Fullerton, A. M., T. C. Fu and Y. S. Hong (2006), “The Induced Forces and Motions of a Tumblehome Hullform Undergoing Forced Roll,” *Proc. 26th Symp. on Naval Hydrodynamics*, Rome.

Fullerton, A. M., T. C. Fu and A. M. Reed (2008), “The Moments on a Tumblehome Hull Form Undergoing Forced Roll,” *Proc. 27th Symp. on Naval Hydrodynamics*, Seoul.

Gawn, R. W. L. (1940), “Rolling Experiments with Ships and Models in Still Water,” *Trans. of the Royal Institution of Naval Architects*, 82.

Gersten, A. (1969), “Roll Damping of Circular Cylinders With and Without Appendages,” Naval Ship Research and Development Center, Report 2621.

Gersten, A. (1971), “Scaling Effects in Roll Damping,” *Proc. 16th American Towing Tank Conf.*, Sao Paulo, Brazil, August.

Gleick, J. (1987), *Chaos: Making a New Science*. New York: Viking.

Grant, D. J. (2008) “Full Scale Investigation of Bilge Keel Effectiveness at Forward Speed,” M.S. Thesis, Virginia Tech.

Grant, D. J., A. Etebari, and P. Atsavapranee (2007), “Experimental Investigation of Roll and Heave Excitation and Damping in Beam Wave Fields,” *Proc. 26th Intl. Conf. on Offshore Mechanics and Arctic Engineering*, San Diego, CA.

Grant, D., C. Bassler, S. Percival, and D. Walker (2010), “Design and Use of a 3DoF Motion Mechanism for Large Amplitude Forced Oscillation Model Testing,” *Proc. 29th American Towing Tank Conf. (ATTC)*, Annapolis, MD, August.

Greeley, D. S. and B. J. Petersen (2010), “Efficient Time-Domain Computation of Bilge Keel Forces,”*Proc. 23rd Symp. on Naval Hydrodynamics*, Pasadena, CA, 12-17 September.

Grochowalski, S. (1990) “Hydrodynamic Phenomenon Generated By Bulwark Submergence and its Influence On Ship Susceptibility to Capsizing,” *Proc. 4th Intl. Conf. Stability of Ships and Ocean Vehicles*, Gdansk.

Grochowalski, S., C. C. Hsiung, Z. J. Huang & L. Z. Cong (1998) “Theoretical Modeling of Ship Motions and Capsizing in Large Steep Waves.” *Trans. SNAME*, 106:241-267.

Guckenheimer, J. and P. Holmes (1983), Nonlinear Oscillations, Dynamical Systems, and Bifurcations of Vector Fields, New York: Springer-Verlag.

Haddara, M. R. (1973), “On Nonlinear Rolling of Ships in Random Seas,” *Intl. Shipbuilding Progress*, 20.

Hamilton, J., S. Fish, and D. Anthony (1993), “Flow Field Measurements at Free Surface Using Digital Particle Image Velocimetry,” *Proc. 23rd American Towing Tank Conference*, New Orleans, LA, pp.253-259.

Hayashi, C., Y. Ueda, N. Akamatsu and H. Itakura (1970), “On the Behavior of Self-Oscillatory Systems with External Force,” *Trans. IECE Japan*, 53A (3), pp. 150–158.

Hayden, D. D., R. C. Bishop, J. T. Park, and S. M. Laverty (2006), “Model 5514 Capsize Experiments Representing the Pre-Contract DDG51 Hull Form at End of Service Life Conditions,” Hydromechanics Dept. Report, NSWCCD-50-TR-2006/020, April.

He, Q., S. Zhu, & J. Lou (2006), “Study on the Computation Method of Bilinear System with Piecewise Damping,” *Proc. ASME 2006 Intl. Mechanical Engineering Congress and Expo.*, 5-10 Nov., Chicago.

Himeno, Y. (1981), “Prediction of Ship Roll Damping-State of the Art,” U. Michigan Dept. of Naval Arch. and Marine Engineering, Report 239.

Hutchinson, B.L. (1991) “The Transverse Plane Motions of Ships,” *Marine Technology*, 28 (2).

Ikeda, Y., Y. Himeno, and N. Tanaka (1978a), “On Roll Damping Force of Ship- Effect of Friction on Hull and Normal Force of Bilge Keels,” Report of the Department of Naval Architecture, University of Osaka Prefecture, No. 00401. (see also Ikeda, Y., Y. Himeno, and N. Tanaka (1976), “On Roll Damping Force of Ship – Effects of Friction of Hull and Normal Force of Bilge Keels,” *J. Kansai Society of Naval Architecture, Japan*, 161, pp.41-49.)

Ikeda, Y., K. Komatsu, Y. Himeno, and N. Tanaka (1978b), "On Roll Damping Force of Ship-Effect of Hull Surface Pressure Created by Bilge Keels," Report of the Department of Naval Architecture, University of Osaka Prefecture, No. 00402. (see also Ikeda, Y., K. Komatsu, Y. Himeno and N. Tanaka (1977), "On Roll Damping Force of Ship – Effects of Hull Surface Pressure Created by Bilge-Keels," *J. Kansai Society of Naval Architecture, Japan*, 165, pp.31-40.)

Ikeda, Y., Y. Himeno, and N. Tanaka (1978c), "On Eddy Making Component of Roll Damping Force on Naked Hull," Report of the Department of Naval Architecture, University of Osaka Prefecture, No. 00403. (see also Ikeda, Y., Y. Himeno and N. Tanaka (1977), "On Eddy Making Component of Roll Damping Force on Naked Hull," *J. Society of Naval Architects of Japan*, 142, pp.59-69).

Ikeda, Y., Y. Himeno, and N. Tanaka (1978d), "Components of Roll Damping of Ship at Forward Speed," Report of the Department of Naval Architecture, University of Osaka Prefecture, No. 00404. (see also Ikeda, Y., Y. Himeno, and N. Tanaka (1978), "Component of Roll Damping of Ship at Forward Speed," *J. Society of Naval Architects of Japan*, 143, pp.121-133, in Japanese).

Ikeda, Y., Y. Himeno, and N. Tanaka (1978e), "A Prediction Method for Ship Roll Damping," Report of the Department of Naval Architecture, University of Osaka Prefecture, No. 00405.

Ikeda, Y., T. Fujiwara, Y. Himeno, and N. Tanaka (1979), "Velocity Field Around Ship Hull During Roll Motion," Report of the Department of Naval Architecture, University of Osaka Prefecture, No. 00406. (see also Ikeda, Y., T. Fujiwara, Y. Himeno, and N. Tanaka, 1978f, "Velocity Field Around Ship Hull During Roll Motion," *J. Society of Naval Architects of Japan*, 171).

Ikeda, Y. (1984), "Roll Damping," *Proc. 1st Symp. on Stability of Ships*, Society of Naval Architecs of Japan, pp.241-250.

Ikeda, Y. and T. Katayama (2000), "Roll Damping Prediction Method for a High-Speed Planing Craft," *Proc. 7th Intl. Conf. on the Stability of Ships and Ocean Vehicles*, Tasmania, Australia.

Ikeda, Y. (2004), "Prediction Methods of Roll Damping of Ships and Their Application to Determine Optimum Stabilization Devices," *Marine Technology*, 41(2), April.

IMO (2008), "Draft Terminology for the New Generation Intact Stability Criteria," International Maritime Organization SLF 51/WP.2, Annex 2, 16 July.

IMO (2008), MSC. Res. 267(85), "Adoption of the International Code on Intact Stability, 2008 (2008 IS Code)," 4 December, London, UK.

Irvine, M., P. Atsavapranee, J. Carneal, A. Engle, S. Percival, R. Bishop, D.Grant, C. Lugni, F. Di Kan, M., T. Saruta, and H. Taguchi (1992), "Capsizing of a Ship in Quartering Waves," *Naval Architecture and Ocean Engineering*, The Society of Naval Architects of Japan, Vol. 29.

Jiang. C. A. W. Troesch, and S. W. Shaw (2000), "Capsize Criteria for Ship Models with Memory-Dependent Hydrodynamics and Random Excitation," *Phil. Trans. R. Soc. London A*, 358, pp. 1761-1791.

Kaplan, P. (1966), "Lecture Notes on Nonlinear Theory of Ship Roll Motion in a Random Seaway," *Proc. 11th Intl. Towing Tank Conf. (ITTC).*

Katayama, T., T. Taniguchi, and M. Kotaki (2008), “A Study on Viscous Effects of Roll Damping of a High-Speed Catamaran and a High-Speed Trimaran,” *Proc. 6th Osaka Colloquium on Seakeeping and Stability of Ships*, Osaka, Japan.

Kato, H. (1957), “On the Frictional Resistance to the Rolling of Ships,” *J. Society of Naval Architect of Japan*, 102, pp.115-122 (in Japanese).

Kato, H. (1965) “Effect of Bilge Keels on the Rolling of Ships.” *J. Soc. Naval Arch., Japan*, 117, pp. 93–114.

Kawahara, Y., K. Maekawa & Y. Ikeda (2009) “A Simple Prediction Formula of Roll Damping of Conventional Cargo Ships on the Basis of Ikeda’s Method and Its Limitation,” *Proc. 10th Intl. Conf. on Stability of Ships and Ocean Vehicles*, St. Petersburg, Russia.

Keulegan, G. M. and L. H. Carpenter (1958), “Forces on Cylinders and Plates in an Oscillating Fluid,” *J. Research of the National Bureau of Standards*, 60.

Klaka, K., J. D. Penrose, R. R. Horsley, and M. R. Renilson (2007), “Hydrodynamic Tests on a Plate in Forced Oscillation,” *Ocean Engineering*, 34, pp. 1225-1234.

Kleczka, M., E. Kreuzer, & W. Schiehlen (1992), “Local and Global Stability of a Piecewise Linear Oscillator,” *Phil. Trans.: Physical Sciences and Engineering*, 338 (1651), pp. 533-546.

Korpus, R. A. and J. M. Falzarano (1997), “Prediction of Viscous Ship Roll Damping by Unsteady Navier-Stokes Techniques,” *J. Offshore Mechanics and Arctic Engineering*, 119, pp. 108-113.

Landweber, L. and M. C. Macagno (1957), “Added Mass of Two-Dimensional Forms Oscillating in a Free Surface,” *J. of Ship Research*, 1, pp. 20-30.

Lee, C.-H., (1995), “WAMIT Theory Manual,” Massachusetts Institute of Technology, Department of Ocean Engineering, Report No. 95-2, October 1995.

Lofft, R. F. (1973), “RFA Engadine: The Effect of Bilge Keel Size on Rolling and Motion in Head Seas,” Admiralty Experiment Works Report 16/17.

Levinson, N. (1949), “A Second-Order Differential Equation with Singular Solutions,” *Ann. Math.*, 50, pp.127-153.

Lewandowski, E. M. (2004), *The Dynamics of Marine Craft: Maneuvering and Seakeeping*. New Jersey: World Scientific.

Lewison, G. R.G. (1976), “Optimum Design of Passive Roll Stabilizer Tanks,” *The Naval Architect*.

Lin, W. M., and D.K.P. Yue (1990), “Numerical Solutions for Large-Amplitude Ship Motions in the Time-Domain,” *Proc. 18th Symp. on Naval Hydrodynamics*, Ann Arbor, MI.

Lin, W. M., S. Zhang, K. Weems, and D. Liut (2006), “Numerical Simulations of Ship Maneuvering in Waves,” *Proc. 26th Symp. on Naval Hydrodynamics*, Rome, Italy.

Liut, D. A. (1999), “Neural-Network and Fuzzy-Logic Learning and Control of Linear and Nonlinear Dynamic Systems,” *Ph.D. Dissertation*, Virginia Tech.

Liut, D. A. and W.M. Lin (2006), “A Lagrangian Vortex-Lattice Method for Arbitrary Bodies Interacting with a Linearized Semi-Lagrangian Free Surface,” *Intl. Shipbuilding Progress*, 53, pp. 1-32.

Lloyd, A. R. J. M. (1998), *Seakeeping: Ship Behaviour in Rough Weather*. London: International Book Distributors, Ltd.

Lorenz, E.N., "Deterministic Non-Periodic Flow," *J. Atmosperic Sci.* 20, 130–141, 1963.

Ma, Q. (2005), "A Study of the Dynamic Behavior of Piecewise Nonlinear Oscillators with Time-Varying Stiffness," PhD Dissertation, The Ohio State University.

Ma, Q. & A. Kahraman (2005), "Period-One Motions of a Mechanical Oscillator with Periodically Time-Varying, Piecewise-Nonlinear Stiffness," *J. Sound and Vibration*, 284 (3-5), pp. 893-914.

Martin, M. (1958), "Roll Damping Due to Bilge Keels," Iowa University Institute of Hydraulics Research Report to the Office of Naval Research.

McCue, L.S. and B. Campbell (2007), "Approximation of Ship Equations of Motion from Time Series Data," *Proc. 9th Intl. Ship Stability Workshop*, Hamburg, Germany, August.

McCue, L. S., B. L. Campbell, and W. F. Belknap (2007), "On the Parametric Resonance of Tumblehome Hullforms in a Longitudinal Seaway," *Naval Engineers Journal*, 3, pp. 35-44.

McNowan, J. S. and L. W. Wolf (1956), "Resistance to Unsteady Flow: I. Analysis of Tests with Flat Plate," Engineering Research Institute, U. Michigan, 2446-I-P (Internal Report to Sandia Corp.), June.

McEntee, W. (1920), "Revised Report of Pitching and Roll Experiments on a Model of Battle Cruisers 1 to 6: With and Without Bilge Keels," United States Experimental Model Basin, January.

McEntee, W. (1931), "Rolling in Waves: Effect of Variations of Form on Roll," United States Experimental Model Basin, Report No. 303, June.

Meirovitch, L. (1970), *Methods of Analytical Dynamics*, Dover Publications (Reprint, 2003).

Meirovitch, L. (2001) *Fundamentals of Vibrations*, New York:McGraw-Hill.

Menter, F. R. (1994), "Two-Equation Eddy Viscosity Turbulence Models for Engineering Applications," *AIAA J.*, 32, pp. 1598-1605.

Miller, E. R., J. J. Slager, and W. C. Webster (1974), "Development of a Technical Practice for Roll Stabilization System Selection," NAVSEC Report 6136-74-280.

Miller, R. W., J. J. Gorski, and D. Fry (2002), "Viscous Roll Predictions of a Circular Cylinder with Bilge Keels," *Proc. 24th Symp. on Naval Hydro*., Fukuoka, Japan.

Miller, R. W., C. C. Bassler, P. Atsavapranee, and J. J. Gorski (2008), "Viscous Roll Predictions for Naval Surface Ships Appended with Bilge Keels Using URANS," *Proc. 27th Symp. on Naval Hydrodynamics*, Seoul, South Korea.

Minnick, L. M., C. C. Bassler, and S. Percival (2012), "Analysis of the Physics of Bilge Keel Vortex Generation," *Proc. 31st Intl. Conf. on Ocean, Offshore, and Arctic Engineering*, Rio de Janeiro, Brazil, June 10-15.

Minorsky, N. (1962), *Nonlinear Oscillators*, New Jersey: D. Van Nostrand Company, Inc.

Morison, J. R., M. P. O'Brien, J. W. Johnson, and S. A. Schaaf (1950), "The Forces Exerted by Surface Waves on Piles," *Petroleum Trans.*, AIME, 189, pp. 149-157.

Morison, J. R., J. W. Johnson, and M. P. O'Brien (1953), "Experimental Studies of Forces on Piles," *Proc. 4th Conf. Coastal Engineering*.

Natsiavas, S. (1990), "On the Dynamics of Oscillators with Bi-Linear Damping and Stiffness," *Intl. J. of Non-Linear Mechanics*, 25 (5), pp.535-554.

Natsiavas, S. (1991), "Dynamics of Piecewise Linear Oscillators with Van der Pol Type Damping," *Intl. J. of Non-Linear Mechanics*, 26 (3-4), pp.349-366.

Newton, I. (1687), Philosophiae Naturalis Principia Mathematica.

Noack R. (2005), "SUGGAR: A General Capability for Moving Body Overset Grid Assembly," *Proc 17th AIAA Computational Fluid Dynamics Conf.*, Toronto, Ontario, Canada.

O'Dea, J. F. (2001), "Prediction of Second Order (Quadratic Forces)," NSWCCD 5500 Internal Memo, 19 June.

Poincaré, H. J. (1890), "Sur le problème des trois corps et les équations de la dynamique," *Acta Mathematica*, 13, 1–270.

Rayleigh, J. W. S. (1896), *The Theory of Sound*, New York: Dover Publications (Reprint).

Reed, A. M. (2009), "A Naval Perspective on Ship Stability," *Proc. 10th Intl. Conf. on Stability of Ships and Ocean Vehicles*, St. Petersburg, Russia, 22-26 June.

Ridjanovic, M. (1962), "Drag Coefficients of Flat Plates Oscillating Normally to Their Planes," *Schiffstechnik*, Bd. 9, Heft 45.

Roberts, J. B. and P. D. Spanos (2003), *Random Vibration and Statistical Linearization*, New York: Dover Publications, Inc.

Roddier, D., S. W. Liao, and R. W. Yeung (2000), "On Freely-Floating Cylinders Fitted with Bilge Keels," *Proc. 10th Intl. Offshore and Polar Engineering Conference*.

Rugh, W. J. (1981), *Nonlinear System Theory: The Volterra/Wiener Approach*. Baltimore: The Johns Hopkins University Press.

Sarchin, T. H., and L. L. Goldberg (1962), "Stability and Buoyancy Criteria for U.S. Naval Surface Ships," *Trans. SNAME*, 70, pp. 418–458.

Sarpkaya, T. (1981), "A Critical Assessment of Morison's Equation and Its Applications," *Proc. Intl. Conf. on Hydrodynamics in Ocean Engineering*, Trondheim, Norway, pp. 447-467.

Sarpkaya, T. and M. Isaacson (1981), *Mechanics of Wave Forces on Offshore Structures*. New York: Van Nostrand Reinhold Co.

Sarpkaya, T. and J. L. O'Keefe (1996), "Oscillating Flow Around Two and Three-Dimensional Bilge Keels," *J. Offshore Mechanics and Arctic Engineering*, 118, pp. 1-6.

Sasajima, H. (1954), "On the Action of Bilge Keels in Ship Rolling," *J. Society of Naval Architects of Japan*, 86 (in Japanese).

Schmitke, R. T. (1978), "Ship Sway, Roll, and Yaw Motions in Oblique Seas," *Trans. SNAME*, Vol. 86 pp. 26-46.

Seah, R. K. M. (2007), "The SSFSRVM Computational Model for Three-Dimensional Ship Flows With Viscosity," Ph.D. Dissertation, University of California Berkeley.

Seah, R. K. M. and R. W. Yeung (2008), “Vortical-Flow Modeling for Ship Hulls in Forward and Lateral Motion,” *Proc. 27th Symp. on Naval Hydrodynamics*, Seoul, South Korea.

Stefun, G.. P. (1955), “The Roll Damping of a Cylinder with Half-Circular Sections,” David Taylor Model Basin, Hydromechanics Laboratory Technical Note, No. 10-55.

Serat, M. E. (1933), “Effect of Form on Roll,” *Trans. SNAME*, 41.

Shaw, R. (1981), “”Strange Attractors, Chaotic Behavior and Information Flow,” *Z. Naturf.*, 36a, pp. 80-112.

Shaw R. (1984), *The Dripping Faucet as a Model Chaotic System*, Aerial Press: Santa Cruz, CA.

Shaw, S. W. & P. Holmes (1983a), “A Periodically Forced Impact Oscillator With Large Dissipation,” *ASME J. Appl. Mech.*, 50, pp. 849-857.

Shaw, S. W. & P. Holmes (1983b), “A Periodically Forced Piecewise Linear Oscillator,” *J. Sound Vib.*, 90, pp. 129-144.

Shaw, S. W. & P. Holmes (1983c), “Periodically Forced Linear Oscillator With Impacts: Chaos and Long-Period Motions,” *Phys. Rev. Lett.*, 51, pp. 623-626.

Shin, Y. S., V. L. Belenky, J. R. Paulling, K. M. Weems, & W. M. Lin (2004), “Criteria for Parametric Roll of Large Containerships in Longitudinal Seas,” *Trans. SNAME*, 112.

Smale, S. (1963), “Diffeomorphisms With Many Periodic Points,” In *Differential and Combinatorial Topology*. S. S. Cairns (Ed.), pp. 63-80, Princeton. NJ: Princeton University Press.

Soliman, M. S. and J. M. T. Thompson (1991), "Transient and Steady State Analysis of Capsize Phenomena," *Applied Ocean Research*, 13(2).

Spear, L. (1896), “Bilge Keels and Rolling Experiments- U.S.S. Oregon,” *Trans. SNAME*, 6.

Spyrou, K. J. (1996), “Dynamic Instability in Quartering Seas: The Behaviour of a Ship During Broaching,” *J. Ship Res.*, 40(1).

Spyrou, K. J. (1997a), “Dynamic Instability in Quartering Seas:- Part II: Analysis of Ship Roll and Capsize for Broaching. *J. Ship Res.*, 40(4).

Spyrou, K. J. (1997b), “Dynamic Instability in Quartering Seas:- Part III: Nonlinear Effects on Periodic Motions,” *J. Ship Res.* 41(3).

Spyrou, K. J. (2000), “The Nonlinear Dynamics of Ships in Broaching,” *Annals of Marie Curie Fellowship Assoc.*, Vol. 1.

Spyrou, K. J. (2004), “Non-Linear Damping Coefficients from an Asymmetric Roll Decay Time Series: An Analytical Method,” *Proceedings of the Institution of Mechanical Engineers, Part M: Journal of Engineering for the Maritime Environment*, 218(1), pp. 11-22.

Spyrou, K. J. and J. M. T. Thompson (2000), “Damping Coefficients for Extreme Rolling and Capsize: An Analytical Approach,” *J. Ship Research*, 44(1).

St. Denis, M. & W. J. Pierson (1953), “On the Motions of Ships in Confused Seas,” *Trans. SNAME*, 61.

Stefun, G.. P. (1955), “The Roll Damping of a Cylinder with Half-Circular Sections,” David Taylor Model Basin, Hydromechanics Laboratory Technical Note, No. 10-55.

Strogatz, S. H. (1994), *Nonlinear Dynamics and Chaos*, Westview Press.

Szabo, Z. & A. Lukacs (2007), "Numerical Stability Analysis of a Forced Two-D.O.F. Oscillator with Bilinear Damping," *J. Comput. Nonlinear Dynamics*, 2 (3), pp. 211-217.

Takagi, M., K. Saito, and S. Nakamura (1984), "Comparisons of Simulation Methods for Motions of a Moored Body in Waves," *Proc. 3rd Annual ASME OMAE Symp.*, New Orleans, pp.214-224.

Takaki, M. and F. Tasai (1973), "On the Hydrodynamics Derivative Coefficients of the Equations of Lateral Motions of Ships," *Trans. West-Japan Society of Naval Architects*, 46 (in Japanese).

Tamiya, S. and T. Komura (1972), "Topics on Ship Rolling Characteristics with Advance Speed," *J. Society of Naval Architects of Japan*, 132, pp.159-168 (in Japanese).

Tanaka, N. (1957), "A Study on the Bilge Keel- Part 1," *J. Society of Naval Architects of Japan*, 101 (in Japanese).

Tanaka, N. (1958), "A Study on the Bilge Keel- Part 2," *J. Society of Naval Architects of Japan*, 103 (in Japanese).

Tanaka, N. (1959), "A Study on the Bilge Keel- Part 3," *J. Society of Naval Architects of Japan*, 105 (in Japanese).

Tanaka, N. (1961), "A Study on the Bilge Keel- Part 4," *J. Society of Naval Architects of Japan*, 109 (in Japanese).

Takaki, M. and F. Tasai (1973), "On the Hydrodynamics Derivative Coefficients of the Equations of Lateral Motions of Ships," *Trans. West-Japan Society of Naval Architects*, 46 (in Japanese).

Tamiya, S. and T. Komura (1972), "Topics on Ship Rolling Characteristics with Advance Speed," *J. Society of Naval Architects of Japan*, 132, pp.159-168 (in Japanese).

Teich, M. C., S. E. Keilson, & S. M. Khanna (1989), "Models of Nonlinear Vibration. II. Oscillator with Bilinear Stiffness," *Acta Otolaryngol, Suppl.* 467, pp. 249-256.

Themelis, N. I. (2008), "Probabilistic Assessment of Ship Dynamic Stability in Waves," *Ph.D. Dissertation*, National Technical University of Athens.

Thews, J. G.. (1938), "Discontinuous Anti-Rolling Keels," U. S. Experimental Model Basin Report No. 450, Washington, D.C

Thompson, J. M. T. and H. B. Stewart (1986), *Nonlinear Dynamics and Chaos*, New York: John Wiley and Sons.

Thompson, J. M. T., A. R. Bokaian, R. Ghaffari (1984), "Subharmonic and Chaotic Motions of Compliant Offshore Structures and Articulated Mooring Towers," *J. Energy Resources Technology*, 106, June.

Todd, F. H. (1953), "Some Further Experiments on Single-Screw Merchant Ship Forms," *Trans. SNAME*, Vol. 61 pp. 516-589.

Ueda, Y., N. Akamatsu, and C. Hayashi (1973), "Computer Simulations and Non-Periodic Oscillations," *Trans. IEICE Japan*, 56A (4), pp. 218–225.

Van der Pol, B. (1927), "Forced Oscillations in a Circuit with Nonlinear Resistance," *Phil. Mag.* (7), 3, pp. 65-80.

Vassilopoulous, L. (1971), “Ship Rolling at Zero Speed in Random Beam Seas with Nonlinear Damping and Restoration,” *J. Ship Research*, 15.

Vugts, J. H. (1968), “The Hydrodynamic Coefficients for Swaying, Heaving, and Rolling of Cylinders in a Free Surface,” NSRC Report 112S.

Westerweel, J. (1997), “Fundamentals of Particle Image Velocimetry,” *Measurement Science & Technology*, 8, pp. 1379-1392.

Wilson, R. V., P. M. Carrica, F. Stern (2006), “Unsteady RANS Method for Ship Motions with Application to Roll for a Surface Combatant,” *Computers and Fluids*, 35, pp. 501-524.

Xu, L, M. W. Lu, and Q. Cao (2002), “Nonlinear Vibrations of Dynamical Systems with a General Form of Piecewise-Linear Viscous Damping By Incremental Harmonic Balance Method,” *Physics Letters A*, 301, pp. 65-73.

Yamanouchi, Y. (1964), “On Some Remarks on the Statistical Estimation of Response Functions of Ships,” *5th Symp. on Naval Hydrodynamics,* Bergen, Norway.

Yeung, R. W, S. W. Liao, and D. Roddier (1998), “Hydrodynamic Coefficients of Rolling Rectangular Cylinders,” *Intl. J. Offshore and Polar Engineering*, 8(4).

Yeung, R. W., D. Roddier, B. Alessandrini, L. Gentaz and S. W. Liao (2000), “On the Roll Hydrodynamics of Cylinders Fitted with Bilge Keels,” *Proc. 23rd Symp. on Naval Hydrodynamics*.

Appendix A: Additional Details on the State-of-the-Art Models

A.1 Overview

This Appendix provides additional details from the discussion presented in Chapter 2, including the equations for roll damping components, calculation of the roll axis, methods for obtaining roll damping, a derivation of a Morison equation based approach for a bilge keel force model, a zero speed bilge keel force model, specification of coefficients in the zero speed model and KC number dependency, and additional considerations for bilge keel force models.

A.2 Equations for Roll Damping Components

Details concerning each of the physical components for damping, and the associated equations for determining them, are given in the sub-sections below.

A.2.1 Hull Friction Damping

Friction damping results from the energy loss due to the skin-friction stresses on the barehull. A formulation for friction damping was presented in Ikeda, et al. (1978a).

The zero speed friction coefficient is given by

$$B_{F0} = \frac{4}{3\pi}\rho \cdot S_f \cdot {r_f}^3 \cdot \phi \cdot \omega \cdot C_f \tag{A.1}$$

where

$$r_f = \frac{1}{\pi}\left(\left(0.887 + 0.145 \cdot C_B\right)\left(1.7d + C_B \cdot B\right) - 2OG\right) \tag{A.2}$$

$$S_f = L\left(1.7d + C_B B\right) \tag{A.3}$$

The total friction component, at speed, is given by

$$B_F = B_{F0}\left(1 + 4.1\frac{U}{\omega \cdot L}\right) \tag{A.4}$$

where the forward speed correction is made using the formulation of Tamiya & Komura (1972).

The friction damping component is determined using Kato's method (Kato, 1957). Here the skin friction coefficient is given by

$$C_f = 1.328\left(\frac{3.22 \cdot {r_{mid}}^2 \cdot \phi^2}{T \cdot \upsilon}\right)^{-\frac{1}{2}} \tag{A.5}$$

where the distance at amidships from the roll axis to the hull surface, or bilge keel, r_{mid}, can be calculated using the formula detailed in the next section, at the midship location..

A.2.2 Hull Eddy Damping

Eddy damping is attributed to the damping resulting from the rapid change in pressure gradient on the bare hull, excluding the effect of waves and bilge keels, resulting in flow separation. The formulation for eddy damping was presented in Ikeda, et al. (1978c). The eddy damping component at zero speed, B_{E0}, is given by

$$B_{E0} = \frac{4}{3\pi}\rho \cdot d(x)^4 \cdot \omega \cdot \phi \cdot C_R \tag{A.6}$$

where

$$B_{E0}(x) = \frac{4}{3\pi}\rho\, d(x)^4\, \phi_A\, \omega \left\{ \left(1 - f_1(x)\frac{R(x)}{d(x)}\right)\left(1 - \frac{OG}{d(x)}\right) + f_2(x)\left(H_0(x) - f_1(x)\frac{R(x)}{d(x)}\right)^2 \right\} C_p(x)\left[\frac{r_{\max}(x)}{d(x)}\right]^2 \tag{A.7}$$

where

$$f_1(x) = 0.5\left[1 + \tanh\left\{20\left(\sigma(x) - 0.7\right)\right\}\right] \tag{A.8}$$

$$f_2(x) = 0.5\left(1 - \cos\pi\sigma(x)\right) - 1.5\left[1 - \exp\left\{-5\left(1 - \sigma(x)\right)\right\}\right]\left(\sin^2\pi\sigma(x)\right) \tag{A.9}$$

$$C_p(x) = 0.5\left\{0.87\exp\left(-\gamma(x)\right) - 4\exp\left(-0.187\gamma(x)\right) + 3\right\} \tag{A.10}$$

The equations for obtaining C_p are taken from Himeno (1981). γ is the ratio of the maximum velocity and mean velocity on the hull surface and is given by

$$\gamma(x) = \frac{\sqrt{\pi}\, f_3(x)}{2d(x)\left(1 - \dfrac{OG}{d(x)}\right)\sqrt{H_0'(x)\sigma'(x)}}\left(r_{\max}(x) + \frac{2M(x)}{H(x)}\sqrt{A(x)^2 + B(x)^2}\right) \tag{A.11}$$

where

$$M(x) = \frac{B(x)}{2(1 + a_1(x) + a_3(x))}$$

$$H_0'(x) = \frac{H_0(x)}{1 - \dfrac{OG}{d(x)}} \tag{A.12}$$

$$\sigma'(x) = \frac{\sigma(x) - \dfrac{OG}{d(x)}}{1 - \dfrac{OG}{d(x)}}$$

and where

$$
\begin{aligned}
H(x) &= 1 + a_1(x)^2 + 9a_3(x)^2 + 2a_1(x)(1-3a_3(x))\cos 2\psi - 6a_3(x)\cos 4\psi \\
A(x) &= -2a_3(x)\cos 5\psi + a_1(x)(1-a_3(x))\cos 3\psi + \left\{\left(6-3a_1(x)\right)a_3(x)^2 + \left(a_1(x)^2 - 3a_1(x)\right)a_3(x) + a_1(x)^2\right\}\cos\psi \\
B(x) &= -2a_3(x)\sin 5\psi + a_1(x)(1-a_3(x))\sin 3\psi + \left\{\left(6+3a_1(x)\right)a_3(x)^2 + \left(3a_1(x) + a_1(x)^2\right)a_3(x) + a_1(x)^2\right\}\sin\psi \\
r_{\max}(x) &= M(x)\left[\left\{\left(1+a_1(x)\right)\sin\psi - a_3(x)\sin 3\psi\right\}^2 + \left\{\left(1-a_1(x)\right)\cos\psi + a_3(x)\cos 3\psi\right\}^2\right]^{1/2}
\end{aligned}
\tag{A.12}
$$

and

$$
a_1(x) = b(x)\left(\frac{1-\dfrac{1}{H_0(x)}}{2}\right), \qquad a_3(x) = b(x)\left(\frac{1+\dfrac{1}{H_0(x)}}{2}\right) \tag{A.13}
$$

where a_1 and a_3 are the Lewis form conformal mapping parameters (Landweber & Macagno, 1957) for the given ship section.

$$
\psi = \begin{Bmatrix} 0 & = \psi_1 \quad when\ r_{\max}(\psi_1) \geq r_{\max}(\psi_2) \\ 0.5\cos^{-1}\left(\dfrac{a_1(x)(1+a_3(x))}{4a_3(x)}\right) & = \psi_2 \quad when\ r_{\max}(\psi_1) < r_{\max}(\psi_2) \end{Bmatrix} \tag{A.14}
$$

and

$$
f_3(x) = 1 + 4\exp\left\{-1.65\times 10^5\left(1-\sigma(x)\right)^2\right\} \tag{A.15}
$$

For simplification, the eddy damping coefficient for zero-speed, for a given ship section, may also be computed using the flat plate formulation, where end-effects are neglected. The coefficient, C_R, in the first formulation for zero-speed eddy-making damping is obtained using,

$$
C_R(x) = 1.5\left(1 - \frac{OG}{d(x)}\right) \tag{A.16}
$$

where this formulation is used to compute the forward and aft end of the ship, for user-specified stations.

The eddy damping component, including forward speed effects, is given by

$$
B_E = B_{E0}\frac{(0.04\cdot\omega\cdot L)^2}{\overline{U}^2 + (0.04\cdot\omega\cdot L)^2} \tag{A.17}
$$

Hull eddy-making damping decreases rapidly with forward speed, and Himeno (1981) states that it becomes small enough to be neglected for Fn > 0.2. This is likely due to the consideration for vortex convection downstream with increased forward speed, as observed in the URANS results presented in Chapter 3 (Figure 3-5).

A.2.3 Hull Lift Damping

The formulation for lift damping on the barehull was presented in Ikeda, et al. (1978e). The lift damping component is given by

$$B_L = \frac{\rho}{2} U \cdot L \cdot d \cdot k_N \cdot l_0 \cdot l_R \cdot \left(1 - 1.4 \frac{OG}{l_R} + 0.7 \frac{OG^2}{l_0 \cdot l_R} \right) \tag{A.18}$$

where

$$l_0 = 0.3d, \qquad l_R = 0.5d \tag{A.19}$$

$$k_N = 2\pi \frac{d}{L} + \kappa \left(4.1 \frac{B}{L} - 0.045 \right) \tag{A.20}$$

and where

$$\kappa = \begin{Bmatrix} 0 & C_M \le 0.92 \\ 0.1 & 0.92 < C_M \le 0.97 \\ 0.3 & 0.97 < C_M < 1.00 \end{Bmatrix} \tag{A.21}$$

A.2.4 Hull Wave-Making Damping

The wave-making damping component is given by the result for B_{44} from the radiation force calculation. This is typically done using a strip-theory, or slender body approach, including forward speed corrections. The forward speed correction to the zero-speed damping coefficient, B_{W0} is given by Ikeda, et al. (1978d). Recent developments to expand calculations of the radiation force to large amplitude motions are given in Belknap & Reed (2010) and Belknap, et al. (2010).

A.2.5 Bilge Keel Damping

Even for small roll amplitudes, the bilge keel component of roll damping is typically nearly half of the total roll damping for a ship, and increases with increasing roll amplitude. A formulation for the bilge keel damping component was presented in Ikeda, et al. (1978a, 1978b, 1978e). The bilge keel damping component is comprised of three sub-components: the normal force on the bilge keel, B_{BKN}, the bilge keel-hull interaction, B_{BKH}, and wave-making due to the bilge keels, B_{BKW}.

$$B_{BK} = B_{BKN} + B_{BKH} + B_{BKW} \tag{A.22}$$

Both the bilge keel normal force and bilge keel-hull interaction components are functionally dependent on the Keulegan-Carpenter number, *KC*, (Keulegan & Carpenter, 1958). Ikeda, et al. (1978e) assumes the bilge keel is attached to the hull at the midpoint of the quarter circle circumscribed by the bilge circle radius.

A.2.5.1 Bilge Keel Normal Force Damping

The bilge keel normal force damping component is related to the drag which occurs on the bilge keels as they oscillate in a fluid. The formula for the bilge keel normal force component of roll damping is given in Ikeda, et al. (1978a). The bilge keel normal force component at zero speed, B_{BKN0}, is given by

$$B_{BKN0}(x) = \frac{8}{3\pi} \rho \cdot r(x)^2 b_{BK}(x)^2 \omega \cdot f(x)^2 \left[\frac{22.5}{\pi \cdot f(x)} + 2.4 \frac{r(x)\phi}{b_{BK}(x)} \right] \tag{A.23}$$

where ρ is the fluid density, r is the distance from the roll axis to the bilge keel, b_{bk} is the bilge keel span, ω is the roll frequency, ϕ is the roll angle, and f is an empirical function of the section coefficient.

$$f(x) = 1 + \left(0.3 \cdot \exp\left(-160\{1 - \sigma(x)\}\right)\right) \tag{A.24}$$

where $\sigma(x)$ is the sectional area coefficient for a given ship section.

The total bilge keel normal force component, B_{BKN}, is given by

$$B_{BKN}(x) = B_{BKN0}(x) + \frac{\pi}{2}\rho\, b_{bk}(x)^2\, r(x)^2 U \tag{A.25}$$

where U is the forward speed and the other terms are defined above.

A.2.5.2 Bilge Keel Hull Interaction Damping

This component is related to the pressure change on the hull surface due to the presence of the bilge keels. The formula for the bilge keel-hull interaction component of roll damping is given by Ikeda, et al. (1978b). The bilge keel-hull interaction component, B_{BKH}, is given by

$$B_{BKH}(x) = \frac{4}{3\pi}\rho\, r(x)^2\, d(x)^2\, f(x)^2\, \omega\phi \int C_p \cdot ldG \tag{A.26}$$

where d is the draft, C_p is the pressure coefficient on the local section of the hull due to the presence of the bilge keel, l is the moment lever for a ship section, and these are integrated over the girth of the hull, and the other terms are defined previously.

$$\int C_p \cdot ldG = \left(-A_3(x)C_p^{\,-}(x) + B_3(x)C_p^{\,+}(x)\right) \tag{A.27}$$

$$C_p^{\,-}(x) = -22.5\frac{b_{BK}(x)}{r(x)\cdot f(x)\cdot\phi\cdot\pi} - 1.2 \tag{A.28}$$

where the drag coefficient was approximated as 1.2 by Ikeda, et al., based on predictions with the KC number (Keulegan & Carpenter, 1958), and where

$$\int C_p \cdot ldG = \left(-A_3(x)C_p^{\,-}(x) + B_3(x)C_p^{\,+}(x)\right) \tag{A.29}$$

$$C_D(x) = C_p^{\,+}(x) - C_p^{\,-}(x) \tag{A.30}$$

where $C_p^{\,+}$ and $C_p^{\,-}$ are pressure coefficients on the top and bottom of the bilge keel where it is attached to the hull surface. $C_p^{\,+}$ was determined empirically by Ikeda, et al. (1978b) based on model tests with conventional ships,

$$C_p^{\,+}(x) = 1.2 \tag{A.31}$$

and the drag coefficient, C_D, was based on a zero speed formulation and empirical predictions using the KC number.

$$C_D(x) = 22.5\frac{b_{BK}(x)}{r(x)\,f(x)\phi\pi} + 2.4 \tag{A.32}$$

therefore,

$$C_p^{-}(x) = -22.5\frac{b_{BK}(x)}{r(x)f(x)\phi\pi} - 1.2 \tag{A.33}$$

The additional coefficients in the pressure coefficient term are given as

$$A_3(x) = (m_3(x) + m_4(x)) \cdot m_8(x) - m_7(x)^2 \tag{A.34}$$

$$\begin{aligned} B_3(x) = {} & \frac{m_4(x)^3}{3 \cdot (H_0(x) - 0.215 \cdot m_1(x))} + \frac{(1 - m_1(x))^2 \cdot (2m_3(x) - m_2(x))}{6 \cdot (1 - 0.215 \cdot m_1(x))} \\ & + m_1(x) \cdot (m_3(x) \cdot m_5(x) + m_4(x) \cdot m_6(x)) \end{aligned} \tag{A.35}$$

where

$$\begin{aligned} & m_1(x) = \frac{R(x)}{d(x)}, \quad m_2(x) = \frac{OG}{d(x)}, \quad m_3(x) = 1 - m_1(x) - m_2(x), \\ & m_4(x) = H_0(x) - m_1(x), \\ & m_5(x) = \frac{0.414H_0(x) + 0.0651 \cdot m_1(x)^2 - (0.382H_0(x) + 0.0106) \cdot m_1(x)}{(H_0(x) - 0.215 \cdot m_1(x))(1 - 0.215 \cdot m_1(x))} \\ & m_6(x) = \frac{0.414H_0(x) + 0.0651 \cdot m_1(x)^2 - (0.382 + 0.0106H_0(x)) \cdot m_1(x)}{(H_0(x) - 0.215 \cdot m_1(x))(1 - 0.215 \cdot m_1(x))} \\ & m_7(x) = \begin{cases} \dfrac{S_0(x)}{d(x)} - 0.25\pi \cdot m_1(x) & S_0(x) > 0.25\pi \cdot R(x) \\ 0 & S_0(x) \le 0.25\pi \cdot R(x) \end{cases} \\ & m_8(x) = \begin{cases} m_7(x) + 0.414 \cdot m_1(x) & S_0(x) > 0.25\pi \cdot R(x) \\ m_7(x) + \sqrt{2}\left(1 - \cos\left(\dfrac{S_0(x)}{R(x)}\right)\right) \cdot m_1(x) & S_0(x) \le 0.25\pi \cdot R(x) \end{cases} \end{aligned} \tag{A.36}$$

$$S_0(x) = (0.3\pi \cdot f(x) \cdot r(x) \cdot \phi) + 1.95 \cdot b_{BK}(x) \tag{A.37}$$

A.2.5.3 Bilge Keel Wave-Making Damping

This component is related to the effects of the bilge keel on the free surface, but it is typically neglected. The wave-making component of bilge keel damping, B_{BKW}, is difficult to calculate. This is partially due to the phase difference between the wave-making from the ship and the wave-making from the bilge keel, which may result in either additive or subtractive effects to the hull damping (Ikeda, et al., 1978d; Himeno, 1981). For bilge keels with b_{BK} = B/60 to B/80, Himeno (1981) assumes that the bilge keel wave-making component can be neglected because at small roll amplitudes, the interaction with the free surface will be negligible, resulting in a small magnitude relative to the other damping components. However, Himeno cautions that for ships with larger bilge keels, such as warships, the bilge keel wave-making component is likely significant. This component may also be more important at larger roll amplitudes, where the bilge keel interaction with the free surface is greater.

A.3 Calculation of the Roll Axis

A formulation for r_{BK} was originally developed for wall-sided-type hull forms, with round bilges (Ikeda, et al., 1978e). Based on the formulation for r_{BK} and R, the bilge keel is assumed to be attached to the hull at the midpoint of the quarter circle circumscribed by the bilge circle radius (Figure A-1), where θ is the angle between r and the free surface for the condition of the ship without heel.

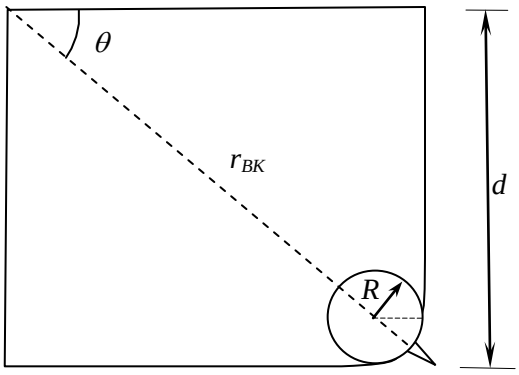

Figure A-1. Illustration of the half-midship section of a wall-sided hull form

In Ikeda's method, the distance from the roll axis to the bilge keel for a given section, $r_{BK}(x)$, is specified using an empirically-based geometric formulation (Ikeda, et al., 1978e). However, this distance, $r(x)$, may instead be specified directly, based on ship-specific geometric information, and may vary significantly based on the ship type (Figure A-2). Using the ship-specific information will provide more accurate calculations for hull form types outside of the considerations for the development of the traditional roll damping model. The roll axis is used by Ikeda, et al. for the calculation of the friction, eddy-making, and bilge keel damping components.

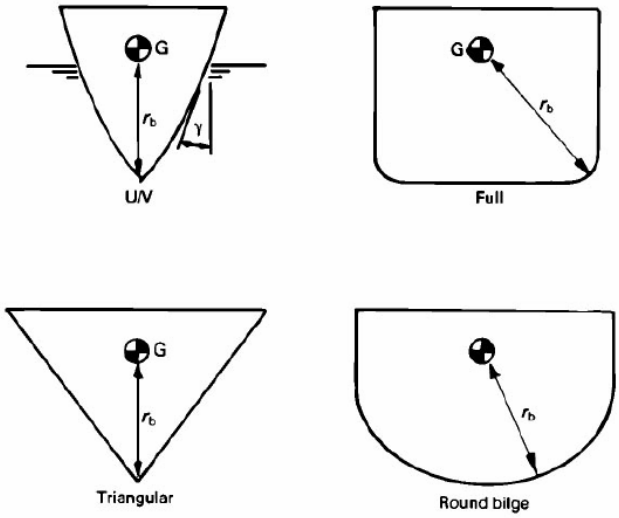

Figure A-2. Hull section shape and the distance from the roll axis (from Lloyd, 1998)

A.4 Methods for Obtaining Roll Damping

A.4.1 Roll Decay Tests

Roll decay tests are performed using a model constrained for horizontal motions (sway and yaw), but commonly with the model free to heave and pitch to account for sinkage and trim effects with forward speed. However, the induced vertical motions should be minimal. The single degree-of-freedom equation for roll decay is given by

$$\left(I_{44} + A_{44}(\omega)\right)\ddot{\phi} + B_{44}\left(\dot{\phi}\right) + C_{44}(\phi) = 0 \tag{A.38}$$

Given an initial roll angle, ϕ_0, subsequent peak amplitudes ϕ_j, ϕ_{j+1}, etc. can be determined, as shown in Figure A-3.

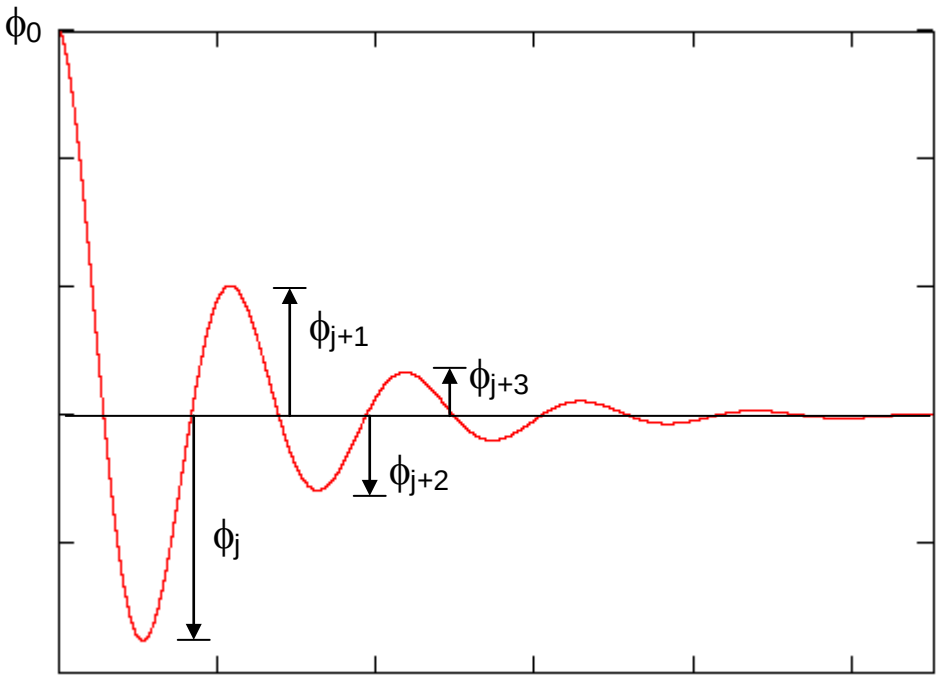

Figure A-3. Example of a roll decay test

Using the roll decay data, either from an experiment or simulation, a mean roll angle, ϕ_m, and roll decrement, $\Delta\phi$, can be determined by

$$\begin{aligned} \phi_m &= \frac{\left|\phi_j\right| + \left|\phi_{j+1}\right|}{2} \\ \Delta\phi &= \left|\phi_j\right| - \left|\phi_{j+1}\right| \end{aligned} \tag{A.39}$$

Plotting the data on a roll extinction curve (ϕ_m, in degrees, on the abscissa and $\Delta\phi$, in degrees, on the ordinate), a cubic polynomial can be obtained, with the y-intercept set to zero. One should be cautious concerning error in the roll decay data to ensure that the linear and quadratic coefficients are positive, due to their physical significance. However, while uncommon, the cubic term can be slightly negative, because of its use to effectively modify the quadratic coefficient.

Using the following relationship between the roll decrement and the mean roll angle (Himeno, 1981),

$$\Delta\phi = \frac{\pi}{2} 2\alpha\phi_m + \frac{4}{3}\beta{\phi_m}^2 + \frac{3\pi}{8}\omega_n\gamma{\phi_m}^3 \tag{A.40}$$

where the natural roll frequency is defined as

$$\omega_n = \frac{2\pi}{T_n} \tag{A.41}$$

The regression coefficients, α, β, and γ may then be determined, using at least three roll decrements (Figure 2-8). Then the linear, quadratic and cubic damping coefficients are obtained using the regression coefficients from the cubic polynomial of the roll extinction curve.

$$\begin{aligned} B_1 &= 2\alpha(I_{44} + A_{44}) \\ B_2 &= \beta(I_{44} + A_{44}) \\ B_3 &= \gamma(I_{44} + A_{44}) \end{aligned} \tag{A.42}$$

where coefficients used to model the nonlinearities in damping are specified as

$$B_{44}(\dot{\phi}) = B_1\dot{\phi} + B_2\dot{\phi}|\dot{\phi}| + B_3\dot{\phi}^3 + ... \tag{A.43}$$

It should be noted that this method does not include consideration of either frequency dependence or forward speed when determining the roll damping coefficients. To enable more accurate simulations, the damping coefficients should be determined for a sufficient number of forward speeds.

A.4.2 Forced Oscillation Tests

Forced roll oscillation tests are performed using a model constrained for all degrees of freedom, except roll.

$$(I_{44} + A_{44}(\omega))\ddot{\phi} + B_{44}(\dot{\phi}) + C_{44}(\phi) = M_{44}(t) \tag{A.44}$$

$$B_{44}(\dot{\phi}) = B_1\dot{\phi} + B_2\dot{\phi}|\dot{\phi}| + B_3\dot{\phi}^3 + ... \tag{A.45}$$

$$B_{44}(\dot{\phi}) = B_e\dot{\phi} \tag{A.46}$$

The equivalent linear damping coefficient can be related to the linear and nonlinear damping coefficients, B_1, B_2, and B_3 using the following equation describing the energy loss, E, during one period of roll motion (Takaki & Tasai, 1973; Himeno, 1981).

$$\phi(t) = \phi_A \sin(\omega t) \tag{A.47}$$

$$\begin{aligned} E &= 4\int_0^{\pi/(2\omega)} B_{44}(\dot{\phi})d\phi = 4\int_0^{\pi/(2\omega)} \left[\begin{matrix} B_1\omega\phi_A\cos(\omega t) + B_2\omega\phi_A\cos(\omega t)|\omega\phi_A\cos(\omega t)| + \\ + B_3(\omega\phi_A\cos(\omega t))^3 + ... \end{matrix}\right]\omega\phi_A\cos(\omega t)d\phi = \\ &= \pi\omega{\phi_A}^2 B_1 + \frac{8}{3\pi}\omega^2{\phi_A}^3 B_2 + \frac{3}{4}\omega^4{\phi_A}^4 B_3 + ... \end{aligned} \tag{A.48}$$

Therefore,

$$B_e(U,\omega,\phi_A) = B_1 + \frac{8}{3\pi}\omega\phi_A B_2 + \frac{3}{4}\omega^2{\phi_A}^2 B_3 \tag{A.49}$$

The equivalent linear damping coefficient can be determined using results from forced oscillation tests at various roll amplitudes, ϕ_A, for a given roll frequency, ω. By performing regression analysis on B_e, the damping coefficients, B_1, B_2, and B_3 can be obtained for a series of roll amplitude, for a given frequency. However, Himeno (1981) cautions that this approach assumes the damping coefficients are independent of roll amplitude.

To enable more accurate simulations, the damping coefficients should be determined for a sufficient number of roll frequencies, based on the wave conditions where the ship performance will be evaluated, and also a sufficient number of forward speeds. Using these results, a look-up table can be generated and provided as input to the ship motions simulation code.

A.5 A Derivation of a Morison Equation Based Approach for a Bilge Keel Force Model

This section describes the development of a zero-speed bilge keel force model using a Morison-type formulation. A derivation of the general approach, application to the development of a bilge keel force model, methods for determination of the coefficients, and issues related to Keulegan-Carpenter number dependency are discussed.

As discussed in Keulegan & Carpenter (1958), McNowan & Wolf (1956) considered the force on a stationary two-dimensional object in an oscillating fluid to be comprised of three components:

$$F = \rho A_0 \frac{d(kU)}{dt} + \oint p_x dS + \frac{1}{2}\rho C_D D U|U| \tag{A.50}$$

where F is the force per unit length on the body in the direction of the flow, x; U is the velocity of the ambient fluid; p_x is the x-component of the ambient pressure (in the absence of the body); C_D is the drag coefficient on the body; k is the virtual mass coefficient; D is the length dimension of the body normal to the fluid motion direction; and A_0 is the area of the fluid related to added mass ($A_0 = \pi D^2/4$), and where

$$\oint p_x dS = \rho A_0 r \frac{dU}{dt} \tag{A.51}$$

therefore,

$$F = \rho A_0 \left[\frac{d(kU)}{dt} + r\frac{dU}{dt} \right] + \frac{1}{2}\rho C_D D U|U| \tag{A.52}$$

where the ratio of the cross-sectional area of the body and the area related to added mass is given as

$$r = \frac{A}{A_0} \tag{A.53}$$

which when accounting for the variability of the mass coefficient, *k*, a new coefficient, *k'*, is defined as

$$k'\frac{dU}{dt} = \frac{d}{dt}(kU) \tag{A.54}$$

and the added mass or inertia coefficient is defined as

$$C_m = (k'+r) \tag{A.55}$$

then

$$F = \rho A_0 C_m \frac{dU}{dt} + \frac{1}{2}\rho C_D D U|U| \tag{A.56}$$

Substituting for A_0, the force per unit length on the body in the direction of the flow is given as

$$F = \rho \frac{\pi}{4} D^2 C_m \frac{dU}{dt} + \frac{1}{2}\rho C_D D U|U| \tag{A.57}$$

which is the Morison equation (Morison, *et al.*, 1950; 1953).

A.6 A Zero Speed Bilge Keel Force Model

The roll velocity of the ship is given as $\dot{\phi}(t)$. The velocity at the centroid of the bilge keel, U_{BK}, is given as the product of the distance from the ship's roll axis to the bilge keel, r_{BK}, and the roll velocity of the ship.

$$U_{BK}(t) = r_{BK}\dot{\phi}(t) \tag{A.58}$$

The hydrodynamic normal force on a bilge keel, F_{BK}, is the measured normal force without the inertial force and weight of the bilge keel in water. An illustration of the bilge keel and corresponding force components is shown in Figure A-4 (Grant, et al., 2007). Here, the force components on the starboard bilge keel are shown, looking forward, as the ship is rolling counterclockwise.

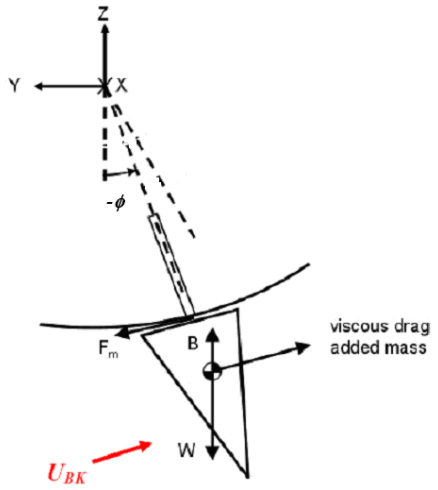

Figure A-4. Diagram of the bilge keel force components, for a starboard section of a bilge keel rolling counterclockwise, looking forward (from Grant, et al., 2007)

For single-degree-of-freedom forced roll motion, the roll, roll velocity, and roll acceleration can be expressed as

$$\begin{aligned}\phi(t) &= \phi_A \sin(\omega t)\\ \dot{\phi}(t) &= \omega\phi_A \cos(\omega t)\\ \ddot{\phi}(t) &= -\omega^2\phi_A \sin(\omega t)\end{aligned} \tag{A.59}$$

where ϕ_A is the roll amplitude and ω is the roll frequency. The velocity at the centroid of the bilge keel is

$$U_{BK}(t) = r_{BK}\dot{\phi}(t) = r_{BK}\omega\phi_A \cos(\omega t) \tag{A.60}$$

Using the Morison equation, for the zero speed condition, the hydrodynamic unit normal force on a bilge keel, F_{BK}, is

$$F_{BK}(t) = \frac{\pi}{4}\rho {D_{BK}}^2 C_m \frac{dU_{BK}(t)}{dt} + \frac{1}{2}\rho D_{BK} C_D U_{BK}(t)\cdot\left|U_{BK}(t)\right| \tag{A.61}$$

Substituting for the velocity at the bilge keel,

$$F_{BK}(t) = -\frac{\pi}{4}\rho {D_{BK}}^2 C_m r_{BK}\omega^2\phi_A \sin(\omega t) + \frac{1}{2}\rho D_{BK} C_D {r_{BK}}^2\omega^2{\phi_A}^2 \cos(\omega t)\cdot\left|\cos(\omega t)\right| \tag{A.62}$$

Equation A.62 gives the hydrodynamic unit normal force on the bilge keel. Because the hydrostatic component from roll has already been separated, by definition, the unit normal force on the bilge keel can be separated into added inertia and damping components. The time-varying bilge keel added inertia and damping components for zero speed single-degree-of-freedom roll are expressed as

$$\begin{aligned}a_{BK}(t) &= -\frac{\pi}{4}\rho {D_{BK}}^2 C_m r_{BK}\omega^2\phi_A \sin(\omega t)\\ b_{BK}(t) &= \frac{1}{2}\rho D_{BK} C_D {r_{BK}}^2\omega^2{\phi_A}^2 \cos(\omega t)\cdot\left|\cos(\omega t)\right|\end{aligned} \tag{A.63}$$

A.7 Specification of Coefficients and KC Number Dependency

Both the inertial and drag coefficients are dependent on the period parameter, or Keulegan-Carpenter number (Keulegan & Carpenter, 1958). The KC number is defined as

$$KC = \frac{U_m T_\phi}{D_{BK}} = \frac{2\pi\cdot r_{BK}\phi_A}{{D_{BK}}^2} \tag{A.64}$$

where U_m is the magnitude of the velocity at the centroid of the bilge keel, T_ϕ is the roll period, and D_{BK} is the effective span of the bilge keel.

Using Fourier decomposition, the added inertia and drag coefficients can be expressed as (see Grant, et al., 2007)

$$C_m = -\frac{4}{\pi}\frac{U_m}{D_{BK}\omega}\left(b_1 + b_2\frac{\sin(2\omega t)}{\sin(\omega t)} + b_3\frac{\sin(3\omega t)}{\sin(\omega t)} + ...\right)$$
$$C_D = \frac{2}{\left|\cos(\omega t)\right|}\left(a_1 + a_2\frac{\cos(2\omega t)}{\cos(\omega t)} + a_3\frac{\cos(3\omega t)}{\cos(\omega t)} + ...\right) \quad \text{(A.65)}$$

where ω is the roll frequency and $U_m = r_{BK}\phi_A\omega$.

Using Ikeda's formulation (1978b) for zero speed, the bilge keel added inertia and drag coefficients can be expressed as a function of the KC number.

$$C_m = 0.14KC + 1.27$$
$$C_D = \frac{22.5}{KC} + 2.4 \quad \text{(A.66)}$$

Atsavapranee, et al. (2007) proposed an alternative formulation for the drag coefficient, C_D, for finite forward speed- using 15.0, instead of 22.5. However, this was only compared to one ship-specific data set and it is unknown if this alternative formulation is more appropriate or accurate.

Another method is to obtain the added inertia and drag coefficients from experimental data of the measured hydrodynamic roll moment, due to the bilge keel. There have been several experiments performed to measure the coefficients as a function of KC number for a flat plate attached to a wall in a harmonically oscillating fluid (e.g. Keulegan & Carpenter, 1958; Martin, 1958; Ridjanovic, 1962; Sarpkaya & O'Keefe, 1996; Klaka, *et al.*, 2007). Cox & Lloyd (1977) used the data from Martin (1958) and Ridjanovic (1962) to determine suitable drag coefficients for the bilge keel. A constant value drag coefficient of 1.17 was proposed by Lloyd (1998).

For the zero-speed condition, the KC number is considered to be independent of roll frequency. Subsequently, at zero speed the inertia and drag coefficients are also independent of roll frequency. However, Klaka, et al. (2007) performed a series of studies with a flat plate oscillating in a 3D flow and observed that the inertia coefficient was the most independent of frequency, but the drag coefficient exhibited weak frequency dependence, increasing with increasing frequency. An alternative formulation for the coefficients was proposed, where the inertia coefficient was a function of both aspect ratio and roll amplitude, and the drag coefficient was also a function of roll frequency.

A.8 Additional Considerations for Bilge Keel Force Models

Some additional considerations for a bilge keel force model are discussed in this section. These include multiple degree-of-freedom motion, wave effects, forward speed effects, and additional effects on the hull due the presence of the bilge keels

A.8.1 Multiple Degree-of-Freedom Ship Motions

Using the formulation presented in detailed in Grant, et al. (2007), the total bilge keel normal velocity can instead be expressed as the sum of the effects of heave motion, in addition to roll

$$U_{BK} = U_{roll} + U_{heave} \quad \text{(A.67)}$$

where the bilge keel roll velocity component is given as before,

$$U_{roll} = R\frac{\partial \phi}{\partial t}$$
$$U_{roll} = r_{BK}\dot{\phi}(t) \tag{A.68}$$
$$U_{roll} = r_{BK}\omega\phi_A \cos(\omega t)$$

and the bilge keel heave velocity component is given as

$$U_{heave} = \frac{\partial z}{\partial t}\sin\phi \tag{A.69}$$

where z is the distance from the calm-water position, without any roll of the ship.

The primary issue related to multiple degree-of-freedom (MDoF) ship motions is the characterization of the forces on the bilge keel, with considerations for the interaction between the bilge keel and the local fluid field at a given time-step. In addition to the above formulation from Grant, et al. (2007) to consider the inclusion of heave motions, pitch motions should also be considered for a bilge keel force model. Although this has not yet been examined in detail, using a sectional approach for the bilge keel force model may help to better account for MDoF ship motions and the local position of the bilge keel relative to the free surface at a given time-step. However, issues related to the local wave effects should also be considered.

A.8.2 Wave Effects

In addition to accounting for ship motions, Grant, et al. (2007) also discusses the effect of the local wave-field on the bilge keel force. Using the above formulation, the total bilge keel normal velocity can also be expressed as

$$U_{BK} = U_{roll} + U_{heave} + U_{BK/wave} \tag{A.70}$$

where the normal velocity of the bilge keel with respect to the wave orbital velocity is

$$U_{BK/wave} = -u_{wave}\cos\phi - v_{wave}\sin\phi \tag{A.71}$$

and where the horizontal and vertical components of the local wave velocity are given as

$$\begin{aligned} u_{wave} &= u_0 \sin(kx + \omega t + \varepsilon) \\ v_{wave} &= v_0 \cos(kx + \omega t + \varepsilon) \end{aligned} \tag{A.72}$$

For small waves, using linear theory, the velocity amplitudes are given by

$$u_0 = v_0 = \frac{gk\zeta_0}{\omega_w}e^{-ky} \tag{A.73}$$

where g is the acceleration due to gravity, k is the wave number, ζ_0 is the wave amplitude, ω_W is the wave frequency, and ε is the phase angle.

A.8.3 Forward Speed Effects

In addition to the added inertia and drag terms in the Morison equation formulation for the hydrodynamic unit normal force on the bilge keel, modificiations were proposed in Irvine, et al. (2006) and further discussed in Atsavapranee, et al. (2007) and Grant, et al. (2007). In this formulation, the unit normal force on the bilge keel can be modeled as the sum of viscous drag and added inertia due to roll motion and the steady lift force on the bilge keel resulting at steady forward speed.

$$F_{BK}(t) = \frac{\pi}{4}\rho {D_{BK}}^2 C_m \frac{dU_{BK}(t)}{dt} + \frac{1}{2}\rho D_{BK} C_D U_{BK}(t)\cdot\left|U_{BK}(t)\right| - \frac{1}{2}\rho D_{BK} C_L {U_\infty}^2 \qquad \text{(A.74)}$$

where U_∞ is the ship speed. In this formulation, the lift coefficient, C_L, must be specified and will be a function of both the bilge keel geometry, angle of attack relative to the local flow field, and forward speed.

Alternatively, the Vortex Lattice Method (VLM), as discussed in the previous section, can also provide consideration of forward speed in the bilge keel force model.

The Morison equation formulation with the forward speed addition may provide reasonable predictions of the unit normal force on the bilge keel for low speed. This model could then be used in conjunction with the VLM at forward speed, linking the two models with a transition region. There are two options for the transition model, a continuous ramp function and smooth transition from one model to the other or a binary function at some specified forward speed. Although the second model would be easier, considerations for robustness of application would favor the implementation of the first type. This exact model remains to be developed.

With the combination of forward speed and roll motion, the vortex shedding due to the bilge keels, bow, and skeg all influence the forces and motions on the hull. Even for the simple case of 1DoF roll motion at forward speed, the convection of shed vortices downstream is significant. Even at moderate roll angles, the vortices shed from the bow dome are convected downstream along the keel beneath the hull and interact with the skeg. The vortices shed from the bilge keels and the skeg, including the influence from the bow dome, are convected downstream and will interact with the propulsor.

MDoF ship motions and wave effects will further influence and complicate vortex shedding along the hull. Using the VLM at forward speed, these additional factors should be considered.

Appendix B: Details of the URANS Computations[17]

B.1 Overview

This Appendix provides additional details of the URANS solver (*CFDShip-Iowa*), dynamic overset grids, and the computational domain, used for the high-fidelity numerical simulations presented and discussed in Chapters 3 and 5.

B.2 URANS Solver

Calculations were performed using the URANS solver CFDShip-Iowa, Version 4. CFDShip-Iowa is a general-purpose research RANS computational fluid dynamics code developed at the University of Iowa.

The governing equations for CFDShip-Iowa, Version 4 are:

$$\partial_i u_i = 0 \tag{B.1}$$

$$\partial_t u_i + u_j \partial_j u_i = -\partial_i \hat{p} + \frac{1}{\mathrm{Re}} \partial_j \partial_j u_i - \partial_j \left(\overline{u_j u_i} \right) \tag{B.2}$$

where u_i are the Reynolds averaged velocities, $\overline{u_j u_i}$ are the Reynolds stresses, and the piezometric pressure is

$$\hat{p} = p + \frac{z}{Fn^2} \tag{B.3}$$

The variables are non-dimensionalized by fluid density, ρ, and kinematic viscosity, ν, gravity, g, ship length, L_{pp}, and reference velocity, U_{ref}, resulting in the Froude, *Fn*, and Reynolds, *Re*, numbers:

$$Fn = \frac{U_{ref}}{\sqrt{g L_{pp}}} \tag{B.4}$$

$$\mathrm{Re} = \frac{U_{ref} L_{pp}}{\nu} \tag{B.5}$$

and time is nondimensionalized by:

$$\frac{L_{pp}}{U_{ref}} \tag{B.6}$$

Basic solver numerical modeling details include 2nd-order upwind convective terms and 2nd-order central differenced viscous terms. For time discretization a 2nd-order backward difference is used. CFDShip-Iowa uses predictor/corrector algorithms to couple the velocity and pressure and to enforce continuity. Turbulence modeling uses the blended k-ε/k-ω model of Menter (1994). The solver uses Message Passing Interface (MPI)-based domain decomposition for parallel processing. Details of the solution algorithm and numerical methods can be found in numerous references, including Carrica, et al. (2006, 2007a, 2007b). Details on previous applications of the code to problems of roll motion and bilge keel forces can be found in Miller, et al. (2002, 2008).

[17] Portions of this Appendix have been published previously in Bassler and Miller (2011) and Bassler, et al. (2011)

The solution of the URANS equations by CFDShip-Iowa provides $\hat{p}$ and u_i, in earth coordinates. The fluid stress tensor at the body surface is

$$T_{ij} = -p\delta_{ij} + \tau_{ij} = -(\hat{p} - \frac{z}{Fn^2})\delta_{ij} + \frac{\left(\partial_j u_i + \partial_i u_j\right)}{\mathrm{Re}} \tag{B.7}$$

The forces and moments on the ship in earth coordinates are determined by summing the surface force per unit area, $R_i = n_j T_{ji}$, over the wetted area. The fluid force on the ship is

$$\vec{F}_{earth} = \int_{Hull} \vec{R} dS \tag{B.8}$$

and the moment is

$$\vec{M}_{earth} = \int_{Hull} \vec{r} \times \vec{R} dS \tag{B.9}$$

Force and moment output from CFDShip-Iowa include contributions to the integrals from the piezometric pressure, $\hat{p}$, buoyancy, $\frac{z}{Fn^2}$, and friction, in ship coordinates:

$$\begin{aligned} \vec{F}_{total} &= \vec{F}_{piezometric} + \vec{F}_{bouyancy} + \vec{F}_{friction} \\ \vec{M}_{total} &= \vec{M}_{piezometric} + \vec{M}_{bouyancy} + \vec{M}_{friction} \end{aligned} \tag{B.10}$$

The rigid body equations are solved using the forces and moments in ship coordinates. The full 6DOF equations and the solution algorithm used by CFDShip-Iowa can be found in Carrica et al. (2007a). For this investigation, the ship was held fixed in surge, sway, heave, pitch, and yaw and the axis of rotation was co-located with the vertical center of gravity.

For the prescribed roll motion, ϕ_x is specified using equation (11) for given amplitude, *A*, and roll frequency, ω.

$$\phi_x = A\sin(\omega t) \tag{B.11}$$

B.2 Dynamic Overset Grids

CFDShip-Iowa uses dynamic overset grids to allow for the relative motion between blocks of meshes. Overset grids are used in a wide variety of applications, including calculations of a static hull embedded in a background grid and dynamically moving, fully-appended ships. Additionally, overset grids remove the necessity of point-to-point matching in structured grid systems. This capability alleviates some of the difficulties involved in creating structured grids for complex configurations, such as hulls appended with shafts and struts. The grid assembling tool SUGGAR (Structured Unstructured Generalized Grid Assembler), Version 2.73 (Noack 2005) was used.

SUGGAR is run as a preprocessor for static calculations, or concurrently with CFDShip-Iowa, using calls to subroutines. The software, USURP, Version 2.39, (Boger & Dreyer, 2006), was used to properly compute area and forces on overlapping surface regions.

At each time-step, the solver obtained the motion and sent the information to SUGGAR to create new grid assembling information. CFDShip-Iowa's implicit motion solver was utilized, resulting in updated grid motion at every inner-iteration of the time-step solution. Typically three to five inner iterations were performed at each time step. At each time step, CFDShip-Iowa uses the new value of roll displacement to re-orient the ship. SUGGAR was then run to update the grid assembly for the new orientation.

Overlapping boundary fitted grids were created for the port and starboard sides of the hull and the port and starboard bilge keel grids. A cross-section of the grid assembly shows the relative grid point densities of the hull, refinement, and background grids (Figure B-1), and also illustrates the use of dynamic overset grids. The moving hull grid assembly was embedded in a stationary intermediate refinement grid, which was embedded in a larger stationary background grid, representing a towing tank. The intermediate refinement grid is used to blend the grid sizes of the very fine boundary layer grid with the coarser background grid. As the hull grid rotates relative to the fixed background grids, new grid connectivity information is calculated by SUGGAR.

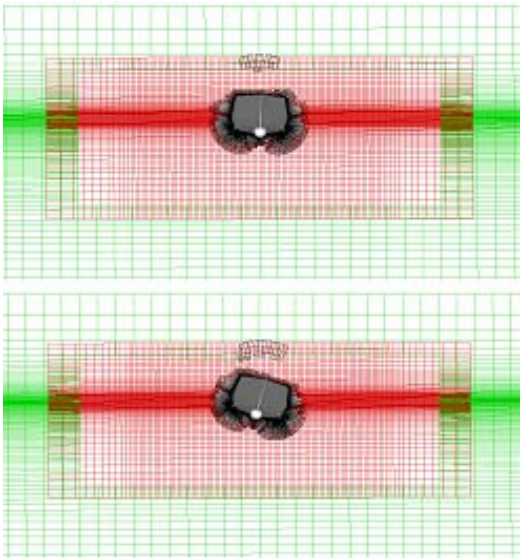

Figure B-1. SUGGAR grid assembly for DTMB Model #5613-1 at two roll positions, with relative grid densities between refinement and background grids

B.2 Computational Domain

The computational domain used for the calculations is shown in Figure B-2. The surface discretization of the hull appended with bilge keels is shown in Figure B-3. No-slip boundary conditions were applied to the hull and appendages, far-field boundary conditions were applied to the side and bottom walls. A constant inlet velocity, $U/U_{ref} = U_S$, $V/U_{ref} = 0$ and $W/U_{ref} = 0$, represents the constant forward speed (Figure B-4). The velocities are extrapolated at the exit.

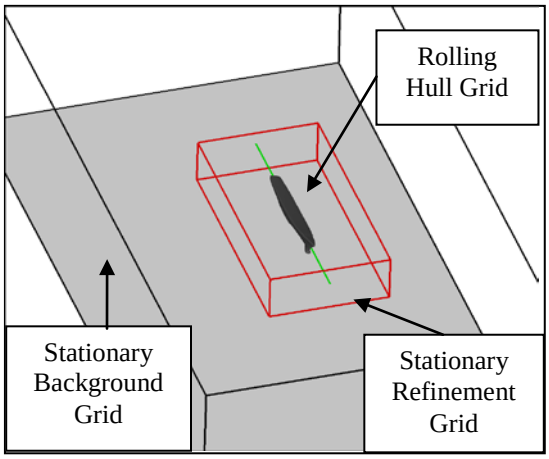

Figure B-2. Computational Domain: Moving hull, grid, stationary refinement, and background grids

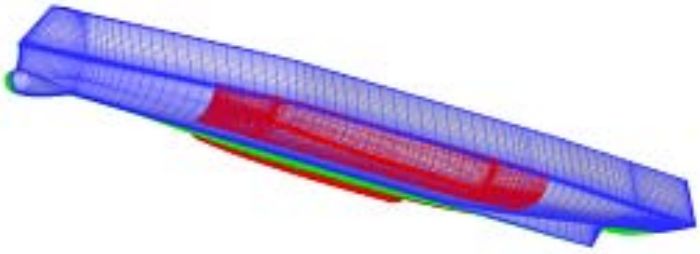

Figure B-3. Hull and bilge keels surface discretizations, shown for DTMB Model #5613-1

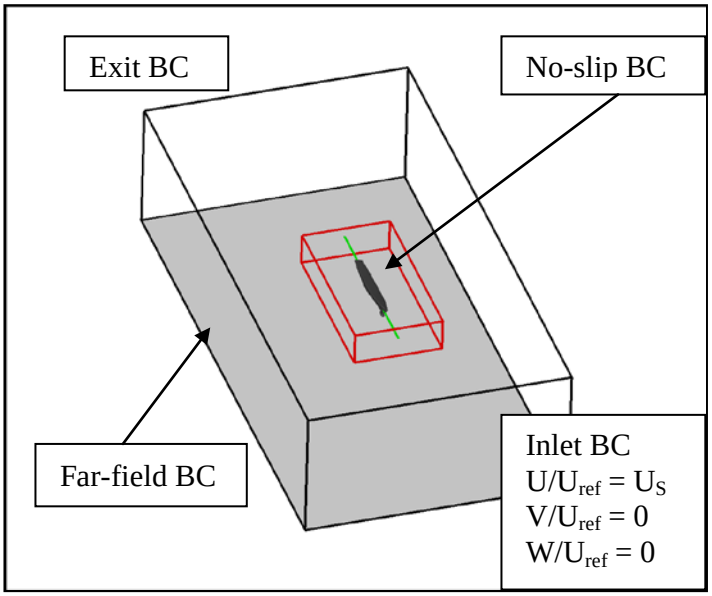

Figure B-4. CFDShip-Iowa boundary conditions

Details of the computational grid size are given in Table B-1. The total number of grid points used for the URANS simulations was about 4.8 million. The skeg was integrated into the hull grid. The domain was decomposed into 45 smaller blocks for parallel processing. One additional processor was used for SUGGAR.

Table B-1. DTMB Model 5613-1 grid sizes and decomposition

Block	**# pts.**	**# proc.**	**# pts/proc.**
Hull Stb	667,116	6	111,186
Hull Prt	667,116	6	111,186
BK Stb	363,750	3	121,250
BK Prt	363,750	3	121,250
Refinement	1,519,035	15	101,269
Background	1,241,240	12	103,436
Total	**4,822,007**	**45**	**Avg = 107,155**

Appendix C: Details of the Experimental Set-up and Instrumentation

C.1 Details of the Experimental Design

This section describes the model properties and construction, model ballasting, instrumentation and uncertainty, details of theory and design of the 3DoF motion mechanism.

C.1.1 Model Properties and Construction

Principal particulars for the model are given in Table C-1. The model was designed for use in the NSWCCD 140 ft basin. The size reflects the largest model which could be used in the 140 ft basin, to allow for more accurate measurements and the use of instrumented appendages. The loading condition was chosen to correspond to GM= 0.75m, full-scale. This is a condition where the limiting GM criteria (Sarchin & Goldberg, 1962) was satisfied for the flared topside (limiting GM=0.19 m full-scale), but not for the tumblehome topside configuration (limiting GM=2.01 m full-scale), and was the same loading conditions used for previous experiments with DTMB #5613 (Bassler, et al. 2007). Thus, DTMB Model #5699 and 5699-1, for the 2D midship section of the flared and tumblehome topsides, respectively, are the geosim extrusions of the midship sections of DTMB Model # 5613 and 5613-1.

Table C-1. DTMB Model #5699 and #5699-1 Principal Particulars

Effective scale ratio, λ	32
Length, *LWL*	2.743 m
Calm-waterplane area, A_{WP}	1.588 m^2
Beam, *B*	0.5875 m
Draft, *T*	0.172 m
KG	0.172 m
GM	0.132 m
k_{44} /*B* (with bilge keel)	0.361 (0.366)
Bilge keel span, b_{BK}	0.039 m
Displacement (freshwater), Δ	232.24 kg

The model was constructed of wood and fiberglass and included a removable plexiglass deck cover to maintain the watertight integrity of the model at large roll angles, when the deck was partially submerged. Removable aluminum endplates, 10.16 cm larger than the outline of the model, were used to maintain the 2D nature of the experiment (Figure C-1). Removable bilge keels, made of Renwood and with aluminum instrumented sections, were also constructed, corresponding to the full-scale 1.25m bilge keel span from the ONR Topside Series (Figure C-2).

Figure C-1. Endplate for DTMB Model #5699

Figure C-2. DTMB Model #5699-1 in the NSWCCD 140 ft basin (left) and the section with instrumented bilge keels, with the strain gages seen protruding through the hull (right)

C.1.2 Model Ballasting

In order to ensure the model had the desired inertial properties, a series of ballasting tests were carried out in air, using the small A-frame in Bldg. 18 (MASK Basin) at NSWCCD (Figure C-3). These tests helped to determine the internal configuration of the instrumentation and additional ballast weight within the model.

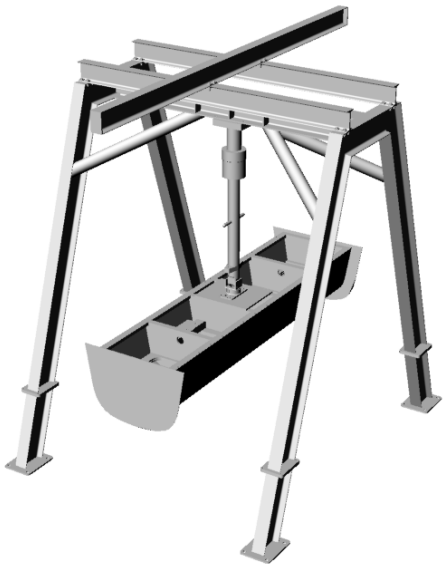

Figure C-3. Illustration of DTMB Model #5699 attached to the small A-frame in Bldg 18, NSWCCD

The ballast condition for the flared topside configuration is shown in Figure C-4. The tumblehome topside configuration had the circular ballast weights, both fore and aft, shifted to a configuration where they were attached to the outer walls of the bulkheads separating the ballast weight compartments and the center compartment with the Kistler dynamometer. This was a result of the reduced volume and topside weight of the tumblehome, compared to the flared topside, and required the vertical position of the internal ballast weights to be increased.

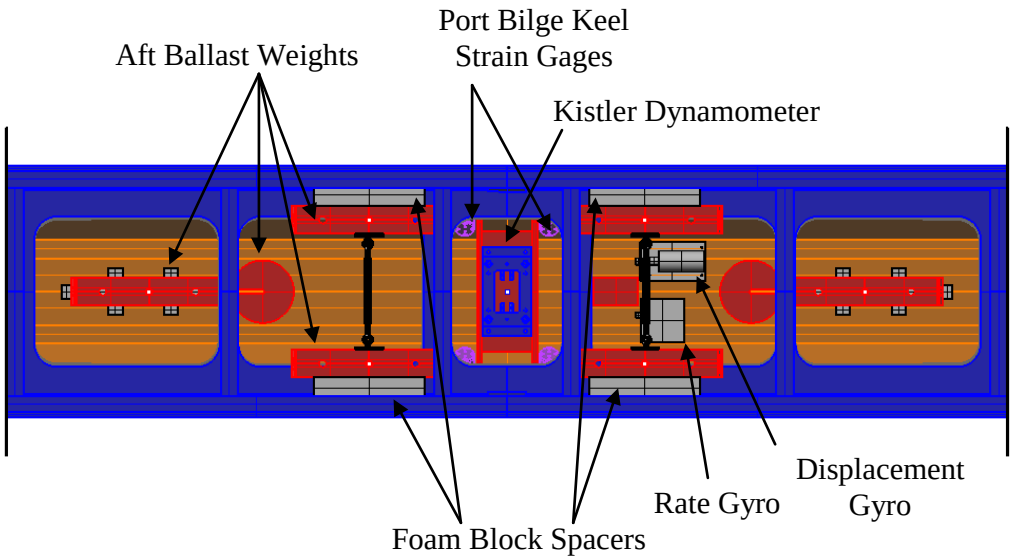

Figure C-4. Illustration top view of internal instrumentation and ballast weight configuration for DTMB Model #5699

Then the final ballast configuration for each topside configuration was recorded and is presented below (Table C-2 and Table C-3). The obtained inertial properties were then checked against the desired properties (Table C-1) and the differences are given in the tables below.

Table C-2. Inertial Properties for DTMB Model #5699

Parameter	***% Difference from Design Condition (Table C-1)***
Displacement, Δ	+1.34%
KG	+0.16%
k_{44} (about CG)	+2.17%
Roll Period, T_ϕ	1.437 seconds
I_{xx}, in-air (kg-m^2)	11.766

Table C-3. Inertial Properties for DTMB Model #5699-1

Parameter	***% Difference from Design Condition (Table C-1)***
Displacement, Δ	-1.35%
KG	+1.5%
k_{44} (about CG)	+1.49%
Roll Period, T_ϕ	1.438 seconds
I_{xx}, in-air (kg-m^2)	11.766

C.1.3 Instrumentation and Uncertainty

This section includes discussion of the instrumentation and uncertainty associated with the force and moment measurements on the hull, bilge keels, motion measurements of the hull, the near-field wave measurements, and the velocity-field measurements.

C.1.3.1 Force and Moment Measurements on the Hull

Forces and moments were measured on both the hull and bilge keels. Six degree-of-freedom forces and moments on the hull were obtained using a Kistler dynamometer, comprised of four piezoelectric force sensors. The dynamometer was placed at midships of the model, at the center-of-gravity, at the waterline. The sampling data rate was 10 Hz and the uncertainty of the force dynamometer is about 1% of the measurement.

Kistler dynamometers are constructed by placing four Kistler force gages in an x-y array between two plates of stainless steel. By knowing the location of the gages and the force measured at that location, forces and moments are calculated for the x, y and z axes (Figure C-5). The Kistler force gage used for this experiment, Model 9602A, was manufactured from quartz

and contained a hermetically sealed charge amplifier. Due to the nature and location of the charge amplifier, potential problems with drift due to environmental conditions were minimized.

The gages are labeled 1 through 4, with a corresponding x-y location: Rx and Ry. The coordinate systems are defined in Figure C-5. Each gage has three voltages associated with it. When the gage voltages are converted into engineering units, using the pre-test calibration, the forces are output as Fx, Fy and Fz. There are twelve force channels from the Kistler gages will be labeled Fx1, Fy1, Fz1 … Fy4, Fz4. An interaction matrix is used to determine the total force components, Fx, Fy and Fz, on the body, acting at the center of the gage.

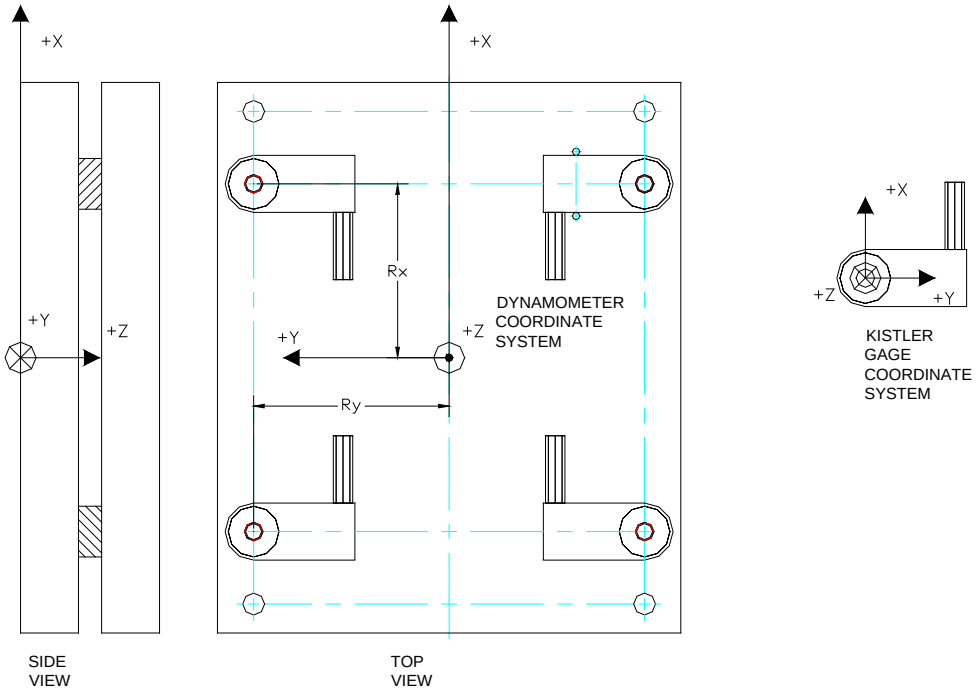

Figure C-5. Typical gage layout for Kistler dynamometer

C.1.3.2 Force and Moment Measurements on the Bilge Keel

Single degree-of-freedom strain gage sensors were embedded into the bilge keels and used to obtain the normal force and moment measurements for the instrumented section of the bilge keels (Figure C-6 and Figure C-7). The strain gages are manufactured by Micro Measurements. This type of strain gage was used in several previous model experiments (Irvine, et al., 2006; Atsavapranee, et al., 2007; Grant, et al., 2007; Etebari, et al., 2008) to obtain appendage force and moment measurements for a surface ship.

The sampling data rate was 50 Hz and the uncertainty of the strain gages is about 1% of the measurement. The instrumented portion of the bilge keel was 0.41m long, in the middle of the model, with strain gages embedded in the forward and aft portions (Figure C-8). This enabled more accurate measurements, due to the reduced length of the bilge keel section, and instrumentation redundancy.

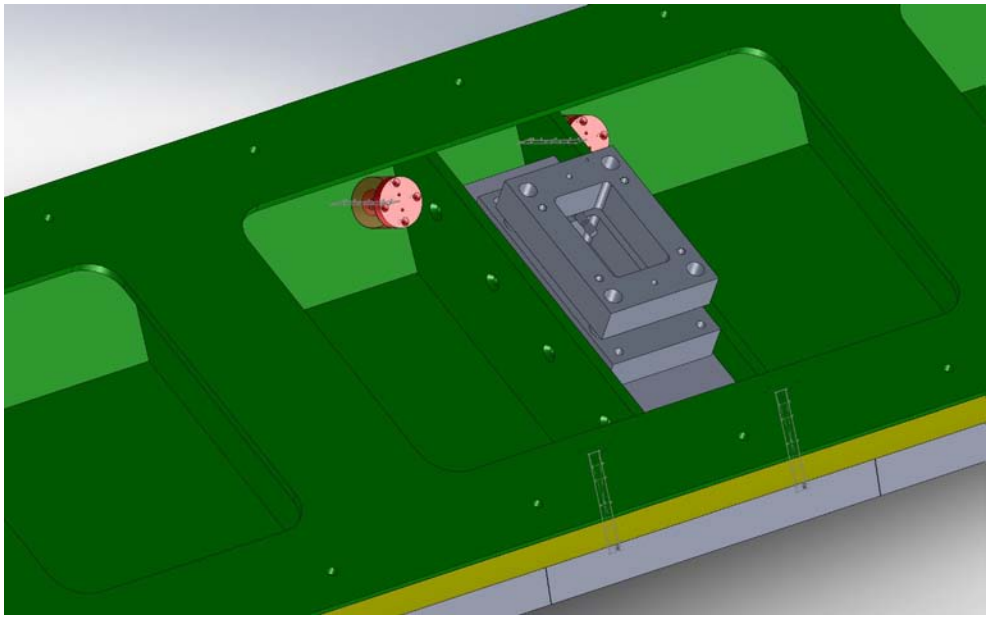

Figure C-6. Illustration the 2D Model with Kistler gage (gray) and instrumented bilge keel sections (red), with hull penetrations, shown

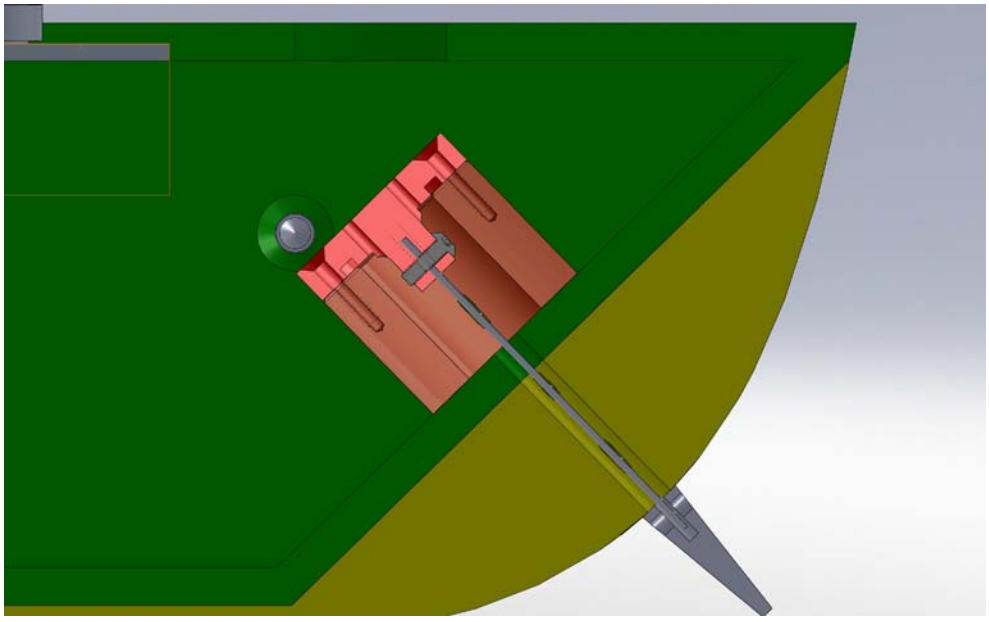

Figure C-7. Illustration of the cross-section of the 2D model with bilge keel strain gages (gray) with strain gages attached to waterproofed end-caps (red) shown

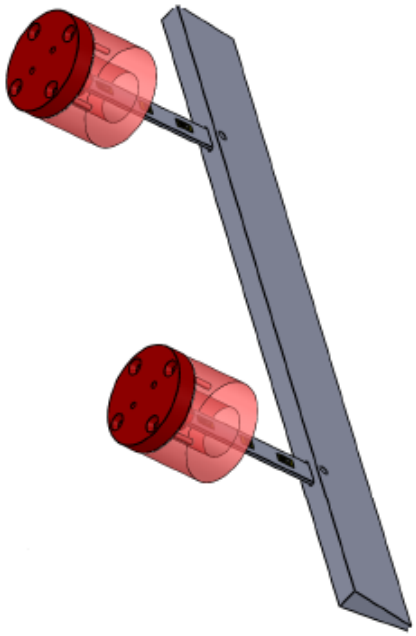

Figure C-8. Illustration of the instrumented bilge keel section with strain gages attached to waterproofed end-caps (red) used to transmit data to the data acquisition system

C.1.3.3 Motion Measurements on the Hull

Motions, including roll and roll rate, were obtained using a Goodrich vertical gyroscope and a BEI solid-state GyroChip II rate gyroscope, respectively (Figure C-9). The miniature dual axis electro-mechanical spinning mass vertical gyro measurements have an accuracy of 0.25 degrees. The rate gyro uses a vibrating quartz tuning fork sensing element in conjunction with a piezoelectric material to produce a voltage proportional to a rate of rotation. The measurement resolution is 0.004 deg/s. The displacement and rate gyros were placed at the waterline of model, on the port and starboard side of the longitudinal axis of rotation, respectively.

Figure C-9. DTMB Model #5699 with topside removed, viewed from forward looking aft, displacement and rate gyroscopes used to obtain motion measurements are shown in foreground (in the near-field compartment)

Figure C-10. Displacement gyroscope (clear box) and rate gyroscope (black cylinder) in the model, with topside configuration and plexiglass deckplating installed

C.1.3.4 Near-Field Wave Measurements

Free-surface elevation measurements of the radiated waves generated from the oscillating hull form were measured using an array of three non-contact ultrasonic sensors (Senix Corporation model ULTRA-SR-BP). The ultrasonic sensor transmits an ultrasonic wave and measures the time of reflection from the target to measure the distance. The data was collected at 25 Hz. The ultrasonic probes were located at perpendicular distances of 0.61 m, 0.76 m, and 0.91 m from model centerline (Figure C-11).

The wave height gages were calibrated relative to the calm water surface in the basin. The output limits of the probes were set to the maximum capability of 0 volts to 10 volts. Each probe has a constant gain and offset value, which is used to convert the voltage output to wave elevation. The repeatability of the measurements is estimated by the manufacturer to be 0.1% of the range. Each probe emits a conical sonic beam with a nominal 12-degree total angle. The wave measurement for steep waves may drop out as the water surface tends to reflect the sonic beam away from the sensor. Data from the probes was collected and processed on a PC.

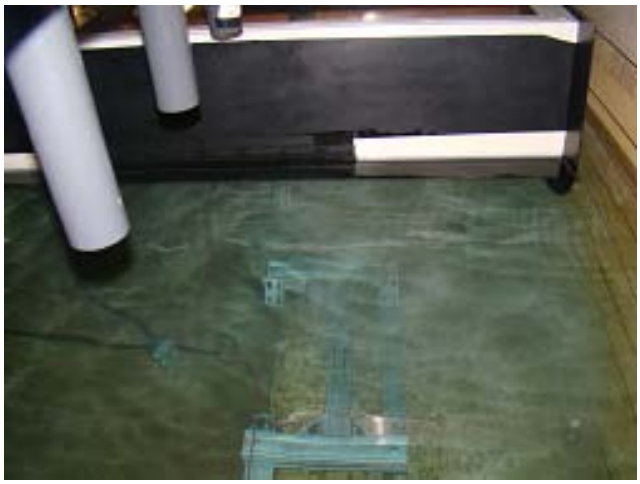

Figure C-11. Three ultrasonic wave probes with housings (gray), suspended at perpendicular distances of 0.61 m, 0.76 m, and 0.91 m from model centerline

C.1.3.5 Velocity-Field Measurements

Particle Image Velocimetry (PIV) was used to obtain velocity field measurements in the near-field around the hull. PIV is an optical, non-intrusive, flow-field measurement that provides in-plane velocity measurements of a planar cross-section of a flow (Hamilton, et al., 1993; Westerweel, 1997). Neutrally buoyant particles were used as flow tracers to provide an indirect velocity measurement.

Two custom-built *Cynosure* flashlamp-pumped dye lasers operating at 585 and 595 nm were used to create a laser sheet, nominally 8 mm thick, to illuminate the flow-field, with two consecutive laser pulses separated by a small time-step. The laser beam was coupled into 600 micron optical fibers, 30 m in length. When operating at full power, a 700 mJ/pulse is recorded at the output end of each fiber.

A series of image pairs between the two illuminations were recorded by a high speed charge-coupled device (CCD) camera. The MegaPlus ES 4.0/E camera was used to capture the PIV images (Figure 4-9). The camera has a spatial resolution of 2048 pixels x 2048 pixels and was operated in dual exposure mode at a frame rate of 10 fps. An image pair was taken every 200 ms and the time between images in a pair (Δt) was varied based on the flow characteristics for the condition being measured. For this experiment, the Δt between successive pulses varied from 1-57 ms, depending on the roll frequency, maximum roll angle, and model configuration being examined. The distance traveled by fluid particles in the measurement region, as observed by the image pairs, was then used to obtain the velocities throughout the measurement region.

A spatial calibration of the PIV images was performed using *La Vision* DaVis software v7.2. A calibration target, 60.96 x 60.96 cm in size and machined to ±0.00254 cm accuracy, is shown in Figure C-12A. The target contains 121 evenly spaced '+' marks on a 5.08 x 5.08 cm grid. The target was mounted so that it was in line with the ultrasonic wave probes. The position of the laser probes was adjusted until the laser light sheet was visually aligned with the face of the calibration target. A calibration image was taken (Figure C-13A) and imported into the DaVis software. The software creates a mapping function as well as applies a de-warping function to correct distortions due to the 30 degree look up angle of the camera. Figure C-13B shows the de-warped image and the results of the mapping function, shown in red.

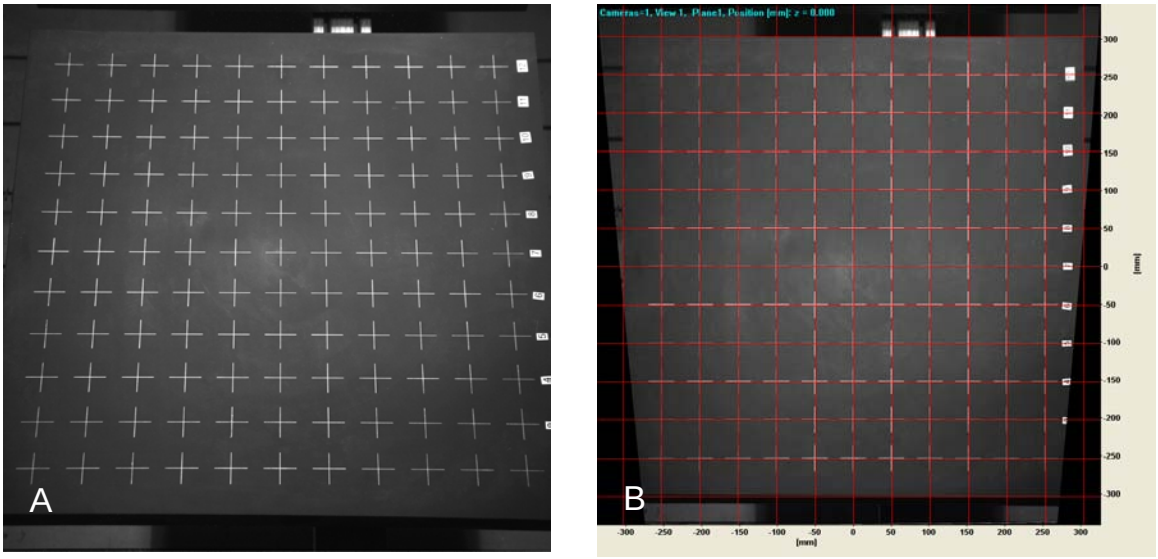

Figure C-12. Calibration image (A) and de-warped image (B), with mapping function shown in red

The PIV data acquisition system used at NSWCCD was constructed by Boulder Imaging, Inc. *VisionNow* software was used to capture and store the field-of-view images at the full camera rate onto a real-time disk array. The collection of the PIV images was time-synchronized with the force and moment data acquisition system and each image pair was time-stamped to ensure correlation with the force and moment data.

Each image is 2048 x 2048 pixels in size and the images were processed in pairs. In the first processing pass the image was divided into interrogation windows that were 64 x 64 pixels in size. A cross-correlation scheme was then applied resulting in a velocity vector for each interrogation window. Two additional passes, each using 32 x 32 pixel interrogation windows,

were then completed building on the information gained from the previous pass. Each velocity vector represents the solution for a given interrogation window and shows the magnitude of the velocity and direction at a given point in the flow field resulting in a velocity vector field of 64 x 64 vectors.

The raw images captured from the camera were then post-processed in MATLAB to create masked images that were imported and processed using *La Vision* DaVis software v7.2. Processing was divided into three steps: image preprocessing, vector field calculation, and vector post-processing. Before the vector field was calculated, the images were preprocessed by applying a sliding background subtraction scheme. This operation acted as a high pass filter, by removing large fluctuations in the image background, which are present due to reflections or glare, without affecting the particle signal used during correlation.

The velocity vector field was calculated using a multi-pass processing technique with decreasing window sizes and a 50% overlap between neighboring interrogation regions. Three passes in total were completed. In the first processing pass the image was divided into interrogation regions, 64 x 64 pixels in size. A cross-correlation operation was then applied resulting in a velocity vector for each interrogation region. The remaining two passes, each using 32 x 32 pixel interrogation regions, were then completed building on the information gained from the previous pass. In the final pass a round Gaussian weighting function was applied to each interrogation region. The 50% overlap between interrogation regions was used to increase the resolution of the final velocity vector map from 64 x 64 vectors to 128 x 128 vectors. The finer grid was beneficial in resolving the details of the vorticies in the flow field.

The resulting velocity vector field was post-processed after each pass to remove spurious vectors, which may influence the final result. The vectors were median filtered, removing vectors whose magnitudes were greater than 2 times the rms value of neighboring vectors. The median filter was helpful for removing individual ‘bad’ vectors, but is unable to remove groups of spurious vectors. Therefore, an additional algorithm was applied to remove groups with less than 5 vectors as well. Blank spaces left by removed vectors were then filled with the average of the non-zero neighboring vectors.

Figure C-13 shows the resulting velocity field calculated by DaVis for a sample image pair. The origin is defined at the center of the PIV measurement plane (x=0, z=0), which is also at the center gravity of the ship. Each velocity vector represents the solution for a given interrogation window and shows the magnitude of the velocity and direction at a given point in the flow field.

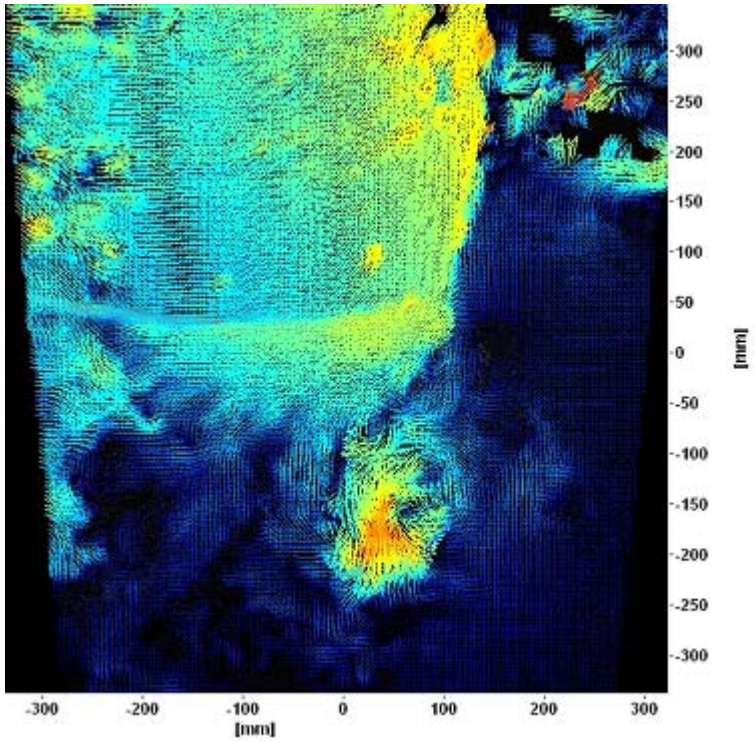

Figure C-13. Sample raw image from a PIV vector-field measurement; post-processing masking and window algorithms were applied to generate vorticity-field measurements

C.1.4 Details of the 3DoF Motion Mechanism- Theory and Design[18]

As discussed in Section 4.3.3, carrying out forced oscillations to large roll angles, while maintaining watertight integrity, cannot be achieved using a mechanical pivot point within the model. However, it is possible to mount the model to a rigid strut that extends outside of the watertight envelope of the model. If the model and fixed strut are rotated about a roll axis, the top of that strut will follow a prescribed arc. This arc can also be achieved externally using concurrent sway and heave actuators.

Incorporating a roll actuator into the base of the heave actuator and attaching the model with its fixed strut allowed the model to be rolled about a prescribed virtual axis, as shown in Figure C-14.

[18] An invention disclosure for this design was submitted and a patent application is pending (Navy Case #100,690). Portions of the discussion related to the design, construction, and use of the mechanism have been published previously in Grant, et al. (2010).

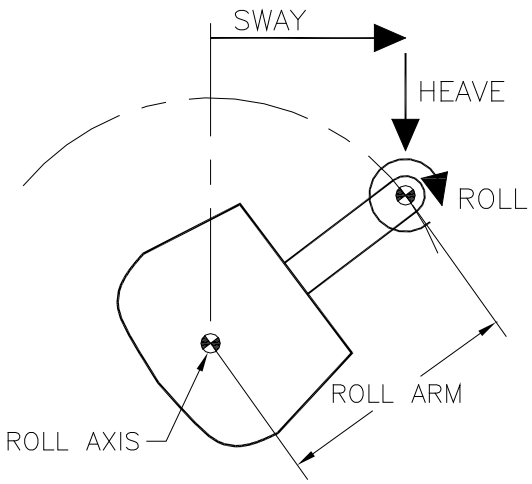

Figure C-14. Combined sway, heave, and roll actuation with the mechanism, to obtain large amplitude 1DoF roll of the model about a specified roll axis

The individual displacements of the three actuators to achieve the desired roll angle (ϕ) are defined by

$$Y_{Actuator} = A_{\phi} \sin(\phi) \qquad \text{(sway)} \qquad \text{(C.1)}$$

$$Z_{Actuator} = A_{\phi}\left[1 - \cos(\phi)\right] \qquad \text{(heave)} \qquad \text{(C.2)}$$

$$\phi_{Actuator} = \phi \qquad \text{(roll)} \qquad \text{(C.3)}$$

where A_{ϕ} is the radial distance from the roll actuator to the virtual roll center of the model. Using this formulation, the location of the ship's roll axis can be adjusted, as required, during operation. The resulting 3DoF mechanism was designed and sized specifically for testing of DTMB Model #5699. The mechanism was also used to carry out additional 1DoF forced sway and heave oscillation experiments with DTMB Model #5699 (Belknap, et al., 2010).

Controlling requirements for the mechanism were roll amplitude, roll frequency, and model mass properties. The actuator travel was sized to accommodate a 50 degree sinusoidal roll, with a 381 mm roll arm. Actuator motors and gearing, as well as the supporting structure, were sized in order to accommodate sinusoidal roll up 50 degrees at 4.83 rad/s for a model I_{XX}= 11.8 kg-m2 (in air). Consideration was also given for the ability to lift a 250 kg model above the free surface, at slow speed, in order to facilitate model rigging and changes during the test. The resulting capabilities are shown in Table C-4.

Table C-4. 3DoF Mechanism Design Capabilities

	Max Stroke	Max Speed
Sway	711 mm	4064 mm/sec
Heave	432 mm	371 mm/sec
Roll	65 deg. (w/ 381 mm arm)	444 deg/sec

The initial design of the mechanism utilized an integrated actuator that was made from a structural extrusion, a drive mechanism, and supporting bearings. While this resulted in a compact and elegant design, when preliminary testing began, the actual moments exerted on the actuators were too large for these components. As a result, a more rigid solution was pursued, and the design of the mechanism was modified.

The resulting final design can be seen in Figure C-15. Roll is actuated using a Kollmorgen AKM53 servo motor coupled to a 30:1 right angle, double shaft, and precision gearbox. The roll arm, or yoke, was attached by keyless couplings to the output shafts.

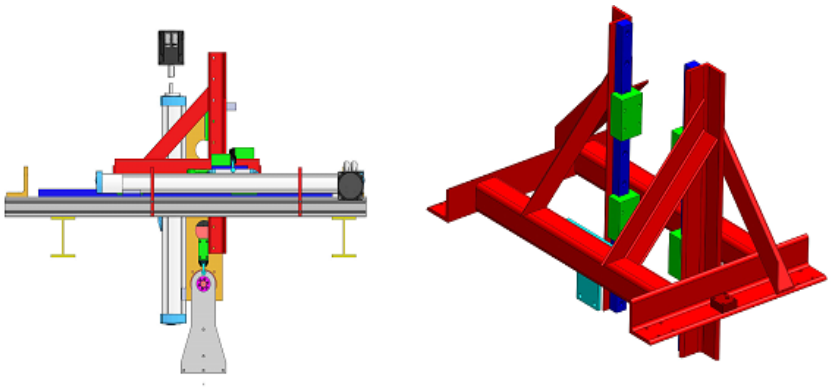

Figure C-15. 3DoF motion mechanism profile view (left) and sway carriage (right) with vertical heave rails (blue and green).

The roll gearbox was supported by a pair of machined angles that together with heave actuator make up the heave carriage. This actuator moved up and down as part the heave carriage, in order to keep the bottom clear of the rolling model, regardless of initial height. With its saddle coupled to the sway carriage, the heave actuator used an AKM53 motor coupled to a 2.54 mm/thread ball screw to move the heave carriage up and down. The carriage was supported by four precision, high-capacity Thompson linear bearings on a pair of vertical rails.

The sway carriage was supported by four additional linear bearings on a pair of horizontal rails that spanned the supporting I-beams. A single AKM54 motor drove the pair of sway actuators, which were coupled together and use belt drives to achieve 130 mm/rev. The actuators were attached to the same supporting extrusions as the sway rails. The saddles were coupled to the sway carriage through spherical bearings. All three actuation axes included limit switches. Both the sway and heave axes also incorporated mechanical limits, or hard stops.

C.1.4.1 Control Theory

For the experiment, the intended condition was 1DoF roll, including large amplitude conditions. The roll motion, ϕ, is given as

$$\phi = \phi_0 \sin(\omega t + \varepsilon) \tag{C.4}$$

where user-specified values are given for the roll amplitude, ϕ_0, the angular velocity, ω, and the initial phase angle, ε. The sway motion control input, Y, including consideration for the contribution from the roll motion, is given as

$$Y = y_0 \sin(\omega t + \varepsilon) - A_\phi \sin(\phi) \tag{C.5}$$

where y_0 is the sway amplitude and A_ϕ is the length of the attachment arm from the roll actuator to the desired roll center of the model. The heave motion, Z, is given as

$$Z = z_0 \sin(\omega t + \varepsilon) - A_\phi (1 - \cos(\phi)) \tag{C.6}$$

C.1.4.2 Construction and Installation

The sway carriage was fabricated as a steel weldment at NSWCCD and then machined true, in order to compensate for warping in any of the mounting surfaces. The remaining components and machined parts were then assembled on-site.

The mechanism was installed in the 140 ft basin at NSWCCD (Figure C-16). The basin is 42.7 m long and 3.05 m wide. For the experiments, the water level in the basin was fixed at at depth of 1.37m.

The mechanism was configured in the middle of the basin to enable the model to be oriented transversely across the basin to support 2D measurements. Aluminum I-beams were modified for higher transverse stiffness and anchored into the concrete side walls of the basin. The sway tracks of the 3DoF mechanism were oriented perpendicular to the I-beams, providing a fixed support structure for the mechanism. Figure C-17 shows the model attached to the 3DoF mechanism in its configuration for the experiment.

Figure C-16. Installation of the 3DoF motion mechanism in the NSWCCD 140 ft basin

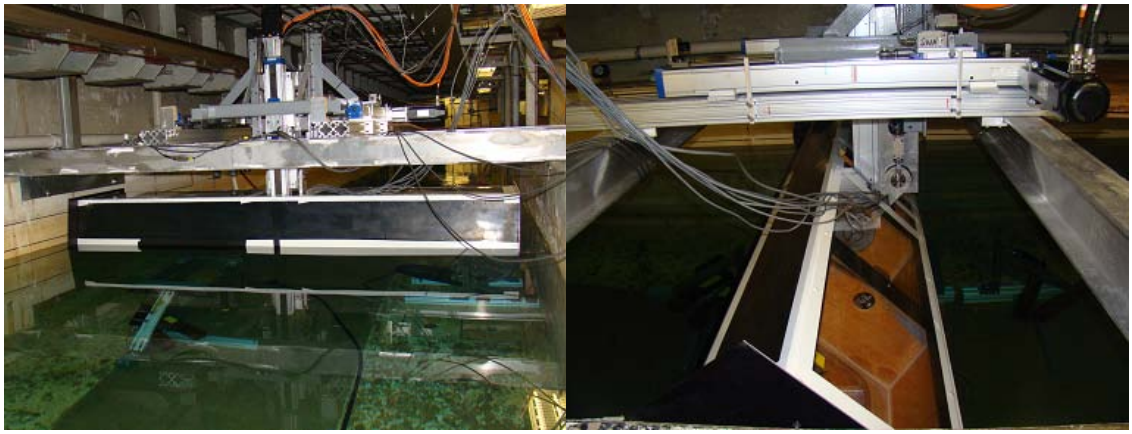

Figure C-17. DTMB Model #5699-1 attached to the 3DoF motion mechanism (left) and undergoing large amplitude forced roll oscillation (right)

C.1.4.3 Mechanism Control and Software

The 3DOF controller consisted of a PC running a National Instruments PCI-7344 motion controller card connected to Copley Controls Xenus XTL-230-40-R servo amplifiers integrated into a custom control box built by G&G Technical, Inc. (Figure C-18). Three analog outputs from the motion card were fed into the corresponding servo amplifiers to drive the motors. The feedback encoder signals and limit switch signals were monitored by the motion card.

The Copley servo amplifiers were run in a velocity mode with the analog signal from the National Instruments motion card providing the control. This allowed the motion card to run a feedback loop, which would compute the necessary velocity to obtain the desired position, and the servo amplifiers would compute the needed acceleration to obtain the requested velocity as fast as possible, while also providing the power to drive the motors.

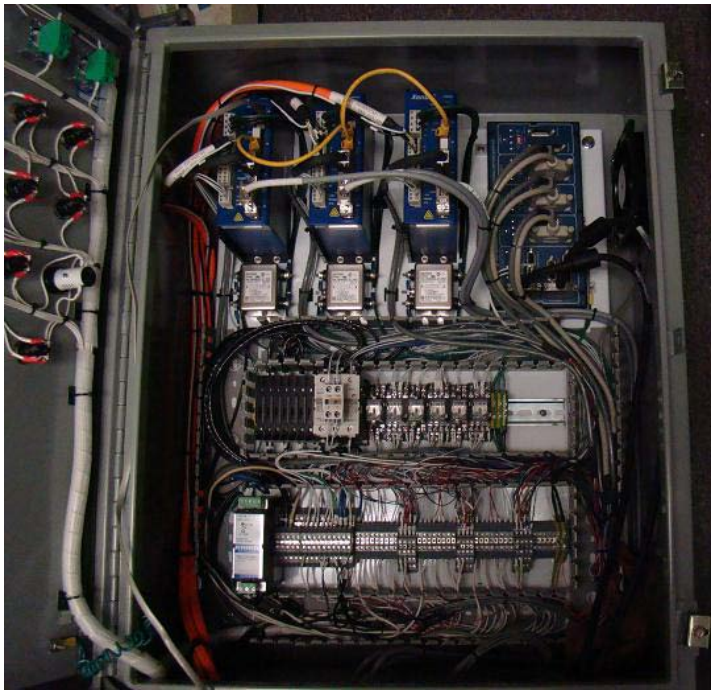

Figure C-18. Control box for the 3DoF motion mechanism

The software providing the user interface for the control of the motors was written using National Instruments Labview software. The primary control loop (i.e. computing the necessary velocity based on the desired position and handling encoder and limit switch feedback) was implemented by the controller card. While the motion card provided an internal processor that could run simple programs, the programming interface for the card did not provide the operations needed to produce the desired oscillations. Therefore, the oscillation position profile was produced using the main processor.

The first iteration of the software used a timed loop that would send a desired position to the motion card at precise intervals. This allowed the operator to update the oscillation position profile on the fly. This was important because the acceleration ramps at the beginning and end of the oscillation were needed to achieve the high speeds with a large model. Another desired capability was the ability to change the frequency and magnitude of the oscillation while the model was oscillating. The real-time position update software produced what appeared to be smooth motion that was synchronized between all three axes. However, it was discovered that the actual motion was not actually smooth, but instead was a very fast step function. This was observed on the model force gages as noise in the signal.

As a result, a spline interpolation method integrated into the motion card was used instead. Given a circular buffer of positions and an update rate, the motion card interpolated between the points to provide an incredibly smooth movement, due to the motion card's ability to update the position much faster than the timed loop. This also allowed us to obtain the highest synchronization possible between the movements of the three axes, as all three motions could be started with one call to the motion card. Therefore, any delays between the motions of the different axes were controlled by whatever delays are inherent in the motion card itself. This method results in a limitation in that the operator has to predetermine the oscillation profile buffer to feed to the card, including acceleration ramps. It also imposes a restriction on the

amount of collection time, could lead to prohibitively large buffers, and does not allow changes frequency and amplitude on the fly.

Fortunately, the conditions of the experiment did not require any restrictions on the timing of the profile changes. Therefore, a hybrid method was adopted, where watchdog software was written that monitored the motion card's progress through the circular buffer. As profile changes were requested, the watchdog software can exclusively make changes to a portion of the buffer that was safe and did not affect the prescribed motions. The buffer size, interpolation update rate, watchdog update rate, and watchdog update size were chosen to ensure that the watchdog software stayed ahead of the motion card's interpolation software.

C.2 Details of the Experimental Set-Up and Test Procedures

C.2.1 Model Configuration for Roll Decay Experiments

In addition to forced roll oscillation experiments, roll decay experiments were also carried out. For the roll decay experiments, the model was attached to the basin cross-structure and allowed to pivot about a single point, located along the centerline of the ship, at the vertical center-of-gravity. This allowed the model to rotate freely in the roll mode of motion, while constraining motion in all other degree-of-freedom. The model was inclined to a desired initial roll angle by applying a vertical force on the starboard deck edge and then instantaneously released so that no additional forces were applied to the model (Figure C-19).

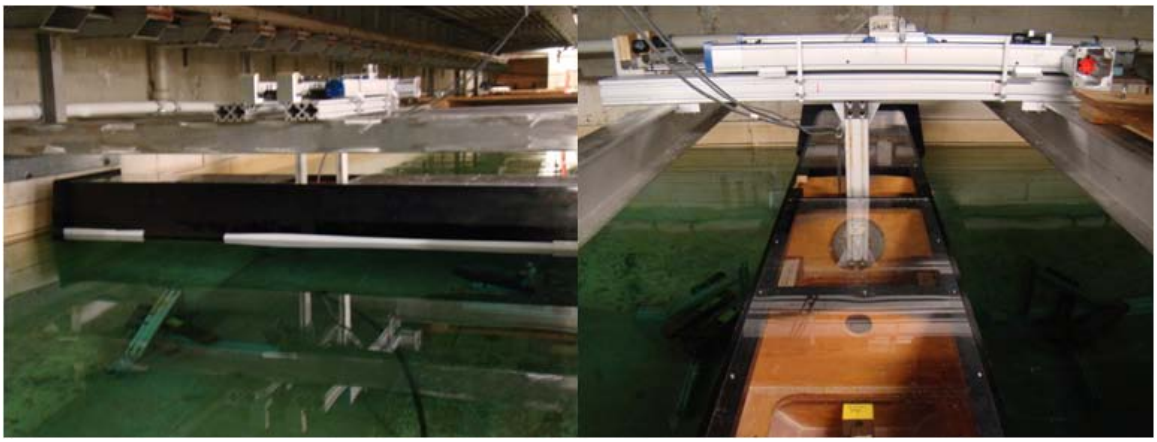

Figure C-19. Roll decay mechanism, shown attached to the model in the NSWCCD 140 ft basin

C.3 Details of the Experimental Results

This section includes discussion of the experimental results for the roll decay condition and analysis using the equivalent linear damping method, and discussion of the analysis of experimental measurement noise and repeatability.

C.3.1 Roll Decay Results

Roll decay results from the experiment are presented in this section. A sample roll motion measurement is shown for a calm water 1DoF roll decay test (Figure C-20).

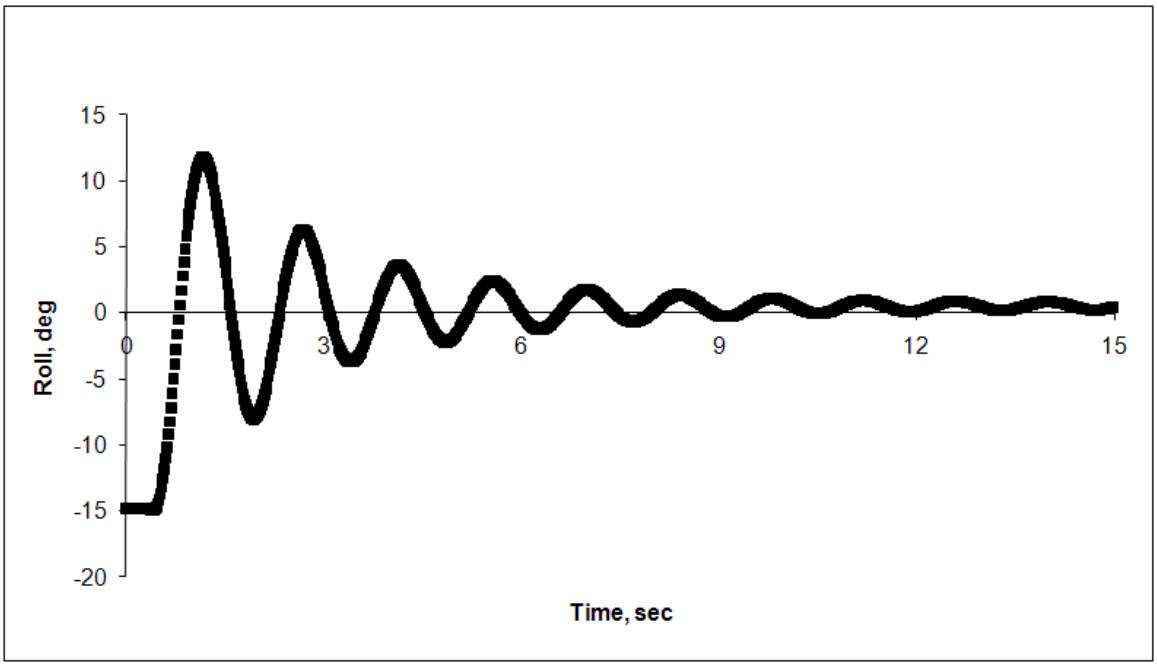

Figure C-20. Sample roll decay measurement for DTMB Model #5699-1, initial heel angle, θ_0 = 15 deg

Using the results of the roll decay tests, for a range of initial heel angles, the roll decrement method (Himeno, 1981) was applied and the regression analysis coefficients for a 3rd-order polynomial function were determined (Figure C-21 and Figure C-22). For the configuration without bilge keels, the quadratic coefficient was negative, which is not physically accurate. This is likely due to the very small quantity and associated experimental uncertainty. Therefore, because the value was also quite small, a value of zero was used for the quadratic coefficient. This was observed not to have a significant affect on the equivalent linear damping coefficient obtained from the linear, quadratic, and cubic damping coefficients.

Thee regression coefficients were then used to obtain the linear, quadratic, and cubic damping coefficients for the 2D midship section, for configurations both with (Table C-5) and without bilge keels (Table C-6). Additional details of this procedure are given in the Appendix A and in Lewandowski (2004).

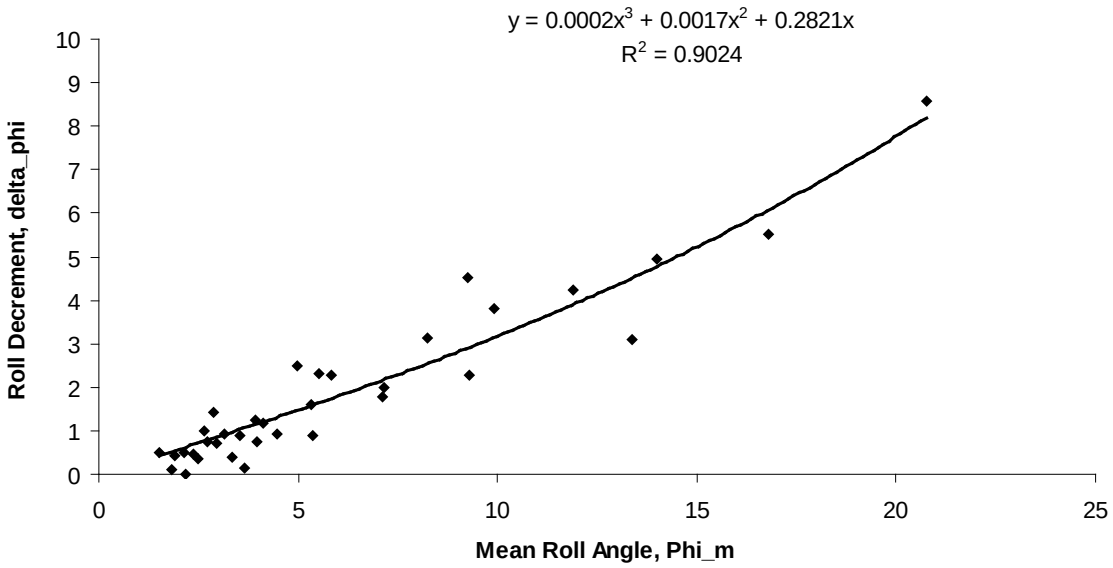

Figure C-21. Roll extinction curve for DTMB Model #5699-1 with bilge keels

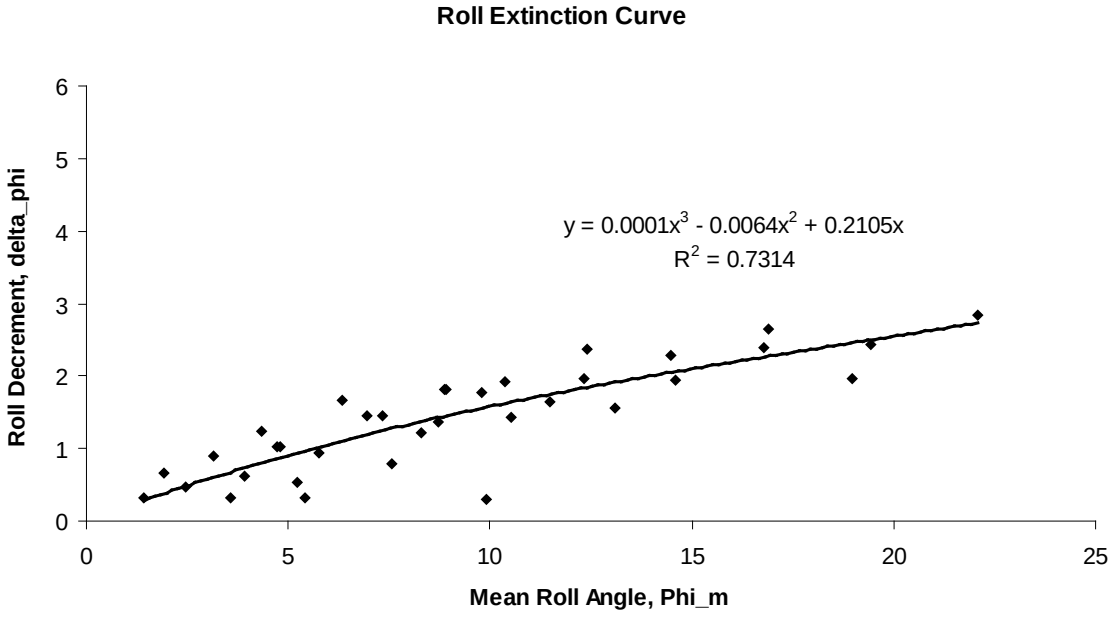

Figure C-22. Roll extinction curve for DTMB Model #5699-1 without bilge keels

Table C-5. Damping Coefficients determined from roll decay tests- DTMB Model # 5699-1 (with bilge keels)

$B_{44,1}$	$B_{44,2}$	$B_{44,3}$
1.416	0.0201	0.000613

Table C-6. Damping Coefficients determined from roll decay tests - DTMB Model # 5699-1 (without bilge keels)

$B_{44,1}$	$B_{44,2}$	$B_{44,3}$
1.056	0	0.000306

The linear, quadratic, and cubic damping coefficients, obtained from the regression analysis results of the roll decay tests, were then used to obtain the equivalent linear damping coefficient for the range of forced oscillation conditions considered, for the configurations both with (Table C-7) and without (Table C-8) bilge keels. Details on this procedure are given in Appendix A, and in Himeno (1981). As shown from the results, the calculated equivalent linear damping increased with both roll amplitude, and roll frequency. As expected, the damping is larger for the hull configuration with bilge keels, than without. However, using the equivalent linear damping method for analysis, the damping is observed to increase with amplitude, which does not correspond to the experimental observations observed for the damping of the roll moment and the bilge keel force, as discussed in Chapter 4.

Table C-7. Equivalent linear damping coefficient, B_e, as a function of roll amplitude and frequency for DTMB Model # 5699-1 (with bilge keels)

Forced Roll Amplitude (deg)	*Forced Roll Frequency (rad/s)*			
	2.17	*2.5*	*2.85*	*3.81*
5	1.418959	1.419456	1.419984	1.421435
15	1.425553	1.427076	1.428698	1.433188
25	1.432279	1.434871	1.437641	1.445347
30	1.435692	1.438834	1.442197	1.451579
35	1.439137	1.442841	1.44681	1.457913
40	1.442616	1.446892	1.45148	1.464348
45	1.446127	1.450986	1.456207	1.470885

Table C-8. Equivalent linear damping coefficient, B_e, as a function of roll amplitude and frequency for DTMB Model # 5699-1 (without bilge keels)

Forced Roll Amplitude (deg)	*Forced Roll Frequency (rad/s)*			
	2.17	*2.5*	*2.85*	*3.81*
5	1.056397	1.0564	1.056403	1.056414
15	1.056463	1.056487	1.056517	1.056617
25	1.056595	1.056662	1.056744	1.057024
30	1.056685	1.056782	1.0569	1.057303
35	1.056793	1.056925	1.057085	1.057634
40	1.056916	1.057089	1.057298	1.058015
45	1.057056	1.057275	1.05754	1.058447

C.3.2 Measurement Noise

Some additional noise was observed in the recorded measurements. After further frequency analysis, the noise was determined to occur at a high-frequency (Figure C-23), most likely resulting from mechanical noise from the 3DoF mechanism and/or the gearbox used to actuate roll motion. A digital filter was applied and the reconstructed signal was used for further analysis of the measurements. Sample reconstructed signals for the roll moment (Figure C-24) and bilge keel force (Figure C-25) are shown.

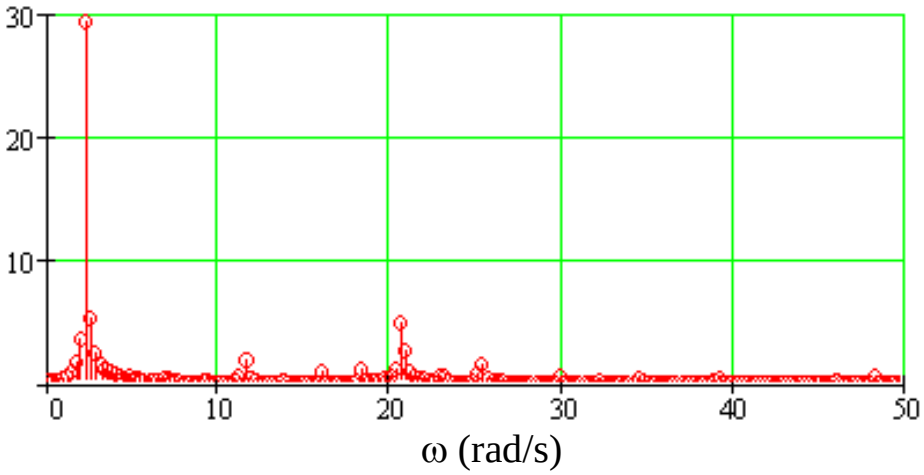

Figure C-23. Decomposition using an FFT of the roll moment signal measurement for the DTMB Model #5699-1, ϕ=15 deg, ω= 2.5 rad/s

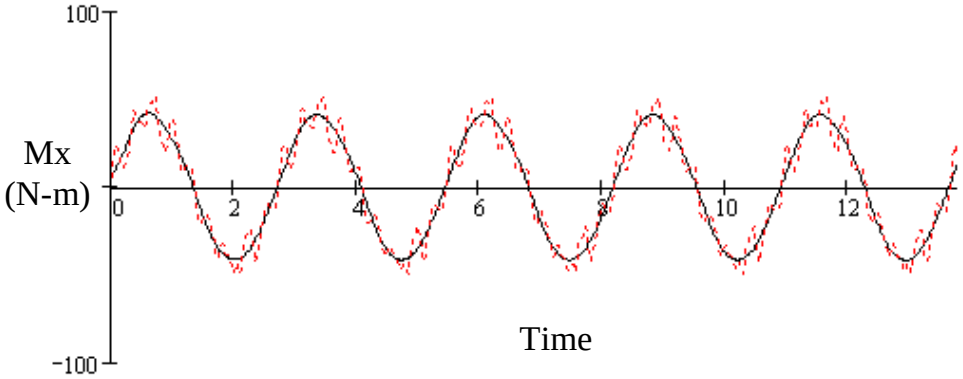

Figure C-24. Roll moment measurement, unfiltered (red) and reconstructed after digital filtering at 10 rad/s (black), for the DTMB Model #5699-1, ϕ=15 deg, ω= 2.5 rad/s

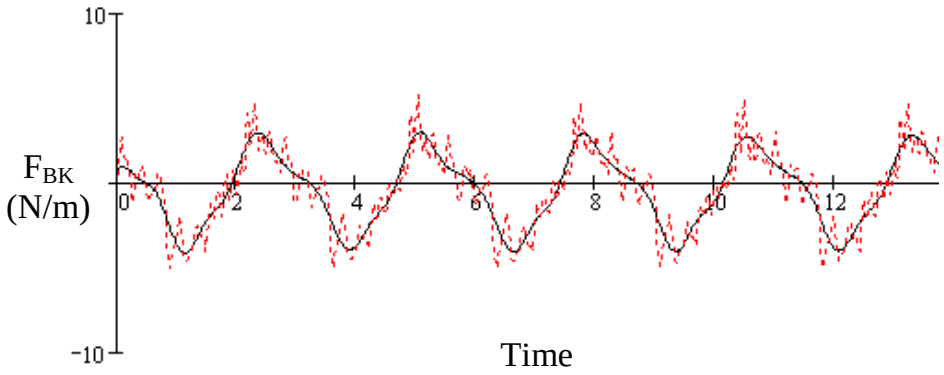

Figure C-25. Unit bilge keel force measurement, unfiltered (red) and reconstructed after digital filtering at 10 rad/s (black), for the DTMB Model #5699-1, ϕ=15 deg, ω= 2.5 rad/s

C.3.3 Repeatability of the Experimental Results

Sample phase plots for several roll amplitude conditions, including where the bilge keel is still deeply submerged (Figure C-26), where the bilge keel is near the free-surface (Figure C-27), and where the bilge keel has exited the free surface (Figure C-28-Figure C-30) are shown for twelve forced roll oscillation cycles. Additional sample phase plots are shown for the roll moment (Figure C-31-Figure C-35) and unit normal bilge keel force (Figure C-36-Figure C-40) for these conditions as well. The repeatability was not observed to vary relative to the other frequency conditions tested.

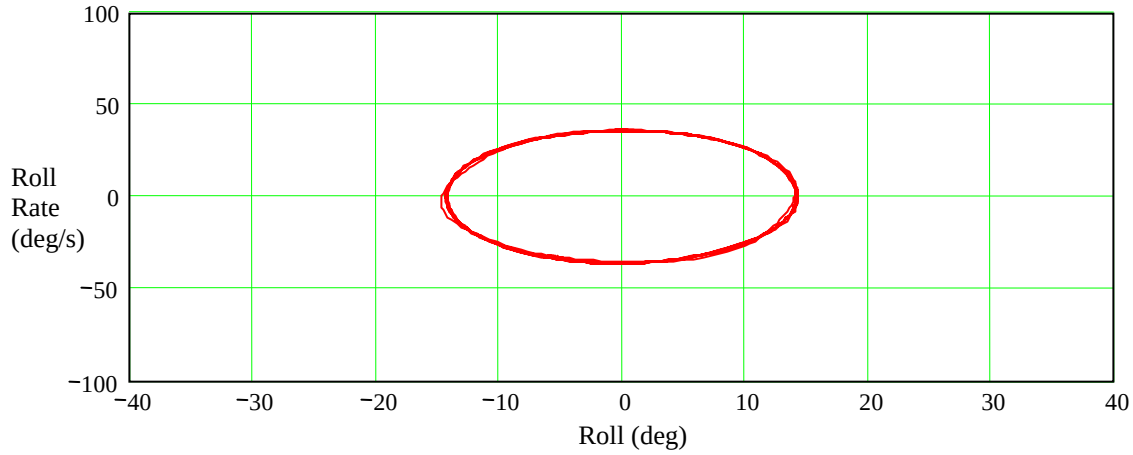

Figure C-26. Phase plot of roll rate vs. roll measurements, filtered, for DTMB Model #5699-1, ϕ=15 deg, ω= 2.5 rad/s

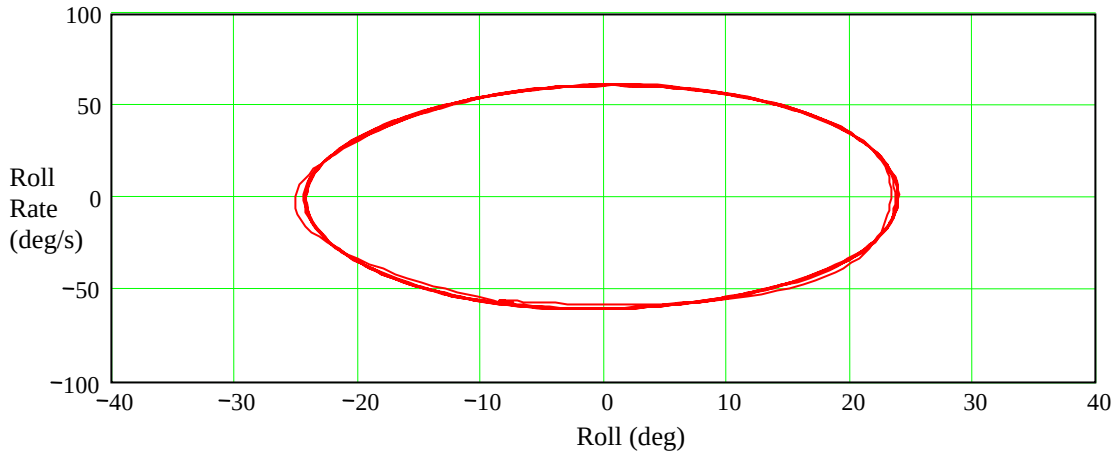

Figure C-27. Phase plot of roll rate vs. roll measurements, filtered, for DTMB Model #5699-1, ϕ=25 deg, ω= 2.5 rad/s

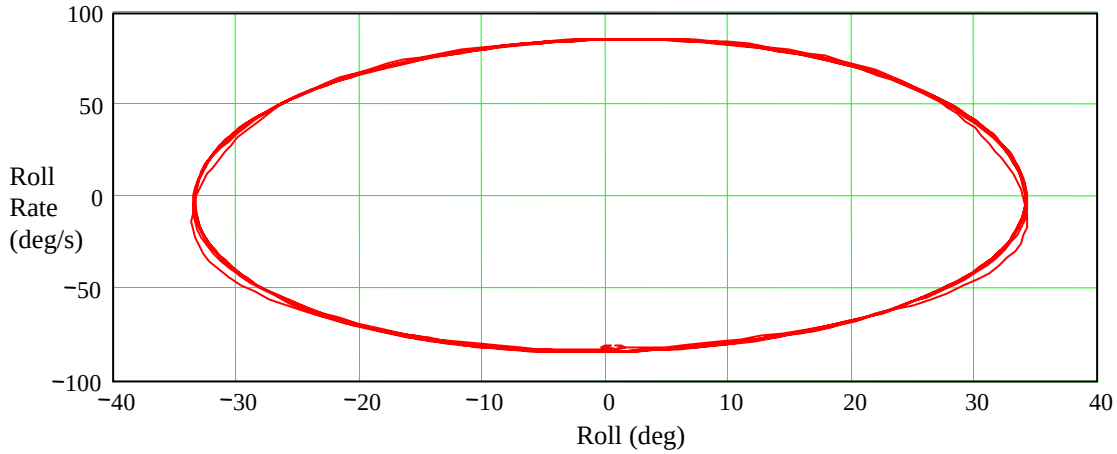

Figure C-28. Phase plot of roll rate vs. roll measurements, filtered, for DTMB Model #5699-1, ϕ=35 deg, ω= 2.5 rad/s

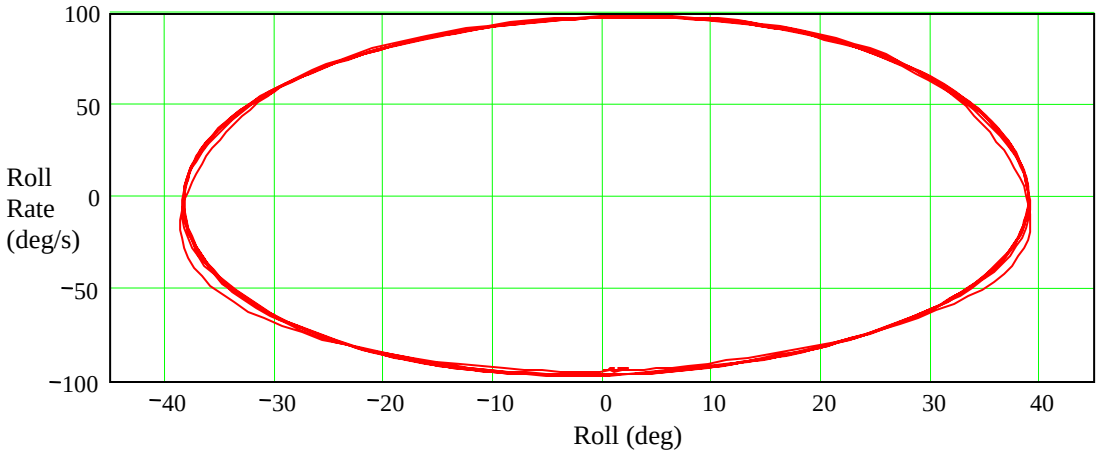

Figure C-29. Phase plot of roll rate vs. roll measurements, filtered, for DTMB Model #5699-1, ϕ=40 deg, ω= 2.5 rad/s

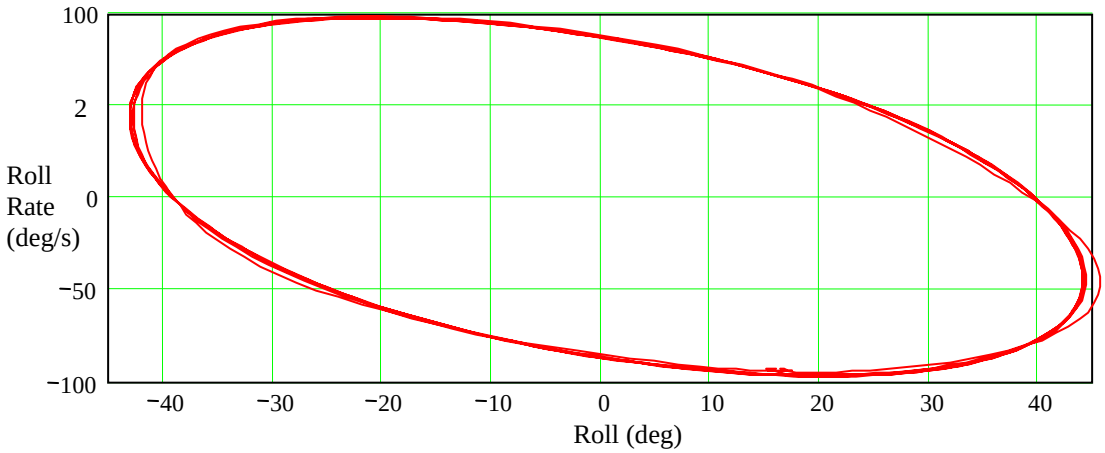

Figure C-30. Phase plot of roll rate vs. roll measurements, filtered, for DTMB Model #5699-1, ϕ=45 deg, ω= 2.5 rad/s

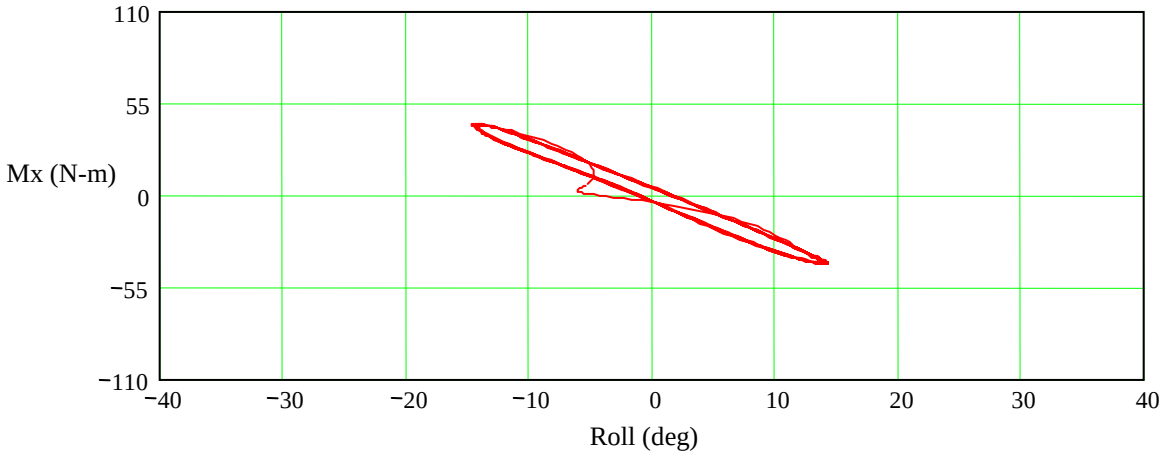

Figure C-31. Phase plot of roll moment vs. roll measurements, filtered, for DTMB Model #5699-1, ϕ=15 deg, ω= 2.5 rad/s

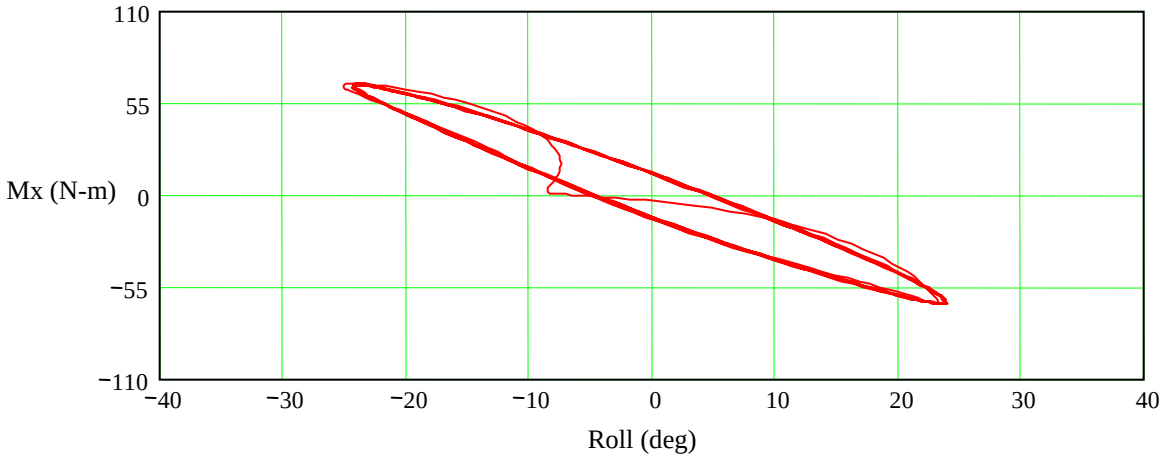

Figure C-32. Phase plot of roll moment vs. roll measurements, filtered, for DTMB Model #5699-1, ϕ=25 deg, ω= 2.5 rad/s

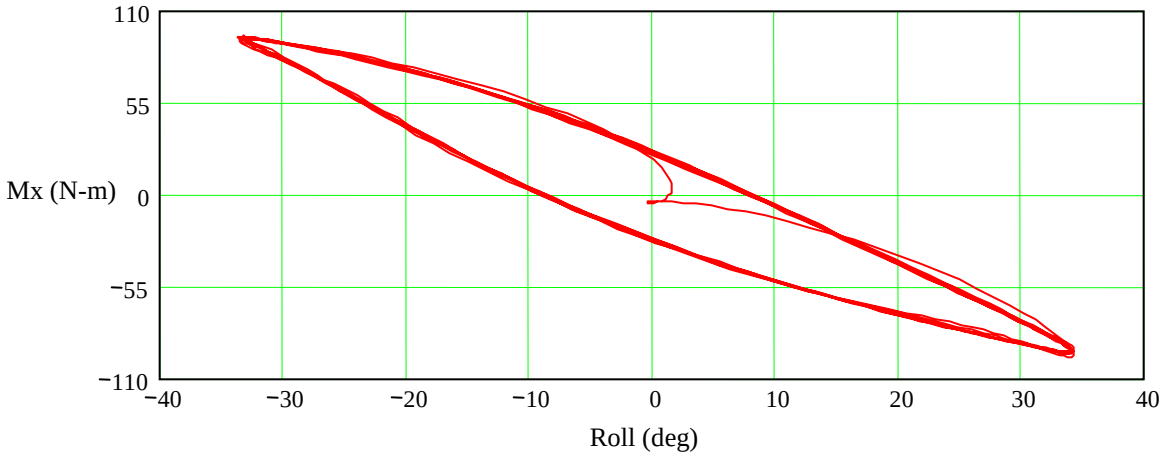

Figure C-33. Phase plot of roll moment vs. roll measurements, filtered, for DTMB Model #5699-1, ϕ=35 deg, ω= 2.5 rad/s

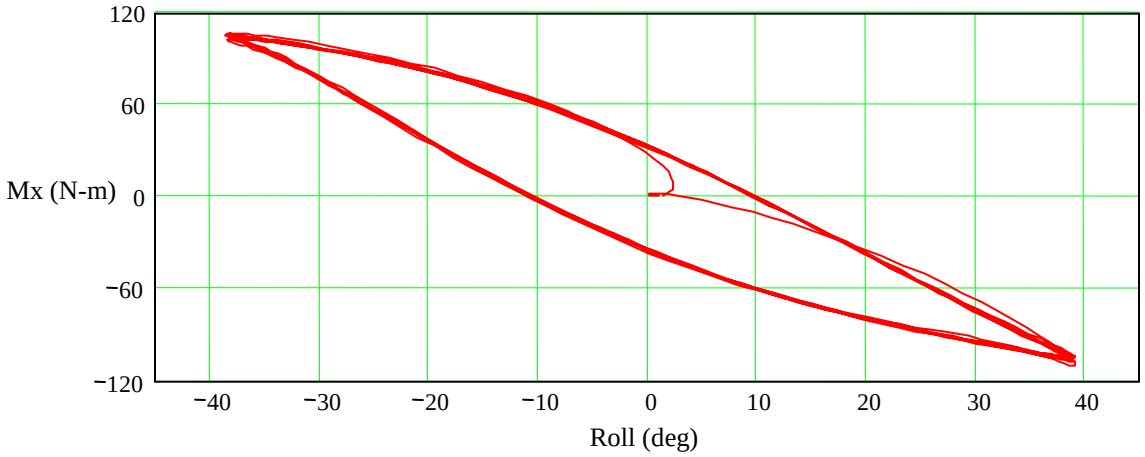

Figure C-34. Phase plot of roll moment vs. roll measurements, filtered, for DTMB Model #5699-1, ϕ=40 deg, ω= 2.5 rad/s

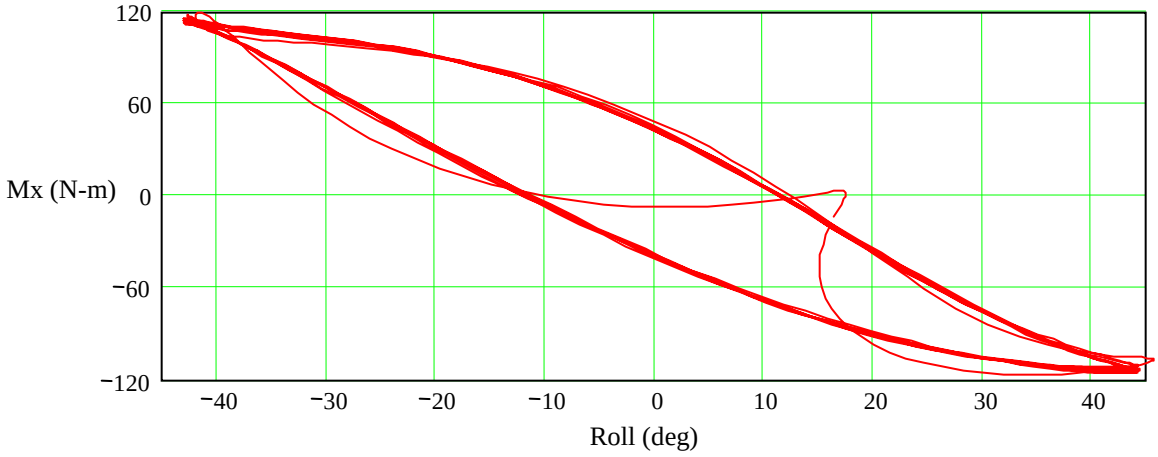

Figure C-35. Phase plot of roll moment vs. roll measurements, filtered, for DTMB Model #5699-1, ϕ=45 deg, ω= 2.5 rad/s

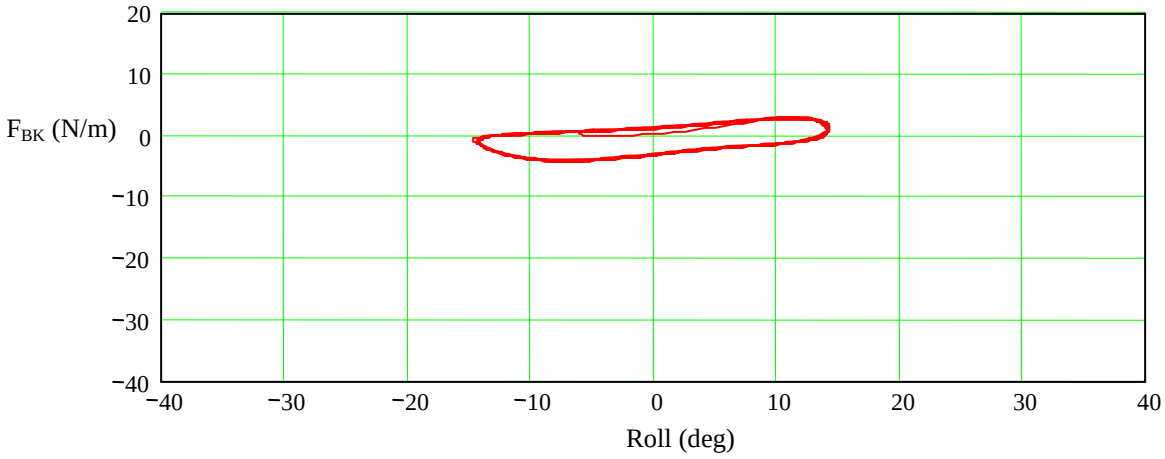

Figure C-36. Phase plot of unit bilge keel force vs. roll measurements, filtered, for DTMB Model #5699-1, ϕ=15 deg, ω= 2.5 rad/s

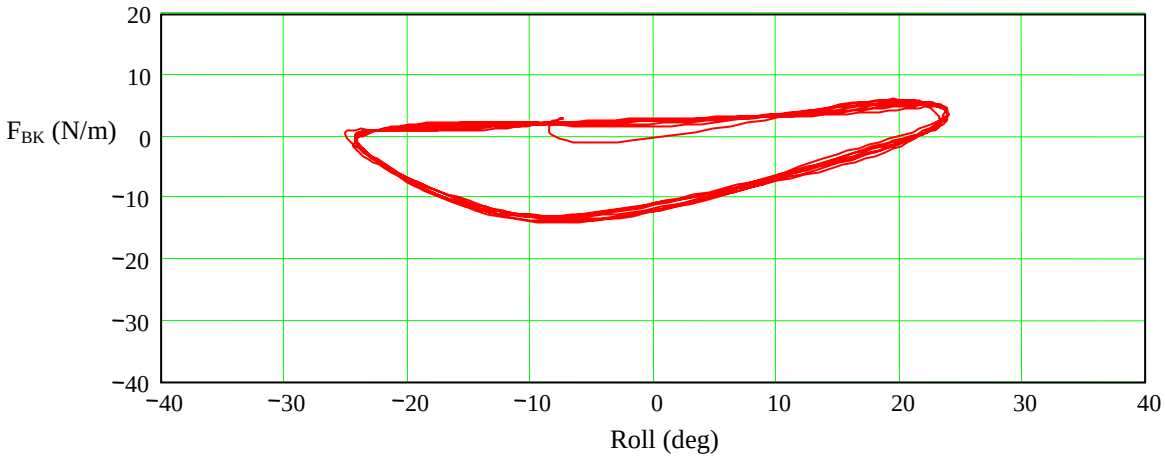

Figure C-37. Phase plot of unit bilge keel force vs. roll measurements, filtered, for DTMB Model #5699-1, ϕ=25 deg, ω= 2.5 rad/s

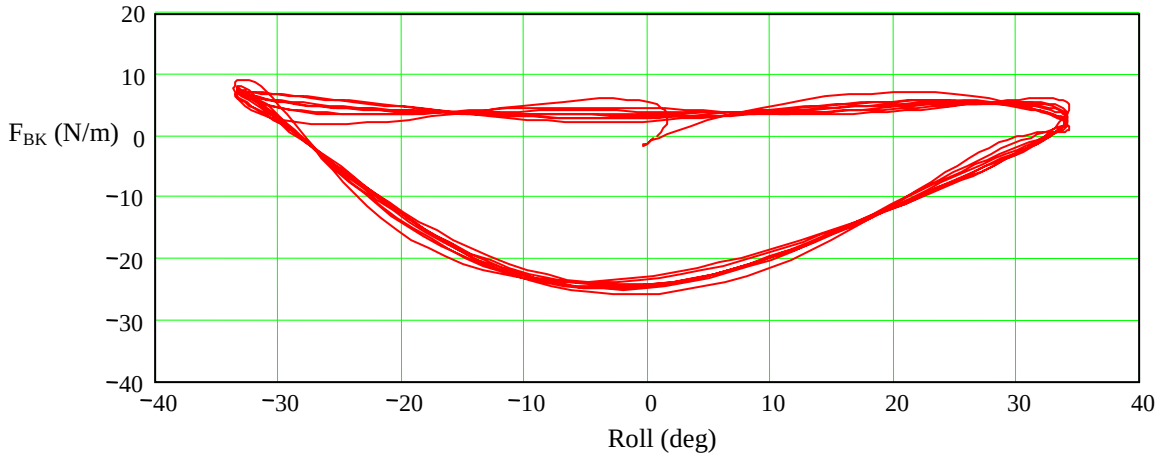

Figure C-38. Phase plot of unit bilge keel force vs. roll measurements, filtered, for DTMB Model #5699-1, ϕ=35 deg, ω= 2.5 rad/s

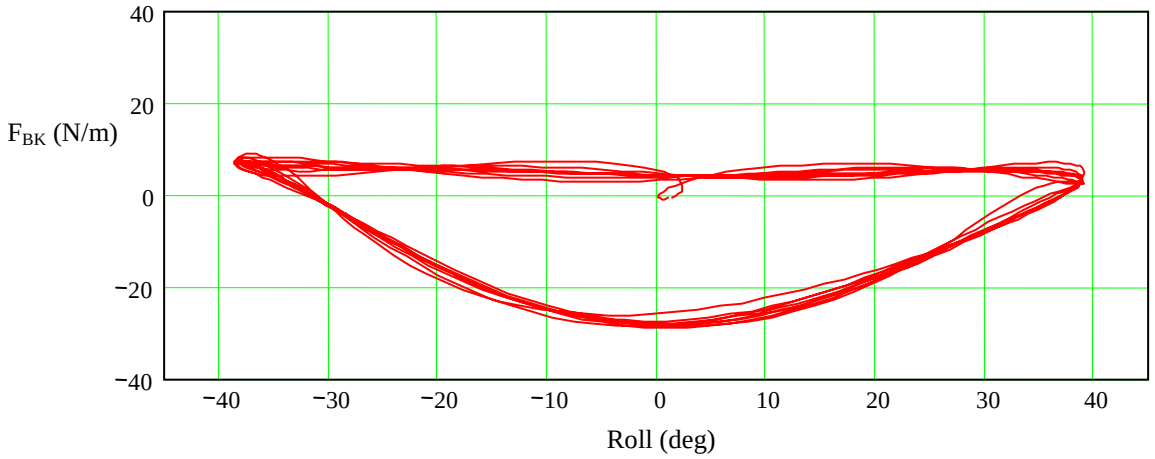

Figure C-39. Phase plot of unit bilge keel force vs. roll measurements, filtered, for DTMB Model #5699-1, ϕ=40 deg, ω= 2.5 rad/s

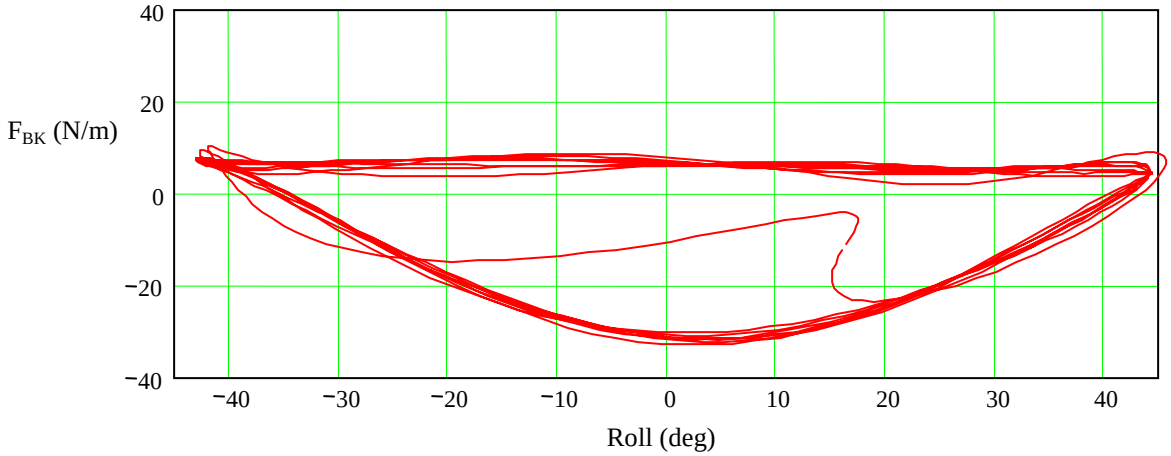

Figure C-40. Phase plot of unit bilge keel force vs. roll measurements, filtered, for DTMB Model #5699-1, ϕ=45 deg, ω= 2.5 rad/s

Appendix D: Additional Data from the Experimental Analysis and Observations

D.1 Hydrostatics

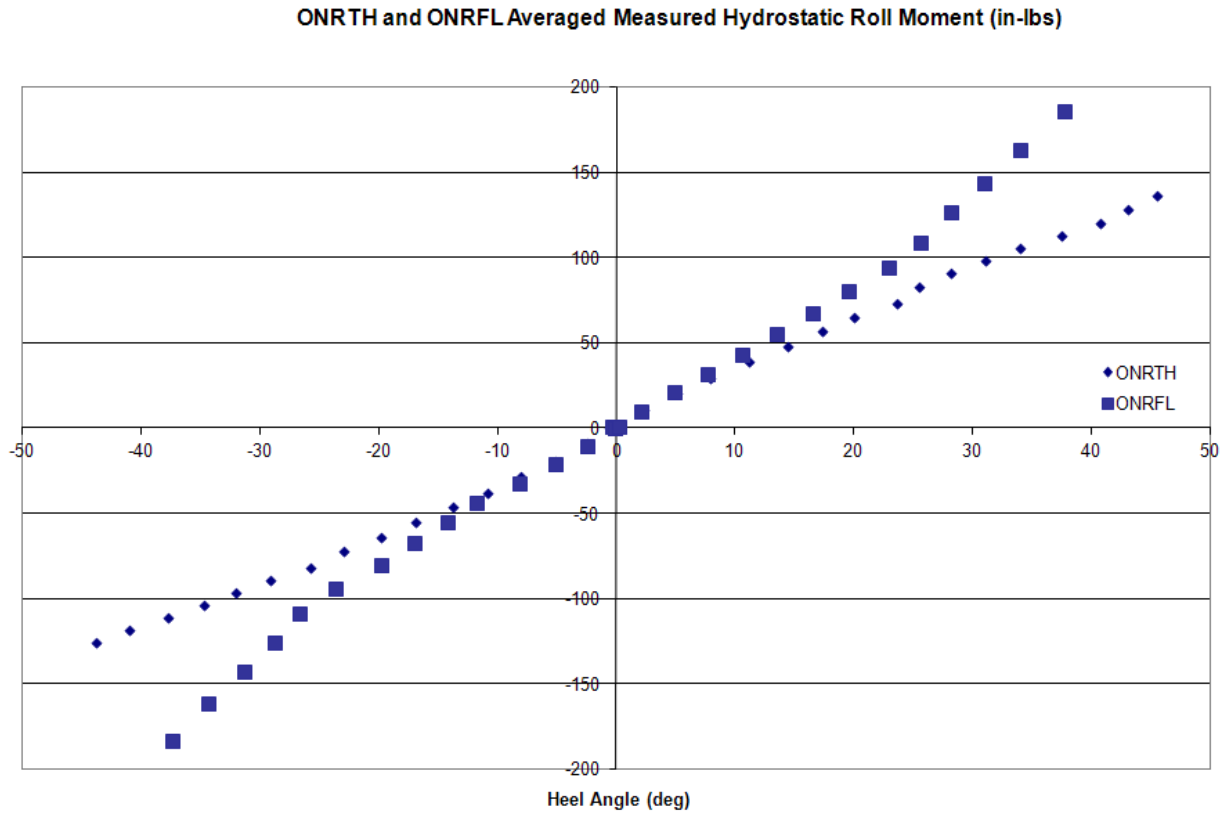

Figure D-1. Measured Hydrostatic Roll Moment, for DTMB Models #5699 and #5699-1 vs heel

The comparison between the measured hydrostatics of the ONRFL and ONRTH are shown in Figure D-1. Regression analysis of the two hydrostatics curves illustrates the differences due to the topside. For the ONRFL, a linear fit has an R^2= 0.9941, while a cubic fit has an R^2= 0.9996. However, for the ONRTH, a linear fit has an R^2= 0.9977, while the cubic fit has an R^2= 0.9995. While a cubic fit is better for both topsides, the flared topside exhibits more nonlinear behavior at larger heel angles.

D.2 Sample Measurements of the Hydrodynamic Components

Results are shown for the ONRFL, 2.5 rad/s, 15 degree forced oscillation condition (Figure D-2). The results are a sample of the types of measurements and analysis that was performed for all of the conditions (amplitudes, frequencies, and topsides).

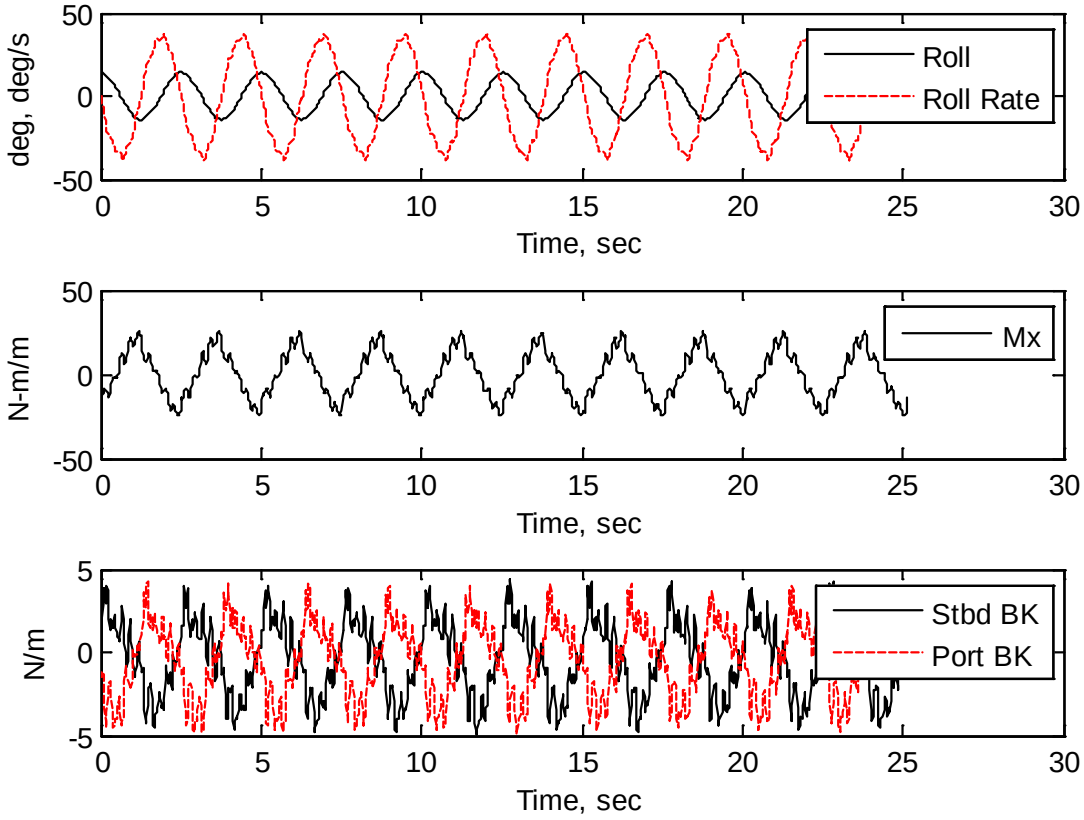

Figure D-2. Time-synchronized measurements of roll and roll rate, (top), unit hydrodynamic roll moment (middle), and starboard and port unit bilge keel force, for DTMB Model #5699, φ= 15 deg, ω=2.5 rad/s

D.3 Variation in the Bilge Keel Force with Roll Amplitude and Roll Frequency

Results are shown for the variation of the unit normal force on the bilge keel with amplitude, compared to the position within the roll cycle. Results for the ONRFL at the three roll frequencies: 2.17 rad/s (Figure D-3), 2.5 rad/s (Figure D-4), and 2.85 rad/s (Figure D-5) are shown. Results for the ONRTH at the three roll frequencies: 2.17 rad/s (Figure D-6), 2.5 rad/s (Figure D-7), and 2.85 rad/s (Figure D-8) are shown. Features are observed in the measured bilge keel force at particular positions during the roll cycle, which are similar across all of the roll frequency conditions. For the 15 deg amplitude condition, the bilge keel is observed to be approximately sinusoidal. However, as the roll amplitude increased, the bilge keel force deviates significantly from this sinusoidal behavior, corresponding to distinct physical processes. These physical processes are discussed further in Chapters 4 and 6.

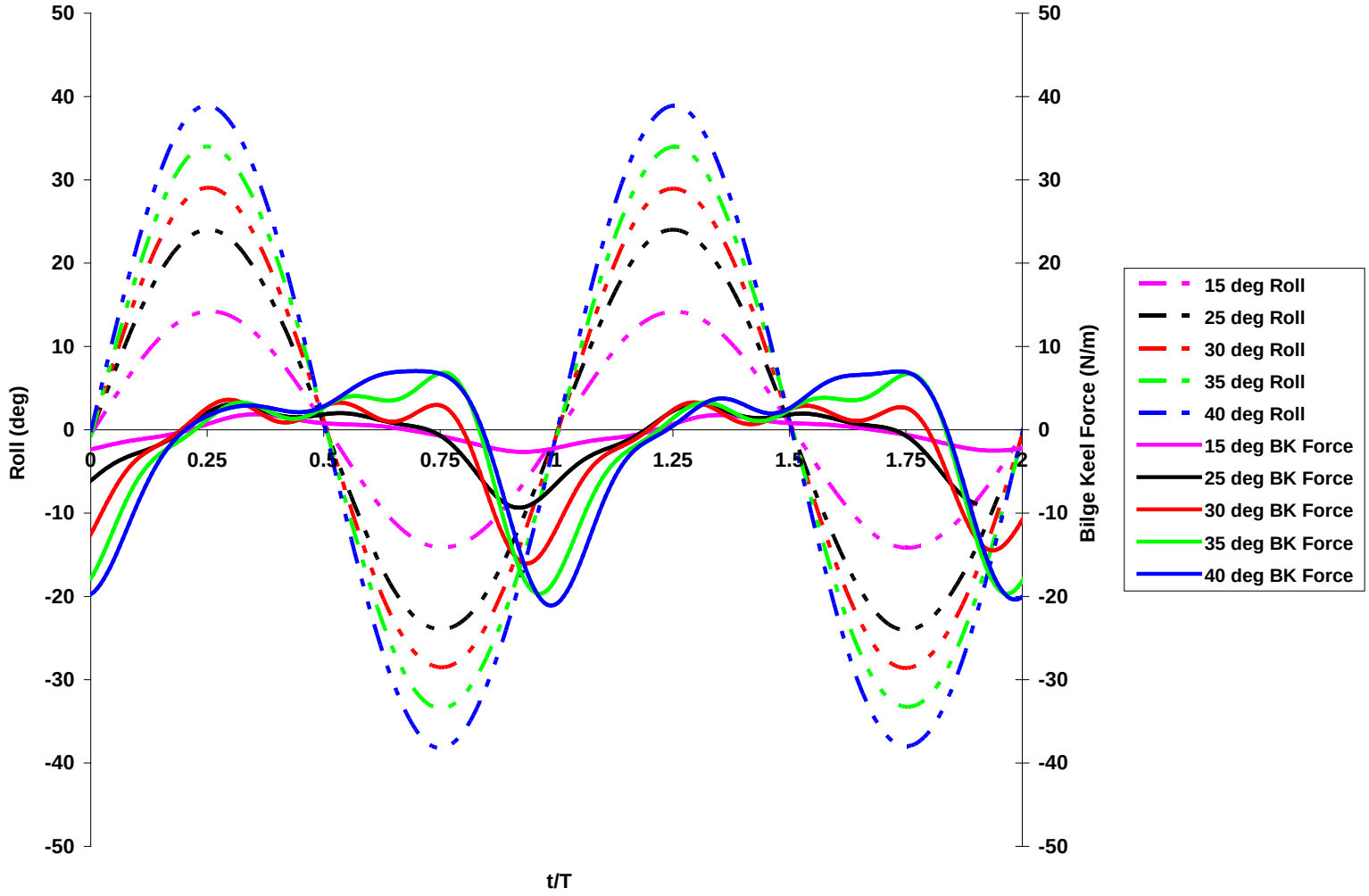

Figure D-3. Filtered roll motion measurements and bilge keel force measurements for the DTMB Model #5699, at various roll amplitudes, ϕ=15 (purple), 25 (black), 30 (red), 35 (green) and 40 (blue) deg, ω= 2.17 rad/s

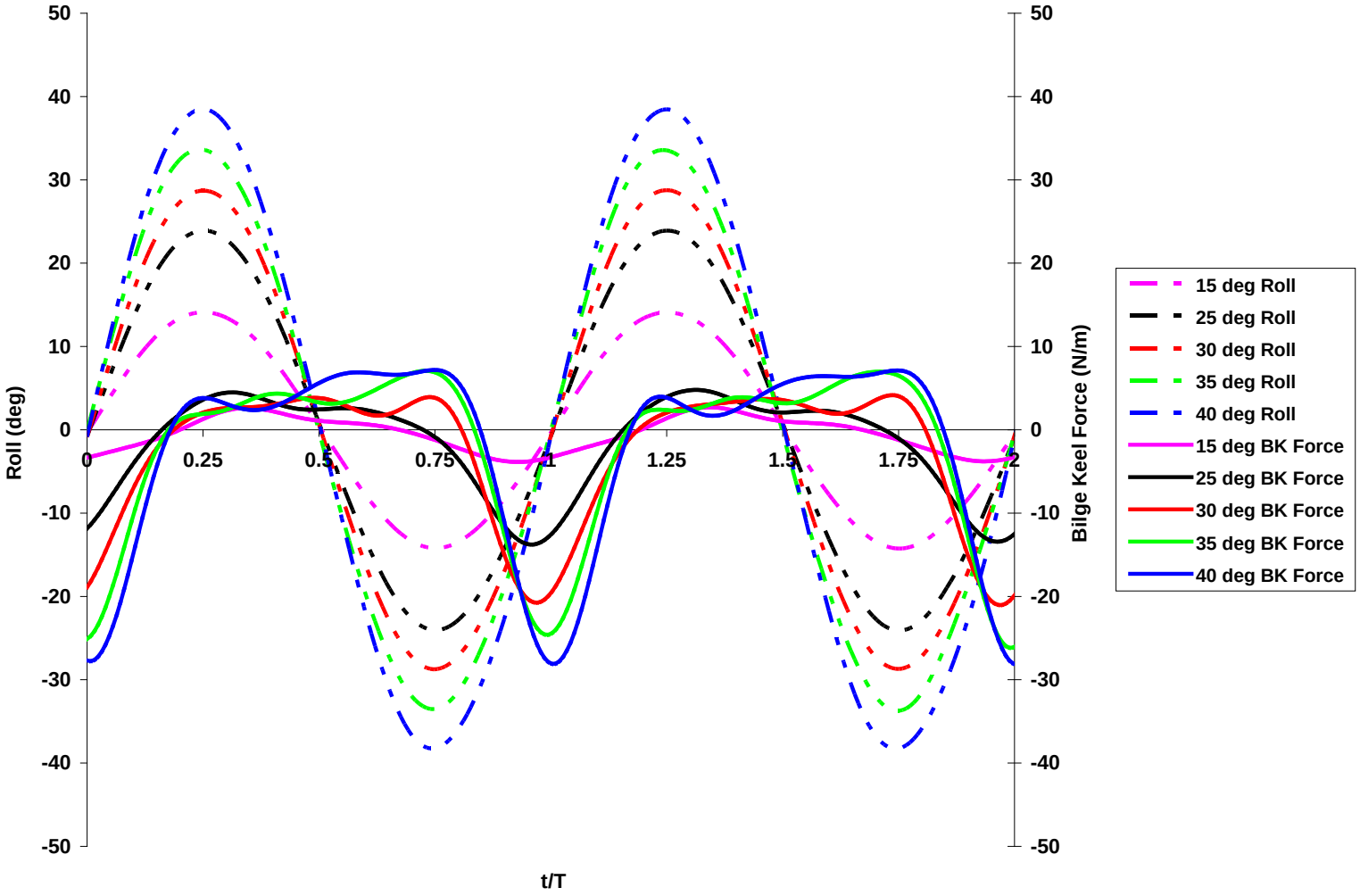

Figure D-4. Filtered roll motion measurements and bilge keel force measurements for the DTMB Model #5699, at various roll amplitudes, ϕ=15 (purple), 25 (black), 30 (red), 35 (green) and 40 (blue) deg, ω= 2.5 rad/s

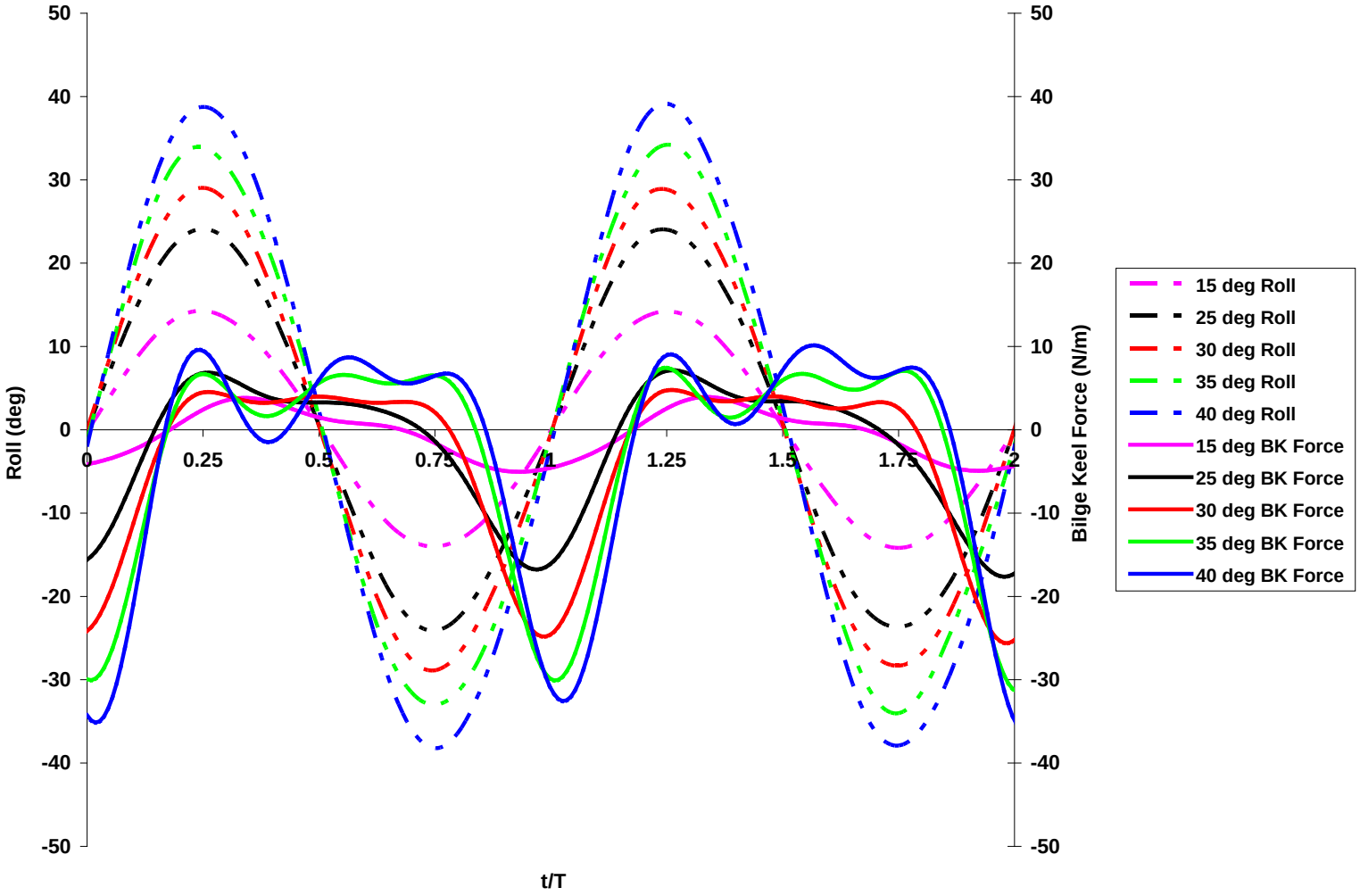

Figure D-5. Filtered roll motion measurements and bilge keel force measurements for the DTMB Model #5699, at various roll amplitudes, ϕ=15 (purple), 25 (black), 30 (red), 35 (green) and 40 (blue) deg, ω= 2.85 rad/s

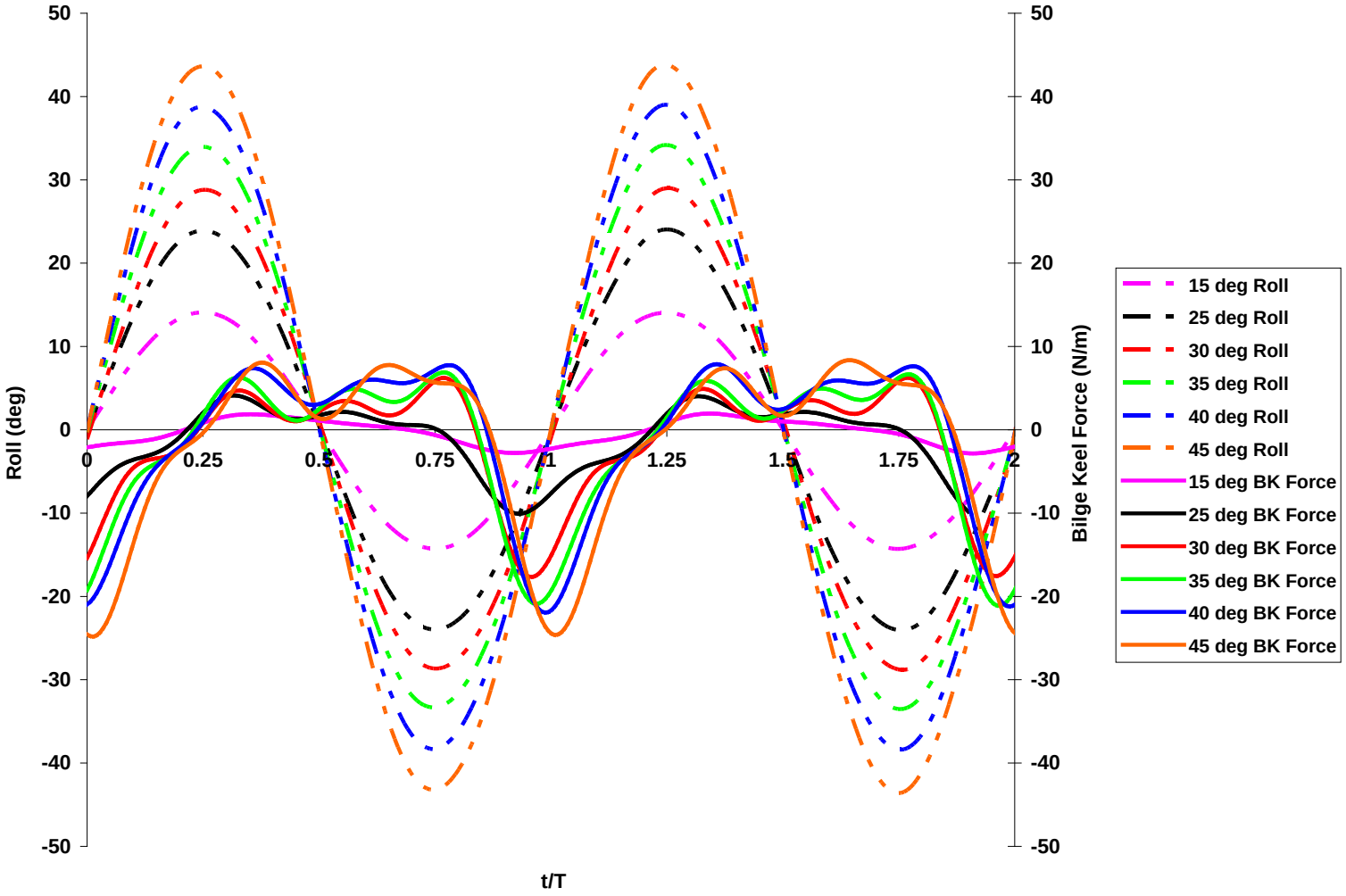

Figure D-6. Filtered roll motion measurements and bilge keel force measurements for the DTMB Model #5699-1, at various roll amplitudes, ϕ=15 (purple), 25 (black), 30 (red), 35 (green), 40 (blue), and 45 (orange) deg, ω= 2.17 rad/s

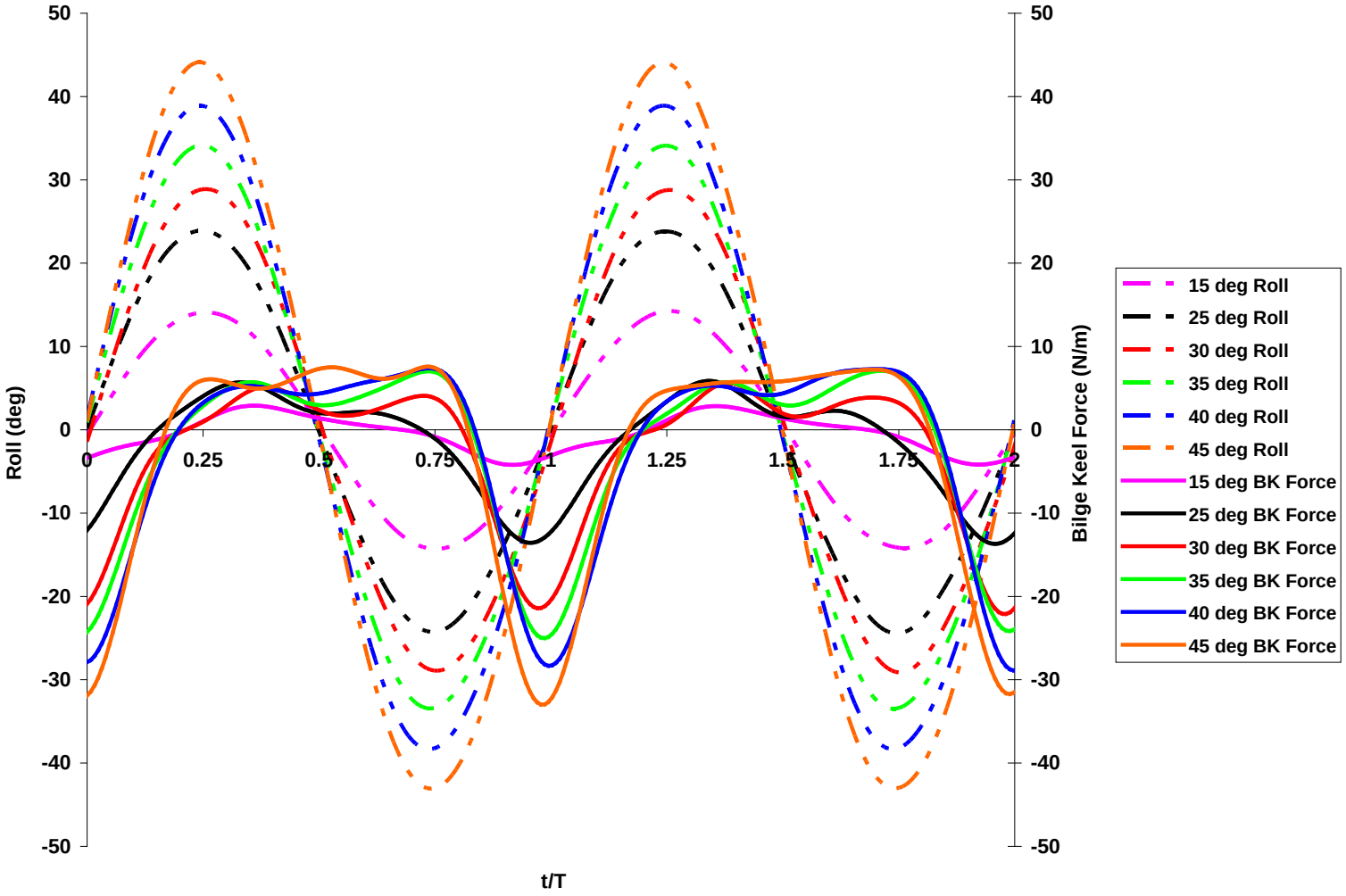

Figure D-7. Filtered roll motion measurements and bilge keel force measurements for the DTMB Model #5699-1, at various roll amplitudes, ϕ=15 (purple), 25 (black), 30 (red), 35 (green), 40 (blue), and 45 (orange) deg, ω= 2.5 rad/s

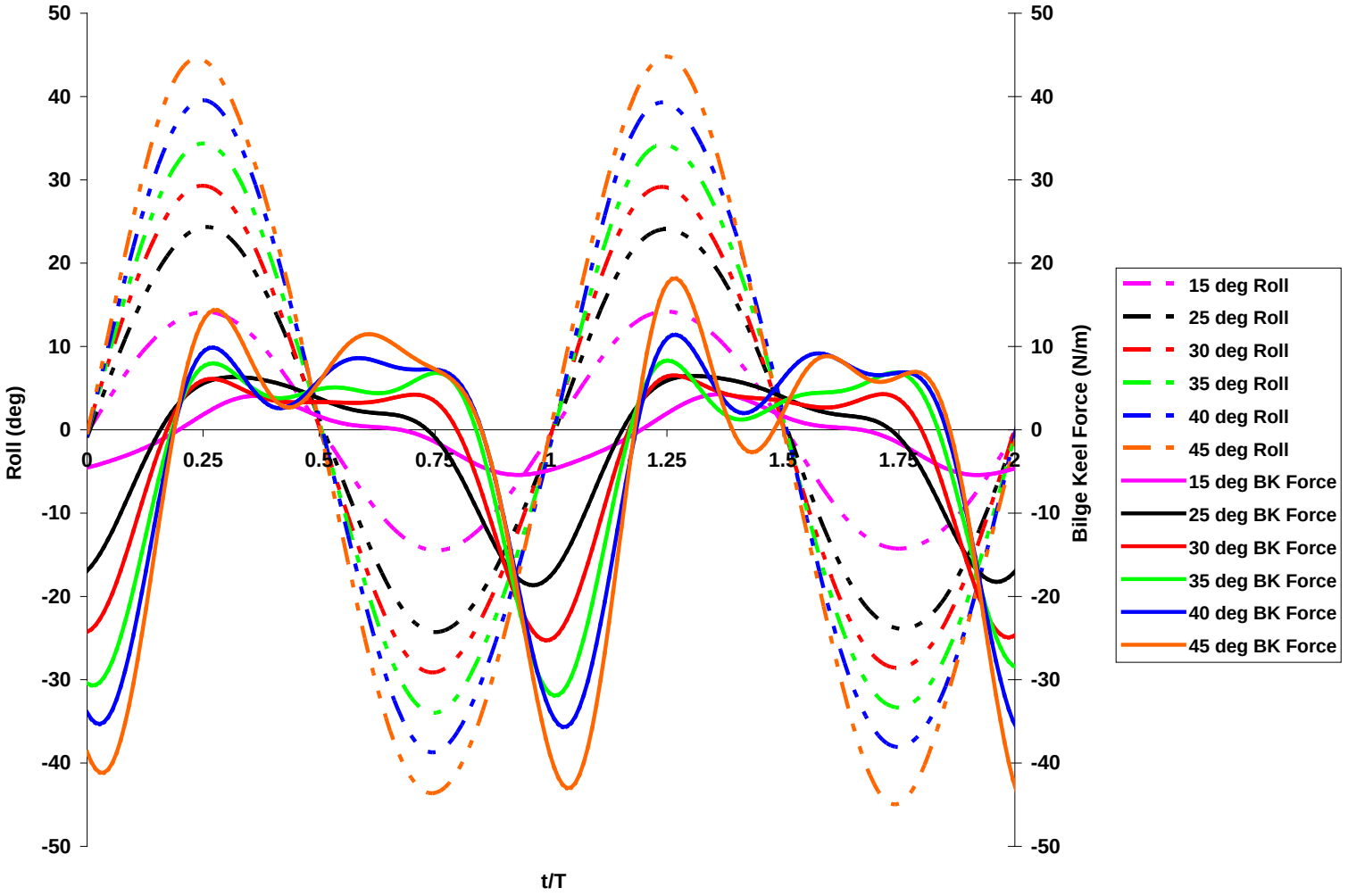

Figure D-8. Filtered roll motion measurements and bilge keel force measurements for the DTMB Model #5699-1, at various roll amplitudes, ϕ=15 (purple), 25 (black), 30 (red), 35 (green), 40 (blue), and 45 (orange) deg, ω= 2.85 rad/s

D.4 Proportion of the Hydrodynamic Roll Moment Due to the Bilge Keels

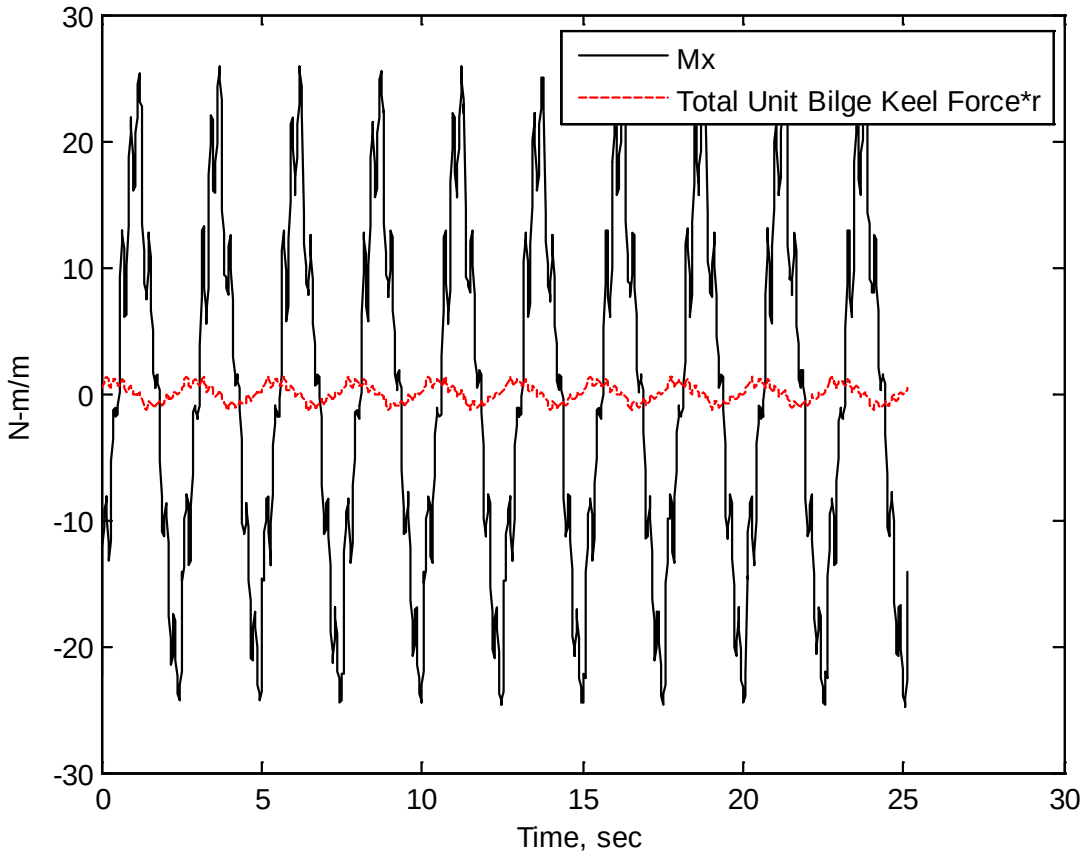

Figure D-9. Comparison of the unit hydrodynamic roll moment and moment contribution of the total unit bilge keel force, for DTMB Model #5699, φ= 15 deg, ω=2.5 rad/s

D.5 Decomposition of the Hydrodynamic Components of the Bilge Keel Force

D.5.1 Decomposition of the Hydrodynamic Roll Moment

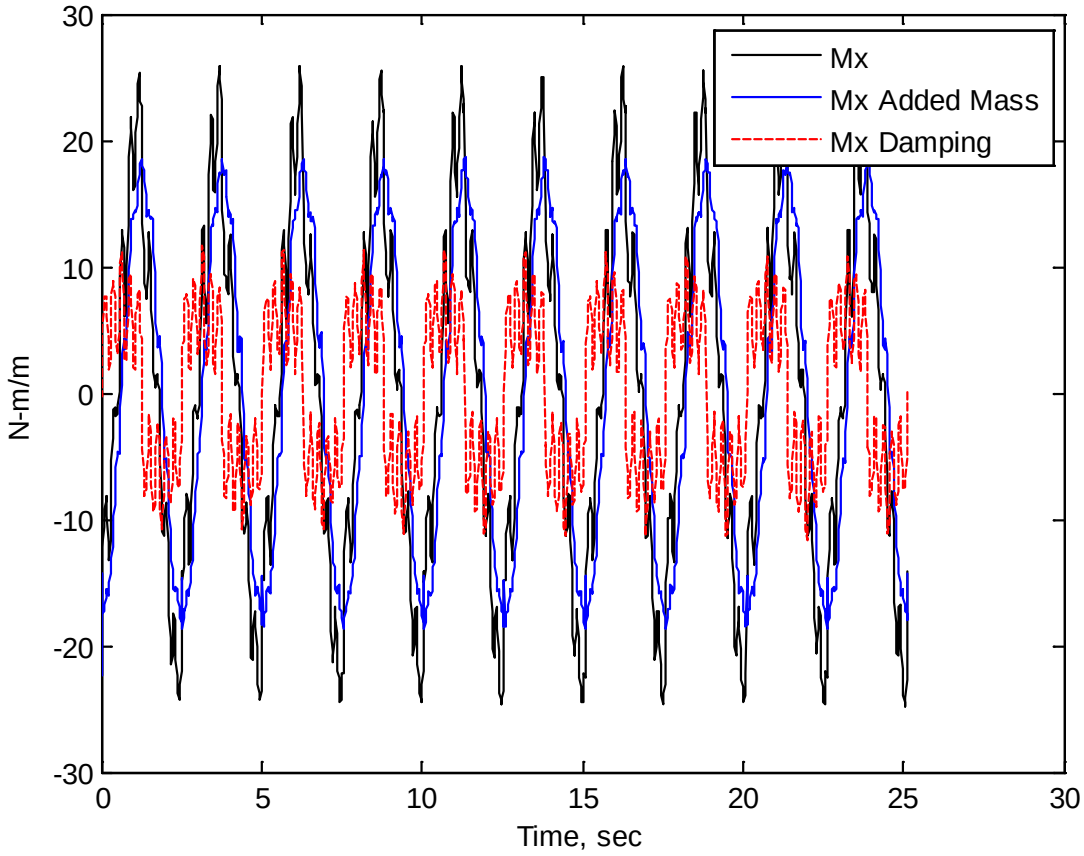

Figure D-10. Comparison of the unit hydrodynamic roll moment and associated hydrodynamic components- added inertia and damping, for DTMB Model #5699, φ= 15 deg, ω=2.5 rad/s

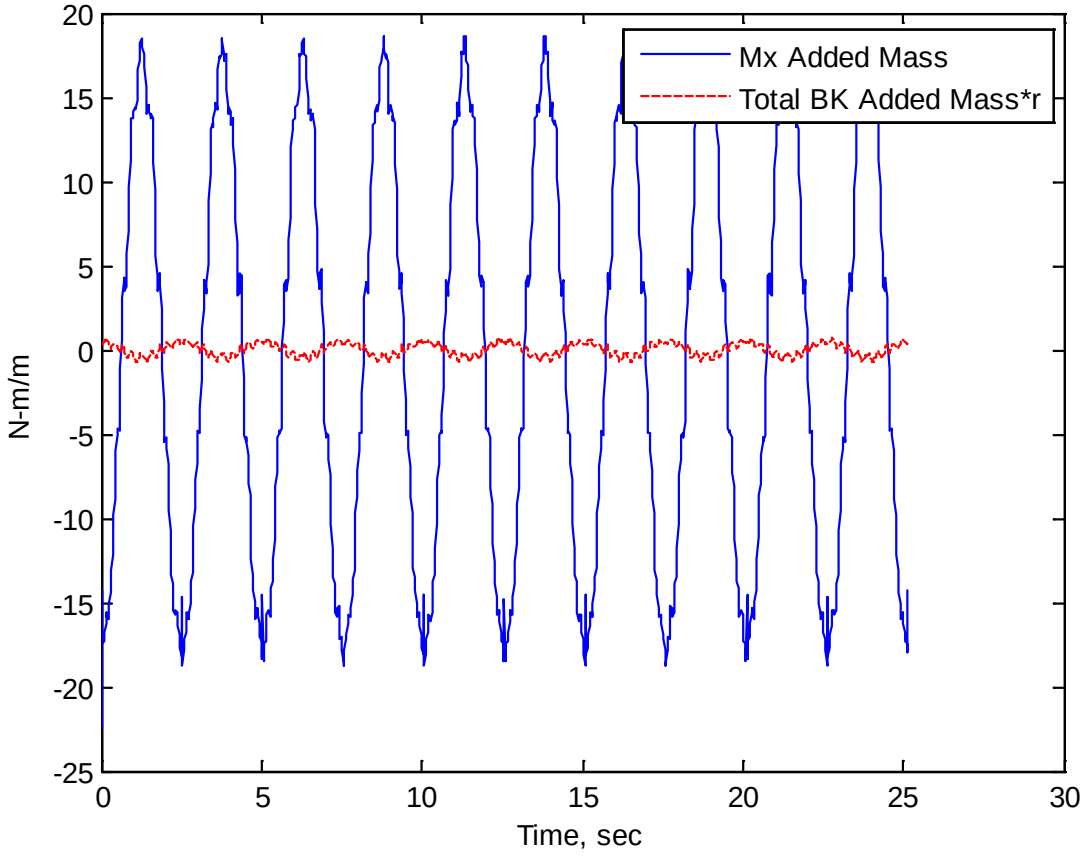

Figure D-11. Comparison of the added inertia of the unit hydrodynamic roll moment and the unit hydrodynamic roll moment due to the bilge keels, for DTMB Model #5699, φ= 15 deg, ω=2.5 rad/s

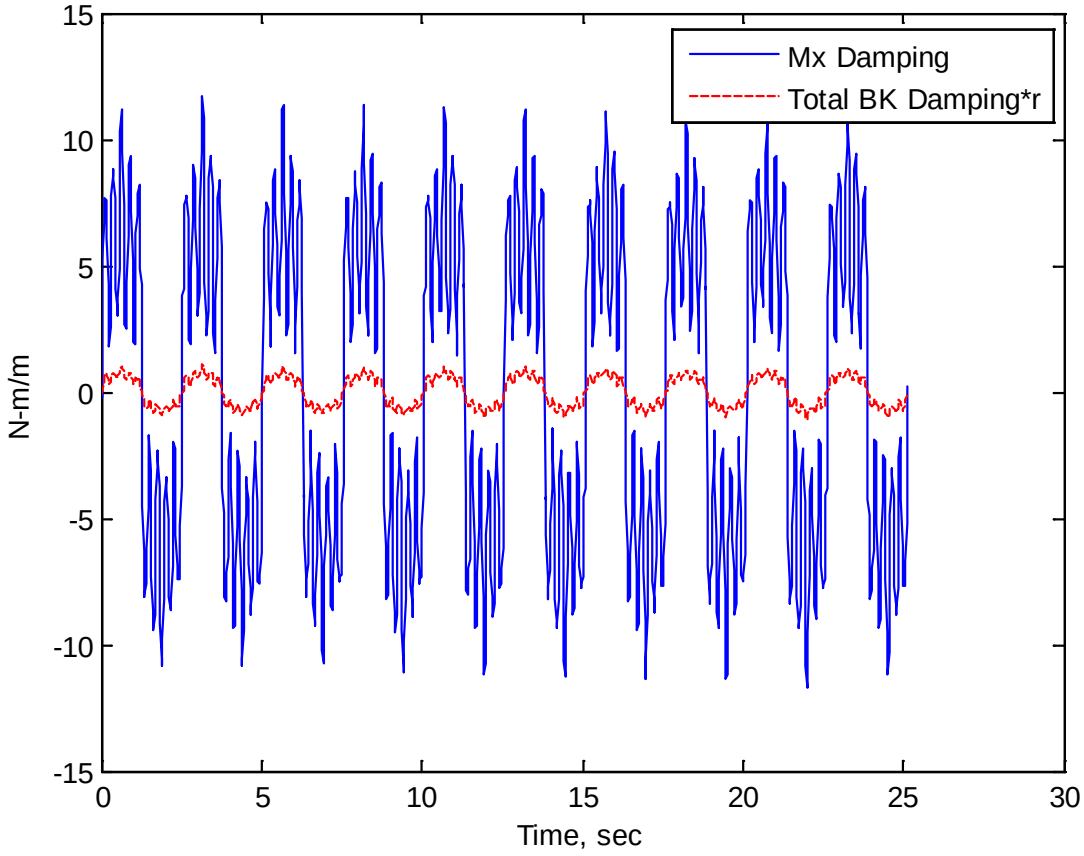

Figure D-12. Comparison of the damping of the unit hydrodynamic roll moment and the unit hydrodynamic roll moment due to the bilge keels, for DTMB Model #5699, φ= 15 deg, ω=2.5 rad/s

D.5.2 Comparison of the Hydrodynamic Components of the Bilge Keel Roll Moment for the Starboard Side Bilge Keel

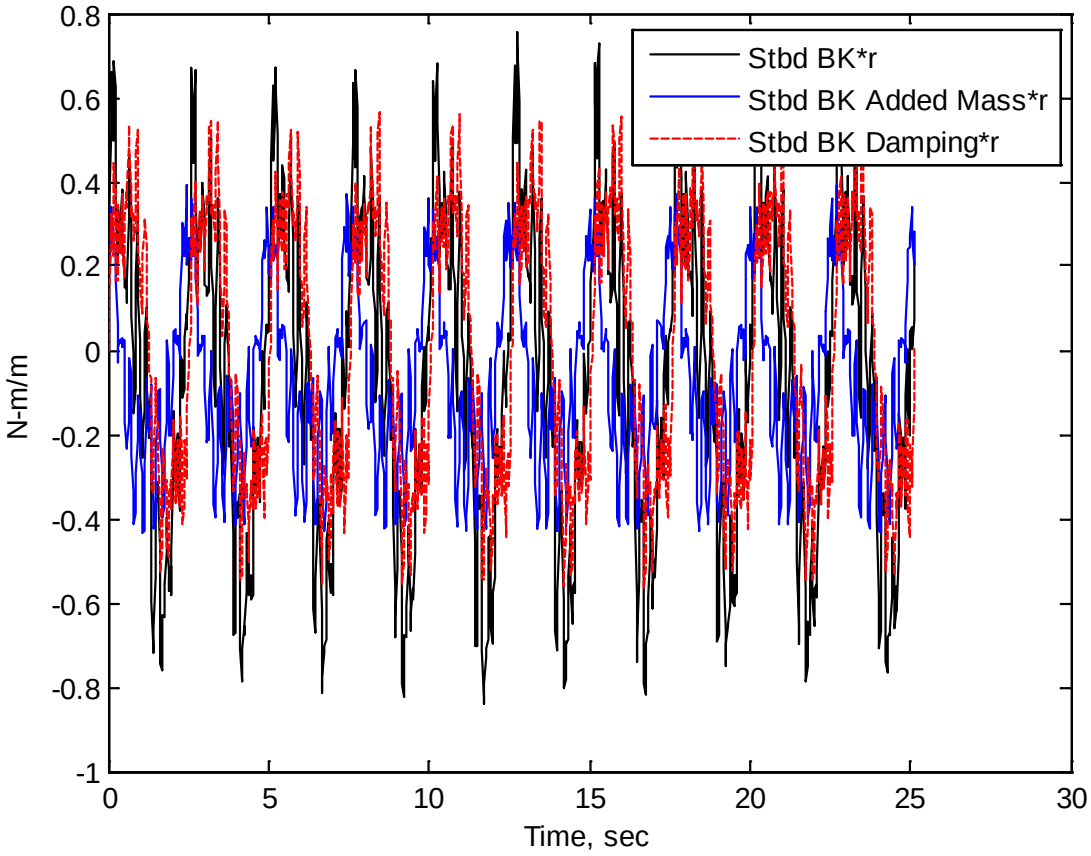

Figure D-13. Comparison of the unit hydrodynamic roll moment due to the starboard bilge keel and associated hydrodynamic components- added inertia and damping, for DTMB Model #5699, φ= 15 deg, ω=2.5 rad/s

D.6 Analysis of Added Inertia and Damping from Experimental Measurements

The total measured hydrodynamic roll moment, Mx (in N-m/m), was decomposed into in-phase (added inertia) and out-of-phase (damping) components. The in-phase portion of the total hydrodynamic roll moment, is given by Mx_A (in N-m/m) and the out-of-phase portion is given by Mx_B (in N-m/m).

In the 1DoF roll equation of motion, constant coefficients can also be used, and for the in-phase portion of the total hydrodynamic roll moment, the added inertia coefficient is given by A44 and the damping coefficient is given by B44. These coefficients can be determined from the respective portions of the total hydrodynamic roll moment, using the following equations:

$$A_{44} = \frac{Mx_A}{\left(Mx\omega^2\right)}$$
$$B_{44} = \frac{Mx_B}{\left(Mx\omega\right)} \qquad \text{(D.1)}$$

The results using the experimental measurements of both the total hydrodynamic roll moment and the roll moment due to the bilge keel, for both the flared and tumblehome topsides, are given in Figure D-14-Figure D-19 below. The damping moment, Mx_B, for the ONRTH and ONRFL, with and without bilge keels is examined in more detail in Figure D-20-Figure D-23.

As observed from the results of the hydrodynamic roll moment, the influence of the addition of the bilge keels is small on the added inertia portion of the roll moment for both the ONRTH (Figure D-14-Figure D-15) and ONRFL (Figure D-16-Figure D-17). The added inertia portion of the roll moment is also larger for the flared topside than for the tumblehome topside, particularly at larger roll amplitudes, illustrating that the influence of the topside geometry on the added inertia. Also, as expected, the roll moment due to damping is much smaller than for added inertia, for both topside configurations.

Examining the hydrodynamic coefficients, the influence of amplitude and topside can be observed. For the flared topside, the added inertia coefficient increased with increasing amplitude and was insensitive to the influence of bilge keels (Figure D-16-Figure D-17). For the tumblehome topside, the added inertia coefficient increased with increasing amplitude for the configuration with bilge keels, until about 35 deg (Figure D-14-Figure D-15). Beyond this amplitude, the effect of the deck edge interaction with the topside can be observed with the reduction of the added inertia coefficient.

For both topside configurations, the damping coefficient generally decreases with increasing amplitude (Figure D-14-Figure D-16). However, for amplitudes where the bilge keel is near the free surface (25-35 deg), the variation with amplitude is not consistent for all frequencies.

To further examine the influence of the bilge keel, the added inertia and damping moments and coefficients for the tumblehome and flared topsides are given in Figure D-18-Figure D-19. The values for the added inertia coefficient of the roll moment due to the bilge keel are an order of magnitude smaller than for the total hydrodynamic roll moment. Both the added inertia and damping increase from 15 to 25 deg roll amplitude, and then decrease above 30 deg, with this trend more noticeable for the damping coefficient. However, some variation is observed across the frequencies. This is likely due to the associated uncertainty with determining the damping portion of the measured total hydrodynamic roll moment. Interaction effects due to the bilge keels and the topside with the free surface can also be observed in the damping moment results and the small variations with frequency. However, within the range of uncertainty of the experimental measurements, general trends of the results can be observed and are clearly nonlinear.

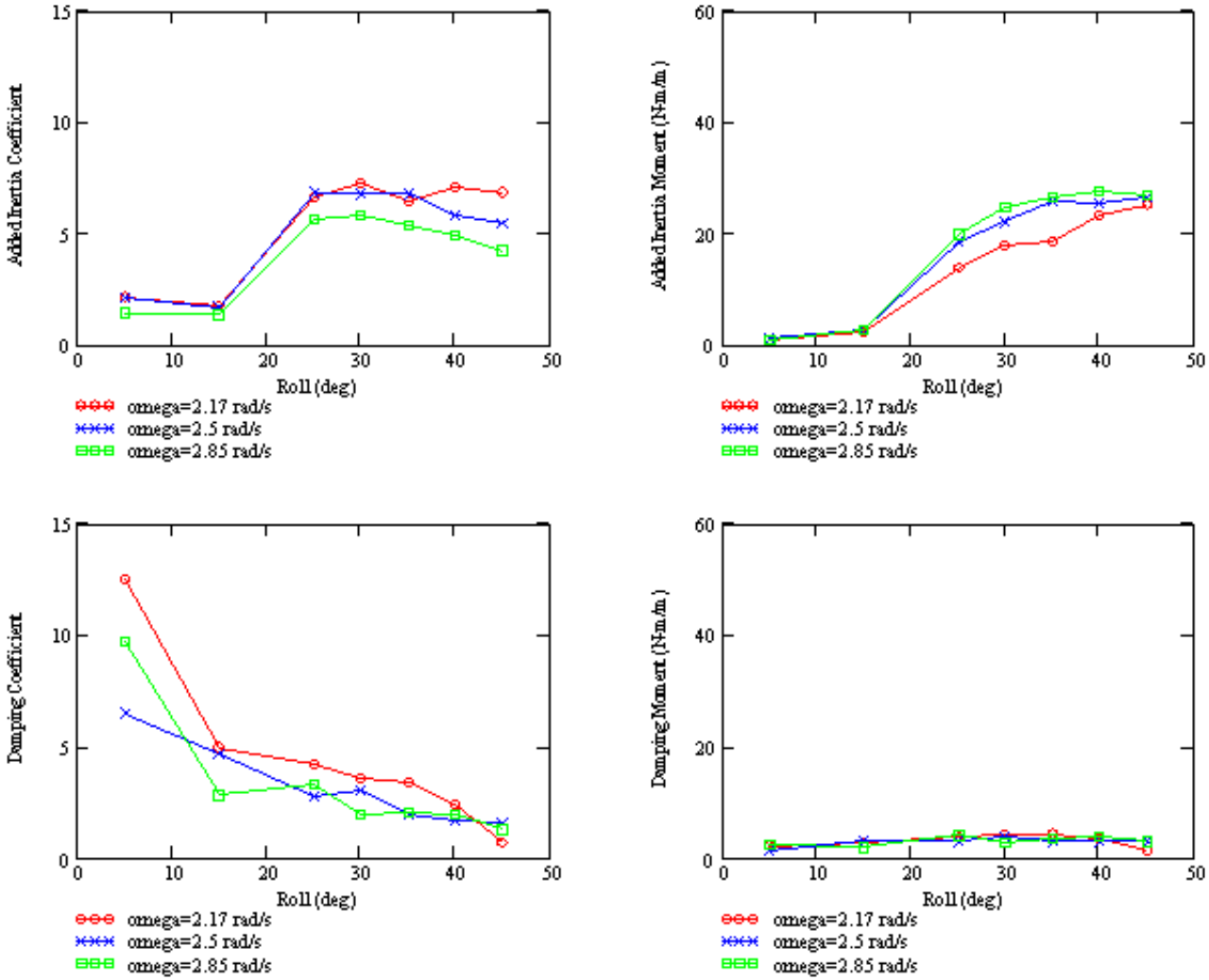

Figure D-14. 2D ONRTH, Hydrodynamic Coefficients for the Measured Mx with Bilge Keels, Added Inertia Moment and Coefficient (top left and right respectively), and Damping Moment and Coefficient (bottom left and right, respectively), for three roll frequencies

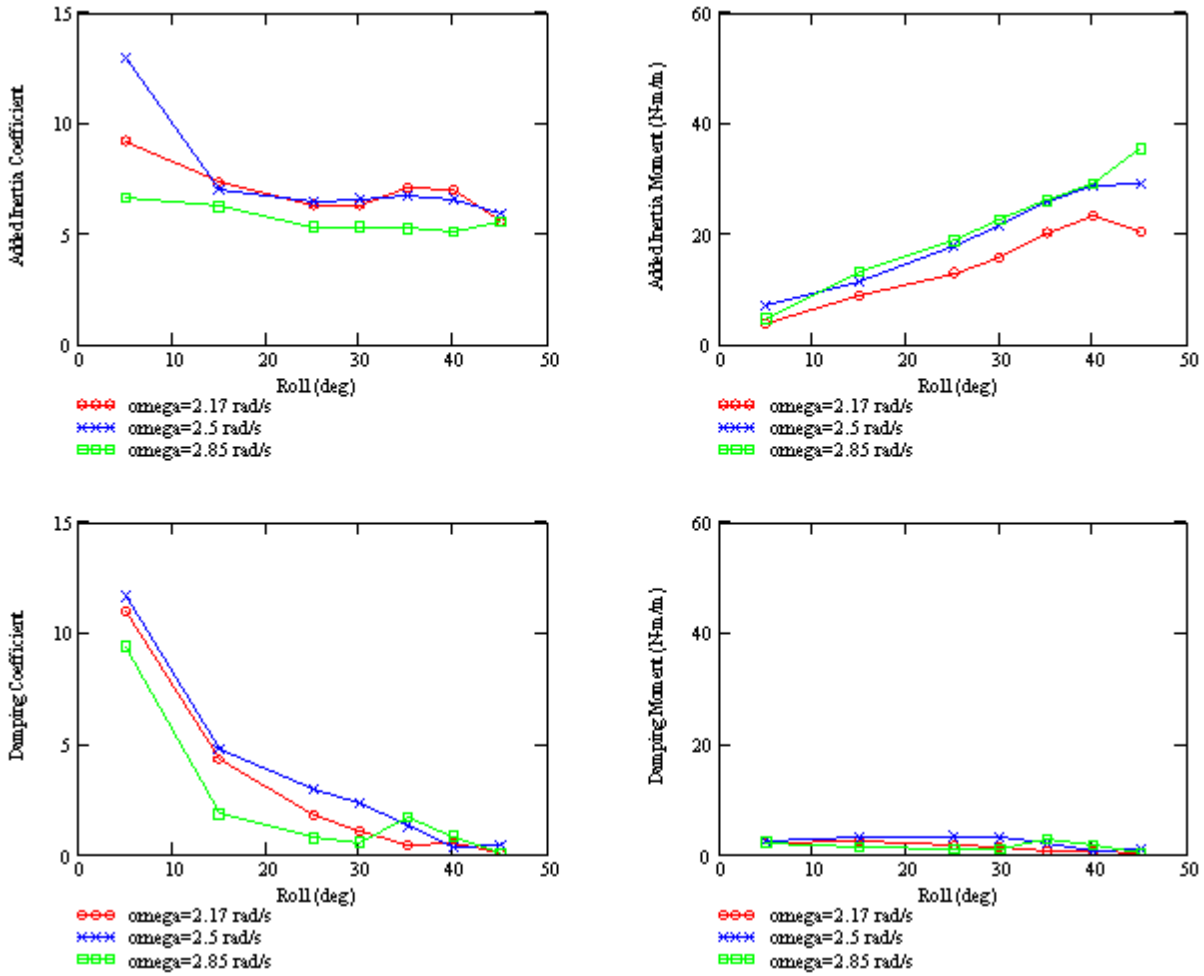

Figure D-15. 2D ONRTH, Hydrodynamic Coefficients for the Measured Mx without Bilge Keels, Added Inertia Moment and Coefficient (top left and right respectively), and Damping Moment and Coefficient (bottom left and right, respectively), for three roll frequencies

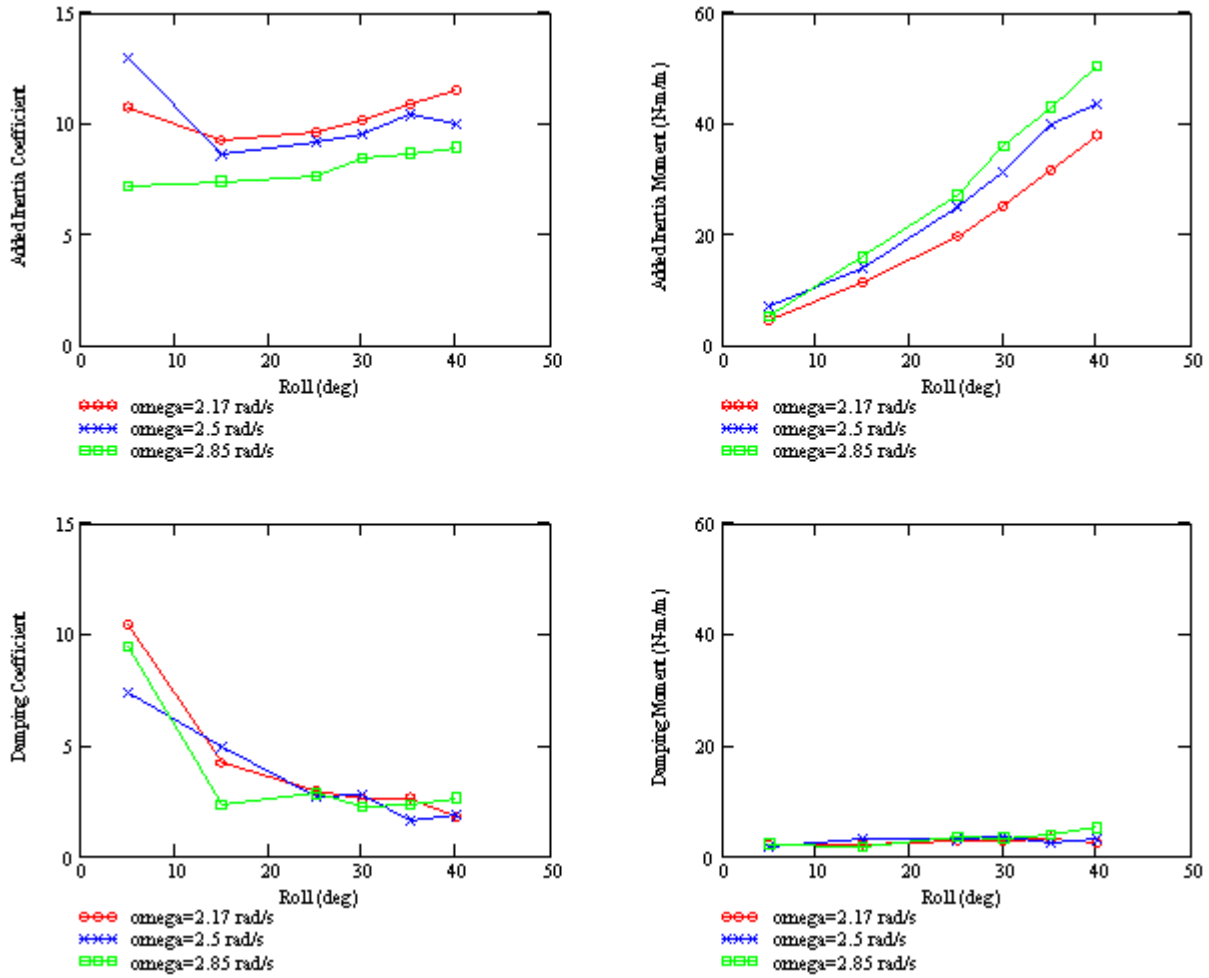

Figure D-16. 2D ONRFL, Hydrodynamic Coefficients for the Measured Mx with Bilge Keels, Added Inertia Moment and Coefficient (top left and right respectively), and Damping Moment and Coefficient (bottom left and right, respectively), for three roll frequencies

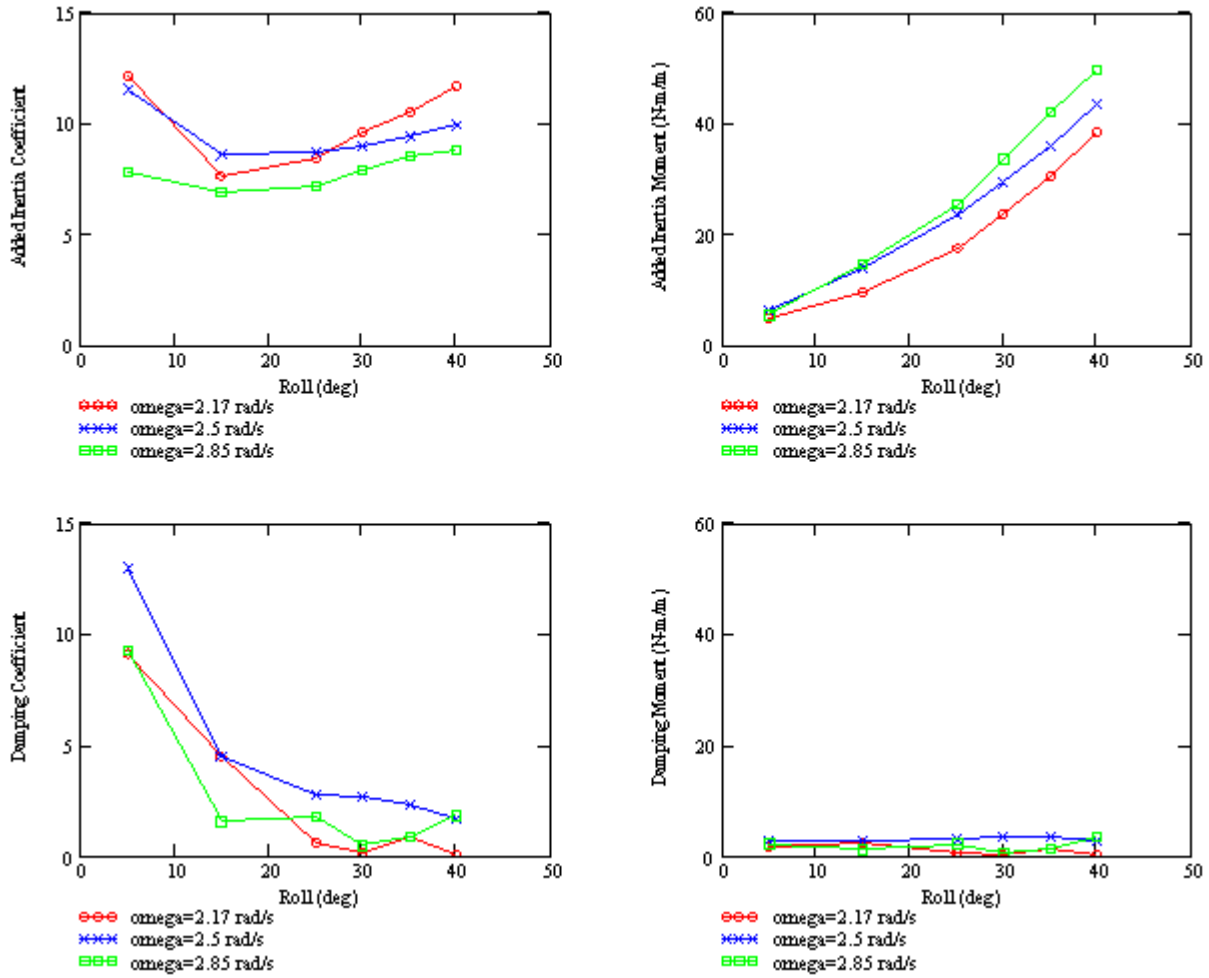

Figure D-17. 2D ONRFL, Hydrodynamic Coefficients for the Measured Mx without Bilge Keels, Added Inertia Moment and Coefficient (top left and right respectively), and Damping Moment and Coefficient (bottom left and right, respectively), for three roll frequencies

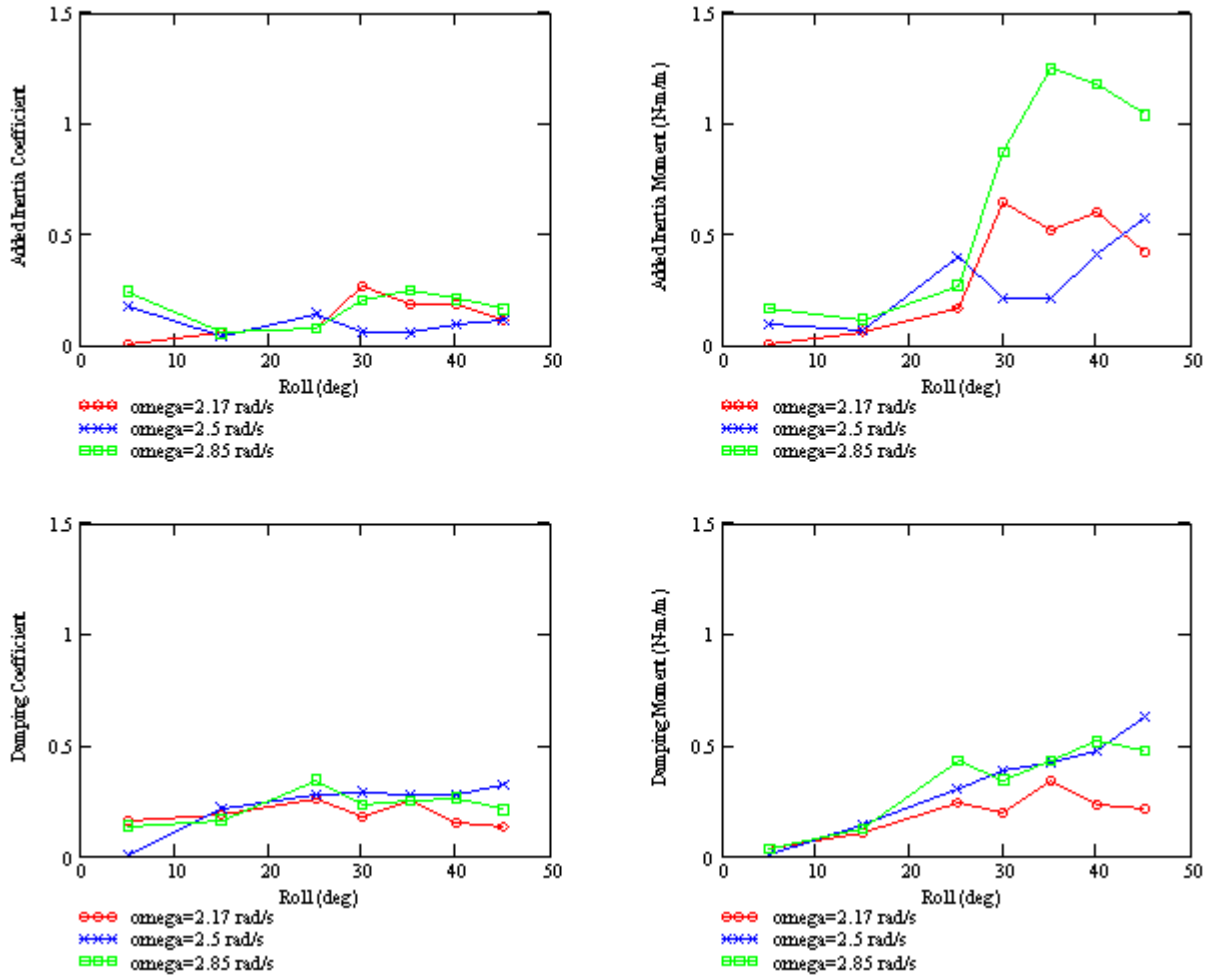

Figure D-18. 2D ONRTH, Hydrodynamic Coefficients for the Measured Roll Moment due to the Bilge Keels, Added Inertia Moment and Coefficient (top left and right respectively), and Damping Moment and Coefficient (bottom left and right, respectively), for three roll frequencies

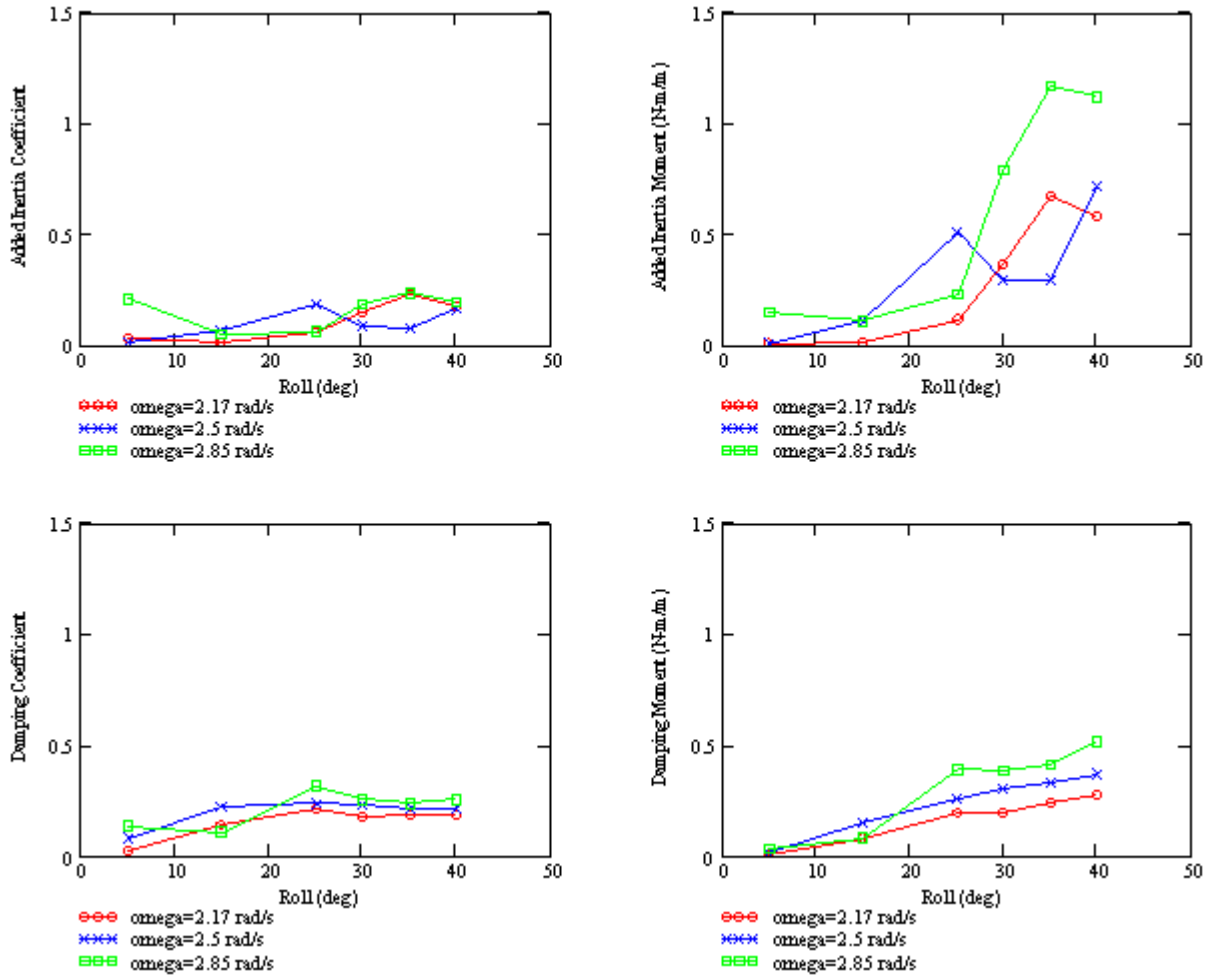

Figure D-19. 2D ONRFL, Hydrodynamic Coefficients for the Measured Roll Moment due to the Bilge Keels, Added Inertia Moment and Coefficient (top left and right respectively), and Damping Moment and Coefficient (bottom left and right, respectively), for three roll frequencies

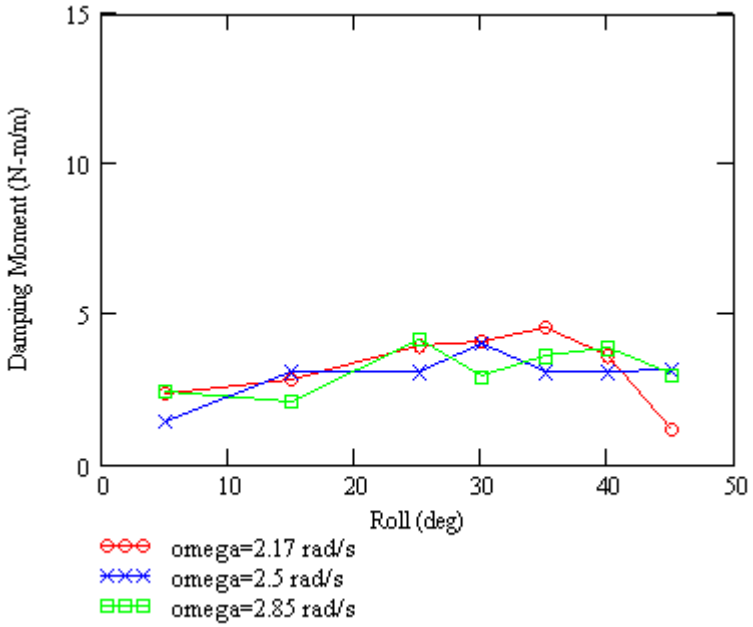

Figure D-20. 2D ONRTH, Damping Coefficient for Measured Mx with Bilge Keels, for three roll frequencies

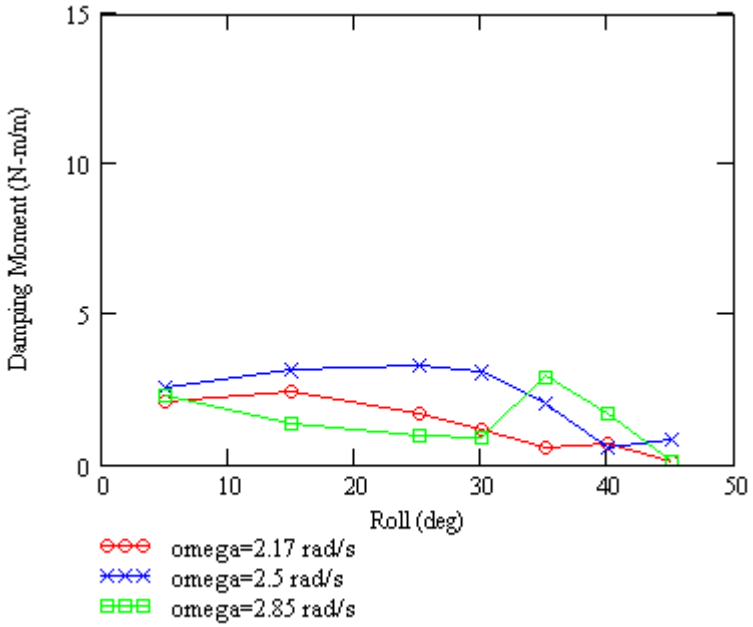

Figure D-21. 2D ONRTH, Damping Coefficient for Measured Mx without Bilge Keels, for three roll frequencies

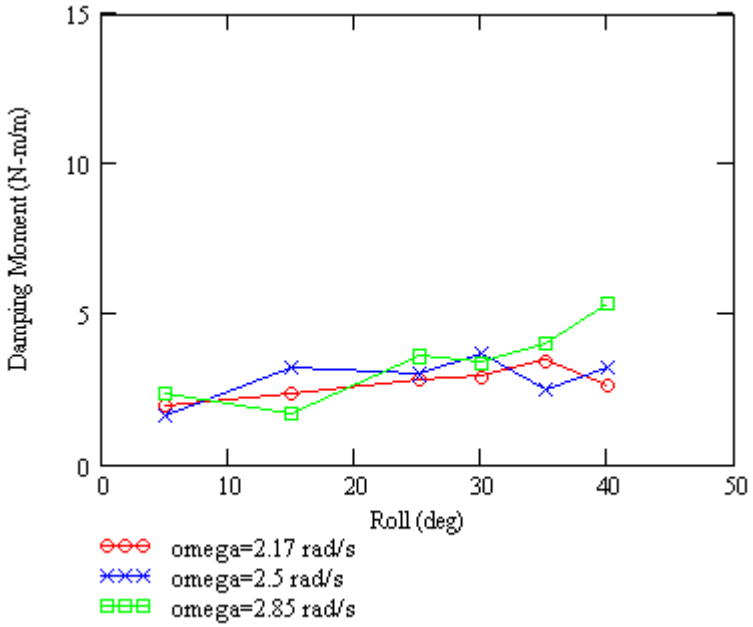

Figure D-22. 2D ONRFL, Damping Coefficient for Measured Mx with Bilge Keels, for three roll frequencies

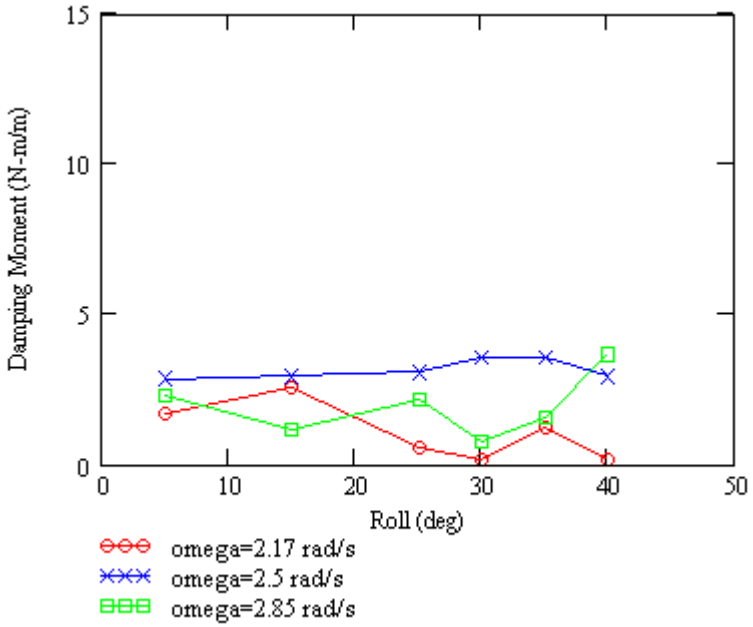

Figure D-23. 2D ONRFL, Damping Coefficient for Measured Mx without Bilge Keels, for three roll frequencies

D.7 Harmonic Analysis of the Hydrodynamic Components

As discussed in Chapter 4, Fourier analysis was used to decompose the measurements of roll motion, the unit hydrodynamic roll moment, and the hydrodynamic roll moment due to the starboard bilge keel force. From the Fourier analysis, the first 10 harmonic components were examined, which were still above the Nyquist frequency for the experimental conditions. The added inertia and damping for the roll motion (Figure D-24 and Figure D-25), the unit hydrodynamic roll moment (Figure D-26 and Figure D-27), and the hydrodynamic roll moment due to the starboard bilge keel force (Figure D-28 and Figure D-29). The same analysis was performed for all of the conditions for both topside configurations, with and without bilge keels, and these results are presented in Chapter 4.

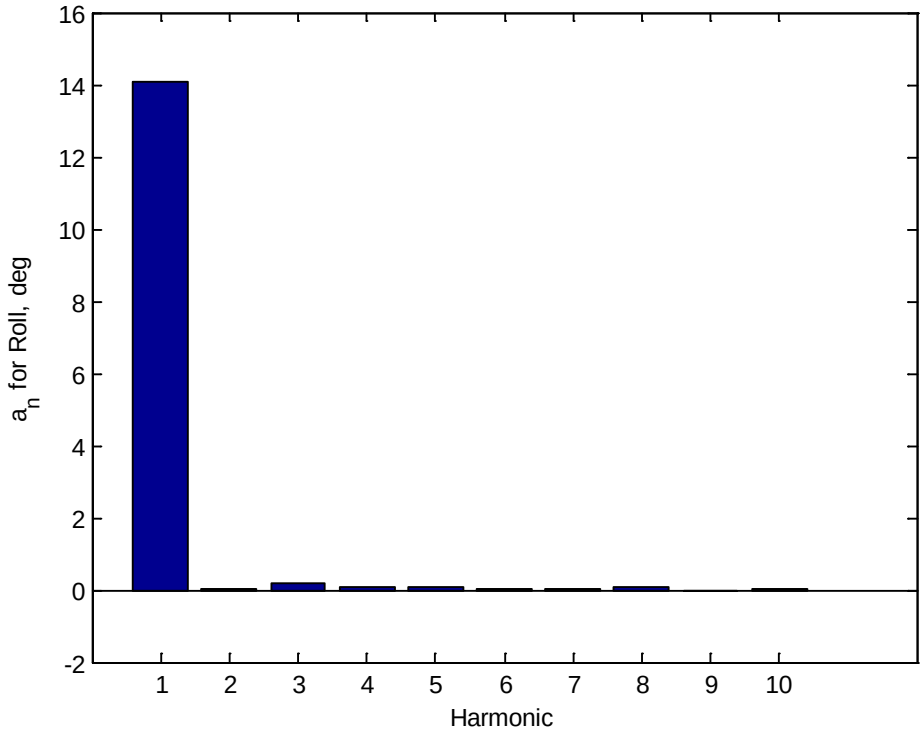

Figure D-24. Comparison of the magnitude of the first 10 harmonics of added inertia for roll motion, for DTMB Model #5699, φ= 15 deg, ω=2.5 rad/s

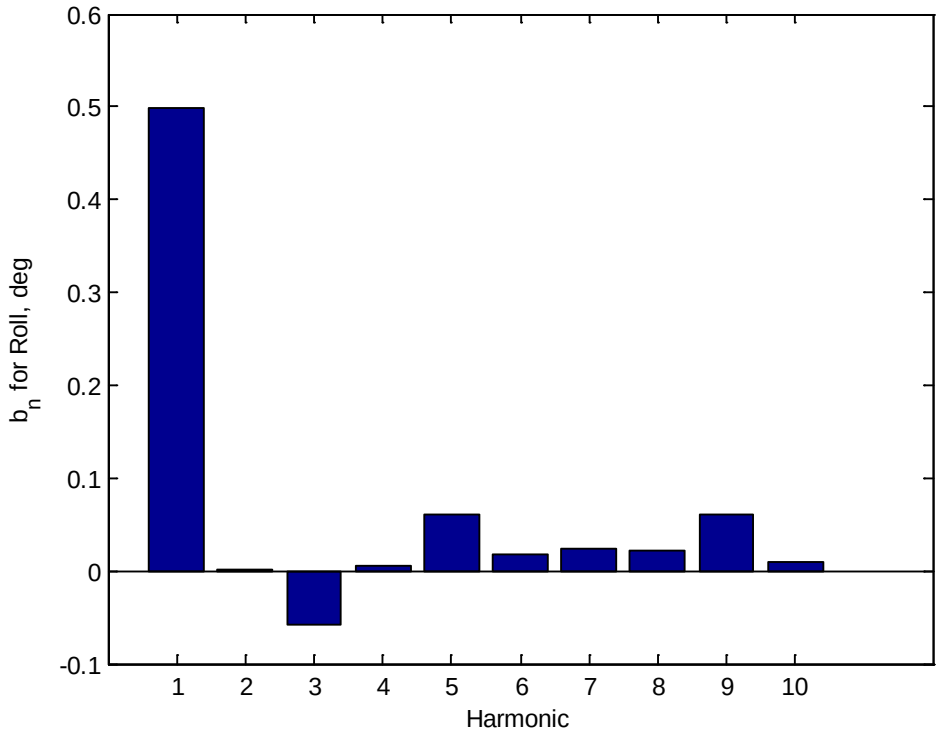

Figure D-25. Comparison of the magnitude of the first 10 harmonics of damping for roll motion, for DTMB Model #5699, φ= 15 deg, ω=2.5 rad/s

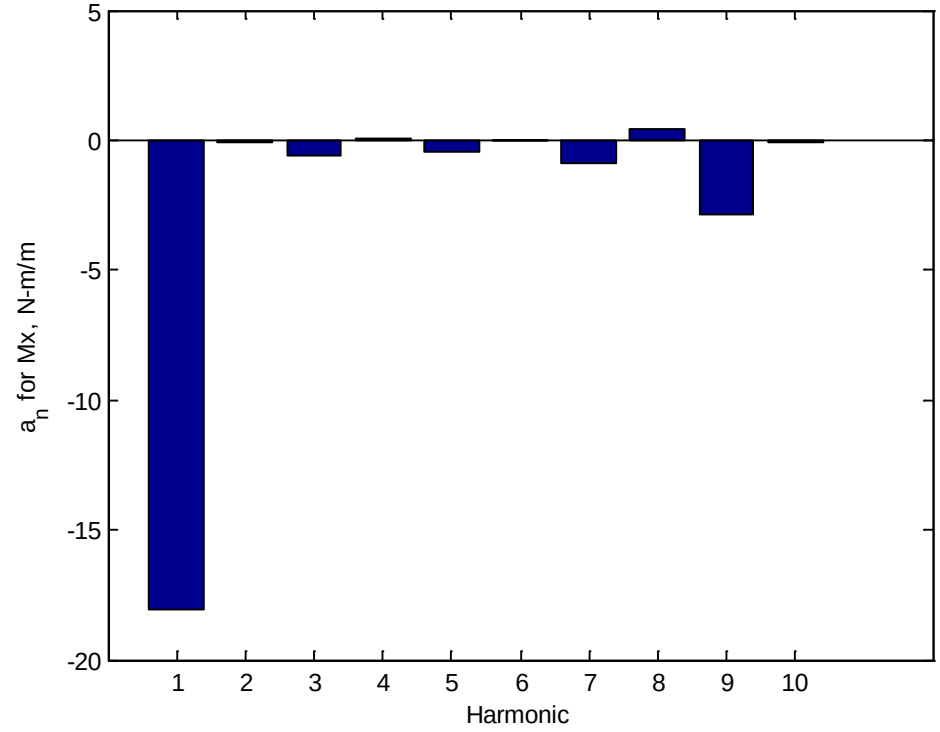

Figure D-26. Comparison of the magnitude of the first 10 harmonics of added inertia for the unit hydrodynamic roll moment, for DTMB Model #5699, φ= 15 deg, ω=2.5 rad/s

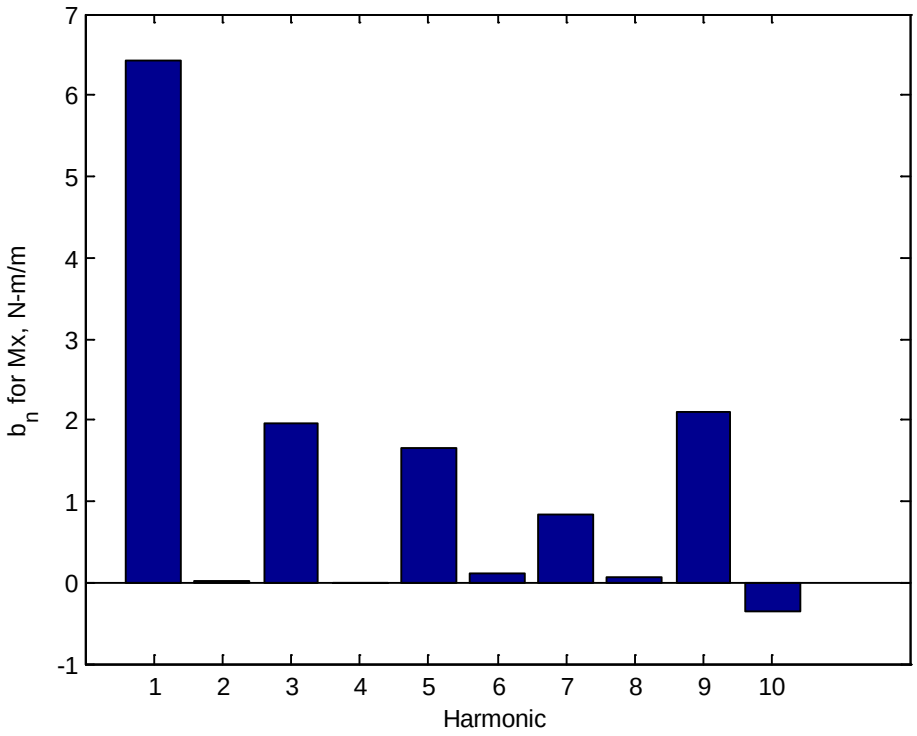

Figure D-27. Comparison of the magnitude of the first 10 harmonics of damping for the unit hydrodynamic roll moment, for DTMB Model #5699, φ= 15 deg, ω=2.5 rad/s

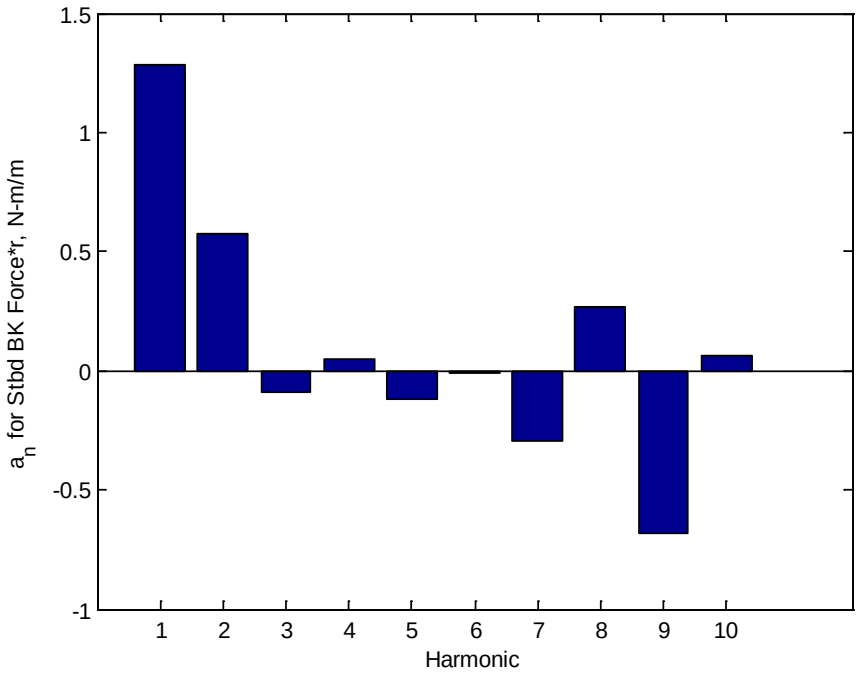

Figure D-28. Comparison of the magnitude of the first 10 harmonics of added inertia for the unit hydrodynamic roll moment due to the starboard bilge keel force, for DTMB Model #5699, φ= 15 deg, ω=2.5 rad/s

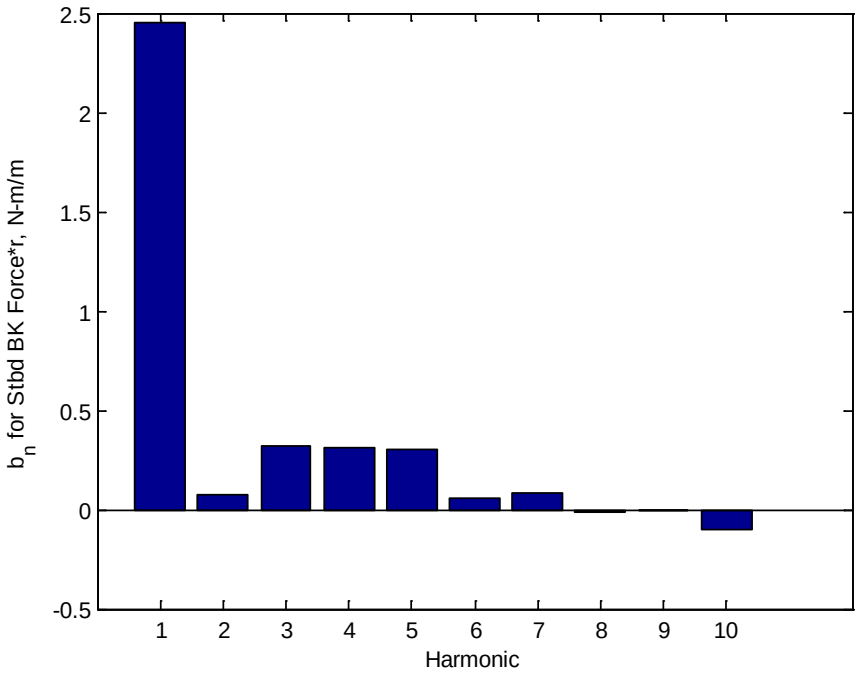

Figure D-29. Comparison of the magnitude of the first 10 harmonics of damping or the unit hydrodynamic roll moment due to the starboard bilge keel force, for DTMB Model #5699, φ= 15 deg, ω=2.5 rad/s

D.8 Hydrodynamic Components as a Function of Amplitude and Topside Configuration

Results for the 2.5 rad/s roll frequency condition were presented in Chapter 4. Additional results for 2.17 rad/s and 2.85 rad/s frequency conditions are presented in this section. However, further analysis and discussion of the results is given in Chapter 4.

D.8.1 Hydrodynamic Components as a Function of Amplitude and Topside for 2.17 rad/s

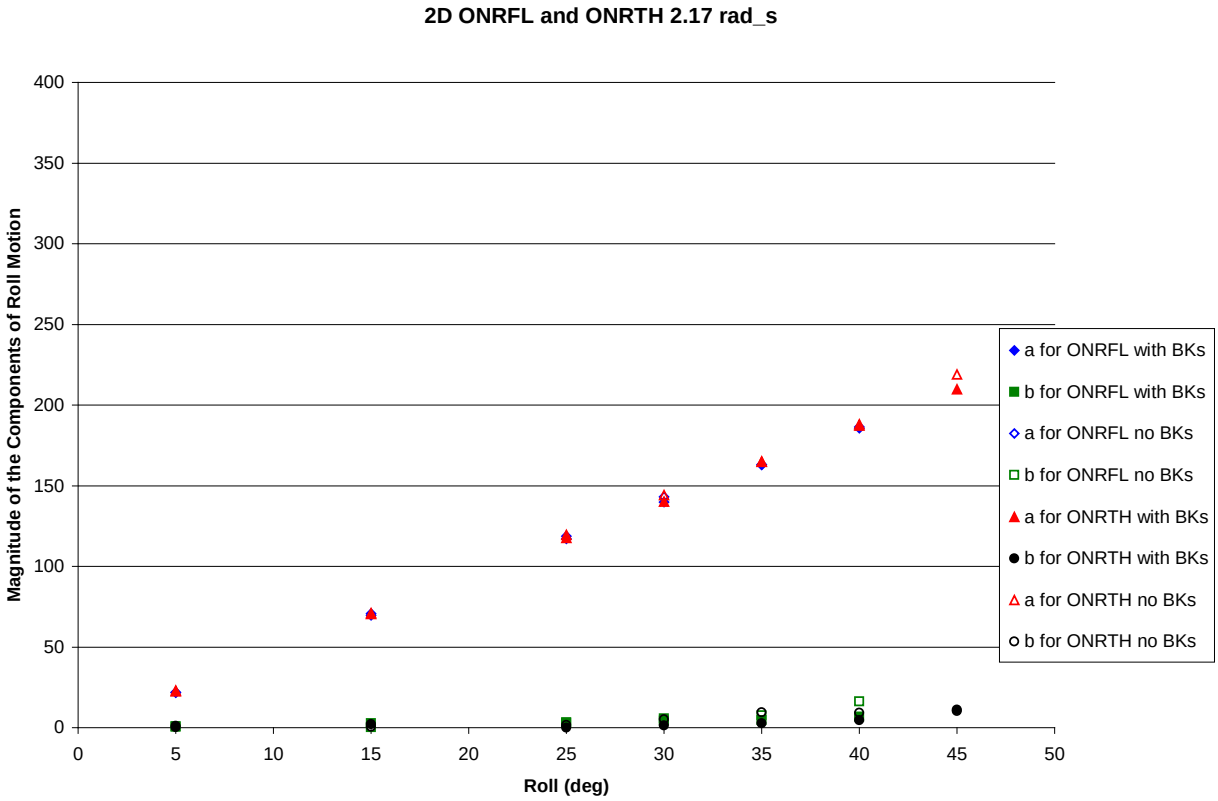

Figure D-30. Comparison of the magnitude of the total of the first 10 harmonics of added inertia and damping for roll motion, for DTMB Models #5699 and #5699-1, with and without bilge keels, ω=2.17 rad/s

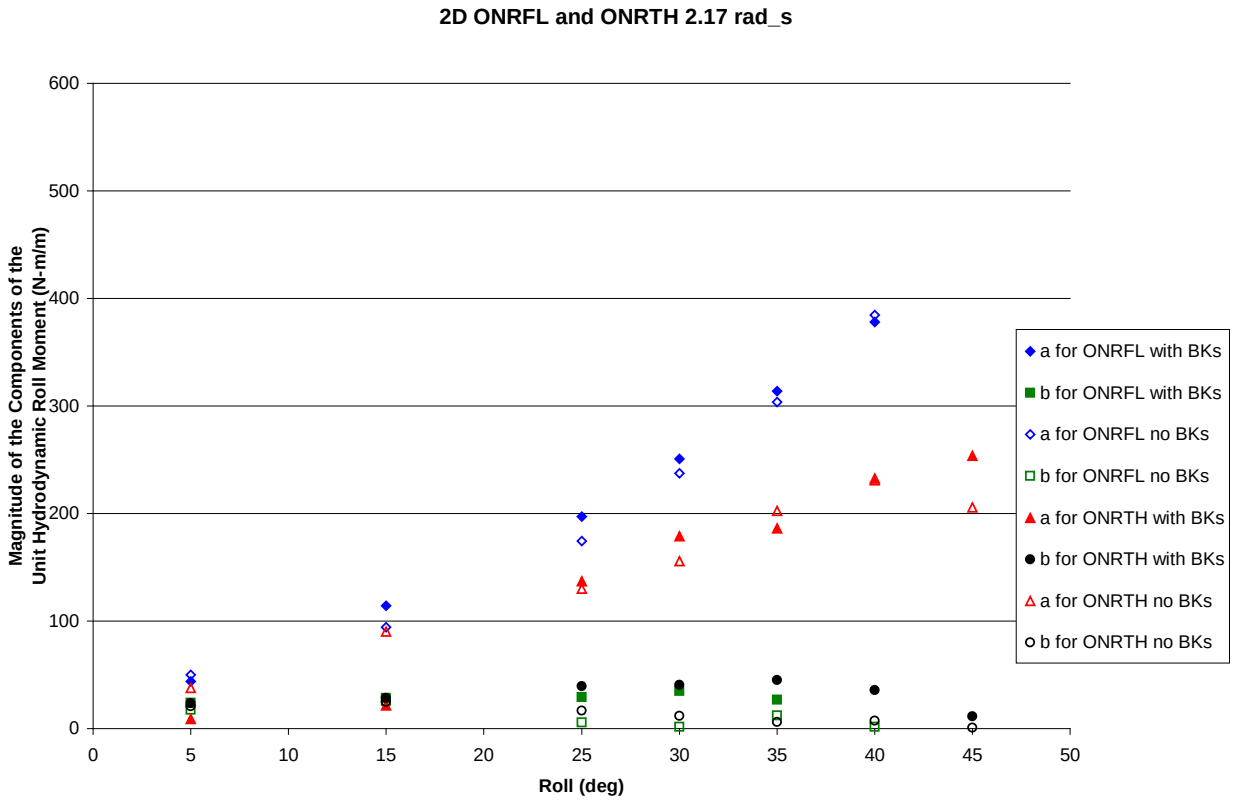

Figure D-31. Comparison of the magnitude of the total of the first 10 harmonics of added inertia and damping for the unit hydrodynamic roll moment, for DTMB Models #5699 and #5699-1, with and without bilge keels, ω=2.17 rad/s

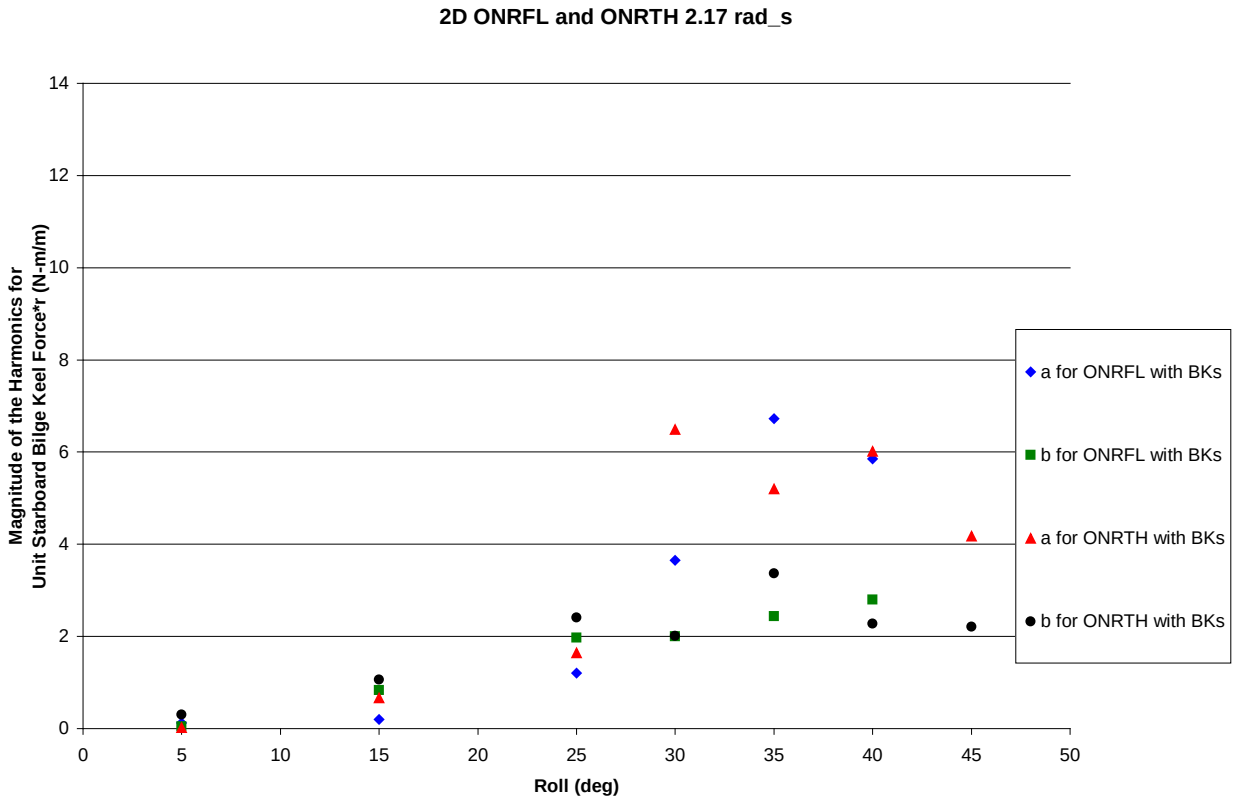

Figure D-32. Comparison of the magnitude of the total of the first 10 harmonics of added inertia and damping for the unit hydrodynamic roll moment due to the starboard bilge keel, for DTMB Models #5699 and #5699-1, ω=2.17 rad/s

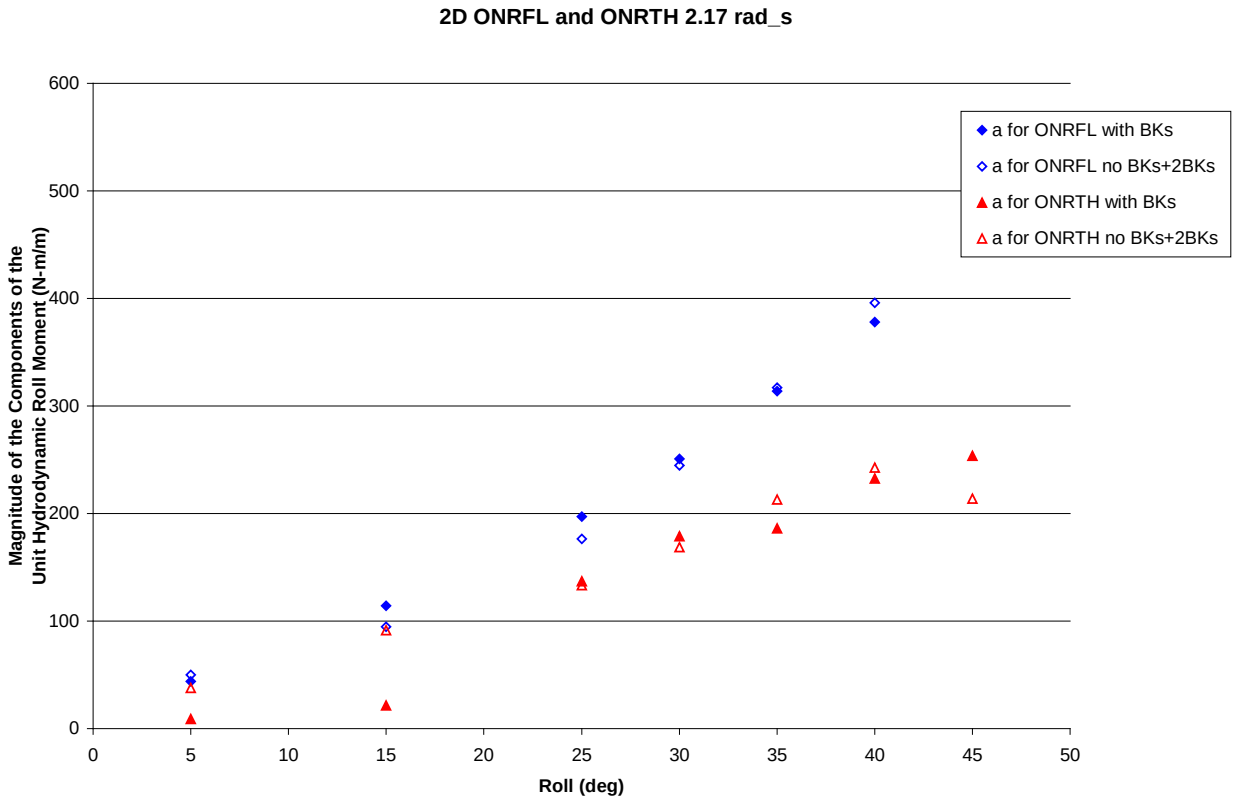

Figure D-33. Comparison of the magnitude of the total of the first 10 harmonics of added inertia for the unit hydrodynamic roll moment, for DTMB Models #5699 and #5699-1, with bilge keels and with the effective influence of the bilge keels, ω=2.17 rad/s

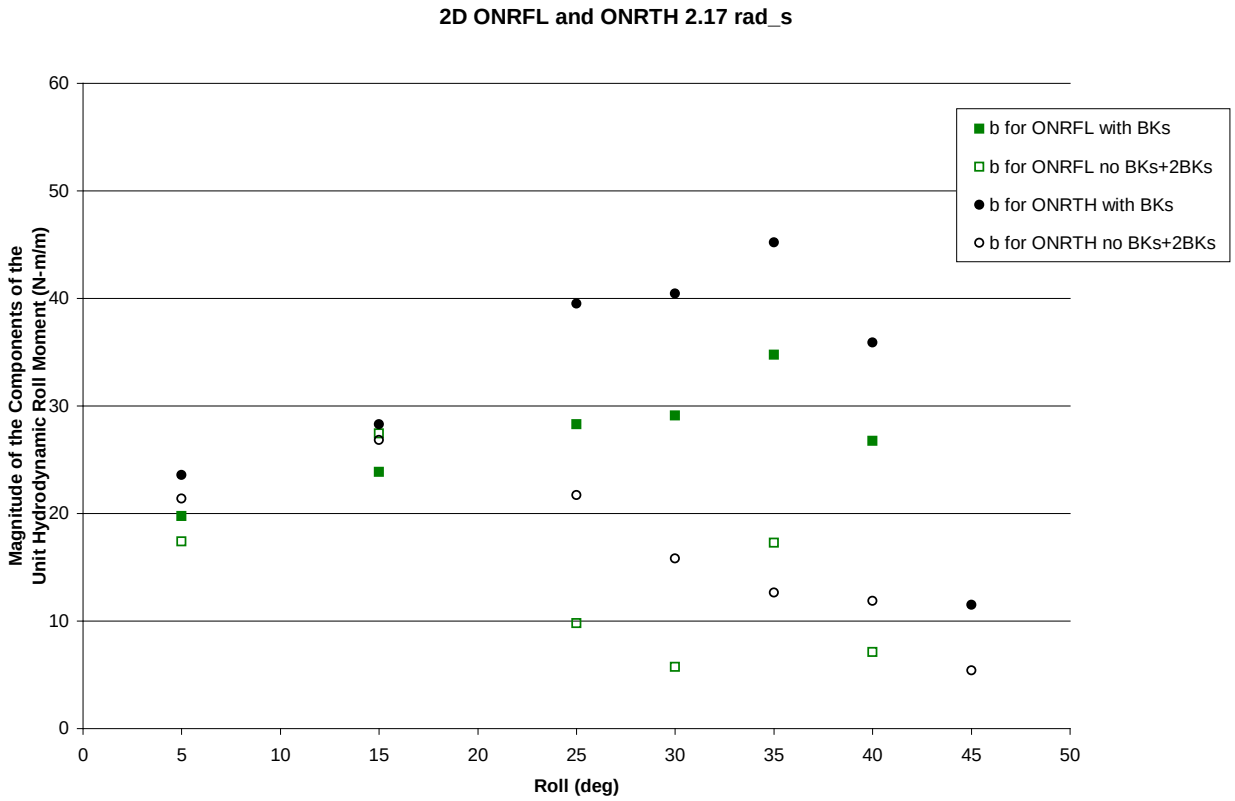

Figure D-34. Comparison of the magnitude of the total of the first 10 harmonics of damping for the unit hydrodynamic roll moment, for DTMB Models #5699 and #5699-1, with bilge keels and with the effective influence of the bilge keels, ω=2.17 rad/s

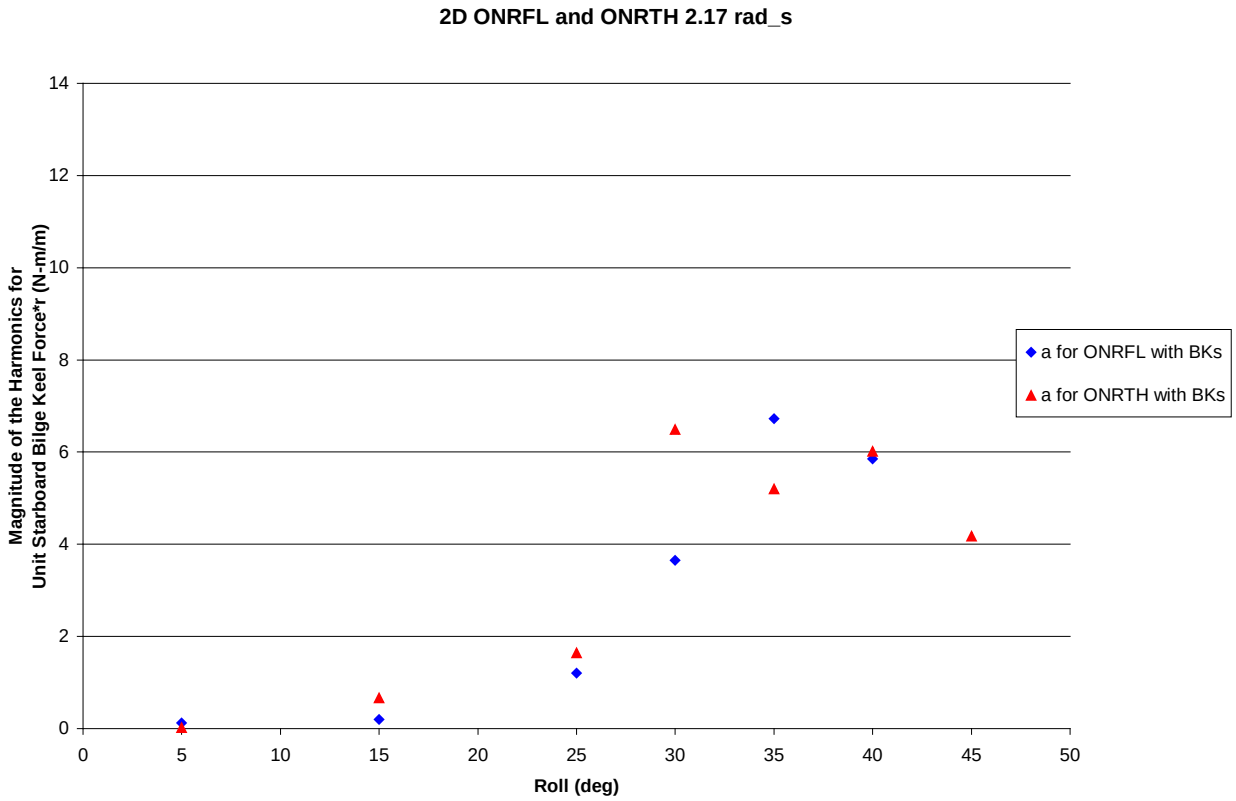

Figure D-35. Comparison of the magnitude of the total of the first 10 harmonics of added inertia for the unit hydrodynamic roll moment due to the starboard bilge keel, for DTMB Models #5699 and #5699-1, with and without bilge keels, ω=2.17 rad/s

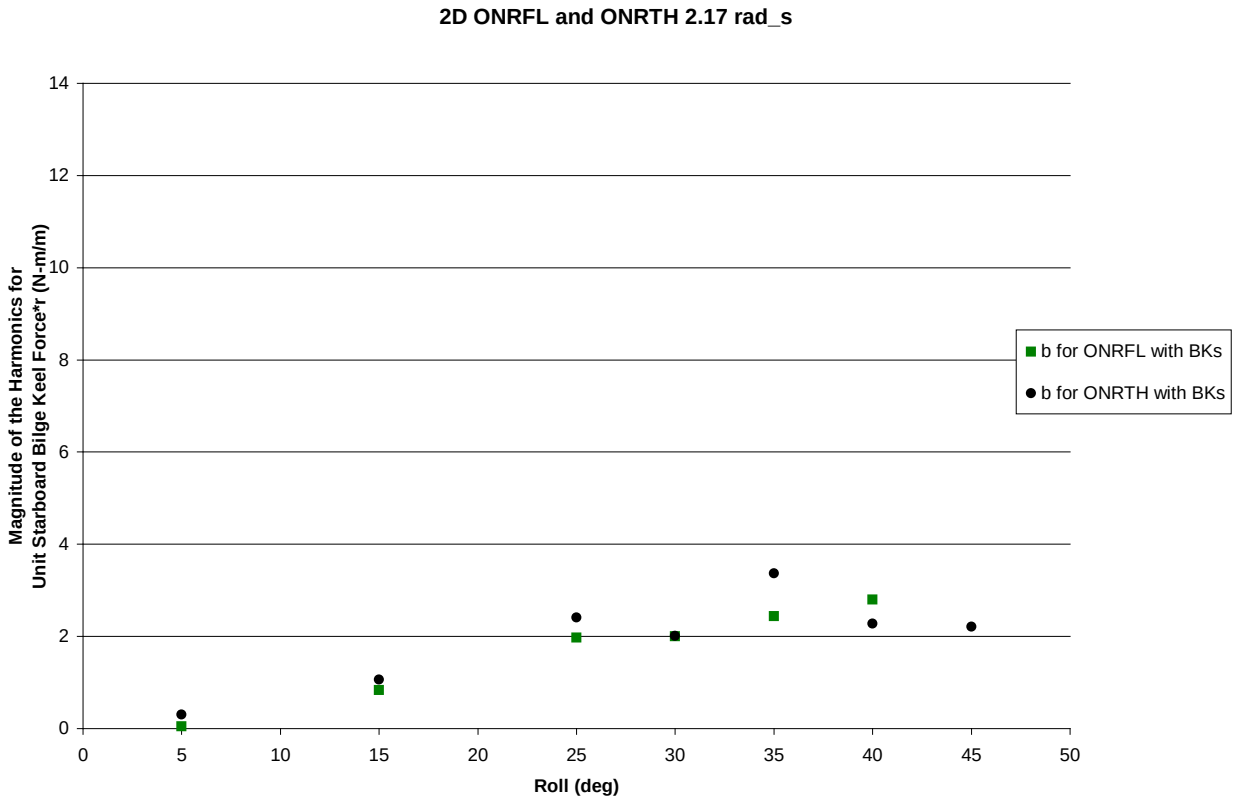

Figure D-36. Comparison of the magnitude of the total of the first 10 harmonics of damping for the unit hydrodynamic roll moment due to the starboard bilge keel, for DTMB Models #5699 and #5699-1, with and without bilge keels, ω=2.17 rad/s

D.8.2 Hydrodynamic Components as a Function of Amplitude and Topside for 2.85 rad/s

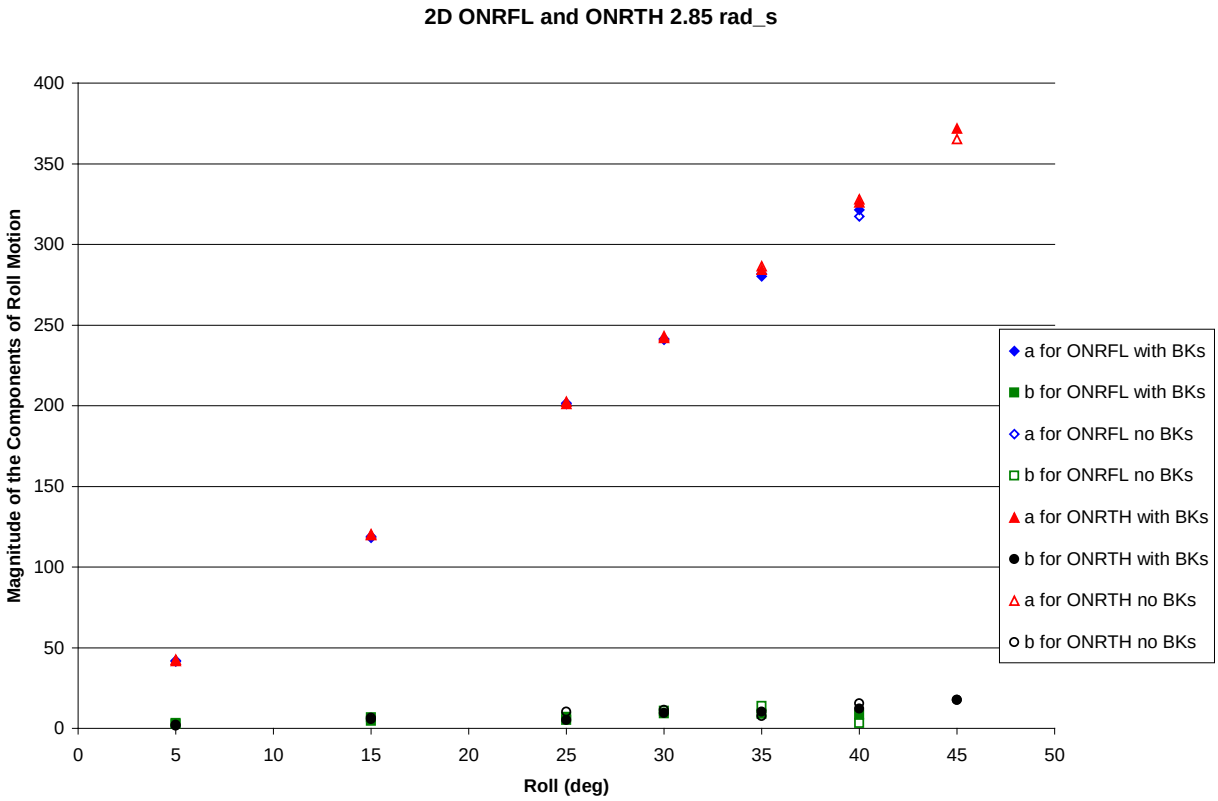

Figure D-37. Comparison of the magnitude of the total of the first 10 harmonics of added inertia and damping for roll motion, for DTMB Models #5699 and #5699-1, with and without bilge keels, ω=2.85 rad/s

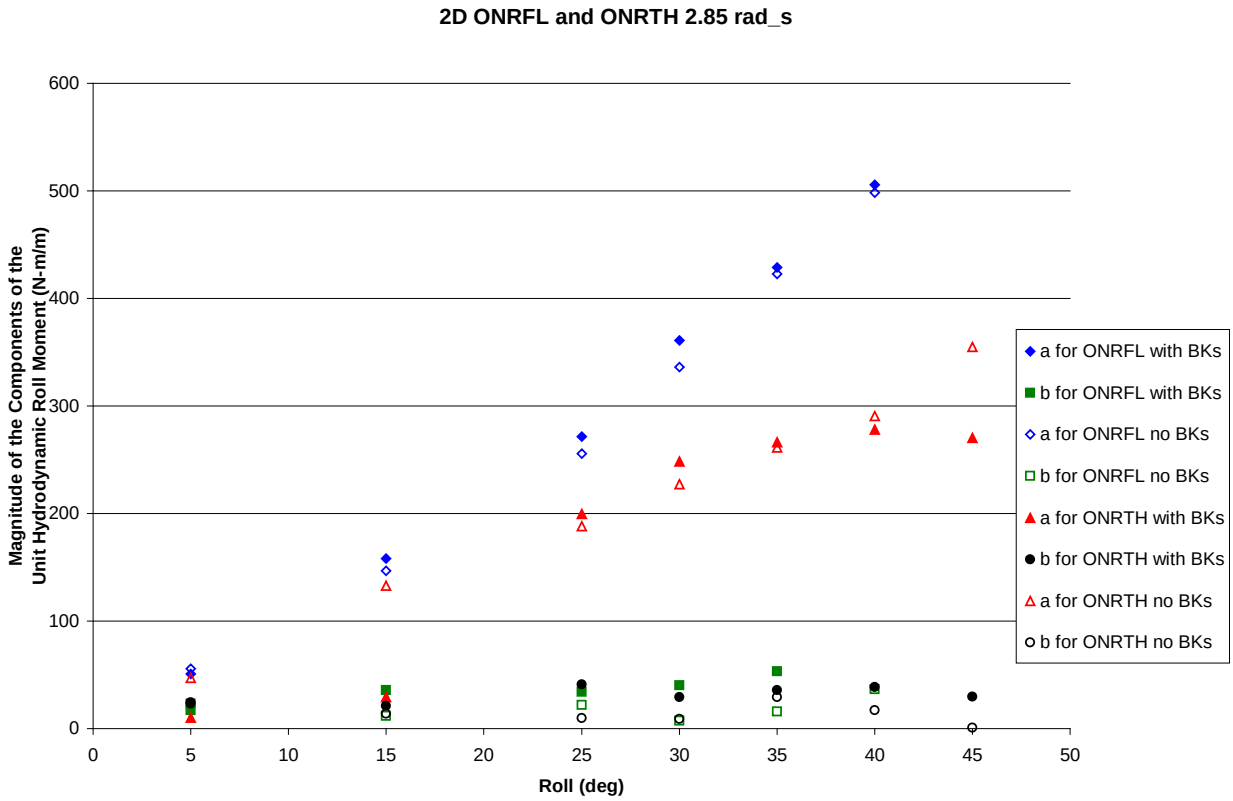

Figure D-38. Comparison of the magnitude of the total of the first 10 harmonics of added inertia and damping for the unit hydrodynamic roll moment, for DTMB Models #5699 and #5699-1, with and without bilge keels, ω=2.85 rad/s

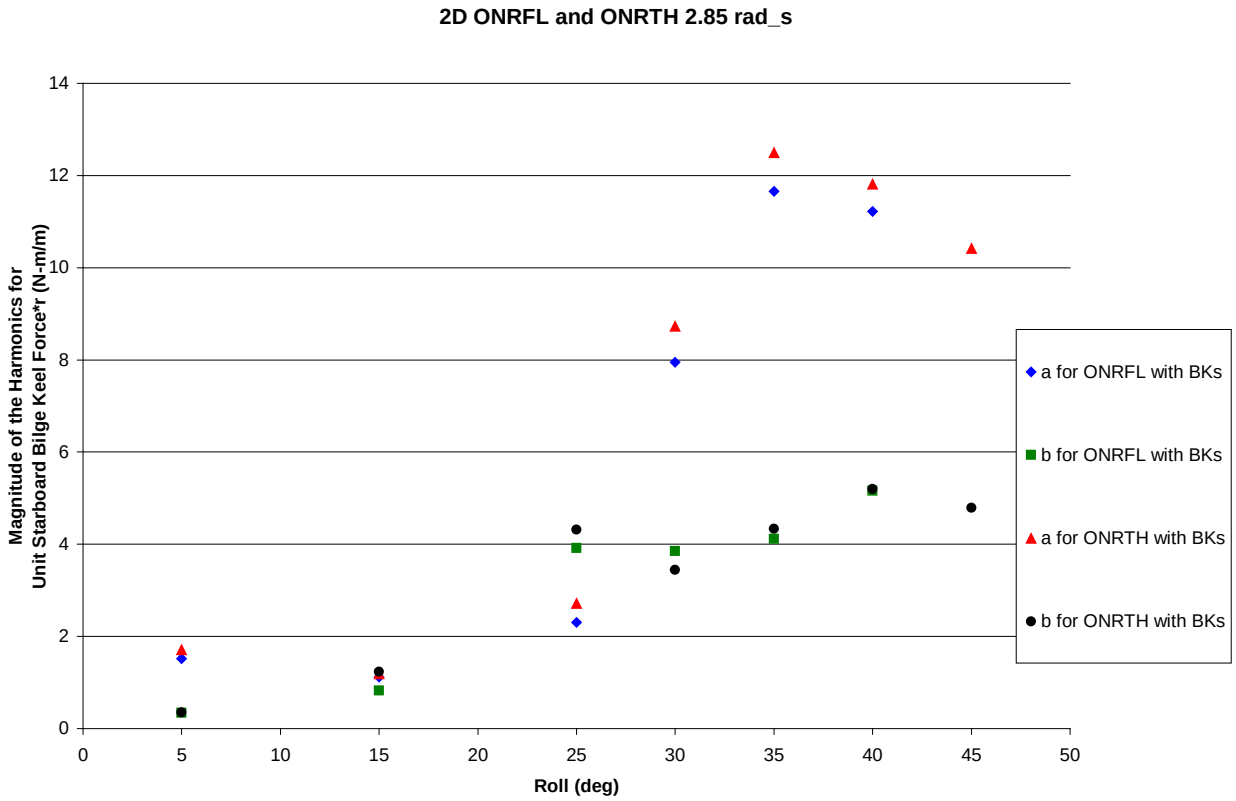

Figure D-39. Comparison of the magnitude of the total of the first 10 harmonics of added inertia and damping for the unit hydrodynamic roll moment due to the starboard bilge keel, for DTMB Models #5699 and #5699-1, ω=2.85 rad/s

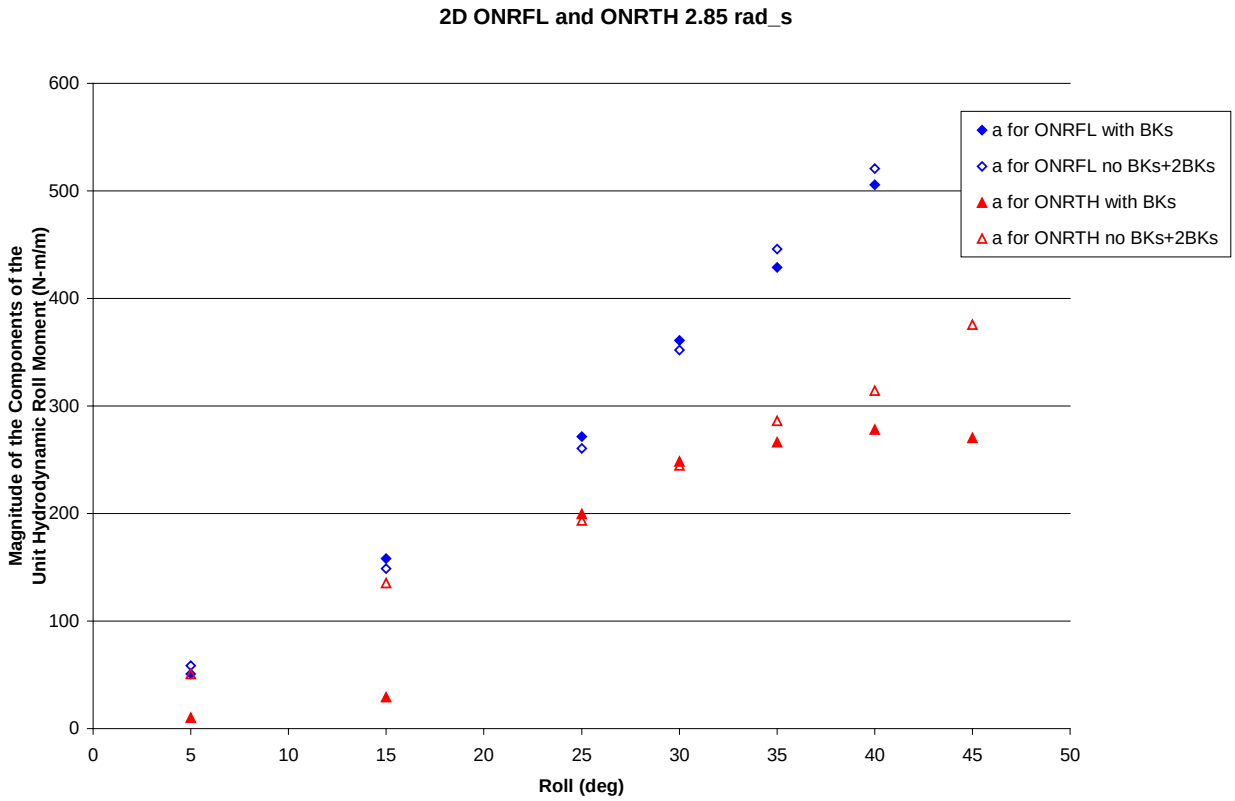

Figure D-40. Comparison of the magnitude of the total of the first 10 harmonics of added inertia for the unit hydrodynamic roll moment, for DTMB Models #5699 and #5699-1, with bilge keels and with the effective influence of the bilge keels, ω=2.85 rad/s

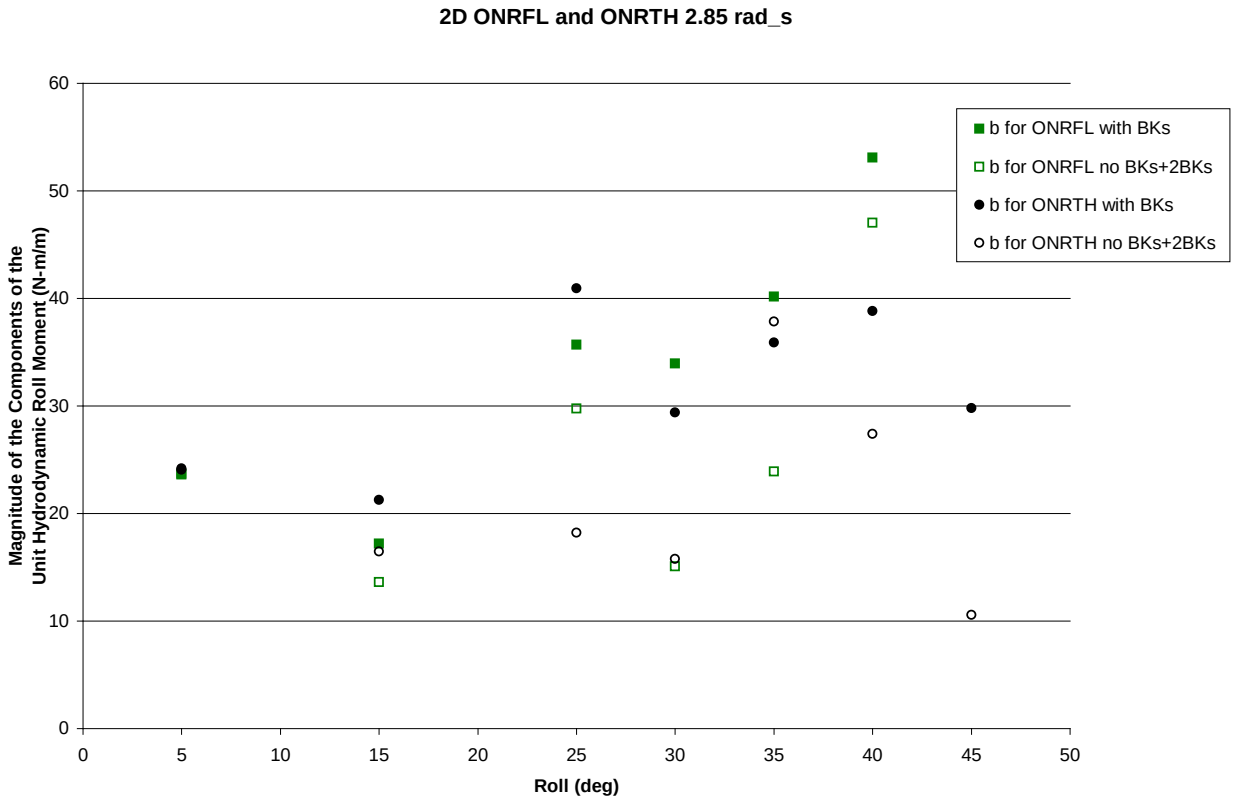

Figure D-41. Comparison of the magnitude of the total of the first 10 harmonics of damping for the unit hydrodynamic roll moment, for DTMB Models #5699 and #5699-1, with bilge keels and with the effective influence of the bilge keels, ω=2.85 rad/s

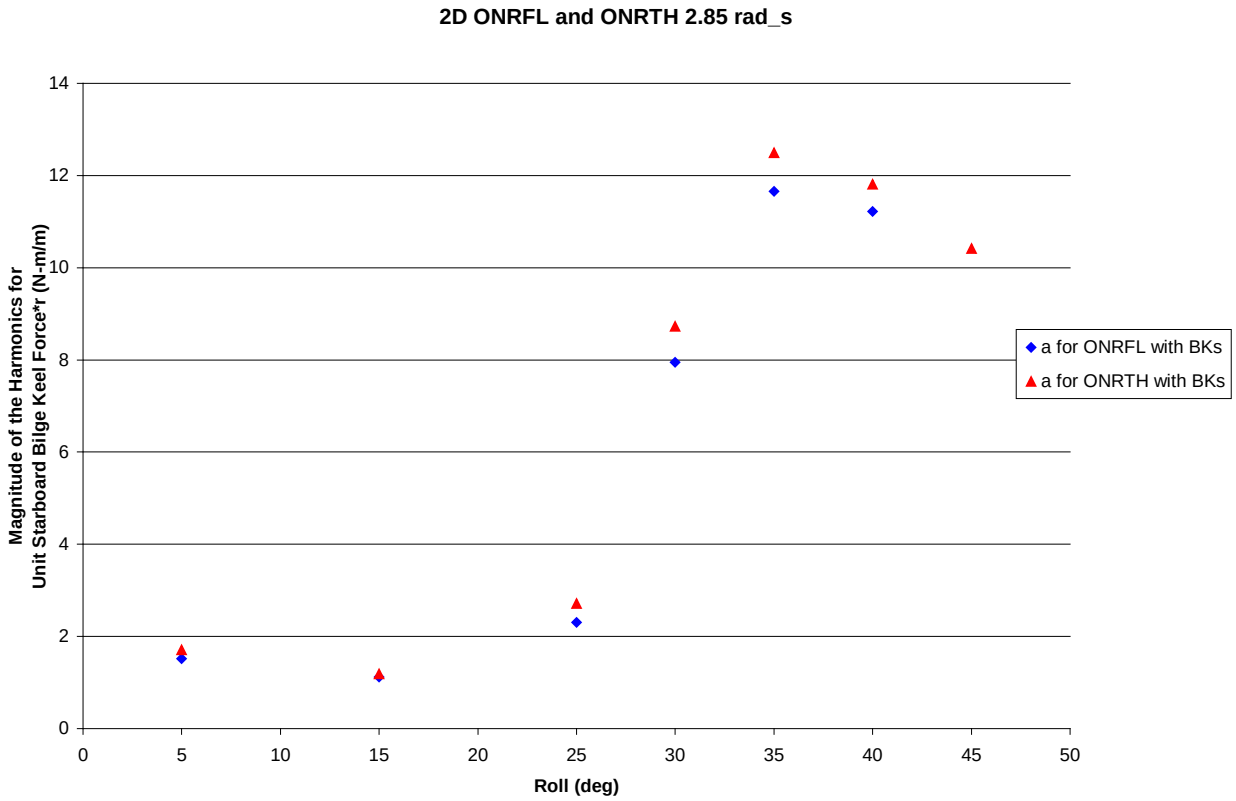

Figure D-42. Comparison of the magnitude of the total of the first 10 harmonics of added inertia for the unit hydrodynamic roll moment due to the starboard bilge keel, for DTMB Models #5699 and #5699-1, with and without bilge keels, ω=2.85 rad/s

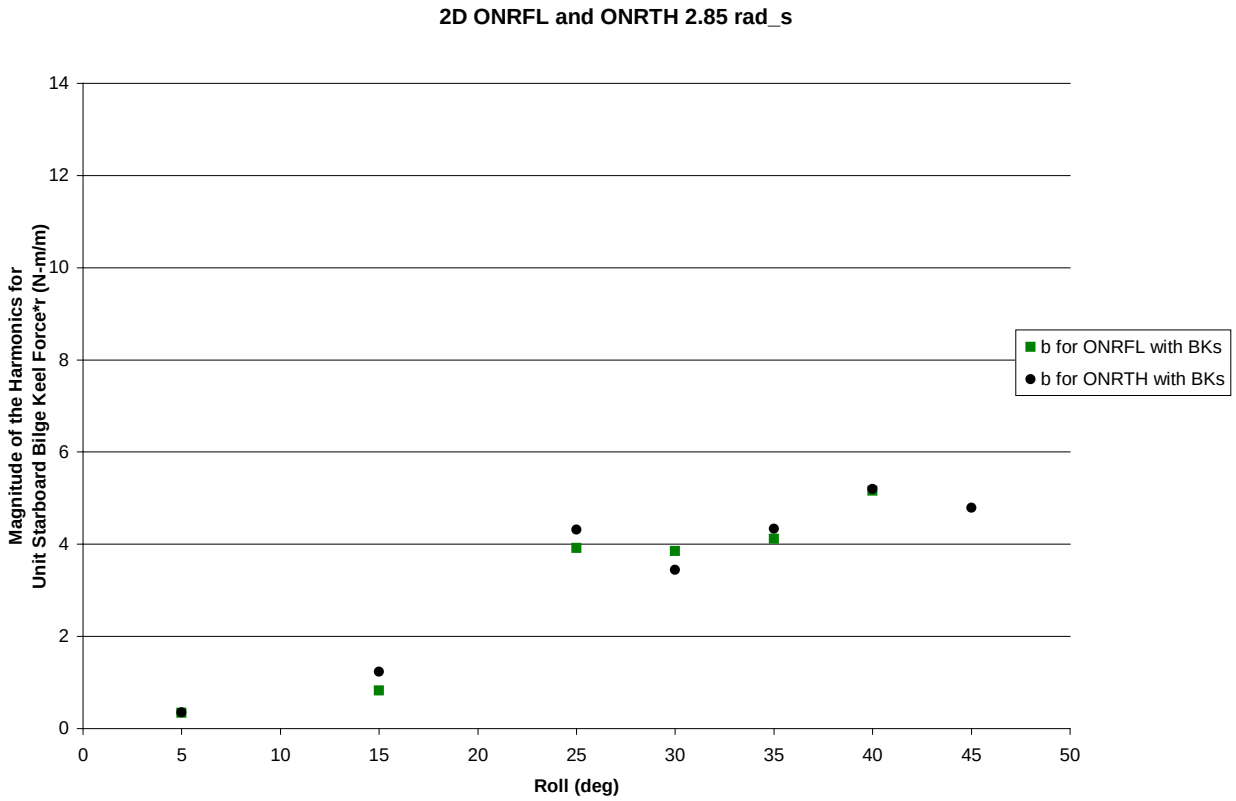

Figure D-43. Comparison of the magnitude of the total of the first 10 harmonics of damping for the unit hydrodynamic roll moment due to the starboard bilge keel, for DTMB Models #5699 and #5699-1, with and without bilge keels, ω=2.85 rad/s

D.9 Vortex Shedding from the Bilge Keels

PIV results are shown for the ONRFL, forced roll oscillation conditions for amplitudes 5 deg through 40 deg (Figure D-44-D-49).

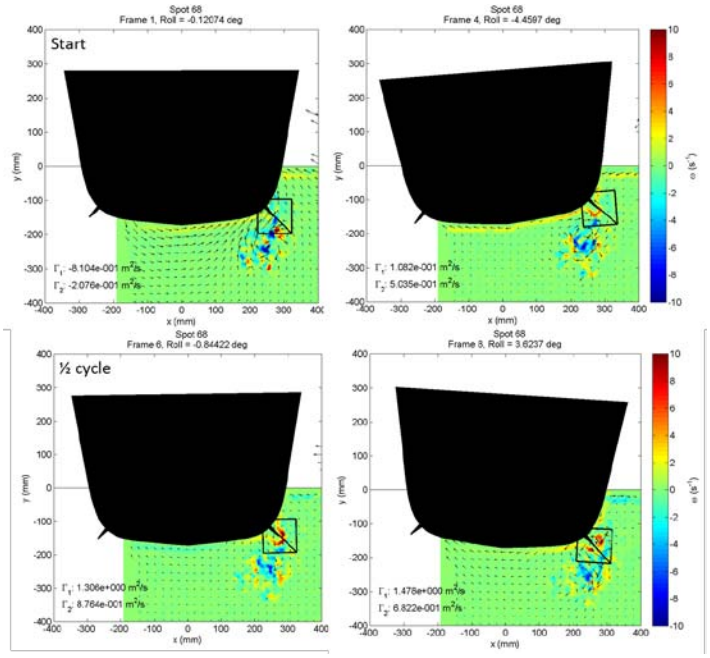

Figure D-44. PIV results of the vorticity field for one roll period, for DTMB Model #5699, φ= 5 deg, ω=2.85 rad/s

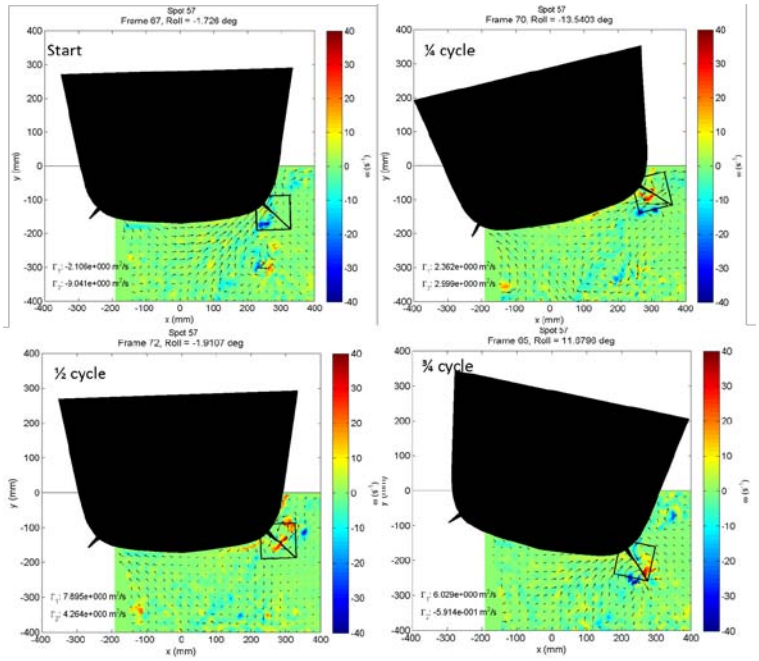

Figure D-45. PIV results of the vorticity field for one roll period, for DTMB Model #5699, φ= 15 deg, ω=2.85 rad/s

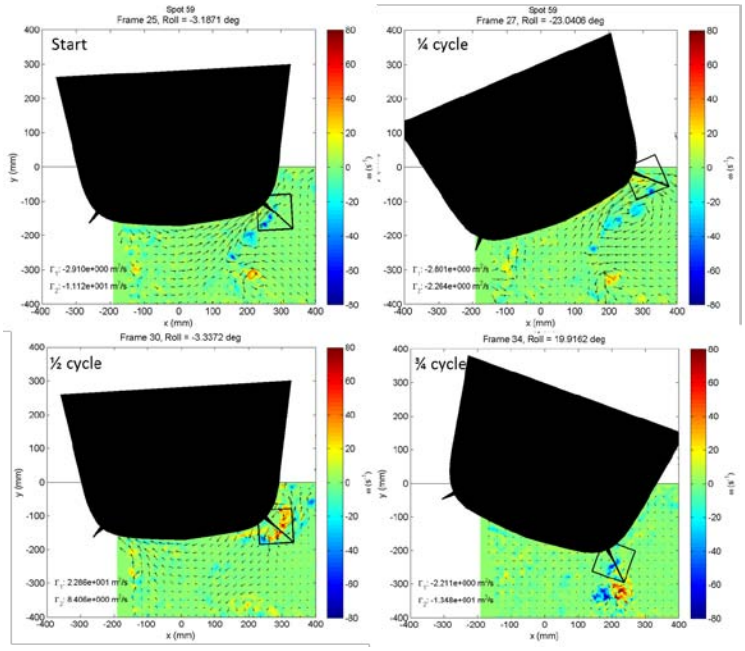

Figure D-46. PIV results of the vorticity field for one roll period, for DTMB Model #5699, φ= 25 deg, ω=2.85 rad/s

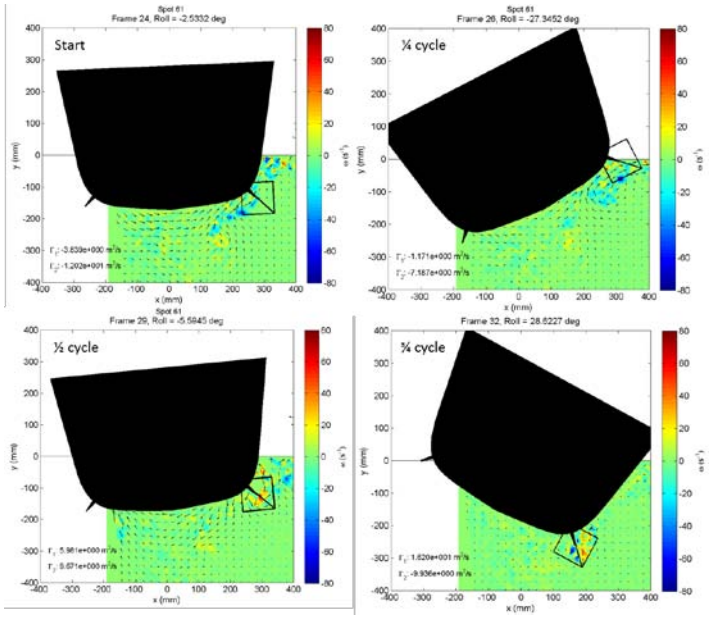

Figure D-47. PIV results of the vorticity field for one roll period, for DTMB Model #5699, φ= 30 deg, ω=2.85 rad/s

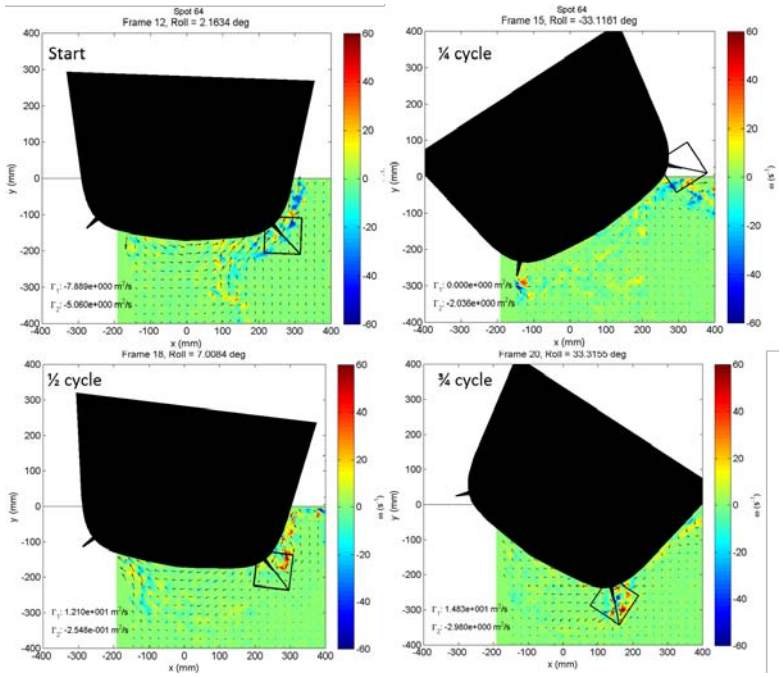

Figure D-48. PIV results of the vorticity field for one roll period, for DTMB Model #5699, φ= 35 deg, ω=2.85 rad/s

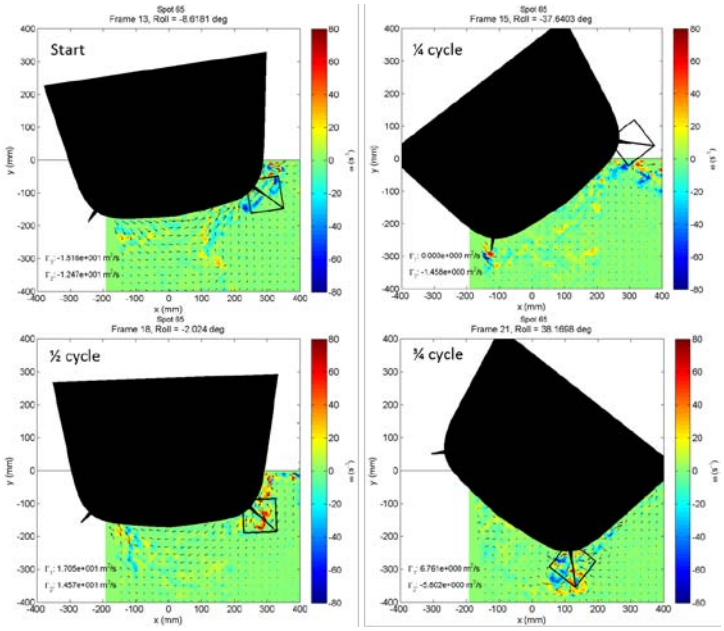

Figure D-49. PIV results of the vorticity field for one roll period, for DTMB Model #5699, φ= 5 deg, ω=2.85 rad/s

D.10 Variations in the Center of Pressure on the Bilge Keel

Variations in the center of pressure along the span of the bilge keel at the midship section of the ship, as measured from experiments with DTMB Model #5699-1, are shown for 15 deg through 45 deg (Figure D-50-D-55).

For large amplitude roll motion, the center of pressure on the bilge keel was also observed to vary. For small to moderate roll motion, the variation formed an "X" pattern, as the center of pressure changed during the roll cycle. For large amplitude roll motion, the "X" type structure of the variation of the center of pressure was degraded and the asymmetry due to the emergence of the bile keel is observed. A strong asymmetry is observed for large roll amplitudes, particularly at 30, 35, 40, and 45 degrees, when the bilge keel emergence has occurred. This variation is important for the determination of a lateral sway force on the hull, particularly during large amplitude roll motions.

As the bilge keel emerges, the center of pressure makes a sharp jump towards the root of the bilge keel, but is distorted by the continued presence of water on the topside of the bilge keel, as discussed previously. Once the excess water is shed, the center of pressure disappears. This is due to the absence of force on the bilge keel. Then after re-entry, and the renewal of force on the bilge keel, the center of pressure continues along the bottom portion of the "X" pattern as it become fully submerged.

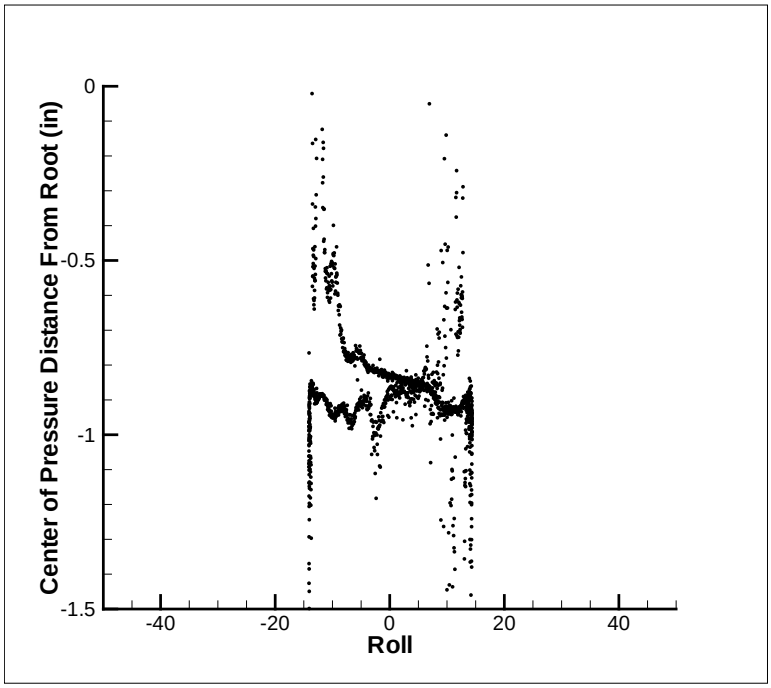

Figure D-50. Variation in the center of pressure on the starboard bilge keel for Fn=0.0, ϕ=15 deg, ω=2.85 rad/s, as measured for DTMB Model #5699-1.

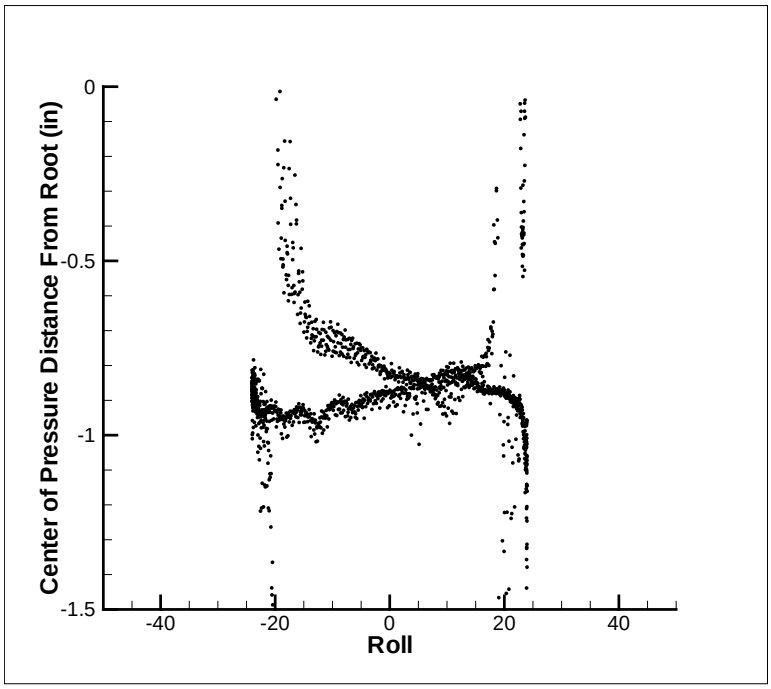

Figure D-51. Variation in the center of pressure on the starboard bilge keel for Fn=0.0, ϕ=25 deg, ω=2.85 rad/s, as measured for DTMB Model #5699-1.

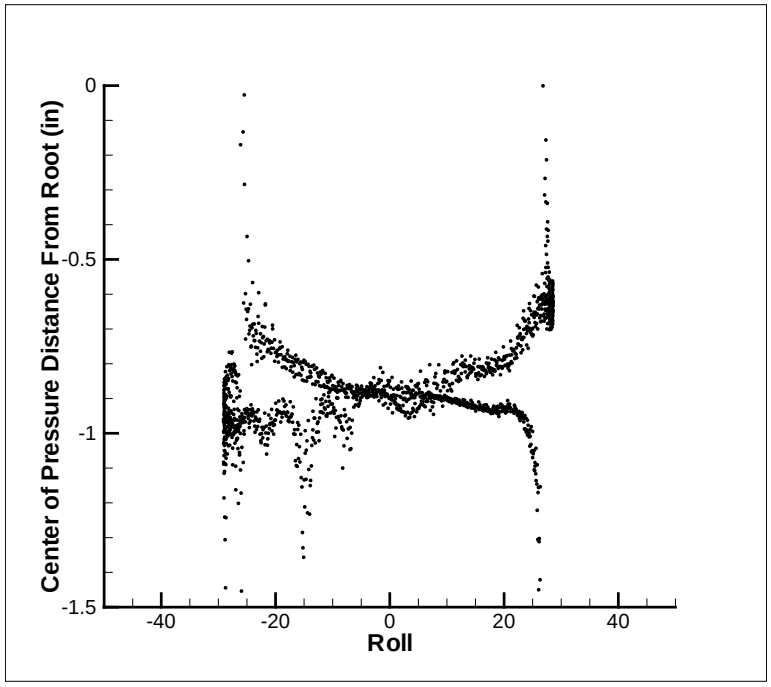

Figure D-52. Variation in the center of pressure on the starboard bilge keel for Fn=0.0, ϕ=30 deg, ω=2.85 rad/s, as measured for DTMB Model #5699-1.

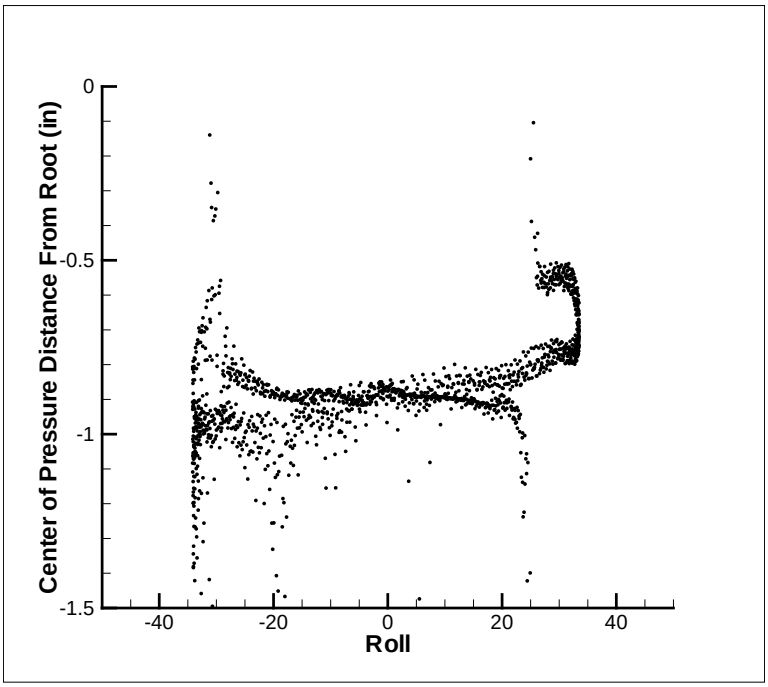

Figure D-53. Variation in the center of pressure on the starboard bilge keel for Fn=0.0, ϕ=35 deg, ω=2.85 rad/s, as measured for DTMB Model #5699-1.

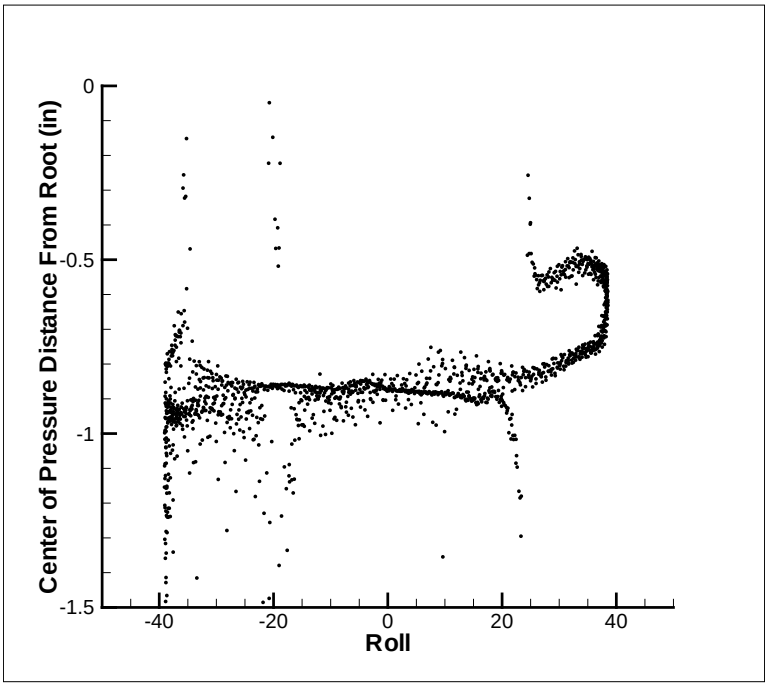

Figure D-54. Variation in the center of pressure on the starboard bilge keel for Fn=0.0, ϕ=40 deg, ω=2.85 rad/s, as measured for DTMB Model #5699-1.

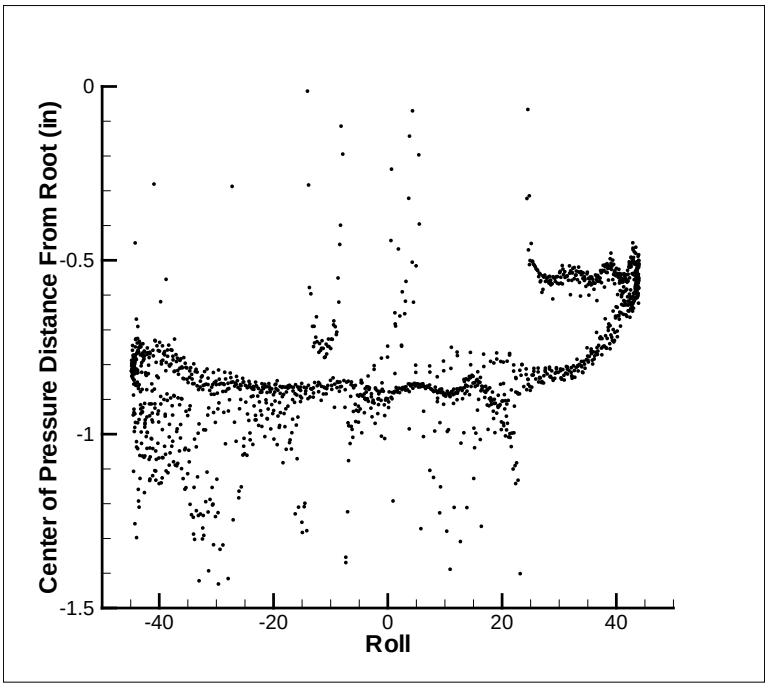

Figure D-55. Variation in the center of pressure on the starboard bilge keel for Fn=0.0, ϕ=45 deg, ω=2.85 rad/s, as measured for DTMB Model #5699-1.

Appendix E: Additional Data from the Numerical Analysis and Observations of the WAMIT Results

Asymptotic frequencies were calculated. At zero frequency, the added inertia, without bilge keels, approaches 2.4.0 kg-m^2/s. At zero frequency, the added inertia, with bilge keels, approaches 3.6 kg-m^2/s. At infinite frequency, the added inertia, without bilge keels, approaches 1.7 kg-m^2/s. At infinite frequency, the added inertia, with bilge keels, approaches 3.2 kg-m^2/s. At zero frequency, the damping, both with and without bilge keels, approaches zero. At infinite frequency, the damping, both with and without bilge keels, approaches zero.

3D plots of the added inertia and damping due to radiation, as a function of both heel angle and roll frequency, calculated using WAMIT are also shown (Figure E-19-Figure E-30) for visualization. These plots were intended to provide additional visualization of the observed trends presented in the 2D plots. From the 3D plots of the variation in the added inertia and damping as a function of both roll amplitude and frequency are generally smoother for the flared topside than for the tumblehome topside. However, the peaks in added inertia and damping are sharper and decreases with heel and roll frequency are generally steeper for the tumblehome topside compared to the flared topside.

For the flared topside, the phase of the total unit hydrodynamic roll moment increases with increasing heel, but with the addition of bilge keels has a temporary reduction around 27-28 deg (Figure E-31). For the tumblehome topside, both with and without bilge keels, the phase of the total unit hydrodynamic roll moment increases with increasing heel around 17-20 deg heel and above 28 deg heel, but remains nearly constant for other heel angles (Figure E-32).

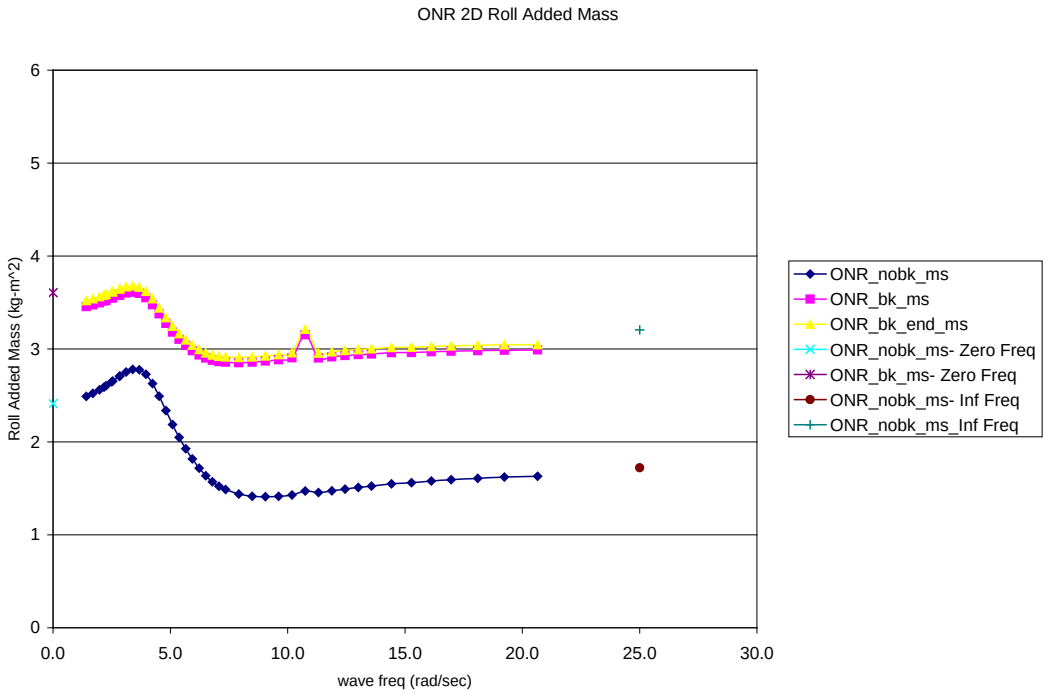

Figure E-1.ONRFL added inertia due to radiation vs. frequency, for 0 deg and 25 deg fixed heel conditions, with and without bilge keels, infinite frequency values shown at 25 rad/s

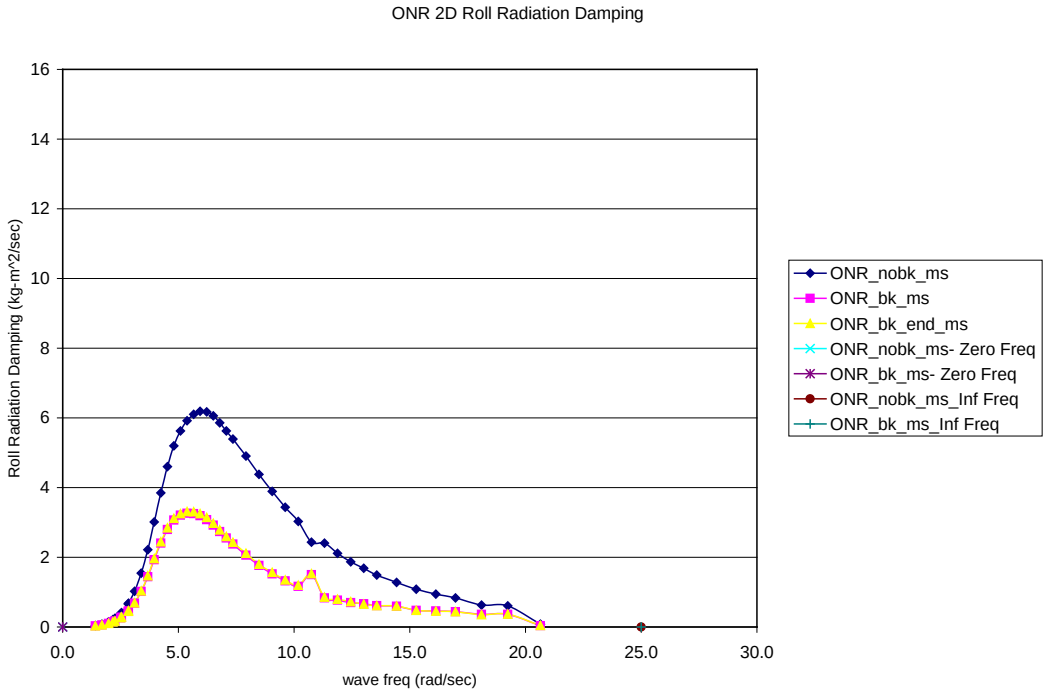

Figure E-2.ONRFL damping due to radiation vs. frequency, for 0 deg and 25 deg fixed heel conditions, with and without bilge keels, infinite frequency values shown at 25 rad/s

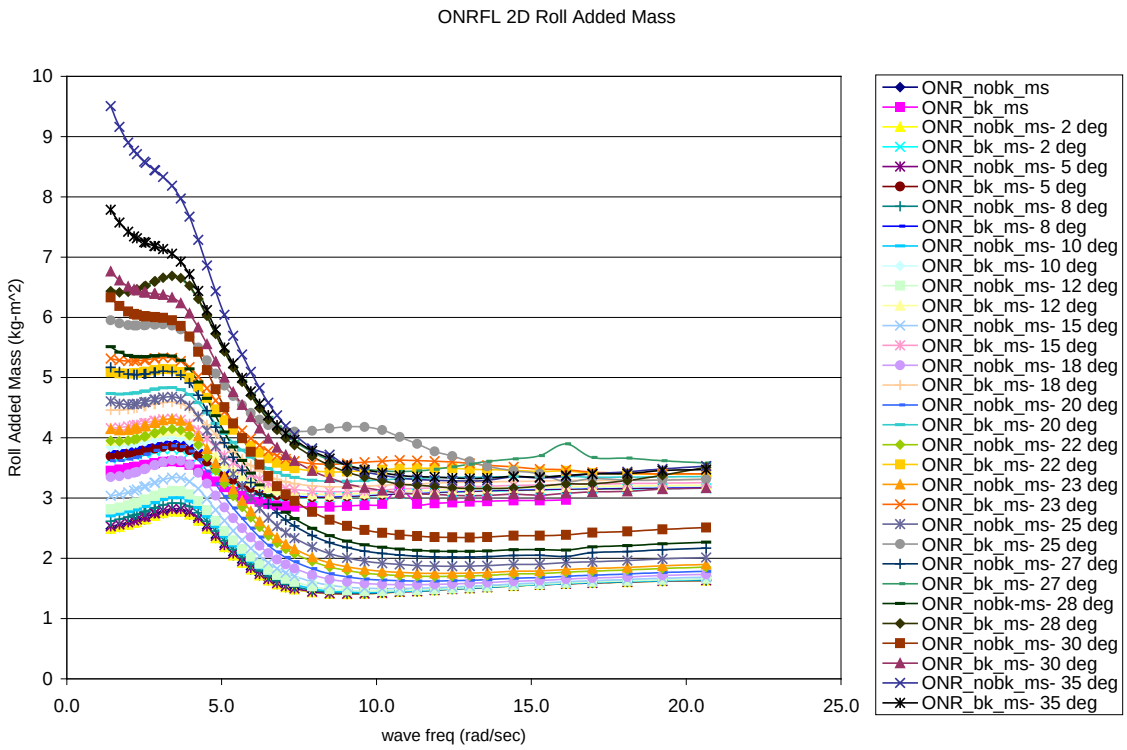

Figure E-3. ONRFL added inertia due to radiation vs. frequency, for 0-35 deg fixed heel conditions, with and without bilge keels

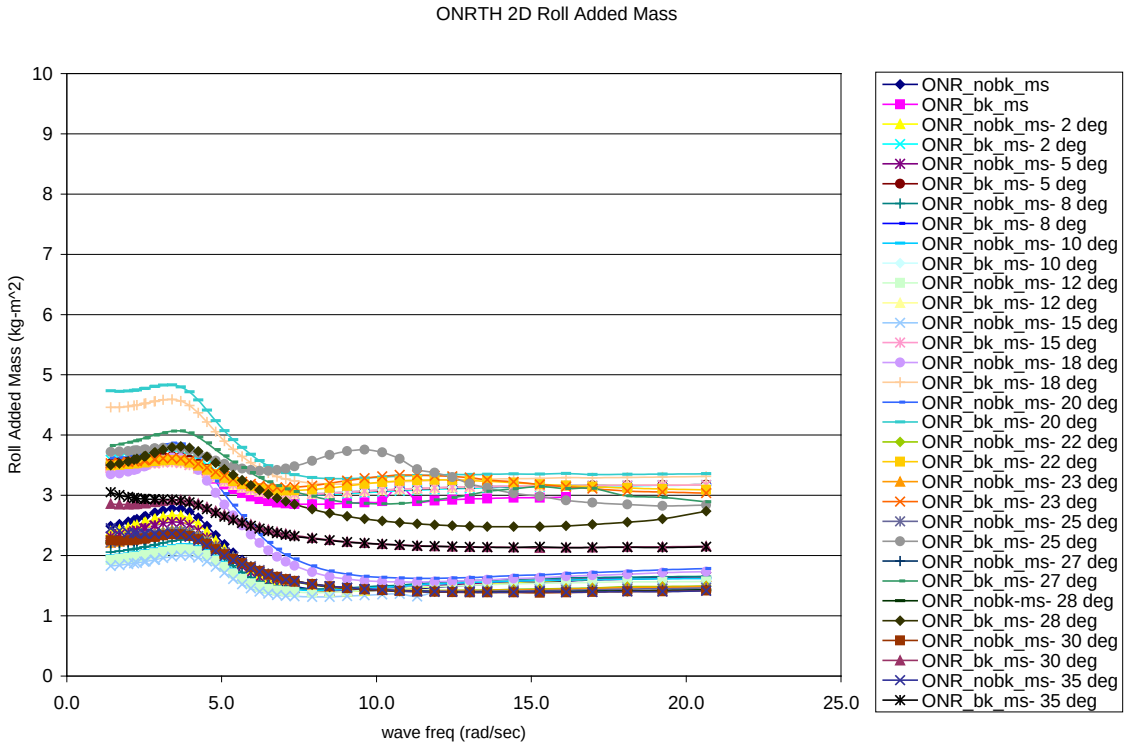

Figure E-4. ONRTH added inertia due to radiation vs. frequency, for 0-35 deg fixed heel conditions, with and without bilge keels

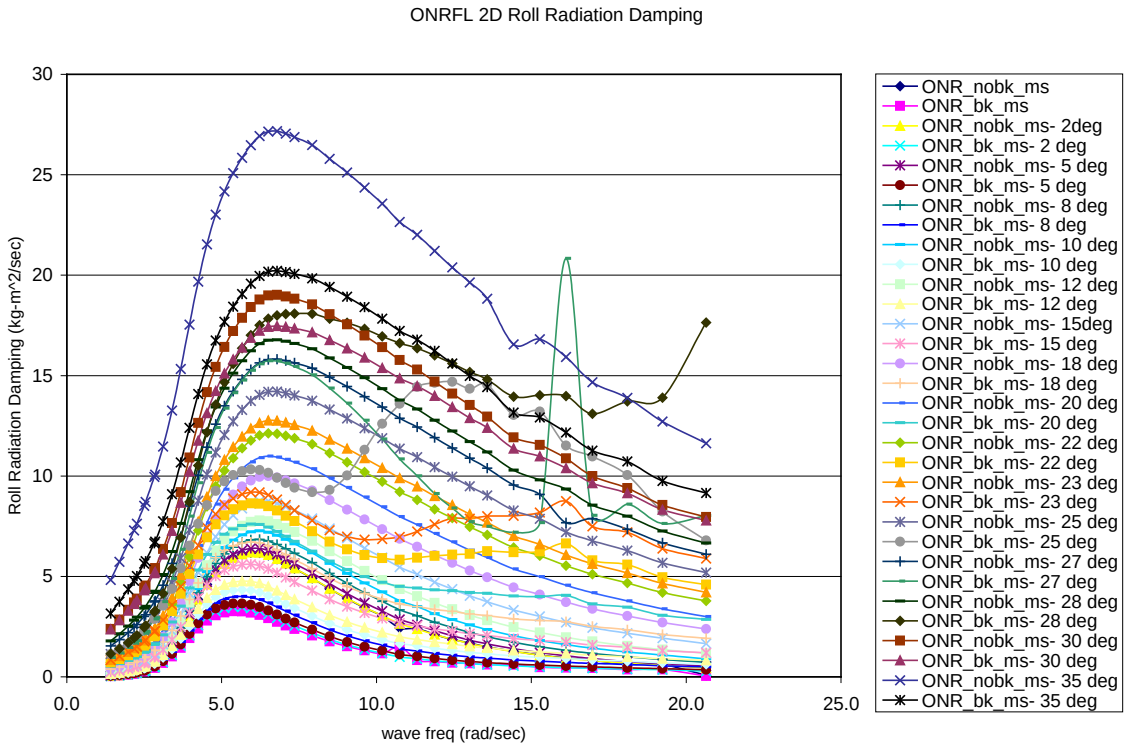

Figure E-5. ONRFL damping due to radiation vs. frequency, for 0-35 deg fixed heel conditions, with and without bilge keels

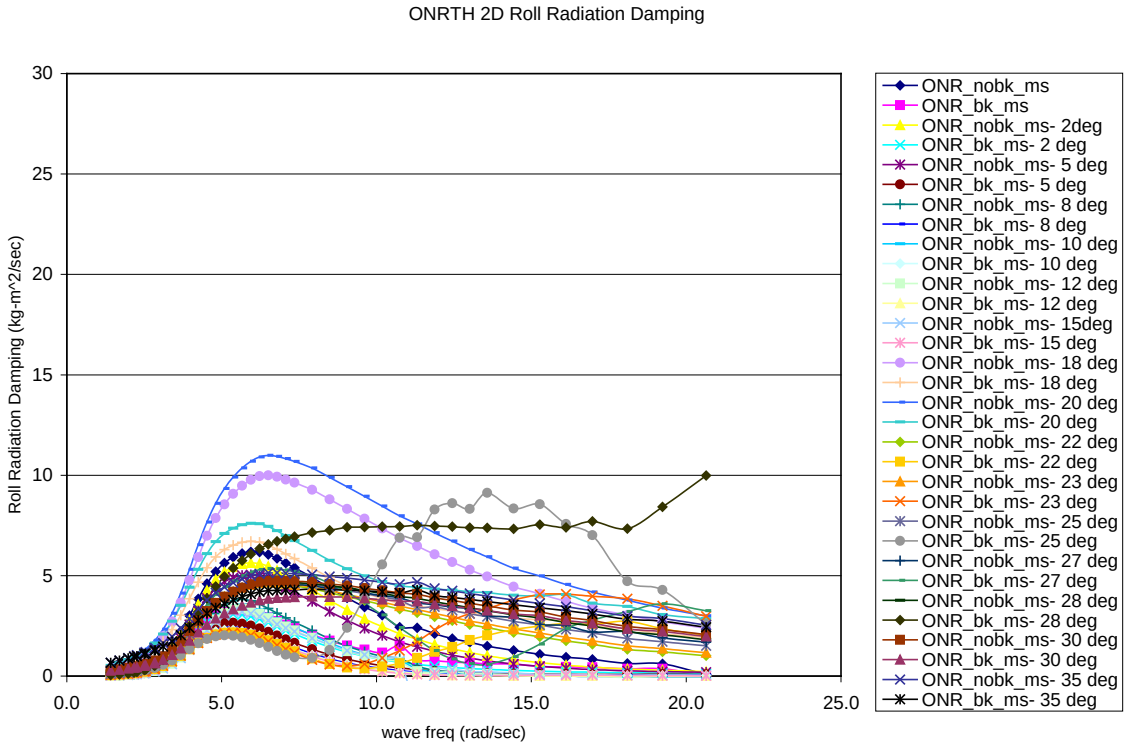

Figure E-6. ONRTH damping due to radiation vs. frequency, for 0-35 deg fixed heel conditions, with and without bilge keels

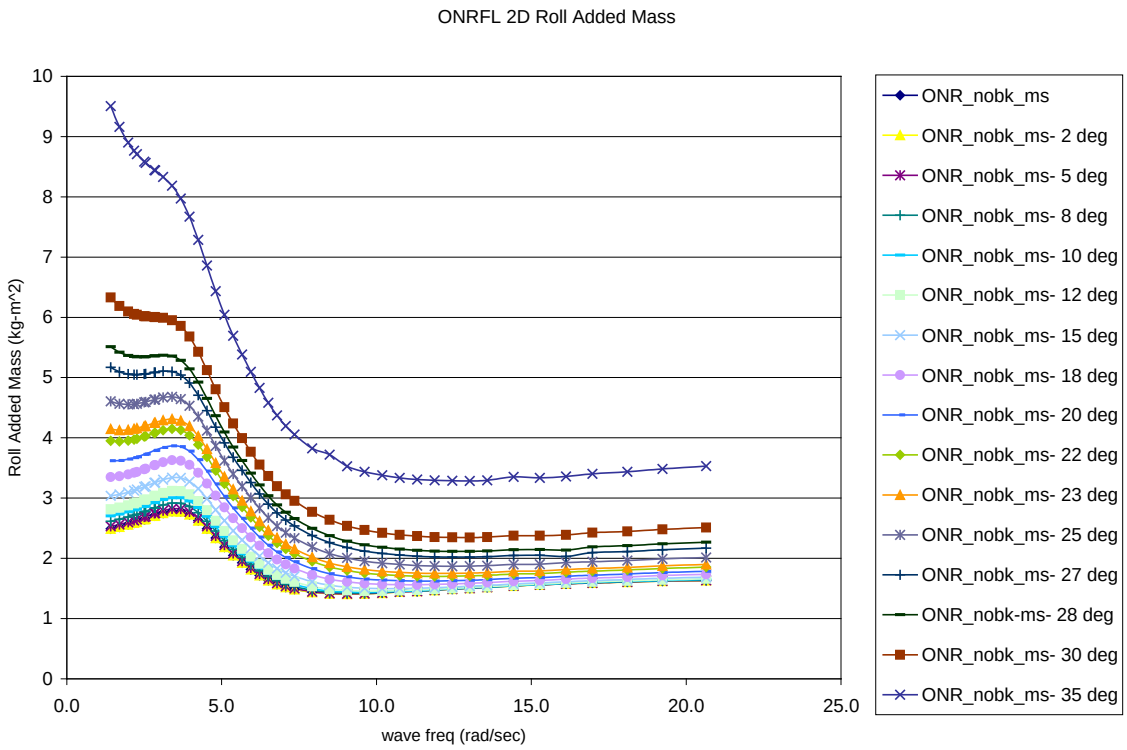

Figure E-7. ONRFL added inertia due to radiation vs. frequency, for 0-35 deg fixed heel conditions, without bilge keels

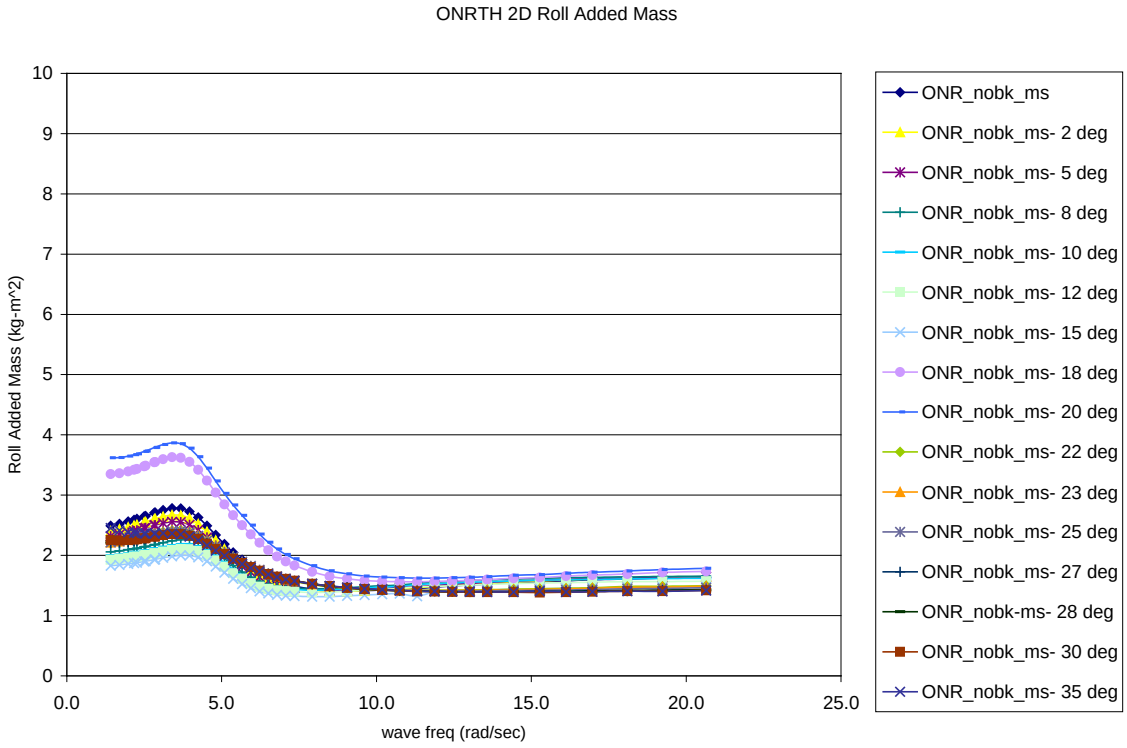

Figure E-8. ONRTH added inertia due to radiation vs. frequency, for 0-35 deg fixed heel conditions, without bilge keels

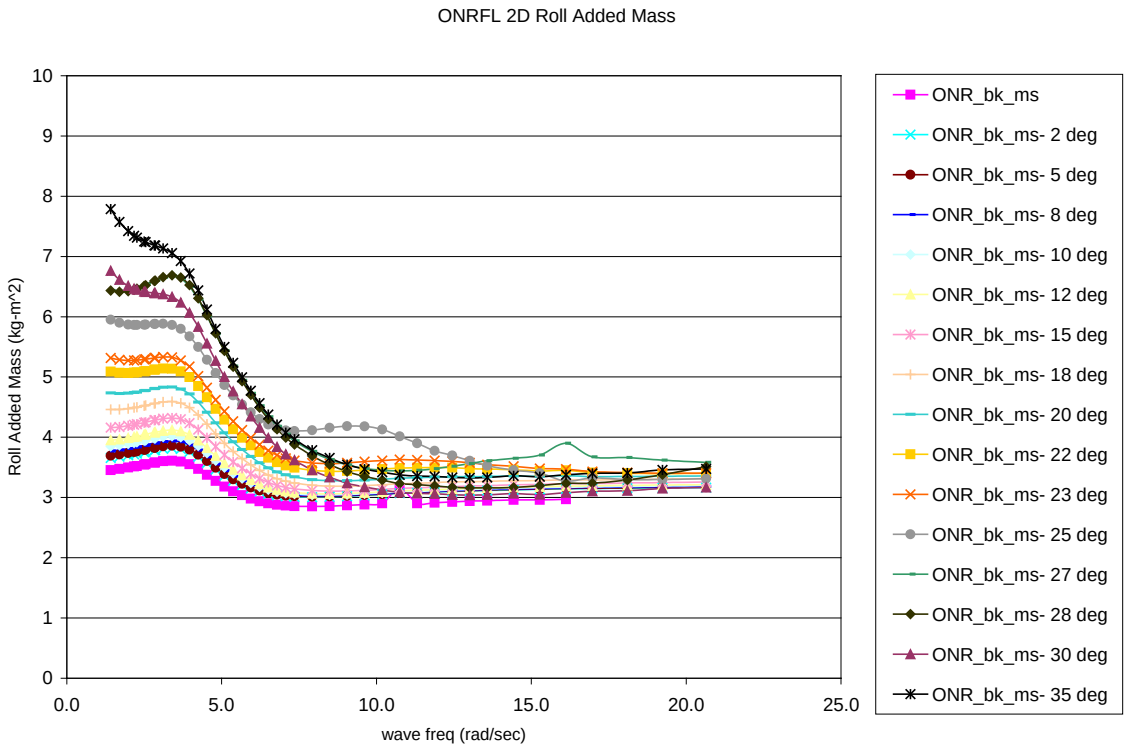

Figure E-9. ONRFL added inertia due to radiation vs. frequency, for 0-35 deg fixed heel conditions, with bilge keels

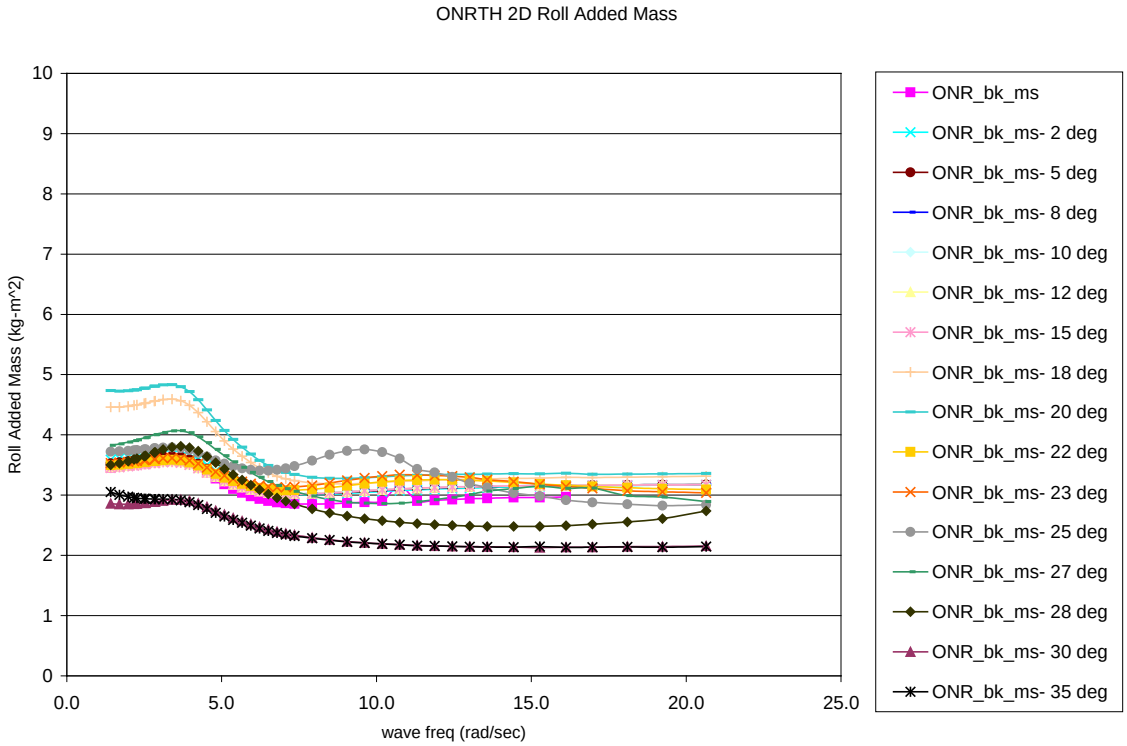

Figure E-10. ONRTH added inertia due to radiation vs. frequency, for 0-35 deg fixed heel conditions, with bilge keels

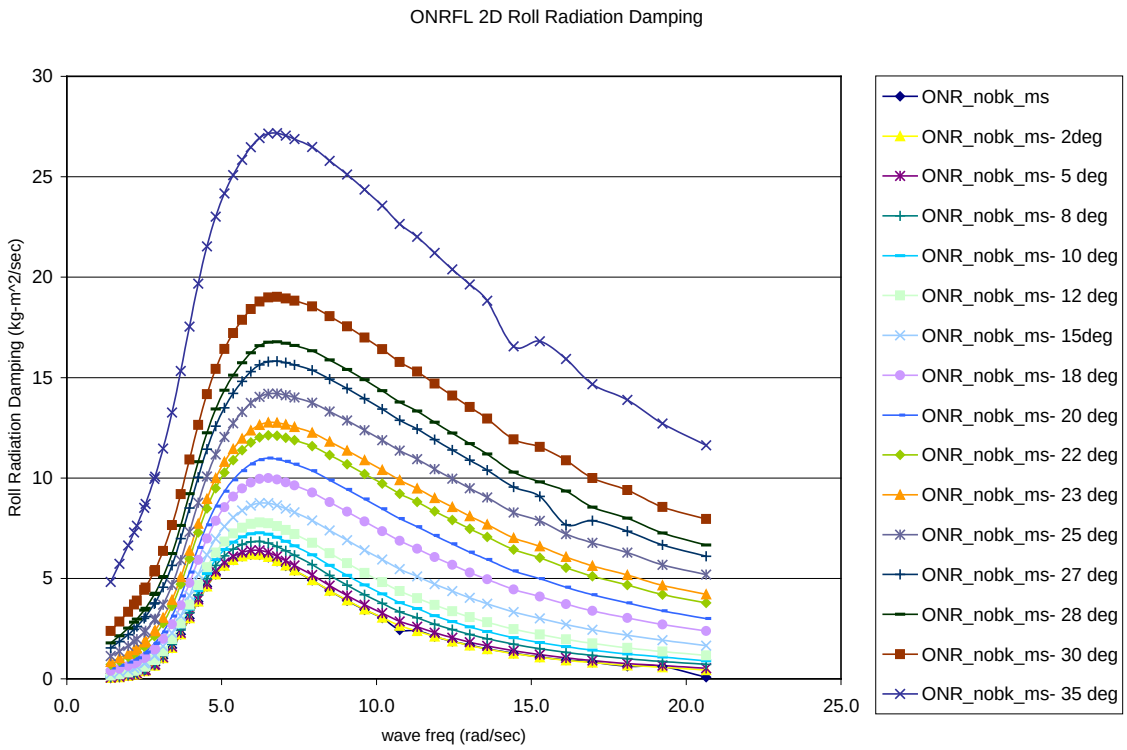

Figure E-11. ONRFL damping due to radiation vs. frequency, for 0-35 deg fixed heel conditions, without bilge keels

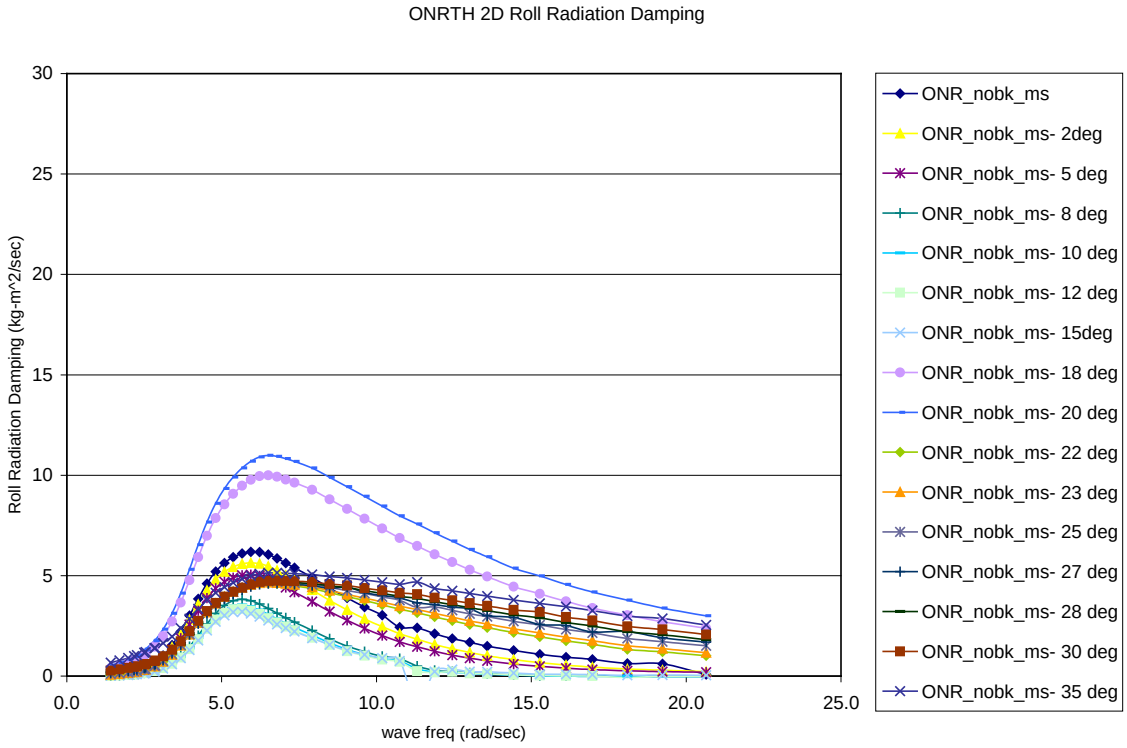

Figure E-12. ONRTH damping due to radiation vs. frequency, for 0-35 deg fixed heel conditions, without bilge keels

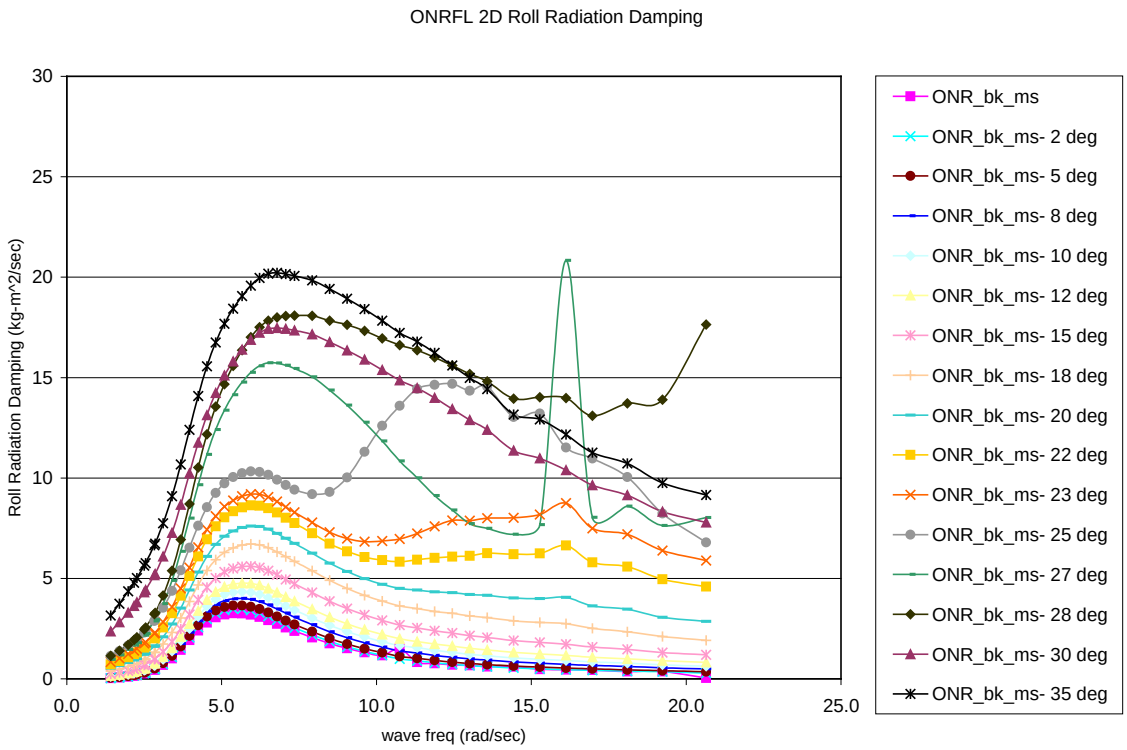

Figure E-13. ONRFL damping due to radiation vs. frequency, for 0-35 deg fixed heel conditions, with bilge keels

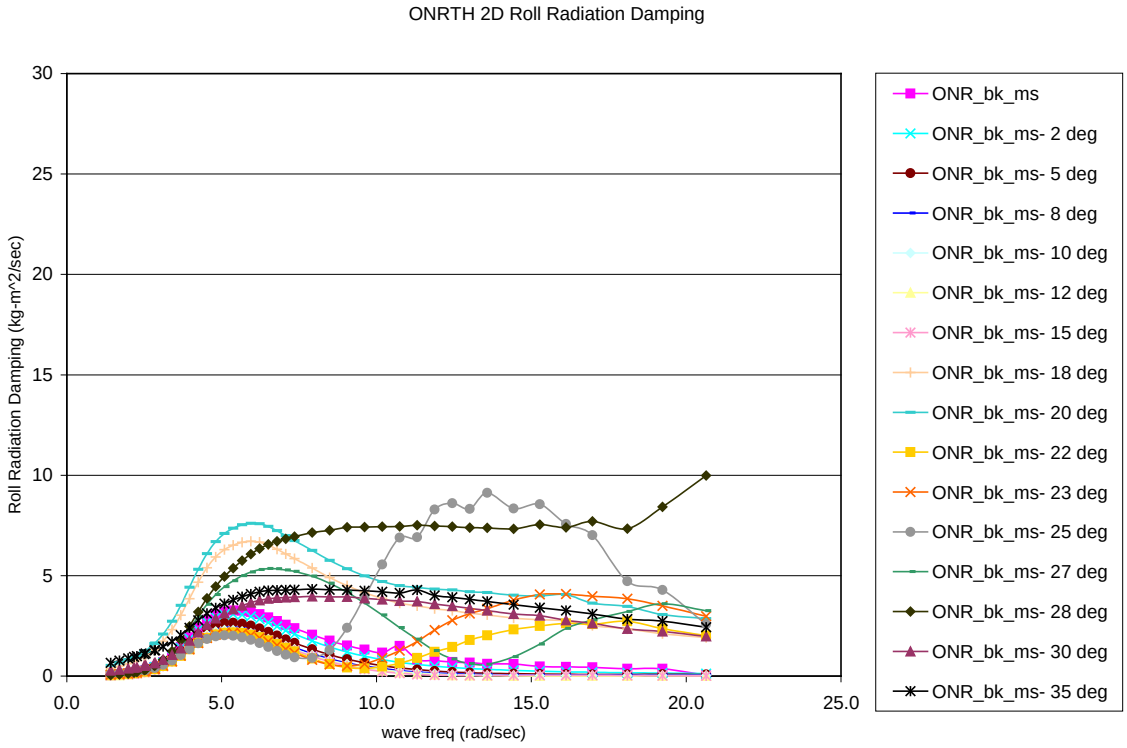

Figure E-14. ONRTH damping due to radiation vs. frequency, for 0-35 deg fixed heel conditions, with bilge keels

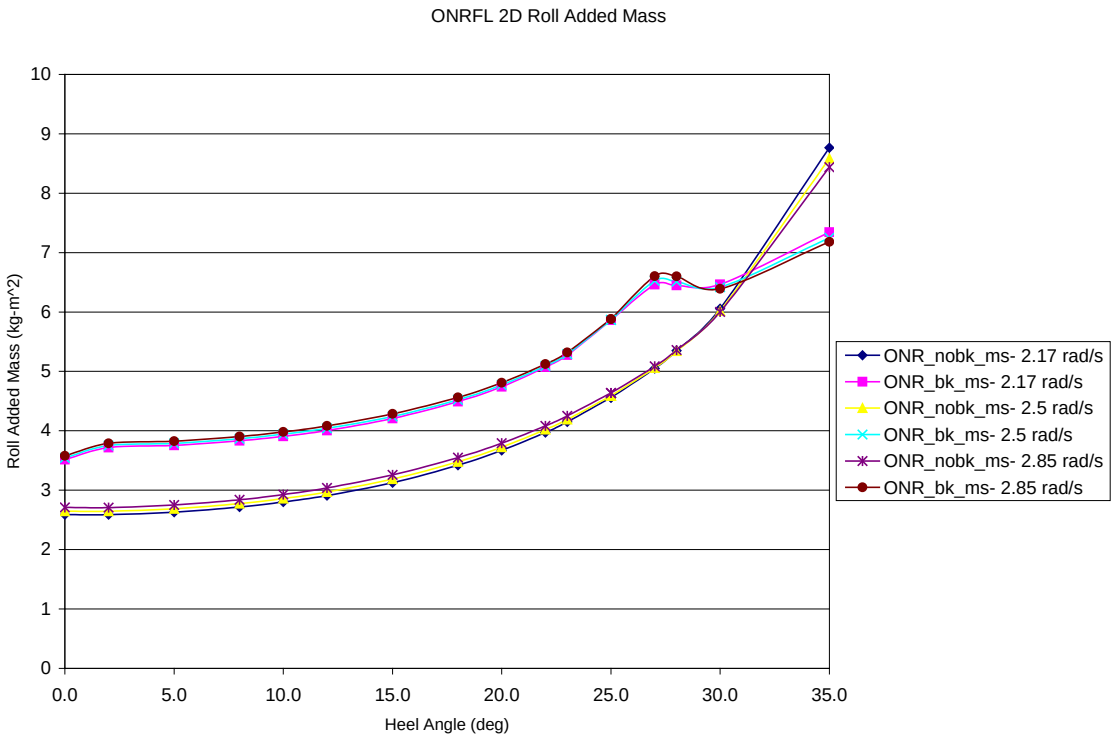

Figure E-15. ONRFL added inertia due to radiation vs heel angle, for three roll frequency conditions (same as the experiment), with and without bilge keels

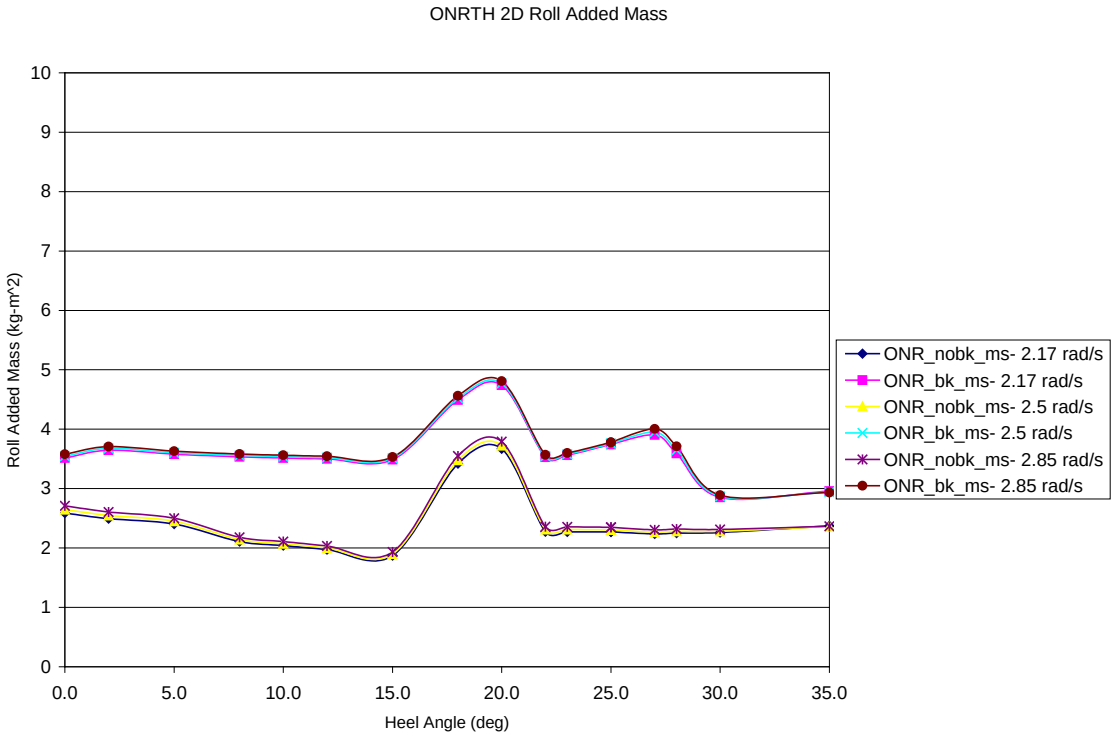

Figure E-16. ONRTH added inertia due to radiation vs heel angle, for three roll frequency conditions (same as the experiment), with and without bilge keels

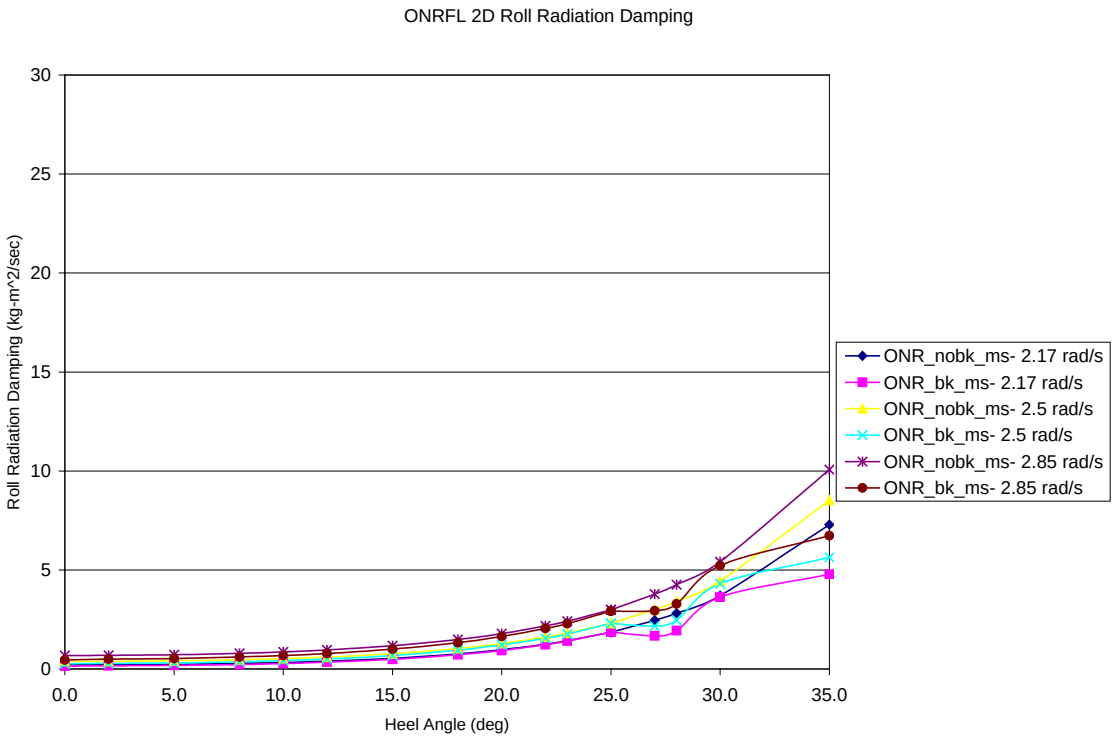

Figure E-17. ONRFL damping due to radiation vs heel angle, for three roll frequency conditions (same as the experiment), with and without bilge keels

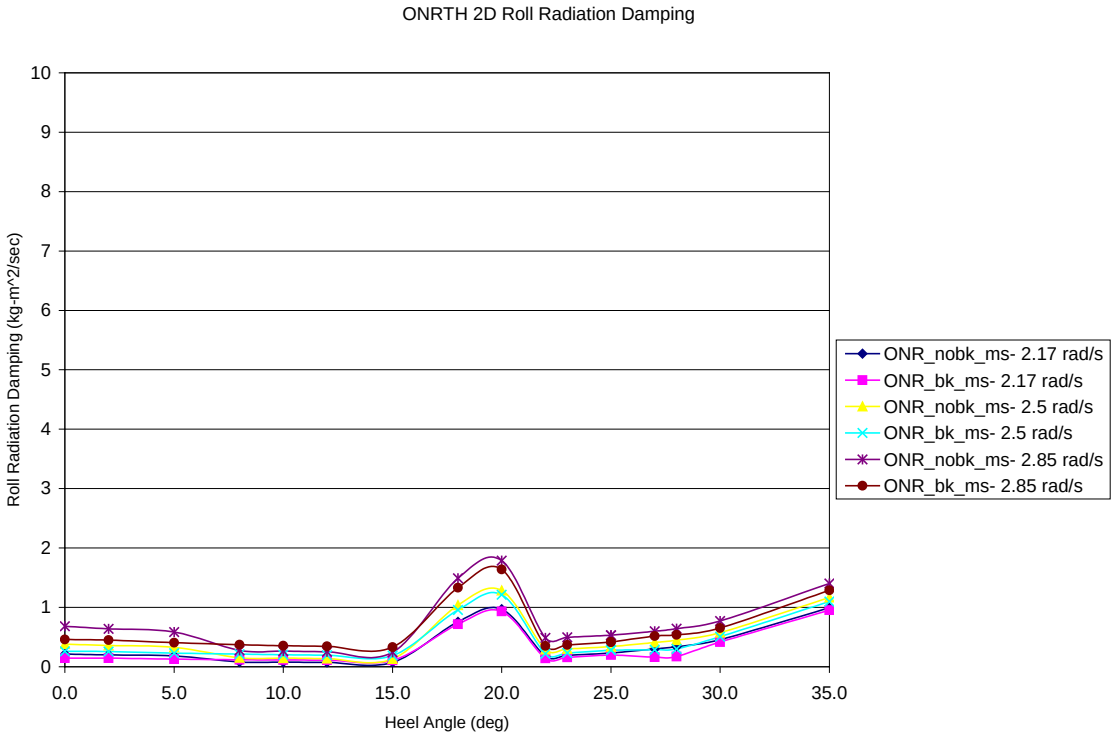

Figure E-18. ONRTH damping due to radiation vs heel angle, for three roll frequency conditions (same as the experiment), with and without bilge keels

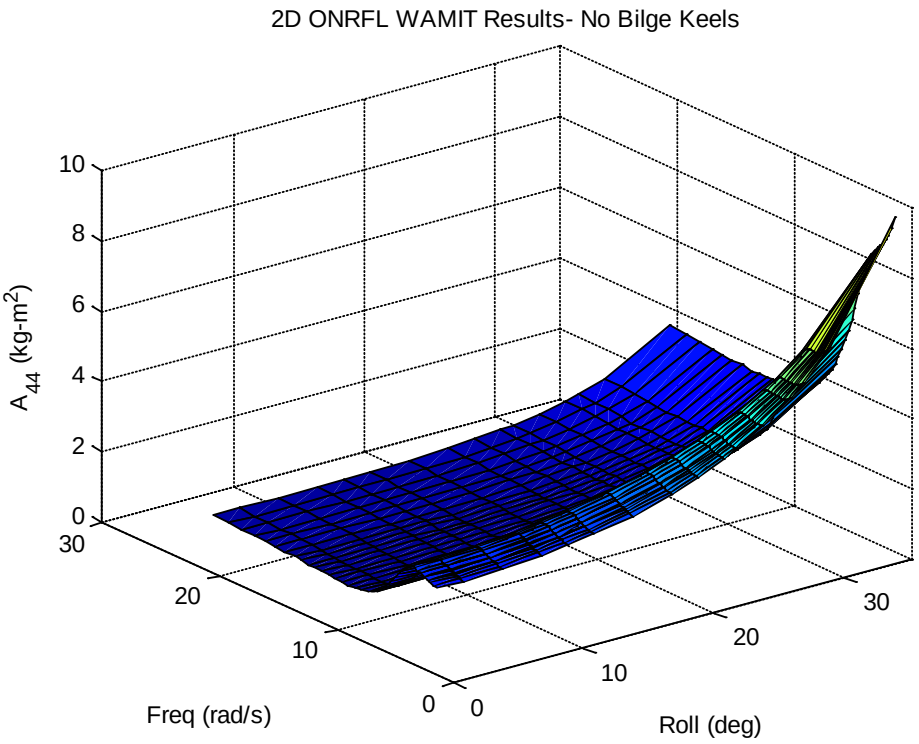

Figure E-19. ONRFL added inertia due to radiation vs heel angle vs frequency, without bilge keels

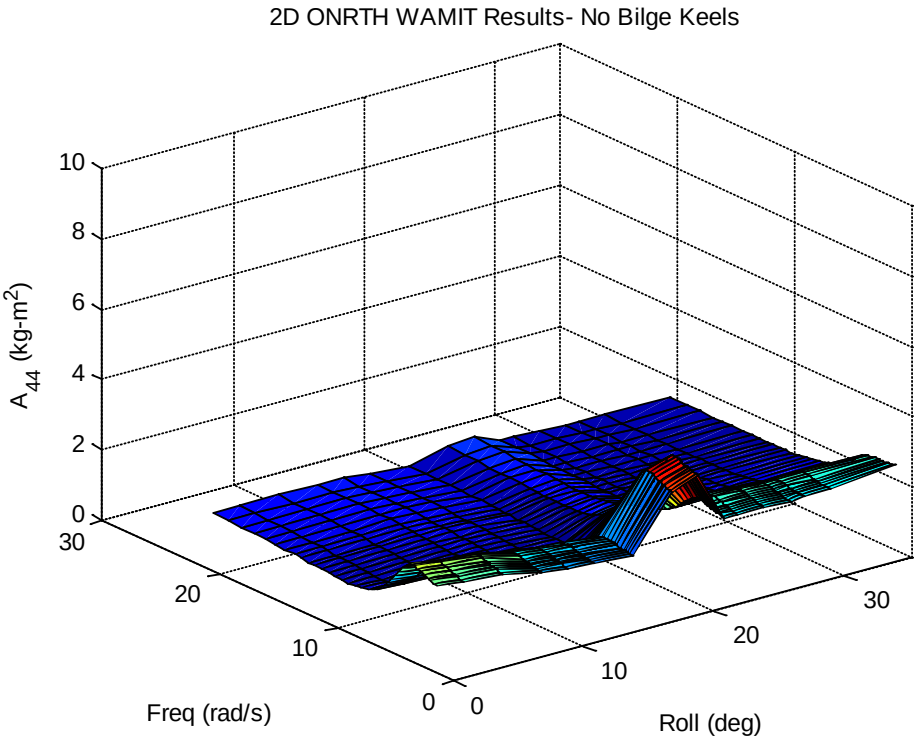

Figure E-20. ONRTH added inertia due to radiation vs heel angle vs frequency, without bilge keels

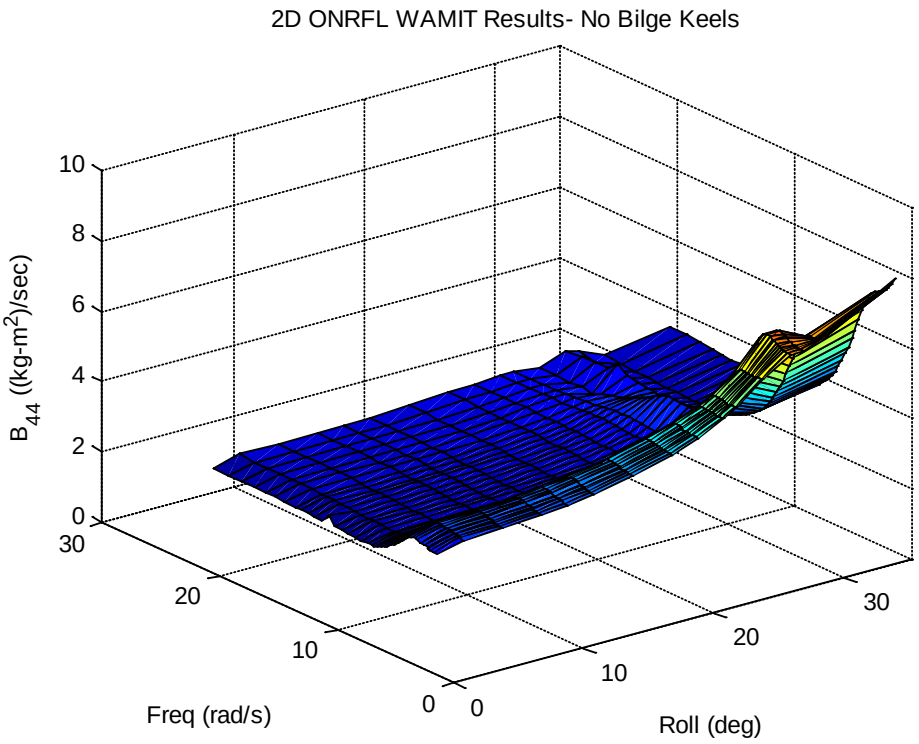

Figure E-21. ONRFL damping due to radiation vs heel angle vs frequency, without bilge keels

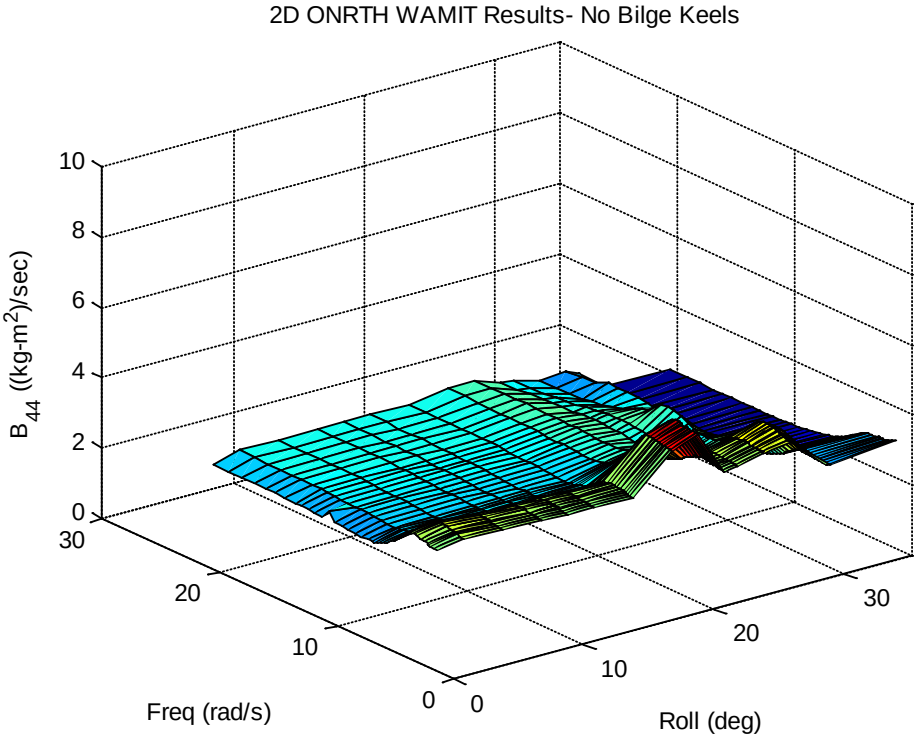

Figure E-22. ONRTH damping due to radiation vs heel angle vs frequency, without bilge keels

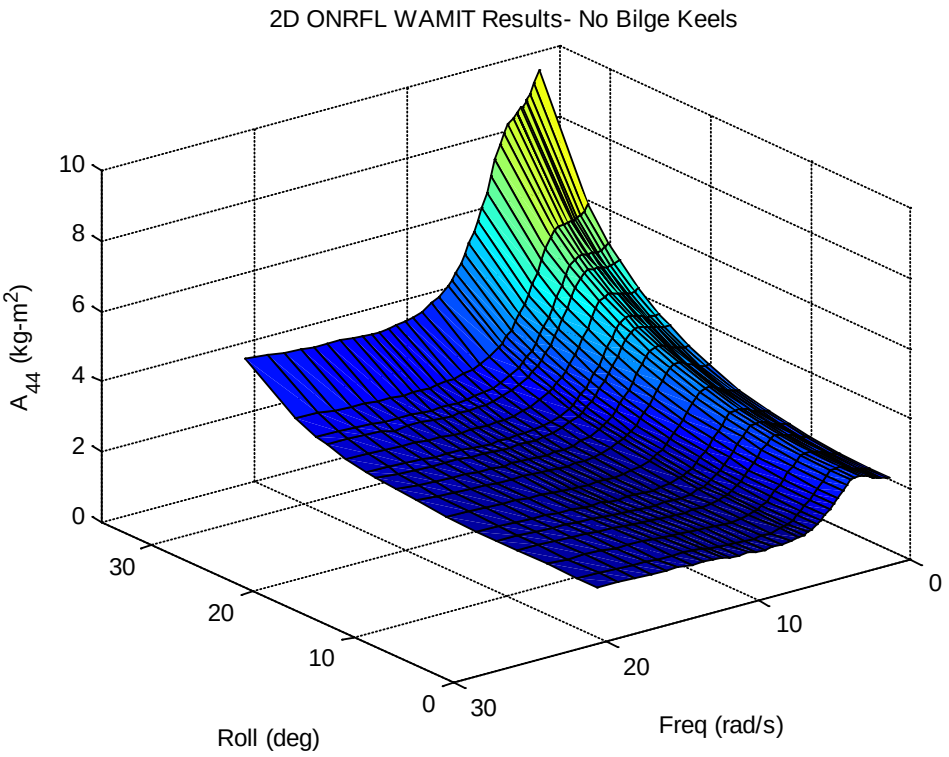

Figure E-23. Alternate view of ONRFL added inertia due to radiation vs heel angle vs frequency, without bilge keels

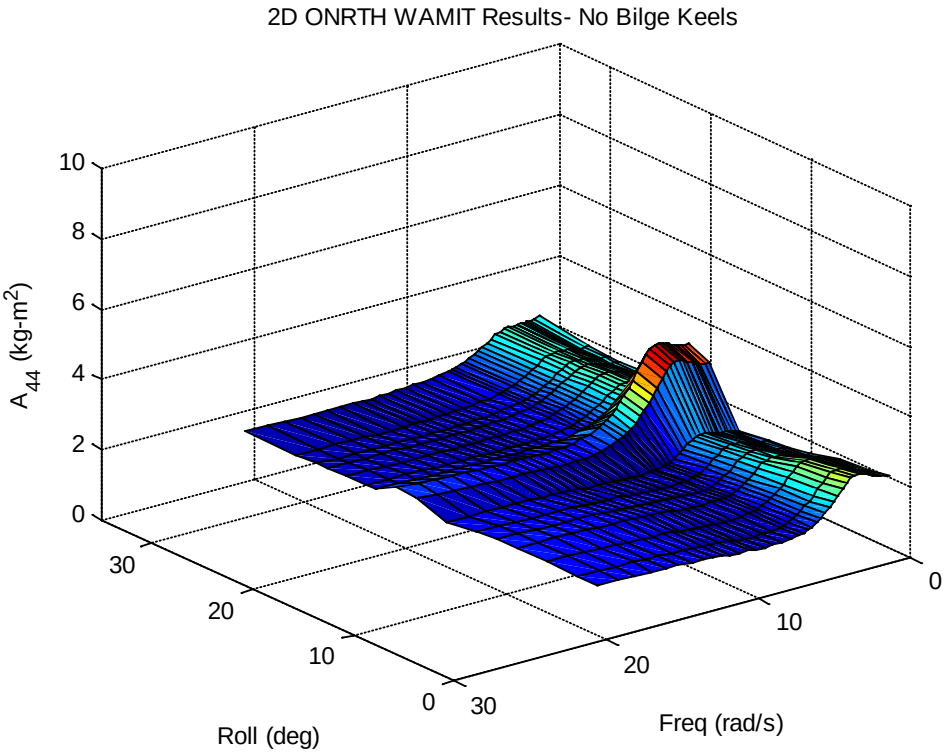

Figure E-24. Alternate view of ONRTH added inertia due to radiation vs heel angle vs frequency, without bilge keels

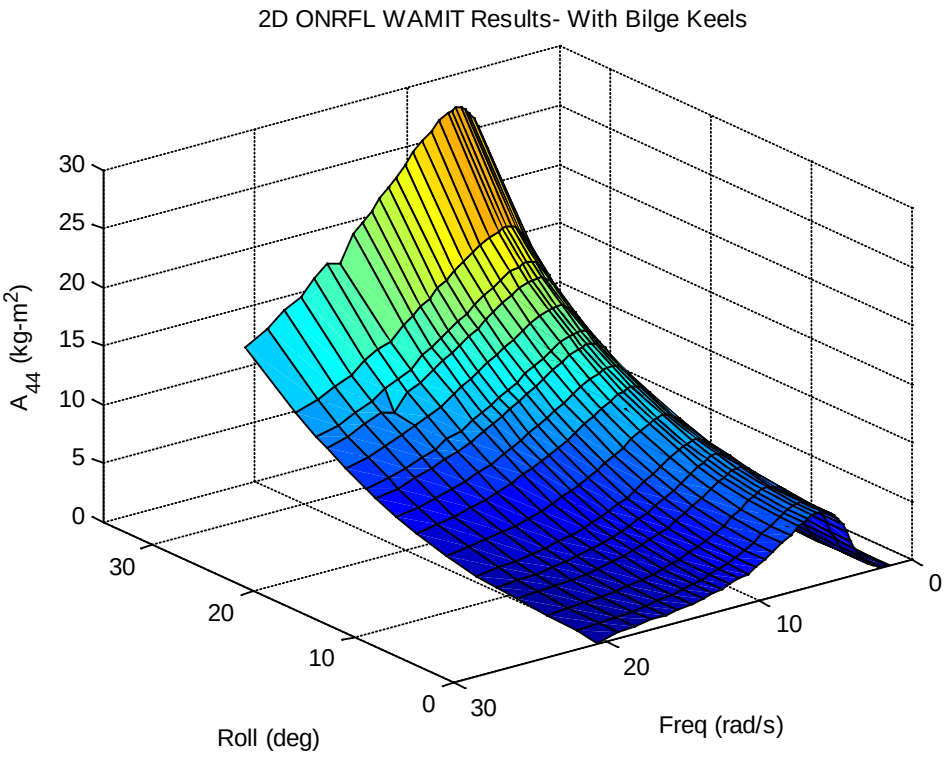

Figure E-25. Alternate view of ONRFL added inertia due to radiation vs heel angle vs frequency, with bilge keels

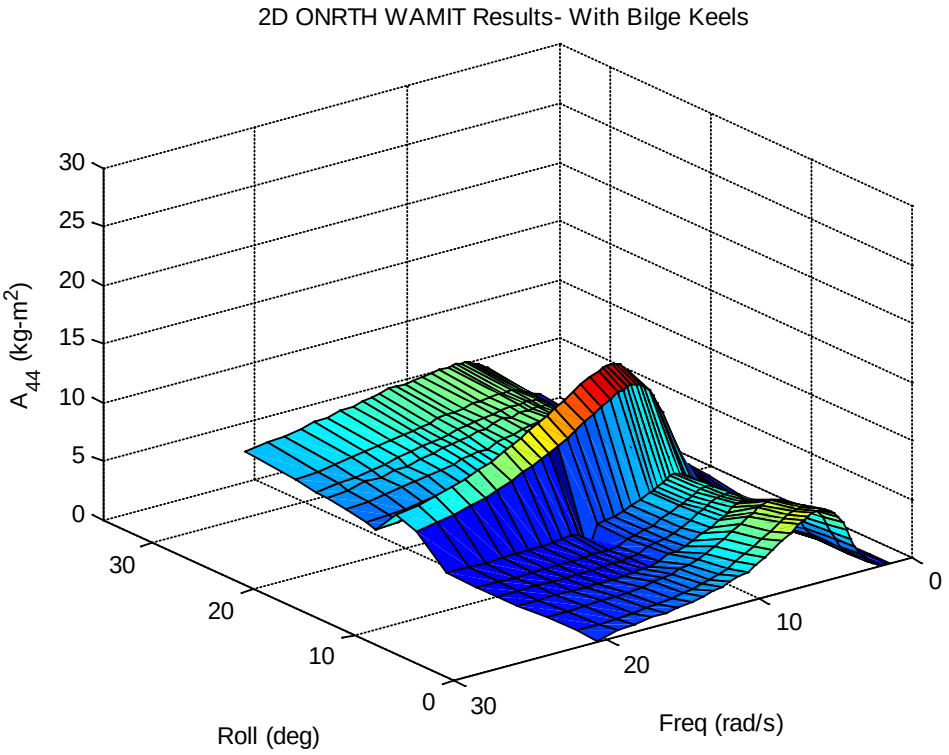

Figure E-26. Alternate view of ONRTH added inertia due to radiation vs heel angle vs frequency, with bilge keels

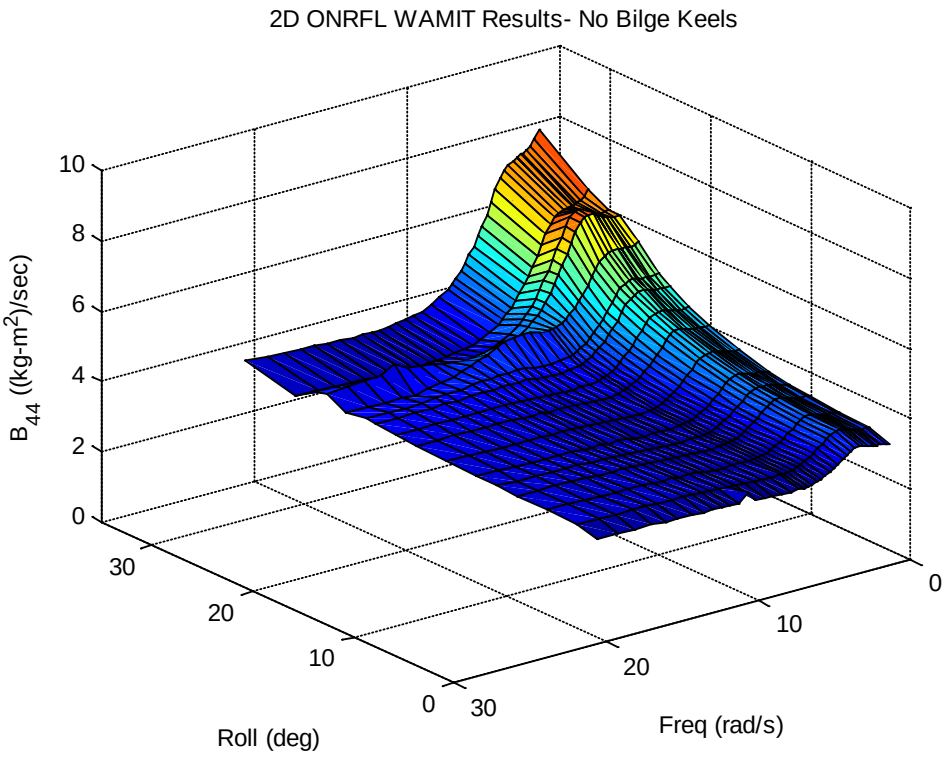

Figure E-27. Alternate view of ONRFL damping due to radiation vs heel angle vs frequency, without bilge keels

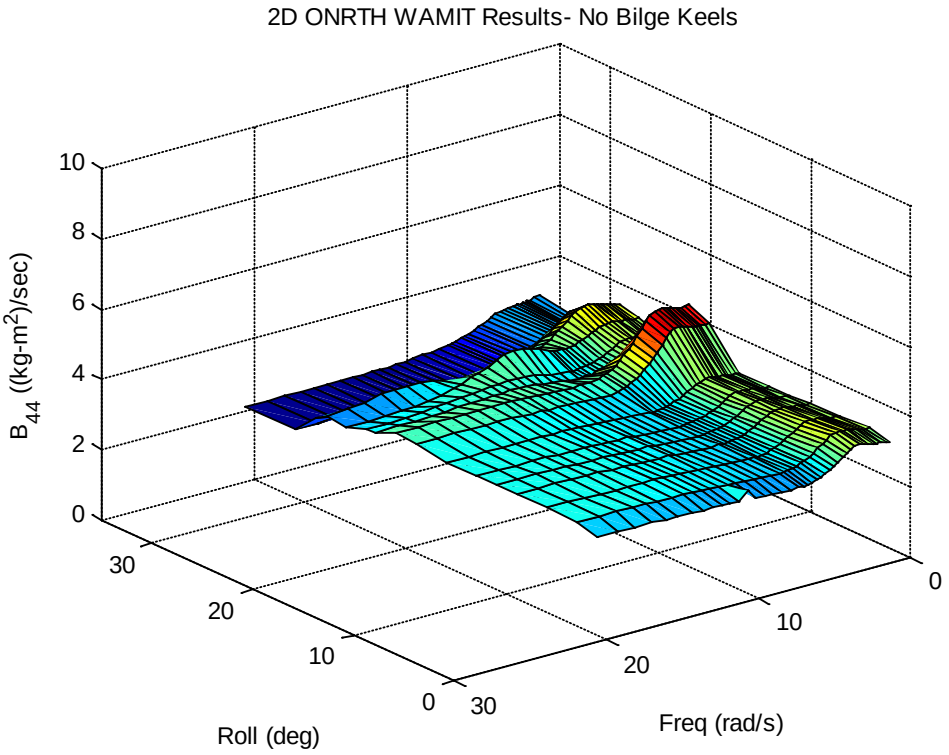

Figure E-28. Alternate view of ONRTH damping due to radiation vs heel angle vs frequency, without bilge keels

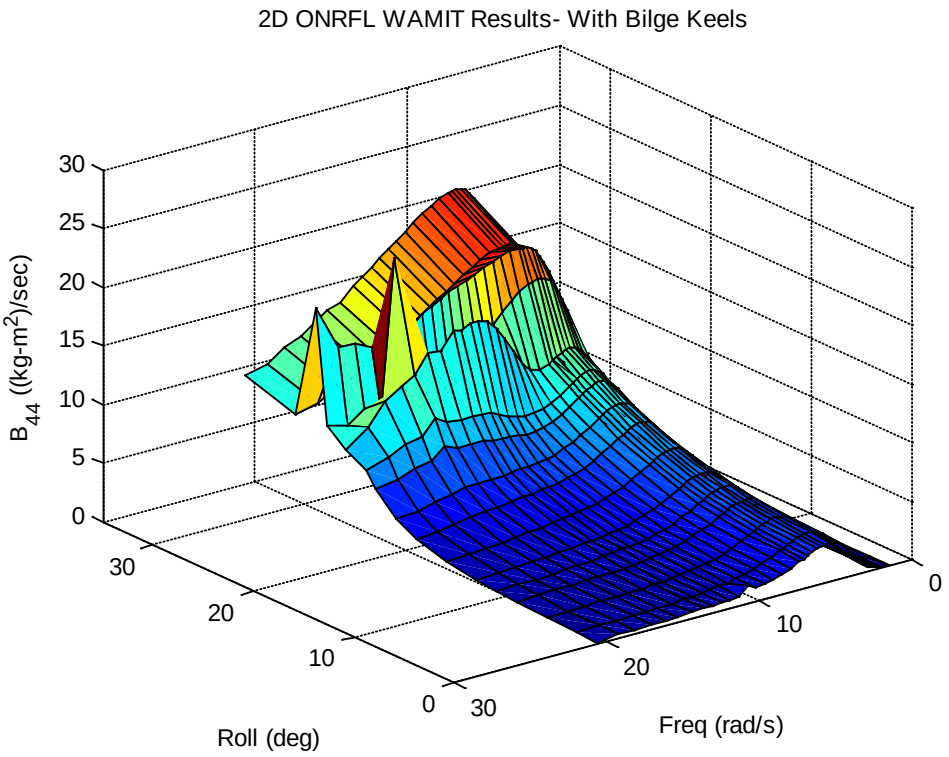

Figure E-29. Alternate view of ONRFL damping due to radiation vs heel angle vs frequency, with bilge keels

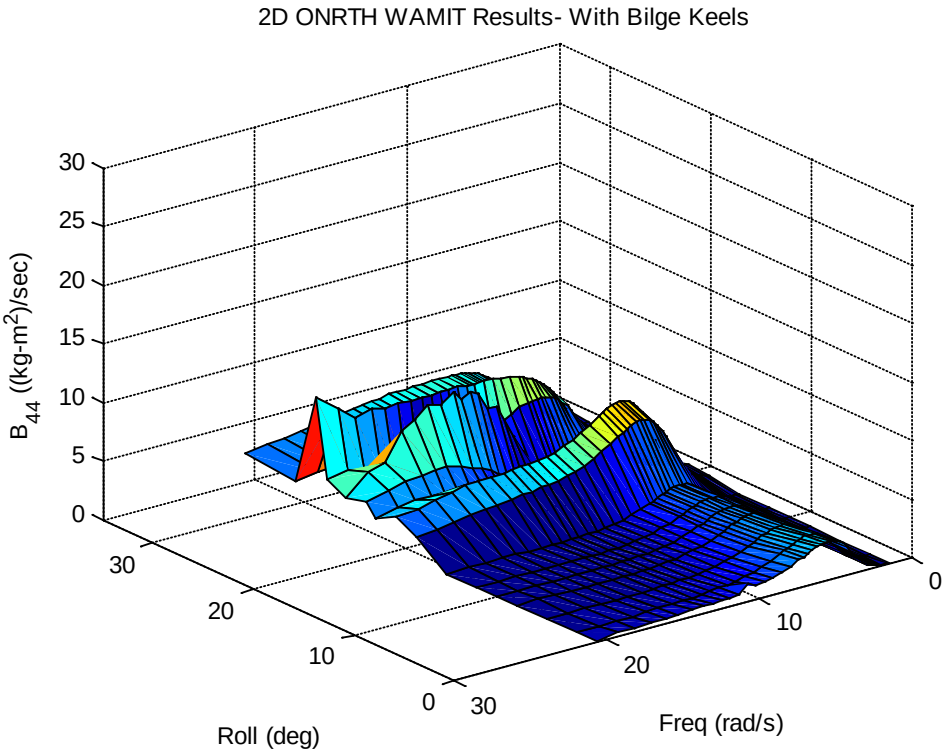

Figure E-30. Alternate view of ONRTH damping due to radiation vs heel angle vs frequency, with bilge keels

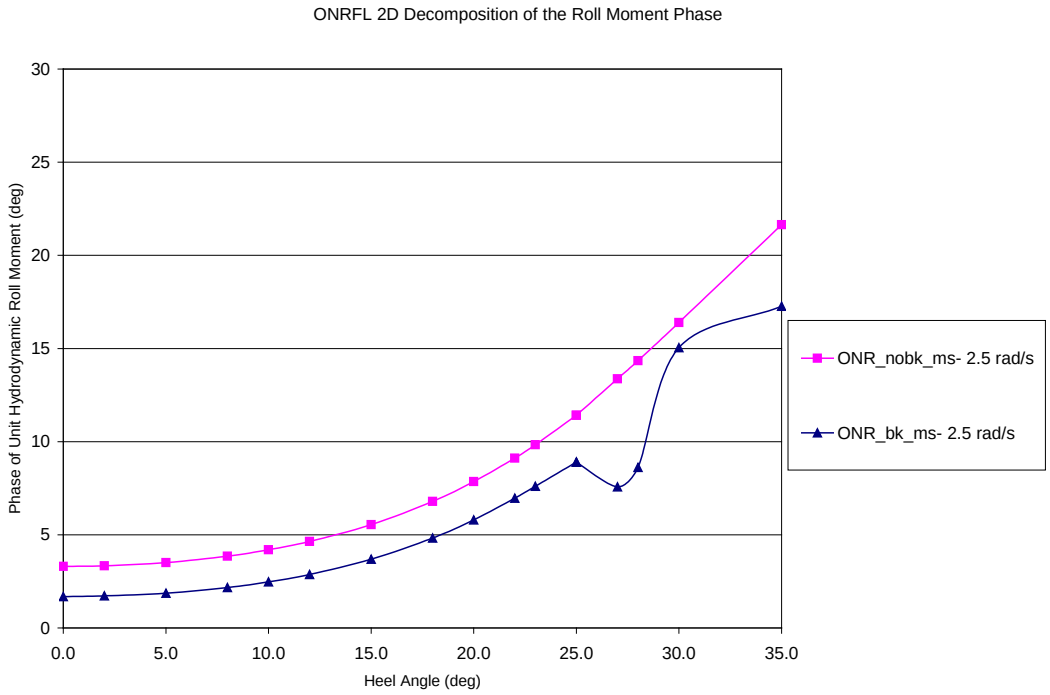

Figure E-31. Comparison of the phase of the unit hydrodynamic roll moment due to radiation for the ONRFL vs heel angle, for ω=2.5 rad/s, with and without bilge keels

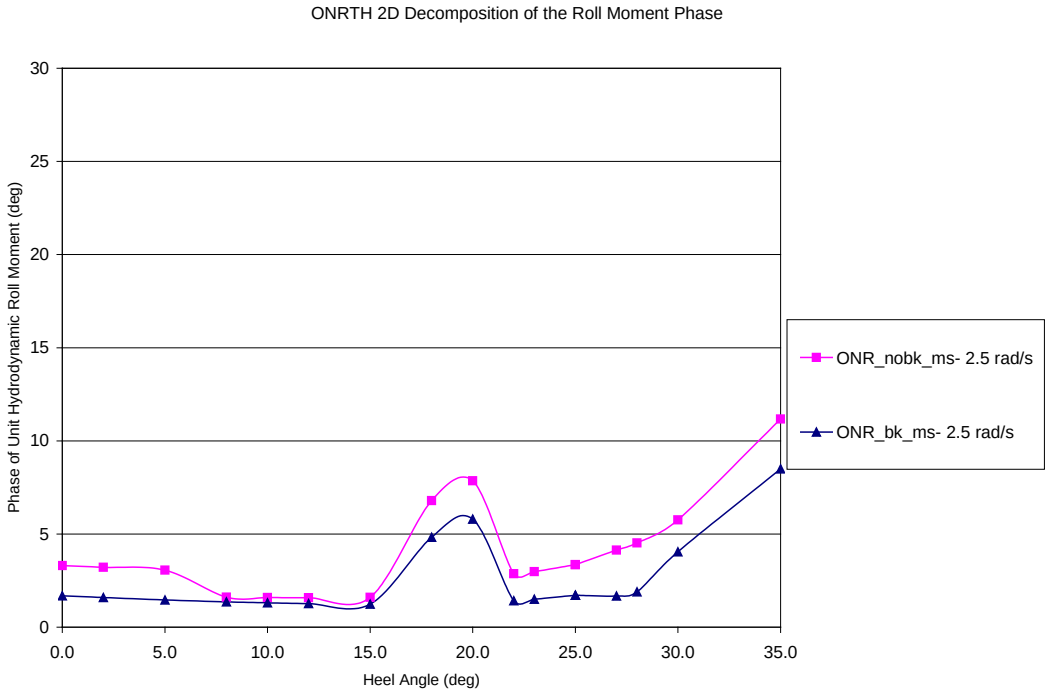

Figure E-32. Comparison of the phase of the unit hydrodynamic roll moment due to radiation for the ONRTH vs heel angle, for ω=2.5 rad/s, with and without bilge keels